# STIFFNESS AND STRENGTH OF FIBER REINFORCED POLYMER COMPOSITE BRIDGE DECK SYSTEMS

Aixi Zhou

Dissertation submitted to the Faculty of the
Virginia Polytechnic Institute and State University
in partial fulfillment of the requirements for the degree of

Doctor of Philosophy
in
Engineering Mechanics

John J. Lesko, Co-Chairman

Thomas E. Cousins, Co-chairman

Romesh C. Batra

Scott W. Case

Liviu Librescu

September 26, 2002

Blacksburg, Virginia, USA

**Keywords:** Bridge Deck, FRP Composites, Stiffness Analysis, Strength Analysis, Failure, Free Edges

# STIFFNESS AND STRENGTH OF FIBER REINFORCED POLYMER COMPOSITE BRIDGE DECK SYSTEMS

**AIXI ZHOU**

(ABSTRACT)

This research investigates two principal characteristics that are of primary importance in Fiber Reinforced Polymer (FRP) bridge deck applications: STIFFNESS and STRENGTH. The research was undertaken by investigating the stiffness and strength characteristics of the multi-cellular FRP bridge deck systems consisting of pultruded FRP shapes.

A systematic analysis procedure was developed for the stiffness analysis of multi-cellular FRP deck systems. This procedure uses the Method of Elastic Equivalence to model the cellular deck as an equivalent orthotropic plate. The procedure provides a practical method to predict the equivalent orthotropic plate properties of cellular FRP decks. Analytical solutions for the bending analysis of single span decks were developed using classical laminated plate theory. The analysis procedures can be extended to analyze continuous FRP decks. It can also be further developed using higher order plate theories.

Several failure modes of the cellular FRP deck systems were recorded and analyzed through laboratory and field tests and Finite Element Analysis (FEA). Two schemes of loading patches were used in the laboratory test: a steel patch made according to the ASSHTO's bridge testing specifications; and a tire patch made from a real truck tire reinforced with silicon rubber. The tire patch was specially designed to simulate service loading conditions by modifying real contact loading from a tire. Our research shows that the effects of the stiffness and contact conditions of loading patches are significant in the stiffness and strength testing of FRP decks. Due to the localization of load, a simulated tire patch yields larger deflection than the steel patch under the same loading level. The tire patch produces significantly different failure compared to the steel patch: a local bending mode with less damage for the tire patch; and a local punching-shear mode for the steel patch. A deck failure function method is proposed for predicting the failure of FRP decks. Using developed laminated composite theories and FEA techniques, a strength analysis procedure containing ply-level information was proposed and detailed for FRP deck systems. The behavior of the deck's unsupported (free) edges was also investigated using ply-level FEA.

# Dedication

*To my mother,*

*my father,*

*my brothers,*

*and my sisters,*

*whose love*

*I cherish*

# Acknowledgements

There are many people I would like to thank for their help and support on my Ph.D. study at Virginia Tech. Without their help, I would not have been able to accomplish this milestone so efficiently and with such good results. Especially, I would like to thank the following people and organizations for their assistances:

- **Dr. John J. Lesko,** my committee co-chair, academic advisor, mentor and friend during my study at Virginia Tech. It is Jack who brought me into the field of composite materials. It has been a great pleasure working with Jack over the past two and half years. His constant enthusiasm, encouragement, patience and optimism have always motivated me; his extraordinary ability to guide student in the right direction has always benefited me. Whenever I had trouble with my research or personal issues, Jack was always here helping me. I can't thank him enough.

- **Dr. Thomas E. Cousins**, my committee co-chair, for his time, patience and knowledge he provided in helping me complete my research. His perspective from the field of bridge design and analysis brought a great deal to my research.

- **Dr. Scott W. Case,** my committee member, for his time, knowledge and assistance for my PhD study and this research. His MRLife code and manual helped me a lot in calculating ply-level material properties.

- **Dr. Liviu Librescu,** my committee member, for his enthusiasm, encouragement and time to assist me develop plate analysis method for bridge deck analysis. His suggestions and help are invaluable to this research.

- **Dr. Romesh C. Batra,** my committee member, for his time serving in my committee, and his patience to read my research proposal and dissertation. His Continuum Mechanics class is one of the best classes I took at Virginia Tech.

- **Dr. Dean T. Mook**, my committee member until August 2002, for his time serving in my committee, and his patience to read my research proposal. Dr. Mook helped me plan my classes for my first semester at Virginia Tech. He saved me a lot of time by suggesting my exemption of taking Mathematics classes. (Dr. Mook was on leaving from Virginia Tech, he could not serve as a defense committee member.)

- **FHWA Innovative Bridge & Construction Program, and Virginia Department of Transportation,** for their funding and support to make this research possible.

- **Strongwell Corporation (Bristol, VA),** for providing testing decks.

- **Mr. Dave Sitton, Mr. Glenn Barefoot, Mr. Dan Witcher, and Mr. Clint Smith** of Strongwell Corporation, who assisted me in the microstructures and ply-level material properties of the deck components.

- **Dr. J. N. Reddy,** of Texas A&M University, for his assistance in calculation of plate deflection with various boundary conditions using the Rayleigh-Ritz method.

- **Dr. Vistasp M. Karbhari**, of University of California – San Diego, who allowed me to use the facilities at UCSD for my dissertation.

- **Mr. Marshal "Mac" McCord,** and **Mr. Robert Simonds,** lab technicians at the ESM department, who assisted me in working at the Material Laboratory in 107 Hancock Hall at Virginia Tech. Special thanks to Mac for his help with the simulated tire patch.

- **Mr. Brett Farmer and Mr. Dennis Huffman,** lab technicians of the Structures and Materials Laboratory at Virginia Tech, who helped with lab setups, equipment procurement and assembly for deck testing.

- **Ms. Shelia Collins, Ms. Beverly Williams, and Ms. Loretta Tickle,** the staff of the Materials Response Group and the ESM department, who have offered invaluable assistances during my study at Virginia Tech.

- **Jason Coleman, Anthony Temeles, Christopher Link, and Miguel Pando,** former and current graduate students of the Dept. of Civil and Environmental Engineering at Virginia Tech, for their friendship and their help with my research.

- **Ke An, Vasanthi Vinjamo, Xingyu Huang, Michael Hayes, John Bausano, Tim Schnniep, Steve Phifer,** and other former and current members of the Materials Response Group, for their friendship during my stay at MRG. I am so proud of being an MRGer!

- The many **faculty, staff and students of ESM department at Virginia Tech,** who have helped and inspired me along the way**.**

And finally, but most importantly, I want to thank my family and friends who have always supported and encouraged me. I would especially like to thank my mother and my father **("Ya and Baba")** for their steadfast love and encouragement. Thank you for everything you have done for me. You made a wild buffalo boy into a PhD degree holder. I would also like to thank my brothers and sisters **("Ge and Jiejie")**, for their constant love and support. It has been an invaluable fortune for me to have you as my brothers and sisters. I'm growing up every day, but I am always your "little brother".

**TABLE OF CONTENTS**

## FIGURES AND TABLES

# CHAPTER I

# INTRODUCTION AND REVIEW OF LITERATURE

## 1.1 Introduction

Society has searched continuously for new and better materials for building structures. New materials usually come to the stage due to the necessity to improve structural efficiency and performance. However, new materials in turn provide opportunities to develop new structural forms, and present material scientists and engineers with new challenges. One of the best manifestations of the abovementioned inter-related process is associated with Fiber Reinforced Polymer (FRP) composite materials in bridge applications to which this research is devoted.

In the past few years, FRP composite bridge deck systems have been experimentally implemented in bridge structures. World wide, there are many finished or currently underway FRP deck projects. However, an examination of the published resources shows that proper characterization methods and generally accepted design and analysis procedures of FRP bridge decks have not yet been established. While technical difficulties limit the development of affordable fabrication methods to produce low-cost, large-scale FRP bridge decks, the lack of comprehensive analysis and design codes and guidelines for FRP bridge decks is one of the key reasons that FRP decks have so far been applied only in demonstration projects.

To develop analysis and design guidelines and overcome any potential reluctance to use FRP decks, every potential aspect of deck behavior over its service life should be examined experimentally and analytically. There exist at least two principal characteristics that are of primary importance in FRP bridge deck applications, namely *stiffness* and *strength*. The *stiffness* of an FRP deck is the ability of the deck to resist changes in shape when a load is applied. In

FRP deck design, a deflection limit is usually used to consider the deck's stiffness. Deck *strength* is the deck's ability to resist permanent deflection from applied loads (static, dynamic and environmental loads etc.). The development of analysis and design guidelines is primarily based on the comprehension of the stiffness deflection and strength capacity characteristics of FRP deck systems. Other issues on the use of FRP decks, such as dynamic response, durability, efficiency and structural optimization etc., are also related to the understanding FRP deck stiffness and strength.

This research develops structural analysis (stiffness and strength) methodologies and proposes design and testing recommendations for the application of fiber reinforced polymer composite bridge deck systems. The research is undertaken by investigating the stiffness and strength of the adhesively bounded FRP bridge deck systems made from pultruded shapes. The work is also applicable to the analysis of other deck systems. The organization of this dissertation is in the following manner: Chapter I is the introduction and literature review of the research, which provides the general background of the development of FRP bridge decks. The objectives of this research are also proposed in this part. Chapter II presents current testing and characterization specifications and lab testing results. The Method of Elastic Equivalence (MEE) for obtaining overall equivalent plate properties of the deck system is developed in Chapter III. In Chapter IV, the application and verification of MEE will be addressed for the investigated deck system; orthotropic plate analyses for various boundary conditions will be detailed. Chapter V will cover the strength analysis of the FRP deck system, including failure function analysis, failure modes and failure mechanisms, and ply-level laminate composite analysis, and unsupported edges' effects. Chapter VI gives the contributions summary of this research and recommendations for future research on this subject.

This research will contribute to the development of a new bridge construction material – Fiber Reinforced Polymer Composites. As an introduction to bridge construction materials, we start this dissertation with a brief review of key engineering materials used in bridge engineering.

## 1.2 Key Materials in Bridge Construction

***Timber and Masonry*** Timber and masonry were dominant in bridge construction until the 19th century. The first bridges built were primarily constructed with wood. There is a renewed interest in timber bridges, specifically for portable or temporary bridges made from glued-laminated timber [Morgan et al. 1999, Wacker & Smith 2001]. Existing bridges with proven service life are masonry bridges. But as longer-spans are required, masonry is no longer appropriate, primarily because of its high weight to strength ratio and construction cost considerations.

***Metals*** There were various proposals for iron bridges during the 17th and 18th centuries, however, the technical and economic difficulties related to iron bridges were not overcome until 1780's with the construction of a cast iron arch bridge [Cusens & Pama, 1975]. In the early 1900s, steel became an economical and popular choice for bridge constructions. Today, four types of structural steels (structural carbon steel, high-strength low-alloy steel, heat-treated low-alloy steel, and high-strength heat-treated alloy steel) are commonly used for bridge structures. More recently, high performance steel's high strength provides greater potential economic benefit [Barker & Schrage 2000]. In recent years, research in the development of Aluminum shows that Aluminum bridge decks may prove to be an alternative to concrete decks for improving the performance of structural bridge systems [Starke & Williams, 1999].

***Concrete*** Concrete was probably already in use by the end of the 3rd century B.C. by the Romans [Davey, 1961]. The great availability and flexibility of concrete material and reinforcing bars have made the reinforced concrete bridge a very competitive alternative. Pre-stressed concrete structures using high-strength materials to improve serviceability and durability are an attractive alternative for long-span bridges, and have been used worldwide since the 1950s. Bridges built with high performance concrete (HPC) can have a service life of 100 years. Analysis of National Bridge Inventory data for structures built since 1950 shows that 17 % of steel bridges in the U.S. are considered "structurally deficient," while for reinforced concrete and pre-stressed concrete, the percentages are only 7 % and 4 %, respectively. More than 70 % of the bridges built today are made of concrete (NCBC, On-line website 2001).

***Composites*** Use of modern composite or hybrid material solutions has seen considerable interest in recent decades due to the significant potential in overall performance improvement. A composite material defined here is a material consisting of at least two different constituent materials with one or more materials as reinforcements and one or more materials as the matrix. Successful combinations of materials yield a synergism, where the performance of the material system is greater than the sum of the parts. In the last 50 years, extensive research made possible a better understanding of the fairly complex phenomena associated with FRP composite performance, design codes evolved significantly towards acceptance of more refined and effective design methods (particularly in aerospace applications), and constructional technology progressed at a brisk pace.

Fiber-Reinforced Polymer (FRP) composite is a relatively new area of composite material in bridge construction. In composites, the fiber reinforcement carry load in pre-designed directions and the polymer matrix acts as a medium to transfer stresses between adjoining fibers through adhesion and also provides protection for the material. This potentially gives the bridge designer a wide range of material choices to fit specific requirements of the bridge structures. In the following sections, detailed information regarding to the development of FRP composites in bridge engineering will be presented.

## 1.3 Fiber-Reinforced Polymer Composites in Bridge Engineering

Polymer matrix composites is a subdivision of the composites field in which the matrix is a polymer and the reinforcement is a fiber (continuous and discontinous). Fiber-reinforced polymer was patented in 1916 [Munley, 2000]. The first known FRP composite product was a boat hull manufactured in the mid 1930s [MDA, 2000]. In the 1940s and 1950s, FRP composite materials were widely used in the defense industry. Basic research in structural behavior of FRP composite sponsored by military was initially conducted in the 1950s. The benefits of FRP composites, especially their corrosion-resistance capabilities, were quickly communicated to the public sectors. Today, FRP composites applications have revolutionized many industries, including aerospace, marine, chemical processing, automobile, and electrical products.

FRP composites have been used as construction material for several decades. FRP composites were first used to reinforce concrete structures in the mid-1950s [MDA, 2000]. In 1976, the first FRP composite bridge was constructed in Israel [Munley, 2000]. In 1986, the world's first highway bridge using FRP composite reinforcing tendons was built in Germany, and the first FRP composite bridge deck was demonstrated in China [Karbhari & Zhao, 2000]. The first all-composites (FRP) pedestrian bridge was installed in 1992 in Scotland. In the U.S., the first FRP reinforced concrete bridge deck was built in 1996 at McKinleyville, West Virginia. In the same year, the first all-composite (FRP) vehicular bridge deck was installed in Russell, Kansas. Today, there are hundreds of finished and underway bridge projects using FRP composite materials all over the world. The application of FRP composites in these bridge projects can be summarized as two categories [Karbhari & Zhao, 2000]: 1) *Bridge Renewal*: primary areas are bridge structures rehabilitation (repair, strengthening and seismic retrofitting) and bridge superstructures (decks, girders) replacement. 2) *New Bridge Construction:* bridge structures made entirely of FRP composites (primarily for pedestrian bridges); concrete bridges with FRP rebar reinforcement, FRP wrapped concrete piles or pylons, and external FRP cable stays; protective or secondary structural systems etc.

High performance and innovative FRP materials developed in last century are finding further uses in the civil and bridge infrastructures. Currently, there are more vehicular bridge projects using FRP materials in the U.S. than in any other country. There are many FRP composite bridge deck projects supported by federal and regional DOTs and companies [Zureick, 1995]; notably among them are: North Carolina State University, California State University-Long Beach, West Virginia University, University of California - San Diego, University of Illinois – Urbana Champaign, Georgia Institute of Technology, Virginia Polytechnic Institute and State University, University of Wisconsin–Madison. The current goal of FRP bridge research is to use FRP composite to help rebuild the American transportation infrastructure and through the rehabilitation of the existing bridges [Tang & Podolny, 1998].

## 1.4 Fundamentals of FRP Composite Bridge Decks

### 1.4.1 What is an FRP bridge deck

A number of terms commonly used to describe a bridge's superstructure are illustrated in Fig. 1.1 [Wacker and Smith, 2001]. The components of the bridge above the bearings are referred to as superstructure, while the substructure includes all parts below. The main body of the bridge superstructure is known as the deck and girders/beams (Figure 1.1). An FRP bridge deck in this discussion is defined as a structural element made from FRP materials that transfers loads transversely to the bridge supports such as longitudinal running girders, cross beams, and/or stringers that bear on abutments.

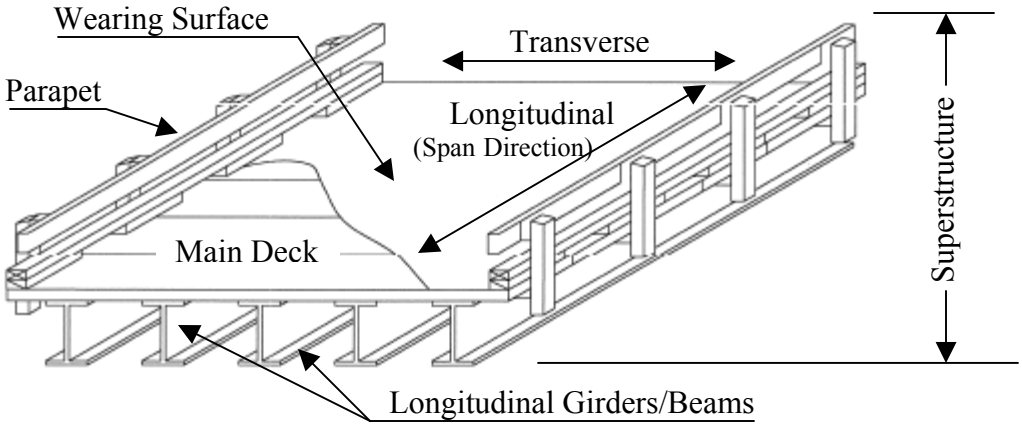


**Figure 1.1** Superstructure of a bridge illustrating bridge engineering terms [Revised from Wacker and Smith, 2001]

### 1.4.2 Why FRP composite bridge deck

The issue of deteriorating of civil infrastructure is increasingly becoming a critical concern across the world. A 2001 report on America's infrastructure provided by the American Society of Civil Engineers shows that as of 1998, 29% of the nations bridges were structurally

deficient or functionally obsolete. It is estimated that it will cost $10.6 billion a year for 20 years to eliminate all bridge deficiencies [ASCE, 2001]. Of all the deficient elements in a bridge superstructure, the bridge deck perhaps requires the most maintenance. It is estimated that [Karbhari et al, 2001] bridges in the U.S. on average last 68 years, whereas their decks last only 35 years; about half of the average bridge life. A similar deterioration and deficiency situation also occurs in many European and Asian countries. In addition to the problem of deterioration and deficiency, renewing bridges today often requires increased load rating over that for which the bridge was initially designed to accommodate increased traffic loads. Furthermore, bridge owners are seeking to repair or replace their bridges at lower costs and more quickly to reduce the impact to the traveling public. FRP bridge decks are believed to possess improved corrosion resistance. Their reduced weight enables rapid installation. In addition, the FRP material can be customized to dimensions of traditional decks and allows the economic reuse of existing support structures. The above-mentioned demands in bridge engineering have resulted in a significant deck replacement market and created tremendous opportunities for FRP bridge decks.

FRP deck research began in 1983 in the U.S. when the U.S. Department of Transportation initiated a research project titled "Transfer of Composite Technology to Design and Construction of Bridges". However, the results from these studies were scattered and unevaluated [Zureick, 1995]. In 1992, the FHWA initiated an investigation with the objectives of compiling and reviewing the literature pertaining to FRP bridge decks research studies. This review was published in 1995 [Zureick, 1995]. Since then, a number of papers and reports concerning research in FRP bridge decks have been published [Karbhari 1997, Lopez-Anido 1997, GangaRao 1999, Hays 2000, Qiao 2000, Zhou, 2001]. Today, the development of FRP decks has expanded beyond the academia. There are a number of companies developing and producing FRP decks [MDA, 2000].

### 1.4.3 Pultruded FRP deck systems

Current fabrication techniques for FRP vehicular bridge decks include: Pultrusion, Filament Winding, Vacuum Assisted Resin Transfer Molding (VARTM), Resin Infusion and Hand/automated Lay-up. FRP decks commercially available at the present time in the U.S. market can be classified according to two types of construction: sandwich structures and adhesively bonded pultruded shapes. The bridge deck investigated in this research is made from adhesively pultruded shapes.

The pultrusion process is the least expensive technique for fabricating high performance, constant cross section FRP structural composite parts. While pultrusion machine design varies with part geometry, the basic pultrusion process concept is described in the following schematic (Fig. 1.2). The process involves pulling raw materials through a heated steel-forming die using a continuous pulling device. The reinforcement materials are in continuous forms such as fiberglass mat and doffs of fiberglass roving. The reinforcements are saturated with the resin mixture ("wet-out") in the resin bath and pulled through the curing die. Upon exiting the die, a rigid, cured profile is formed that corresponds to the shape of the die.

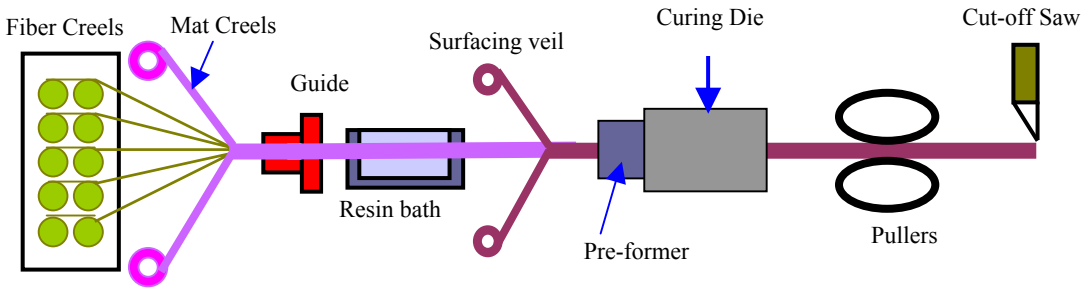


**Figure 1.2** Schematic Diagram of the Pultrusion Process

The product characteristics of pultruded shapes are shown in Table 1.1 [Mittal and Biswas, 2001]. Shown in Table 1.2 are six typical process faults and some of the process conditions that may cause them [Gibson et al, 1989]. These possible processing faults limit the development of affordable fabrication techniques to produce large-scale FRP deck systems.

**TABLE 1.1** Pultruded Product Characteristics

| | |
|---|---|
| Size | Forming system and pulling capacity influence size limitation |
| Shape | Straight, constant cross sections, some curved sections possible |
| Length | No limit |
| Reinforcement | Glass, aramid and carbon fibers, thermoplastic and natural fibers |
| Mechanical Strength | Medium to high, primarily unidirectional approaching isotropic |
| Labor intensity | Low to medium |
| Mould cost | Low to medium |
| Production rate | Shape and thickness related |

**TABLE 1.2** Process Faults That May Arise In Pultrusion

| **No.** | **Fault Type** | **Possible causes** |
|---|---|---|
| 1 | Birds Nest (Reinforcement build up around die entry, causes product to fail in die) | Upstream fiber Breakage. Catenary effects. High resin viscosity. Too much resin pick up. High pull speed. Poor die entrance design. |
| 2 | Cure Instability | High pull speed. Sudden backflow of hot resin. |
| 3 | Scaling (Poor surface finish) | Stress at debond point too high, causes stick-slip. Cure too advanced at debond point. |
| 4 | Die adhesive failure | Fiber volume fracture, filler content, or release agent content too low. |
| 5 | Under-cure | Speed too high, temperature too low or die too short. |
| 6 | Differential cure (Internal cracking due to internal cure lagging far behind surface) | Speed too high. Too large a thickness variation between different parts of the profile. |

Due to the technical difficulties of producing larger parts, some pultrusion companies have developed designs that make use of smaller pultruded module parts /shapes, such as prismatic or box beams and rectangular plates, bonded together to form a large bridge deck assembly. Design flexibility in this type of deck is obtained by changing the constituents of the shapes (such as fiber volume fractions and fiber orientations) and/or the structure forms (the

cross-section) of the shapes. Due to the potentially high cost of pultrusion dies and fiber guides, however, variations in the cross-sections of shapes are feasible only if sufficiently high production warrants the tooling investment. Materials in FRP decks differ primarily in the fiber architecture and resin type. Polyester resins are favored for their low cost, although vinyl ester resins are preferred in corrosive and wet environments. Woven and stitched fabrics are often employed for precise placement of multiaxial reinforcement. Some companies employ through-the-thickness braided preforms as the reinforcement for the triangular tubes.

Figure 1.3 shows typical cross-sections of FRP decks from bonded pultrusion components [Zhou et al, 2001a]: Cross-section of Fig. 1.3(a) is designed by Strongwell Corp.; Fig. 1.3(b) is the cross-section of the Superdeck by Creative Pultrusion, Inc.; Fig. 1.3(c) presents the DuraSpan FRP deck provided by Martin Marietta Composites, Inc.; While Fig. 1.3(d) is the cross-section of the EZSpan (Atlantic Research) FRP deck. Combining off-the-shelf plates and tubes of various sizes provides varied sections with performance suited to particular application requirements. The pultruded shapes are typically aligned transverse to the traffic direction. Each deck design has advantages in terms of stiffness, strength and field implementation.

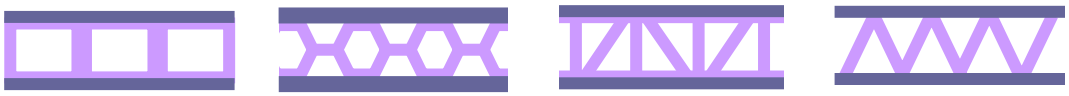

(a) (b) (c) (d)

**Figure 1.3** Typical cross-sections of FRP decks from pultruded components.

### 1.4.4 FRP deck comparisons

A technical comparison of available sandwich and pultruded FRP decks is shown in Table 1.3. Not surprisingly, there is greater flexibility with the sandwich-constructed decks to produce structures of varied depth and therefore stiffness. Weight per unit surface area is typically near 98 kg/m$^2$ with the exception of the corrugated core deck system (Hand/automated lay-up in Table 1.3) the reduced weight appears to suggest extra efficiency in the use of

materials. As indicated by the normalized deflections in Table 1.3 [Lesko et al, 2002, Zhou et al, 2001], there is no current consensus on deck deflections by the manufacturers. The discrepancy can be attributed to the way in which FRP bridge decks are currently designed – i.e. on a case-by-case basis.

**TABLE 1.3** Commercially Available FRP Deck Characteristics

| **Deck systems** *(Available in the U.S.)* | **Depth** *(mm)* | **[1]Weight** *($kg/m^2$)* | **Cost** *($\$/m^2$)* | **[2]Deflection** *Reported* | **[3]Deflection** *Normalized* |
|---|---|---|---|---|---|
| **Sandwich Construction** | | | | | |
| Hardcore Composites (VARTM) | 152-710 | 98-112 | 570-1184 | L/785 | L/1120 |
| KSCI (Hand/automated lay-up) | 127-610 | 76 | 700 | L/1300 | L/1300 |
| **Adhesively Bonded Pultrusions** | | | | | |
| DuraSpan | 194 | 90 | 700-807 | L/450 | L/340 |
| Superdeck | 203 | 107 | 807 | L/530 | L/530 |
| EZSpan | 229 | 98 | 861-1076 | L/950 | L/950 |
| Strongwell | 120-203 | 112 | 700 | L/605 | L/325 |

[1] Without wearing surface. [2]Assumes plate action. [3] Normalized to HS20+IM for 2.4 m center-to-center span.

Although limited field-experience and concerns over costs have slowed the introduction of FRP decks into mainstream bridge applications. The specifications for deflections have presented the greatest number of questions in the design of these systems. AASHTO [1996] contains recommended limits on superstructure deflections. The word "recommended" is in italics to emphasize that these are not allowable deflections imposed by AASHTO but rather they serve as guidelines that designers may exceed at their discretion [Temeles, 2001]. The reason that the deflection limits in AASHTO are optional is that, at present there are no definitive guidelines for the limits of tolerable static deflection or dynamic motion due to vehicular traffic. The deflection criterion most often cited in the FRP deck literature is L/800, where L is the center-to-center distance between supports [Temeles, 2001]. Many researchers have compared the deflection indices of their FRP bridge decks against the L/800 deflection index.

New alternative materials for bridge decks must be selected with great care and foresight over the conventional materials. Some technical criteria must be first satisfied, such as the

material's strength, stiffness and expected life of the structure under a set of defined environmental conditions. If these criteria are satisfied, the most important issue becomes the economics. Initial fabrication costs and weight comparisons for different deck systems based on a unit area are shown in Table 1.4 [Vistasp et al 2001, Zhou et al 2001a]. Costs for conventional systems include those for serving critical functions (barriers, wearing surfaces, and curbs, etc.), whereas those for composite systems are only for the fabrication of the deck itself [Karbhari 2001]. For glulam timber deck, the cost includes the materials, fabrication, treating, and shipping of the glulam bridges [Morgan 1999]. The comparison suggests that FRP decks are lightest among all available decks; one-fourth the weight of concrete decks. This presents an opportunity for rapid replacement and reduction in dead load, thus raising the live load rating of the structure. Clearly, initial costs for FRP decks are high. In terms of fabrication cost, $\$700/m^2$ appears to be the lower bound for current pultruded FRP decks. This cost is greater than the $\$322/m^2$ range typically quoted for the construction of a new bridge or a deck replacement with conventional materials.

**TABLE 1.4** FRP Deck Costs and Weight Comparisons

| **Type of decks** | **Cost** *( $/m^2$ )* | **Weight** *( $kN/m^2$ )* |
|---|---|---|
| Concrete (Cast-in-place, Precast) | 160-220 | 4.0-5.0 |
| Prestressed Concrete | 160-270 | 4.0-5.0 |
| Concrete filled steel grid | 220-270 | 3.5-4.0 |
| Half filled grid | 220-270 | 2.5-3.0 |
| Open grid | 270-325 | 1.0-1.25 |
| Aluminum orthotropic | 530-640 | 1.5-2.0 |
| Steel orthotropic | 640-860 | 4.0-4.5 |
| Glulam timer | 359-380 | 1.9* |
| FRP sandwich construction | 570-1184 | 0.75-1.1 |
| FRP adhesively bonded pultrusions | 700-1076 | 0.88-1.1 |

*: Preservative treated with creosote to a retention of 194 kg/m (12 lb/ft) in accordance with American Wood Preservers' Association Standard C14 (Morgan, 1999).

To overcome initial cost difference between the new materials and the conventional materials, a practical and economic method for evaluating alternative materials in a

comprehensive and consistent manner is needed. [Roychoudhury 2001]. Life Cycle Cost Analysis (LCCA) is defined as "a process for evaluating the total economic worth of a usable project segment by analyzing initial costs and discounted future cost, such as maintenance, reconstruction, rehabilitation, restoring, and resurfacing costs, over the life of the project segment" (FHWA, 2002).

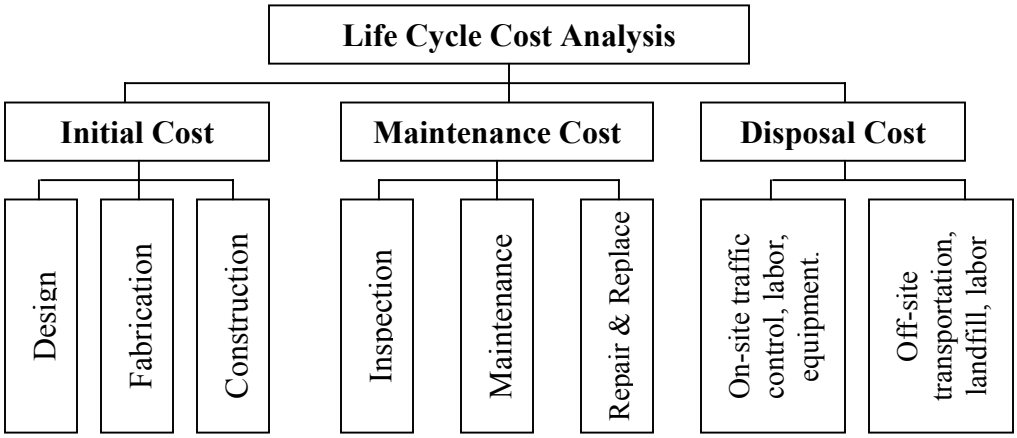


**Figure 1.4** Cost classification scheme for FRP bridge decks

Life cycle costs should be considered in terms of the major activities that occur in time during the entire life cycle of the bridge deck, namely the initial construction costs, the maintenance costs and finally after its useful life, the disposal costs (Figure 1.4). The central idea behind this kind of a cost classification scheme is that through this classification one considers all the cost components in the life cycle model, not only the direct costs (agency costs), but also the indirect costs (user and third party costs). However, due to technical difficulties in LCCA, no FRP bridge project has been implemented using this approach. The use of LCCA is also limited by the fact that state and federal government do not appropriate funds on a LCCA basis. The development of LCCA for FRP bridge deck systems is currently underway.

## 1.5 Development of FRP Deck Systems

To develop effective FRP deck systems, research pertaining to design and analysis of FRP decks should be fully considered. Analyzing an FRP bridge deck system requires full knowledge of the geometric properties and the material properties. The geometric properties are obtained in the design stage of the deck system. The material and mechanical properties of FRP decks are usually obtained though experimental characterization of the mechanical properties at the coupon, component, and full deck scale levels. In the following section, the development of FRP deck geometric configuration and deck characterization techniques will be reviewed. Also, available analytical models for structural analysis of FRP decks will be presented.

### 1.5.1. FRP Deck Configurations

The first FRP deck research programs conducted in the U.S. were limited to the development of conceptual design protocols. The preliminary work reported by Henry [1985], Ahmad and Plecnik [1989], and Plecnik and Azar [1991] examined the performance of several glass fiber reinforced polymer bridge deck configurations by means of finite element analysis. In their research, an FRP deck behaves as a truss member in the direction perpendicular to the traffic flow, and a flexural member in the direction parallel to the traffic flow. The results indicate that the design was always controlled by the deflection limit state rather than the strength limit states. The X-shaped bridge deck, Type II in Figure 1.5 (a), appeared to have the lowest deflection and satisfied the deflection limit, L*/800 (*where *L* is the stringer spacing, i.e., the center-to-center distance between deck supports).

Bakeri and Sunder [1990] used balanced symmetrical lamina to investigate analytically the feasibility of a number of FRP bridge decks that consisted of different material systems. Two different systems were investigated: 1) the entire deck was assumed to made of glass-reinforced polymer; or 2) decks constructed from hybrid materials. They concluded that the hybrid concept composed of glass-reinforced polymer, carbon fiber-reinforced polymer, and light-weight

concrete resulted in a bridge deck system having a deflection less than L/800. Their study indicated that a hybrid FRP/concrete system a promise in infrastructure applications.

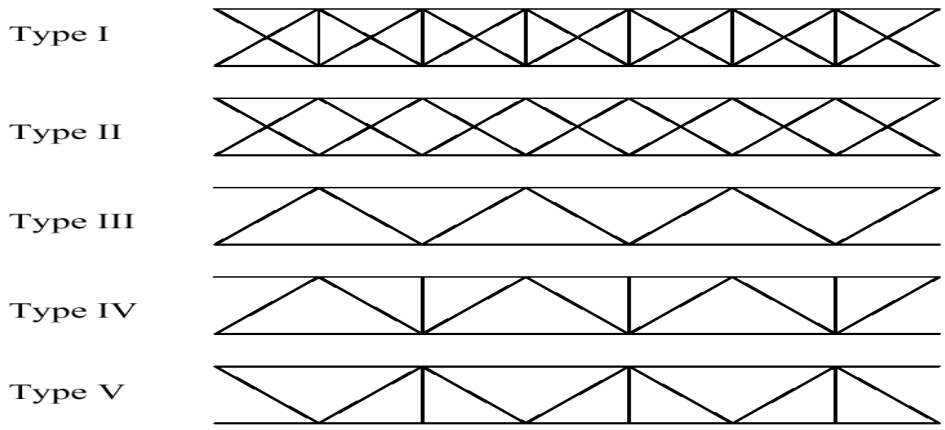


**Figure 1.5** FRP deck cross-section configurations analyzed by previous researchers [Temeles, 2001]

McGhee et al. [1991] presented results of the least-weight design of four cross-section types of FRP bridge decks subjected to AASHTO loading. Types I, II, and III (shown in Fig. 1.5 (a)), as well as a slightly modified version of type IV, were investigated. The mathematical optimization problem was formulated such that the objective function was represented by the weight of the bridge deck while the behavioral constraints including ultimate strength, local buckling, and L/800 deflection limit state. The study concluded that the type III cross section was the most efficient design.

A design and performance analysis of a modular FRP bridge deck manufactured using filament winding process was presented by Aref and Parsons [2000]. The deck is the conceptual design of a composite highway bridge superstructure. All of the results presented in this paper are based on finite element analysis. The comparison of this design with the Lockheed Bridge [Seible 1996] shows similar behavior with dead-to-live load ratios of 0.34 (this design) and 0.36 (the Lockheed design). Moreover, a significant margin of safety is manifested in this design. Three models were designed to compare with the bridge presented by Dumlao et al. [1996].

Zureick [1997] conducted Finite Element analyses on FRP decks with box-shaped cells (Figure 1.6). The deck models considered were 8 feet long by 11 inches deep. They were all simply supported (40-foot span) on two stringers and subjected to one "wheel line" (not an axle) of an AASHTO HS20-44 truck. Four different cases were considered, where fiber directions and orientation of cells were the variable parameters. It was found that the design of this type of FRP deck was always controlled by deflection. After concluding that the box-cell and V-cell deck were optimum, the author tested these designs at larger stringer spacing. At 10-foot and 12-foot stringer spacing, none of the decks were able to satisfy the L/800 deflection index.

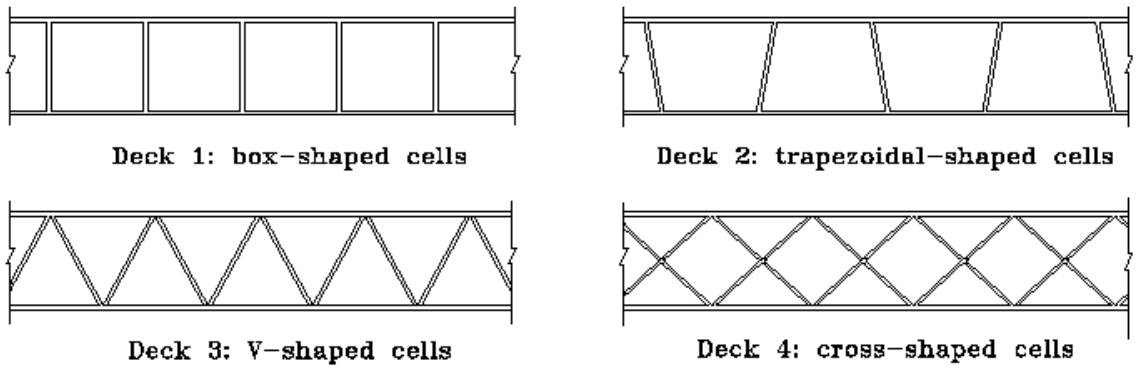


**Figure 1.6** Sections of the FRP deck panels analyzed by Zureick [Temeles, 2001]

A multi-cellular FRP composite bridge deck constructed from adhesively bounded box beams has been developed in West Virginia University [Brown 1998]. Under this research effort, two FRP decks were fabricated. The decks and bridge systems were tested under static loads for various boundary conditions (3-point bending and 4-point bending). The study includes design, modeling and experimental/numerical verification of FRP composite decks and deck-and-stringer bridge systems. Another FRP deck panel composed of hexagonal shaped and double-trapezoidal cells was developed by researchers at West Virginia University in 1999 [GangaRao et al, 1999]. The hexagonal and double-trapezoidal components were composed of E-glass fibers embedded in a vinylester resin. Prior to field installation of the bridge decks, static and fatigue tests were conducted on smaller scale models.

Since the mid 1990s, Virginia Tech has worked with Strongwell Corporation (Bristol, Virginia), Federal Highway Administration and Virginia Department of Transportation to develop and test FRP composite deck panels made from pultruded, off-the-shelf components [Hayes, 1998]. This deck system utilizes square tubes running transverse to the traffic direction, mechanically fastened and adhesively bounded together to form a FRP deck panel. This panel is bounded with two skin plates, top and bottom, using epoxy adhesives to form a FRP deck. The prototype FRP composite deck system [Hayes, 1998] has been updated, and under further investigation by Temeles [2001], Zhou et al. [2001], and Coleman [2002]. The cross section of this FRP deck system is shown in Fig. 1.7. The FRP deck system is fabricated from standard EXTREN® structural shapes and plates. The deck is 4.65m (15'3") in length and 1.52m (60") in width, composed of ten 15.24cm×15.24cm×0.95cm (6"×6"×3/8") pultruded orthotropic box beams (or square tubes), one bottom plate, one top plate, wearing surface and 12 transverse steel bolts. One advantage of this deck assembly is the use of off-the-shelf FRP components. Which is unique to the industry, where specific design and tooling are required to construct a deck.

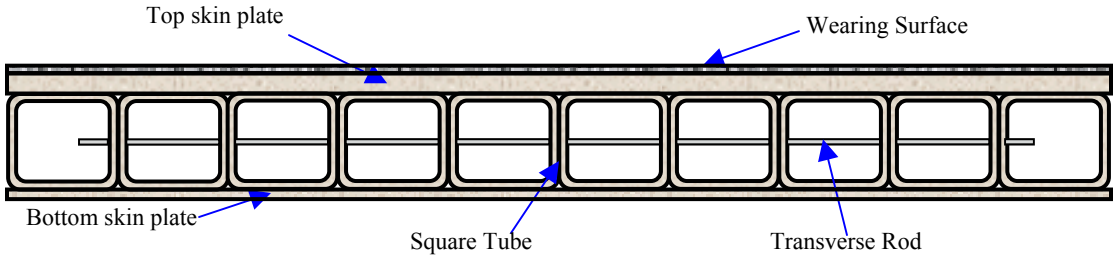


**Figure 1.7** Cross section of the FRP deck in this research

## 1.5.2 Characterization of FRP deck systems

To characterize the mechanical and material properties of FRP composite bridge decks, lab tests on coupons, components, and full deck scale sections have been conducted in several research groups. This discussion will review previous work on experimental characterization of

the mechanical and structural properties of FRP decks. The review will concentrate on these FRP deck components made from adhesively bonded pultrusions only.

In the early 1990s, the FRP deck research group in West Virginia University conducted comprehensive characterization of thin-walled FRP sections [Salim, 1996]. Micro/macro-mechanics models were investigated to allow the modeling of pultruded composite sections. The laminate and beam stiffness properties were predicted by these models. The laminate stiffness was verified by coupon tests in tension and torsion, and the beam stiffness are verified by 3-point, 4-point, and cantilever bending tests. This research was continued by Brown [1998] with the characterization and analysis of a cellular FRP deck system. In Brown's study, a combined analytical and experimental study of FRP composite bridges consisting of cellular box decks and wide-flange I-beam as stringer was presented. The study includes design, modeling and experimental/numerical verification of FRP composite decks and deck-and-stringer bridge systems. A finite element modeling was used to verify the accuracy of design analysis. Based on the analytical/experimental study, simplified design equations were developed for bridge applications, which include global design of deck-and-stringer system accounting for load distribution factors. GangaRao etc. [1999] investigated another FRP deck with hexagonal cells after Brown. First, a 36-inch (914mm) long (traffic direction) deck panel (9' [2743mm] simply supported span) was loaded at a rate of 3 cycles per second up to 2 million cycles. The load range was 2 to 35 kips (156 kN). The load was applied to the deck over a rectangular patch. 20-inch by 10-inch (508mm×254mm) area. After every 500,000 cycles, a static load test was conducted to see if the deck panel had lost any stiffness. Next, two static load-to-failure tests were conducted. The first test was done on the previously fatigued deck while the second test was conducted on a deck panel that had no prior load history. No visual damage was observed after termination of the fatigue test, and less than 4% loss in stiffness of the deck was recorded. The previously fatigued deck panel failed at a load of 124.5 kips and exhibited a maximum deflection (at time of failure) of 1.54 inches (39mm). The second deck panel failed at a load of 126.7 kips (563 kN) and experienced a peak deflection of 1.57 inches (40mm).

An experimental characterization of the mechanical and structural properties of an FRP bridge deck composed of bounded triangular tubes with top and bottom face plates was

addressed by Costa [1999] at Georgia Institute of Technology. Two reinforcement schemes were used in this research: 2-D non-crimp stitched fabrics, and 3-D braid. The mechanical and structural properties were characterized at the coupon, element, and full deck scale levels. At the coupon level, tensile, compressive, and flexural tests were conducted on coupons of various widths to examine the inhomogeneity associated with the 3-D braided perform combined with roving. The results of these tests were then calibrated with those obtained using classical laminate theory to derive a reliability-based reduction factors that accounts for the uncertainties associated with the material property, manufacturing, and dimensional variability. At the element level, three- and four- point bending testing, using a gravity load simulator for applying the load; was proposed to examine not only the material and dimensional non-uniformity but also the structure response of the element under transverse loading. At the full-scale level, experiments were carried out to characterize the flexural response of bridge deck panels. An engineering approach for predicting the deflection, strains and stresses of FRP deck panels was also proposed.

Since 1999, comprehensive field and laboratory tests of FRP bridge decks fabricated from pultruded FRP components were conducted at Virginia Tech [Temeles, 2001 and Coleman, 2002]. In Temeles' research, two 7" (177mm) thick FRP deck panels were manufactured and tested in a controlled service environment. The deck panels were 15' by 5' (4572mm×1524mm) rectangular panels, and were composed of ten 15' (4572mm ) long, 6"×6" ×3/8" (152×152×9.5mm) standard pultruded FRP tubes. The tubes were sandwiched between two 3/8" thick standard pultruded FRP rectangular plates. The cross-sections of the decks are shown in Fig. 1.11. The material constituents of the FRP were E-glass fibers in a polyester matrix. When subjected to two strength tests, the first deck panel exhibited a safety factor with respect to legal truckload of greater than 10. The second deck was subjected to AASHTO design loads under a simulated HS-25 axle with impact effects. The deck exhibited a maximum deflection of L/470. Both FRP decks exhibited elastic behavior well beyond legal loads. The factor of safety between failure loads in the lab tests ranged from 8.5 (deck loaded at an unsupported edge) to 13.2 (deck loaded in the middle of one of the spans). After being subjected to approximately 4 million load cycles (assuming 100,000 5-axle truck crossings per month) over a period of 8 months, the deck exhibited no loss in stiffness. In two post-service strength tests, the second deck exhibited a

safety factor with respect to legal load of greater than 8. However, the author was uncertain what importance to attach to the deflection results. It's pointed out that deflection criteria could be required for FRP composites, but this would certainly require further research. The author's results showed that FRP decks are governed by stiffness rather than strength. In failure tests of the whole deck, the failure mode for the FRP decks was punching shear (Fig. 1.12) when loaded in the middle of its span.

**Figure 1.8** Punching failure using steel patch
[Temeles, 2001]

### 1.5.3 Structural analysis of FRP bridge decks

A major obstacle to the design of FRP bridge decks is the lack of simplified structural analysis and design principles. A systematic structural analysis of the deck system will ensure the serviceability of the deck system and build our confidence to simplify/optimize the deck structure to reduce the fabrication cost. Structural analysis methods for bridge decks are shown in Table 1.5. Current analytical and design tools developed for conventional materials cannot be directly used for FRP shapes due to the orthotropy of FRP materials. Numerical methods such as

finite element analysis (FEA) are often difficult to use, require specialized training, and are not always accessible to design engineers. Thus, there is a need for a simplified design procedure for FRP bridge deck systems.

**TABLE 1.5** Applicability of analyses for bridge decks

| | Beam method | Orthotropic plate theory | Folded Plate method | Space frame method | Planar grillage method | Finite difference method | Finite strip method | Finite element method |
|---|---|---|---|---|---|---|---|---|
| Deck Type | | | | | | | | |
| Slab | x | x | | | x | x | x | x |
| Slab & Beam | x | | | | x | | x | x |
| Box | x | | x | x | x | | x | x |
| Cellular[1] | x | | x | x | x | | x | x |
| Composite[2] | | x | | | x | x | x | x |
| Orthotropic | | x | | | x | x | x | x |
| FRP | x | x | | | | | | x |
| Geometry | | | | | | | | |
| Right | x | x | x | x | x | x | x | x |
| Skew > 20° | | | | x | x | x | | x |
| Curved | | x | | x | x | x | x | x |
| Arbitrary | | | | x | x | x | | x |
| Support | | | | | | | | |
| (S.S.)Simply Supported | x | x | x | x | x | x | x | x |
| S.S. with intermediate supports | x | x | x | x | x | x | x | x |
| Arbitrary | x | | | x | x | x | | x |

[1]Concrete Cellular; [2] Steel-concrete or steel-timber composite.

Mechanics-based methods for designing section properties of a composite shape were detailed by Barbero et al. [1993]. Available analytical theory for whole bridge deck system analysis is based on Huber's theory [Troitsky, 1967]. The basic assumption proposed by Huber for estimating overall bending deflections and bending stress in a stiffened slab, is to replace such a slab to an equivalent orthotropic slab/plate of constant thickness having the same stiffness characteristics. The substitution of the orthotropic plate with the same stiffness characteristics as a stiffened plate is called Method of Elastic Equivalence (MEE). By this method, the structural orthotropy is represented by natural (or material) orthotropy. These mechanics concepts can be translated into approximate methods for estimating the equivalent orthotropic plate behavior of FRP decks. The analysis procedures based on MEE for FRP decks developed by Salim et al [1997, 1999], Brown [1998] and Qiao et al [2000] were for short span decks, or decks with close

supported stringers with two opposite edges simply supported and the other two edges free. In Brown's analysis [Brown, 1998], the MEE procedure was verified with the results obtained through beam analysis and experimental data with 1 and 2 cells. Analyses for decks with mid-span and various boundary conditions are not yet available.

In plate level analysis, composite laminated plate analysis methods can be used as analysis methods for FRP bridge deck analysis after the introduction of MEE. In this procedure, a bridge deck is considered as a statically equivalent, single layer plate having an orthotropic constitutive behavior, and the global bending stiffness and torsional stiffness of the equivalent plate are obtained from the FRP decks using systematic methods for different kinds of deck configurations. By this method, the analysis of an FRP deck becomes the analysis of a single-layer composite laminate plate. The analysis of composite laminated plates in the past have been based on one of the following approaches [Reddy 1997; and 1999]: (1) 2-D equivalent single-layer theories: Classical laminate theory and shear deformation laminate theories; (2) 3-D elasticity theory: Traditional 3-D elasticity formulations and layer-wise theories; and (3) Other 2-D and 3-D multiple model methods. In the 3-D elasticity theory or in a layer-wise theory, each layer of the laminate is modeled as a 3-D solid. While the equivalent single-layer (ESL) theories are derived from the 3-D elasticity theory by making suitable assumptions concerning the kinematics of deformation or the stress state through the laminate. These assumptions allow the reduction of a relatively complicated 3-D problem to a simpler 2-D problem. The classical laminate plate theory and the first-order shear deformation theory are the simplest ESL theories, and they adequately describe the kinematic behavior of most composite laminated plates.

The strength analysis of FRP decks requires the prediction of local stress and strain distributions, typically at the ply-level, since the deck failure always occurs locally, and for FRP material, the strength is determined by ply-level configurations. The local stress and strain distribution of currently used thin-walled multi-cellular FRP decks, sandwich construction and pultrusions, can not be accurately predicted by the equivalent plate method, since this method neglects the local structural effects and consider the whole deck as an statically equivalent plate. The comparison of test results for adhesively bonded pultrusion FRP decks to analytical results obtained from the Equivalence Plate Method (EPM) and complete 3-D finite element analysis

shows that the complete FEA model gives far more accurate results for the structural analysis of this multi-cellular FRP deck [Zhou et al. 2001]. From the complete analysis, significant strain concentrations at the locations throughout various cellular deck systems are observed that cannot be described by the equivalent orthotropic plate theory. A revised analytical model is necessary to predict the observed phenomena. This research indicates that, in addition to global deck deflection criteria, local criteria considering strain/stress concentrations should be imposed to the strength analysis and strength design thin-walled cellular FRP decks. The situation is the same for sandwich FRP decks in local and detailed analysis. To represent local stress/strain states of FRP deck systems, models for local analysis should be developed. The available and effective ply-level strength and failure analysis technique for complex structures can be solved using finite element analysis with composite elements. The ply-level laminated composite analysis using FEA should be conducted to investigate the deck's ply-level strength and failure analysis. Since polymeric composites' matrix is much softer than traditional materials, such as concrete or steel, the effects of the surface contacting and loading conditions will affect the strength and failure of FRP decks.

### 1.5.4 Design guidelines development for FRP decks

Though there is no generally accepted principles for current FRP bridge deck design, the general philosophy is that the designed FRP system must have high stiffness and strength to ensure proper performance and safety with expected life of the structure under a set of defined environmental conditions. In addition, the deck system shall be designed to avoid catastrophic failure under impact, collision, or fire etc [GangaRao et al, 1999].

Clearly, each of the completed bridge deck project using FRP composite was guided by specific design requirements and criteria, but few attempts have been made to formulate comprehensive national and international standards. However, a number of professional organizations have been addressing the recommended use and specification of FRP composites.

The summary of Codes, Standards & Specification Committees for FRP composites is shown in Table 1.6 [MDA 2000]. Several ASTM committees are currently working on consensus test methods for the use of rebars, repair materials, and pultruded structural profiles. ASTM committee D20.18.02 is focused on the development of test methods for FRP pultruded profiles and shapes. ASTM committee D30.30.01 (Composites for Civil Engineering) addresses FRP composites products used in construction. The American Association of State Highway and Transportation Officials (AASHTO) Committee on Bridges and Structures established the Technical Committee for Fiber-Reinforced Polymer Composites (T-21) in 1997. This committee has an ongoing effort to develop design guidelines for the use of composites in bridge applications including FRP reinforced concrete, concrete repair, and vehicular bridge deck panels. Several global activities are underway to implement FRP composites materials and products into respective design codes and guidelines.

**TABLE 1.6** Standards Committees for FRP composites

| ORGANIZATION | COMMITTEE |
|---|---|
| American Concrete Institute (ACI) | 440 – Composites for Concrete; 440F – Repair; 440H – Reinforced Concrete (Rebar); 440L – Durability |
| American Society of Civil Engineers (ASCE) | Structural Composites and Plastics |
| American Society for Testing and Materials (ASTM) | D20.18.01 – FRP Materials for Concrete;<br>D20.18.02 – Pultruded Profiles<br>D30.30.01 – Composites for Civil Engineering |
| American Association of State Highway and Transportation Officials (AASHTO) | Committee on Bridges and Structures, T-21 – FRP Composites |
| International Federation of Structural Concrete (FIB) | Task group on FRP |
| Canadian Society of Civil Engineers (CSCE) | Advanced Composite Materials for Bridges and Structures |
| Japan Society of Civil Engineers (JSCE) | Research Committee on Concrete Structures with Externally Bonded Continuous Fiber Reinforcing Materials |
| Transportation Research Board (TRB) | A2C07 – FRP Composites |

Through the above, it's apparent that codes and design guidelines for the application of FRP composites in civil engineering is under development. There are no universally accepted codes or design guidelines for FRP bridge deck systems. It is suggested that design guidelines for the United States need to be developed and based on well-defined performance criteria, rather than

on material or process specifications [FHWA, 1997]. It is difficult to assess all aspects and implications of the specific design approaches encountered, but the following list highlights some general impressions of the state of design using advanced composite materials in bridge applications [FHWA, 1997]: (1) The high strength and relatively low modulus of affordable advanced composites often result in designs that are stiffness driven and do not fully utilize the strength of the material; (2) Thin FRP laminates, overlays, or members need to be checked and designed for local stability and may require stabilization with structural foam cores or stiffeners; (3) Loss of strength or aging of certain FRP composites under sustained loads, referred to as "stress corrosion," seems to be a potential problem and should be addressed as part of the design process; (4) Cyclic load and fatigue characteristics of FRP composites seem to exceed those of other materials, as long as the stress range and the mean stress do not facilitate stress corrosion; (5) High temperature and fire response characteristics can be controlled by resin additives and coatings and can be comparable to or better than those for conventional materials, such as steel; (6) Durability of advanced composite materials under the typical civil engineering environments still requires a broader database, both from accelerated tests and long-term exposure tests, before durability can be used as a dominant design parameter; (7) Because of the multitude of fibers and fiber architecture, resins and resin formulations, and manufacturing processes for advanced composite materials, strict performance specifications--not material or process specifications--are needed to ensure safety and serviceability; (8) In the design process, more emphasis should be placed on the lightweight property of FRP composites and simplifications that can be derived from this characteristic in the construction process; (9) Detailed cost/benefit models, including maintenance and lifecycle data, should be developed, both for advanced composite materials and conventional materials to provide rational bases for choices of materials.

## 1.6 Objectives of This Research

A relatively large number of FRP decks are already in service [GangaRao et al. 1999, Harik et al. 1999, Temeles 2001] and several others are scheduled for installation in the near future [Davalos et al 2001, Coleman 2002, Zhou et al 2001, Zhao et al 2001, Zhou et al 2002, Cheng et al 2002]. Also, there exists a growing interest in the community on the future of these structures. However, the following technical challenges are critical for today's FRP deck development: (1) development of FRP deck design standards and guidelines; (2) efficient design and characterization of deck-to-deck joints and attachment of decks to stringers; (3) fatigue behavior of decks and connections; (4) failure mechanisms and ultimate strength of FRP deck systems, including local and global buckling modes; (5) durability characteristics under combined mechanical and environmental loads; and (6) efficiency and durability of deck surface overlays. In addition, it's long been realized that the dynamic response of the bridge may be the major factor that influences its long-term behavior [Wang, 1992]. The published resources showed that little experimental and analytical work has been done on the dynamics of FRP deck systems. The effect of dynamic response of FRP deck on the overall behavior of such system also needs to be investigated.

According to AASHTO LRFD specifications, the general design philosophy of bridge system is that the system shall be designed for specified limit states to achieve the objectives of safety, serviceability and constructability with regards to the issues of inspectability, economy and aesthetics. These limit states can be defined in three general categories: Functionality Limit States (Deformation, Dynamic Response, etc.); Safety Limit States (Strength, Stability, etc); and Performance Limit States (Repair, Fire Resistance etc.).

FRP deck systems shall be designed under this philosophy. The overall objective of this research is to establish stiffness and strength analysis methodologies for FRP bridge deck systems, and also provide recommendations for stiffness and strength design. To achieve this goal, more specific objectives are as following:

1. To develop practical approaches for predicting global characteristics (stiffness, deflection criteria) of the whole FRP deck system from manufactured deck components.

2. To develop an engineering method/procedure for stiffness analysis (plate bending analysis) of FRP deck systems, and verify this method with numerical and experimental results.

3. To propose stiffness testing and design recommendations for FRP bridge decks.

4. To investigate the failure modes and failure mechanisms of thin-walled multi-cellular FRP deck systems through testing and numerical simulation.

5. To propose a ply-level analysis philosophy and procedure for laminated FRP bridge deck strength analysis and failure analysis.

6. To propose testing and design recommendations for strength that influence the durability of FRP decks.

# CHAPTER II

# TESTING OF FRP COMPOSITE BRIDGE DECKS

In this chapter, the experimental characterization specifications and testing design for whole FRP deck systems will be provided. Then, testing results obtained from a specially designed FRP deck panel will be presented and discussed.

## 2.1 The Investigated Deck Panel

The cross section of the design is shown in Fig. 2.1 [Zhou et al 2001, Coleman 2002]. The deck is 4.65m (15'3") in length and 1.52m (60") in width, composed of ten 15.24cm×15.24cm×0.95cm (6"×6"×3/8") pultruded orthotropic box beams (or square tubes), one 0.635cm (¼") thick orthotropic bottom plate, one 1.27cm (½") thick orthotropic top plate and 9 transverse steel bolts (the rods were used for fabrication purpose, see following for details). The deck weights about 726 kg (1,600 lbs), with the density of about 910.3 kg/m$^3$.

The fabrication of this deck panel through its components is as follows [Zhou et al, 2001b]: First, holes are drilled for thru-bolt rods in the sidewalls of the square tubes, and internal plugs or hole reinforcement are inserted. Then, epoxy adhesive is applied per manufacturer's instructions. The tubes are positioned and clamped on a flat table and then the threaded rods are installed. Nuts are tightened on rods to close the joints between the tubes. The joined tube assembly is cured sufficiently before handling. Top and bottom surfaces of the tube assembly are abraded after curing. The skin plates are sanded to remove the surface veil. Using complete vacuum bagging, the tube assembly is bonded together with the top and bottom skin plates. The tube assembly and plates are allowed to cure sufficiently. The last step is to apply a wearing

surface, which is composed of multi-layers of vinyl ester resin and aggregate. The resin is proportioned, mixed, and applied per manufacturer's instructions. One attractive feature of this deck is that the thickness, modulus and other properties of the top and bottom skin plates can be customized to various applications with different stiffness requirements.

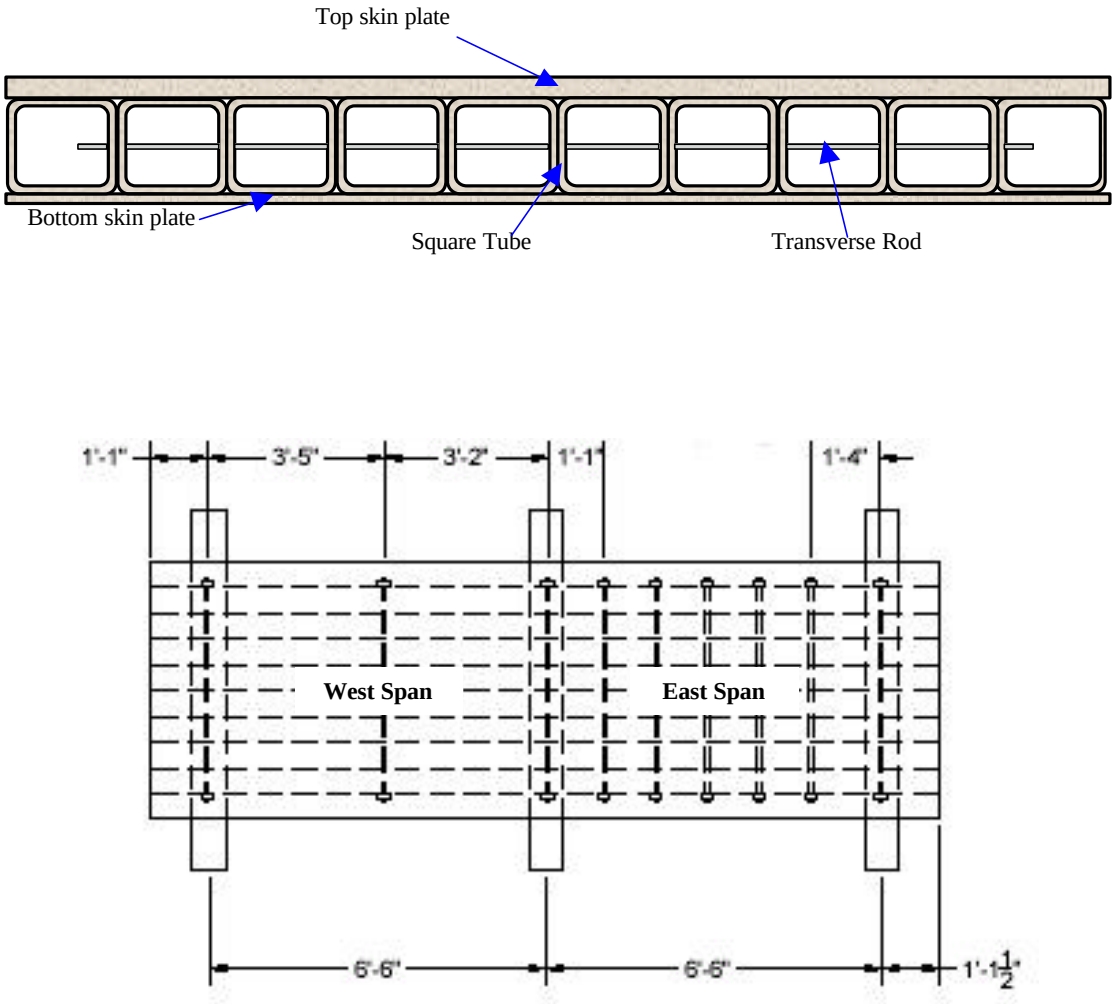


**Figure 2.1** Deck cross section and transverse rods

[Zhou et al 2001b, Coleman 2002]

## 2.2 Specifications for FRP Deck Testing

To date, no official specifications have been proposed for FRP bridge superstructure design and testing. However, the design load and tire contact area specified in AASHTO's Standard Specifications for Highway Bridges [AASHTO, 1996] and the AASHTO LRFD Specifications [AASHTO, 1998] have been used for lab testing by most FRP deck researchers [Temeles, 2001].

According to AASHTO's 16th Edition of Standard Specifications for Highway Bridges [AASHTO, 1996], when designing the superstructure members of a bridge, the specified loads are applied in critical locations to produce the maximum load effect. The load that produces the largest stress is considered to be the design load. Bridge designers can apply the design wheel load over a finite surface area of the deck in computing the load effects in a *reinforced concrete* bridge deck. This area is defined as the "tire contact area" and the equation used to compute it is given in the specifications. The AASHTO Standard Specifications define a tire contact area as the following:

*" The tire contact area shall be assumed as a rectangle with an area in square inches of 0.01P, and a Length in Direction of Traffic/Width of the Tire ratio of 1/2.5, in which P = wheel load in pounds."*

According to the above statement, the value of tire contact area can be obtained as: $A_c = k \cdot P$ where $A_c$ is the tire contact area ($in^2$) and ***P*** is the wheel load (lbs), $k = 0.01$ ( $in^2$/lbs). Let ***L*** be the Length in Direction of Traffic, and ***W*** be the Width of the Tire. In English (or U.S. customary) unit (length in inch, and load in pound), we have: $L = \sqrt{\frac{A_c}{2.5}} = \sqrt{0.004 \cdot P}$ and $W = 2.5 \cdot L = \sqrt{0.025 \cdot P}$. And in SI unit (length in mm, and load in Newton), we have: $L \approx \sqrt{0.5806 \cdot P}$ and $W \approx \sqrt{3.6286 \cdot P}$.

The 2nd edition of AASHTO LRFD Specifications [AASHTO, 1998] proposes a different method to obtain the tire contact area. It states that:

*" The tire contact area of a wheel consisting of one or two tires shall be assumed to be a single rectangle, whose width is 510 mm and whose length is 250mm…" and " The area load applies only to the design truck and tandem. For other design vehicles, the tire contact area should be determined by the engineer. As a guideline for other truck loads, the tire area in mm$^2$ may be calculated from the following dimensions:* ***Tire Width*** = $P/142$ ***and Tire Length*** = $165 \cdot Y \cdot (1 + IM/100)$**,** ***where Y is the load factor, IM is the dynamic load allowance percent, and P is the design wheel load in Newton. ….. The tire pressure shall be assumed to be distributed as follows: On continuous surface, uniformly over the specified contact area; and, on interrupted surface, uniformly over the actual contact area within the footprint with the pressure increased in the ratio of the specified to actual contact area."***

Although the above specifications are proposed to be used for *reinforced concrete* bridge decks, many researchers have used this method to analyze and test their FRP decks using the above tire contact area method [Temeles 2001, Zhou 2001, Coleman 2002]. Since there are currently no provisions related to FRP decks in any of AASHTO's specifications, some researchers have used the HS20 truck load and others have chosen the equivalent of an HS25 design wheel when applying load to their FRP decks [Temeles 2001]. An HS25 design truck is the same as an HS20 truck except that all loads have been increased by 25%. For example: an HS20-44 truck has 32 kips (142 kN) loading on the back two axles with 16 kips (71 kN) on each wheel; for an HS25 truck, the corresponding load is 40 kips (178 kN) at the last two axles, with 20 kips (89 kN) on each wheel. In this research, the design load HS25 was used for stiffness testing. The AASHTO LRFD Specifications use dynamic load allowance to account for the dynamic loading of traveling vehicles. A 30% dynamic load allowance will be used to include dynamic traffic loading effects in lab testing. Therefore, the ultimate load at each wheel in lab testing reaches 26 kips (116kN). The tire contacting area for this loading can be calculated as 11"-20" (280mm-508mm) according to AASHTO LRFD Specifications [AASHTO 1998, Section 3.6.1.2.5, and Temeles, 2001].

## 2.3 Testing Design and Testing Configurations

A comprehensive stiffness and strength laboratory test program was carried out in cooperation with Coleman [2002] to study the stiffness and strength characteristics of this FRP deck system. The failure test was also proposed to investigate the failure modes of the FRP deck, which will be addressed later in Chapter 5.

**Figure 2.2** Lab testing configuration

The testing configuration of this FRP deck in the laboratory is shown in Fig. 2.2. The deck was transversely supported by three steel I beams spaced 78 inches (1981mm) apart. Test load were applied to each deck through specially designed loading patches by a hydraulic cylinder mounted on a load frame. To investigate the local failure of the deck under real truck tire loading, special contact patches made from real truck tires reinforced with silicon rubber were used. The tire patches were specially proposed and designed to investigate the deck failure under real truck tire loading conditions. First, a 22.86cm (9”) wide real truck tire was cut into quarter pieces. Then two pieces were filled with silicon rubber gel. After about 24 hours of curing in room temperature, the rubber-stuffed-tire patches were ready for testing. Stiffness tests were conducted using both kinds of loading patches, i.e., the steel loading patches specified by

ASSHTO and the real tire loading patches developed for current research. Only the rubber-stuffed-tire patch was used for failure test. Pressure sensor films were used to analyze the stress distributions of the steel patch and the tire patch.

The normal stress distribution of a truck tire and the normal stress distribution of a steel patch are shown in Fig. 2.3. The normal stress distribution of a heavy-duty truck tire is shown in Figure 2.3(a) [Pottinger and McIntyre, 1999]. Theoretically, the normal stress of the steel patch is uniformly distributed over the patch area. However, the normal stress distribution obtained from pressure sensor films indicate that failure tests using steel loading patches are not reliable, since there is no contact at all on most of the deck surface and dominated by contact at the edges. The normal stress distribution of the real truck tire is non-uniform as shown in Fig. 2.3 (a) [Pottinger and McIntyre, 1999]. The configuration of the rubber-tire load patched is shown in Fig. 2.4. The failure tests results are important in the local strength analysis and strength design of the FRP deck, which will be addressed in details in Chapter V.

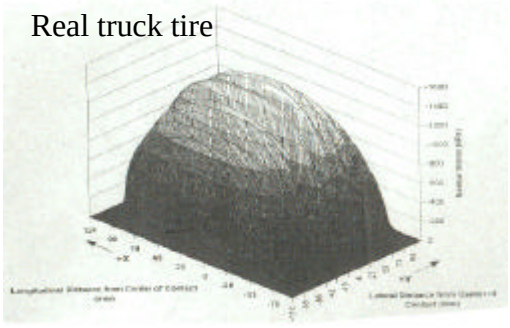


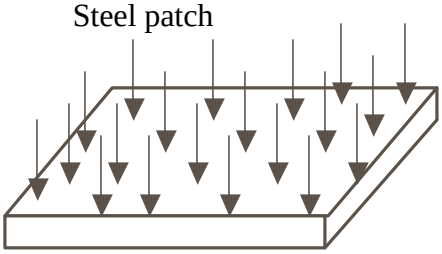


(a) Normal Stress of a real truck tire [Pottinger and McIntyre, 1999]

(b) Normal Stress of a steel Patch

(To be continued on next page)

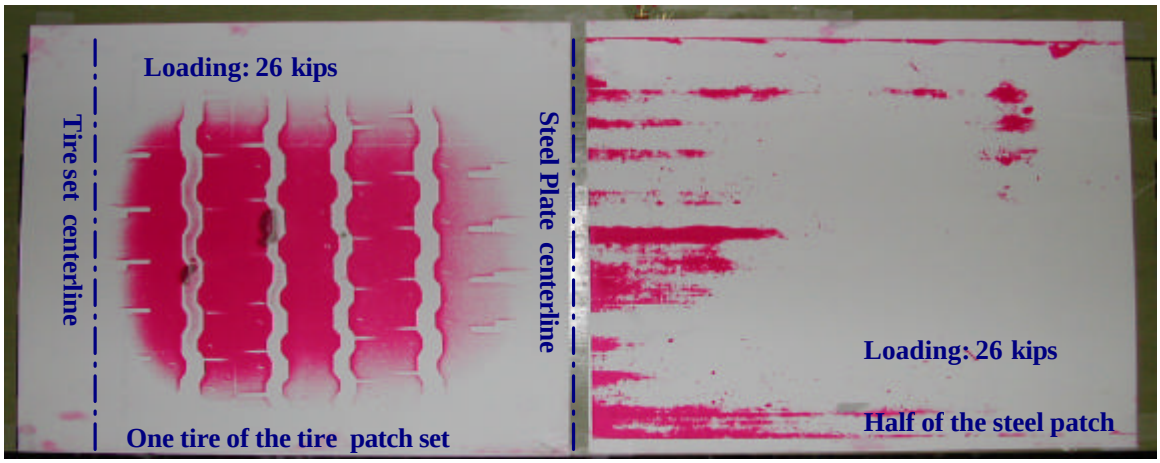


(c) Normal Stress Distributions of a truck tire and a steel plate using pressure film sensor

**Figure 2.3** Normal stress distribution comparisons

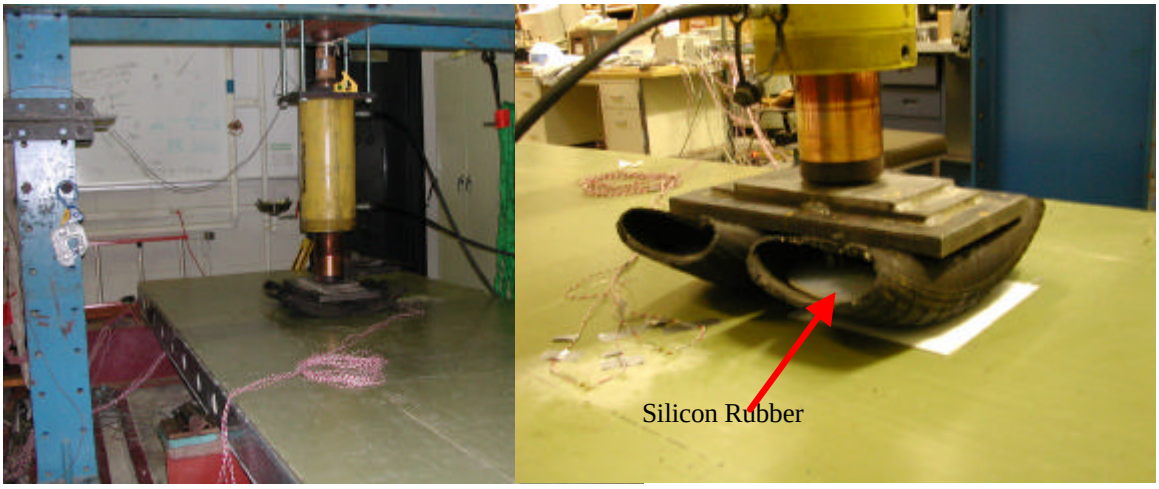


**Figure 2.4** Test configuration and rubber-stuffed-tire patches

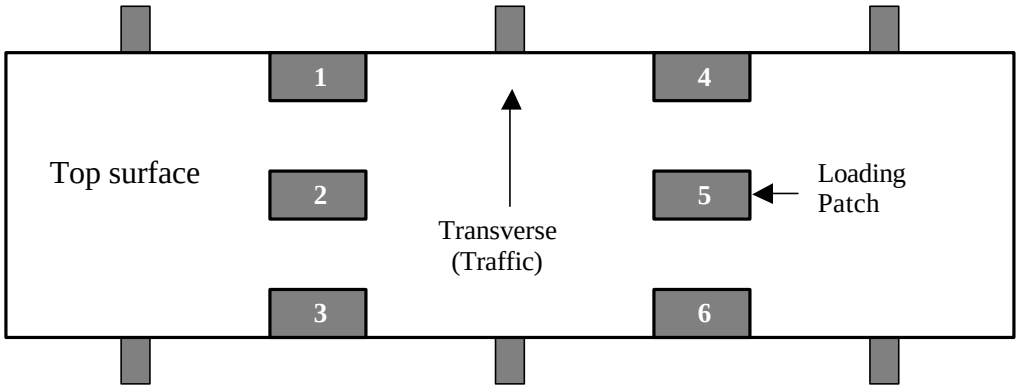


**Figure 2.5** Locations of loading patches

The loading areas are shown in Fig. 2.5. Loading mode 2-5 will be used to simulate a truck axle load. Loading modes 1-4 and 3-6 will be used to simulate an axle load with expectation of producing higher deflections at northwest & northeast and southwest & southeast regions for modes 1-4 and 3-6 respectively. Modes 4-6 and 1-3 will be used as experimental reference data for results comparison from finite element analysis. Mode 2 and mode 5 will be the loading locations for failure tests. Deflections were recorded at six locations, (NW – northwest, CW – central west, SW – southwest, NE – northeast, CE – central east, and SE – southeast), as shown in Figure 2.6.

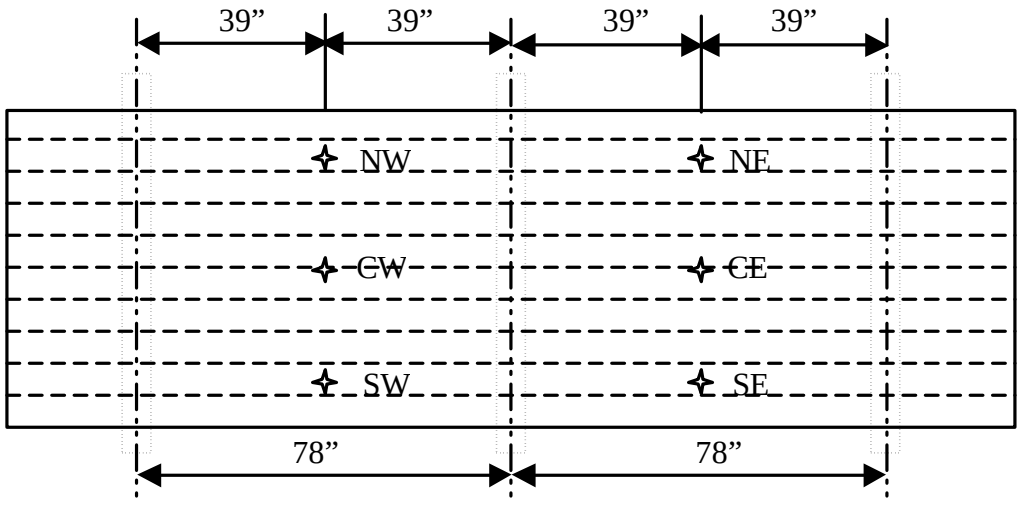


**Figure 2.6** Locations of deflection gauges

The locations for strain gauges are shown in Fig. (2.7) to Fig. (2.10) [Coleman 2002]. Top internal gages were applied between the tube panel and top skin plate, and likewise for the bottom.

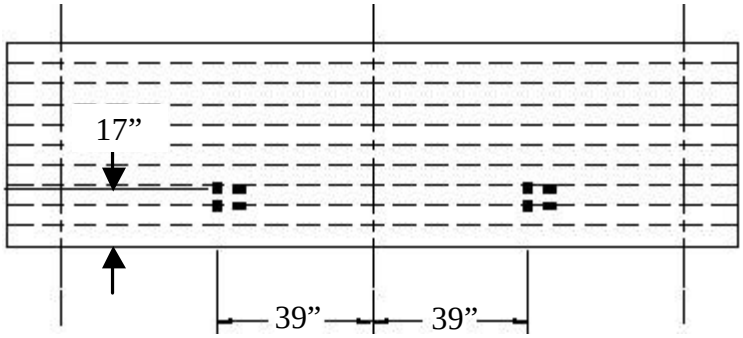


**Figure 2.7** Top surface strain gauges

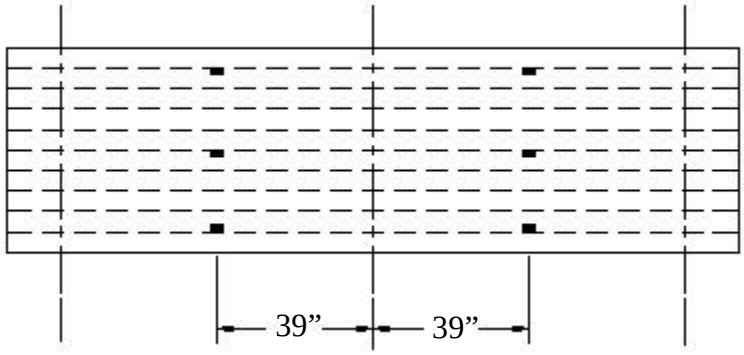


**Figure 2.8** Internal strain gauges between the top plate and tube panel

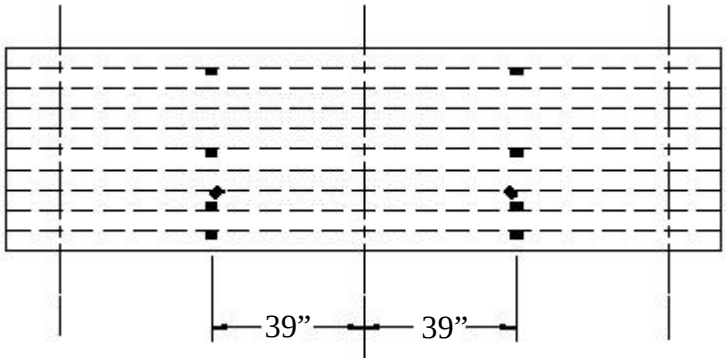


**Figure 2.9** Internal strain gauges between the bottom plate and tube panel

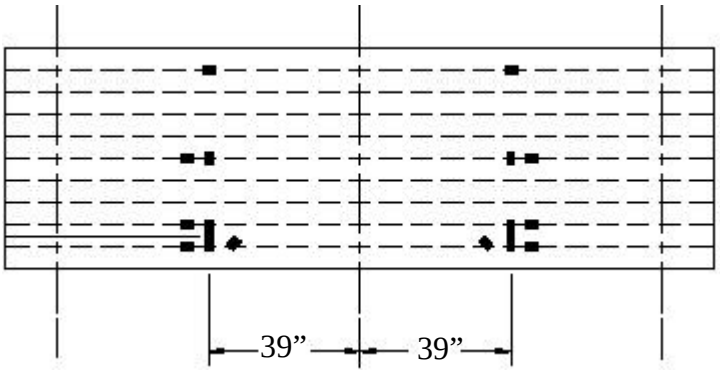


**Figure 2.10** Bottom surface strain gauges

## 2.4 Tested Deflection Results and Discussions

The deflection-load plots from some test data are shown in Fig. (2.11) to Fig. (2.17). Also for all data, the linear equation is presented with displayed R-square value for each recorded deflection. Results from Fig. (2.11) to (2.17) all showed linear deflection – loading relationship, which indicates that the deck can be modeled as a linear material.

For two loading cases, central west (CW, or WP2) and central east (CE, or WP5) in Fig. (2.11) and (2.12) respectively, deflection – loading curves for both the steel patch and the simulated tire patch are presented. For both loading patches, the deflection – loading curves are highly linear for both spans. However, since the tire patch has a smaller contacting area than the steel patch, larger absolute value of slope of the deflection-loading curves are observed for tire patch. For CW or WP2 loading, the curve slope’s absolute value is 0.0095 for tire patch, while 0.0066 for steel patch. For CE or WP5 loading, the curve slopes’ absolute values are 0.0126 and 0.0072 for tire patch and steel patch respectively. From the maximum deflections and curve slopes of Fig. (2.8-a) and (2.8-b), it’s also observed that the west (with 1 transverse rod) is stiffer than the east span (with 5 transverse rods).

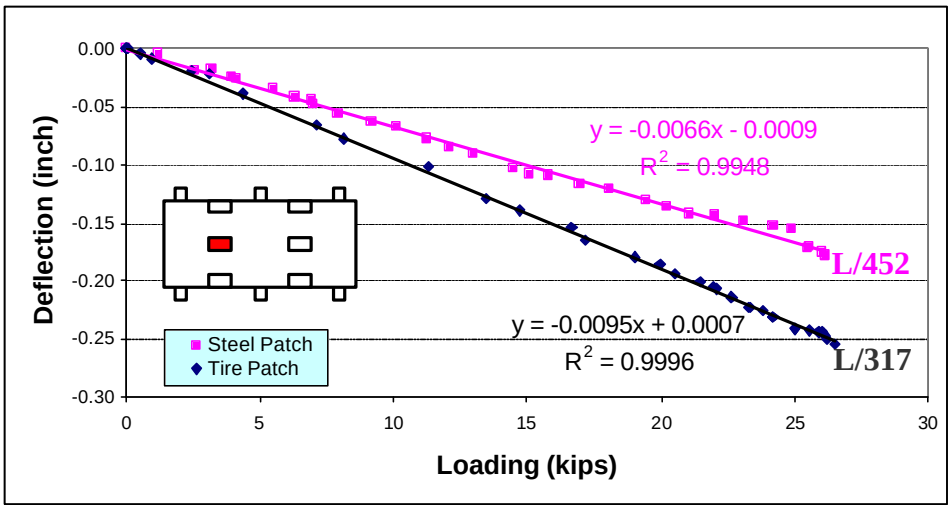


**Figure 2.11** Deflection-load curve as central west (WP2) loaded

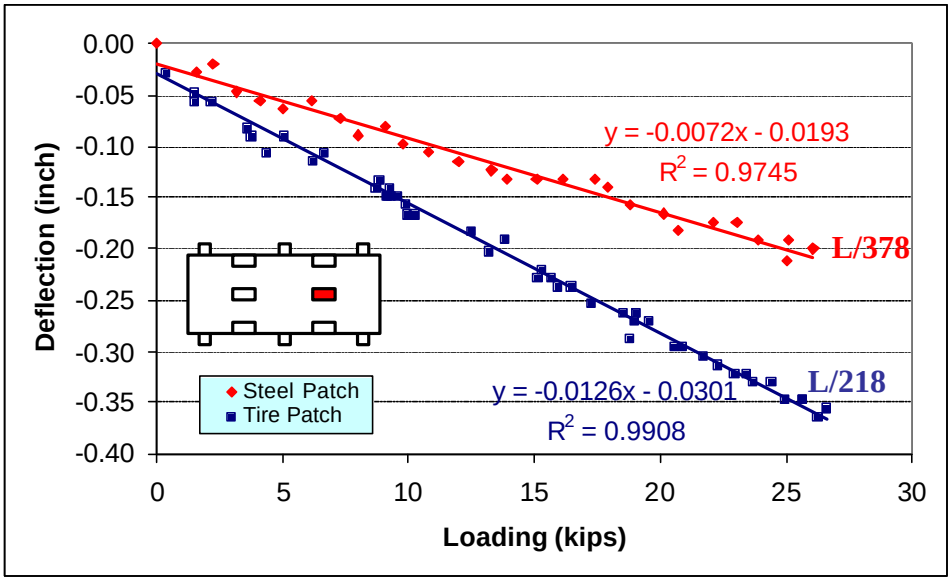


**Figure 2.12** Deflection-load curve as central east (WP5) loaded

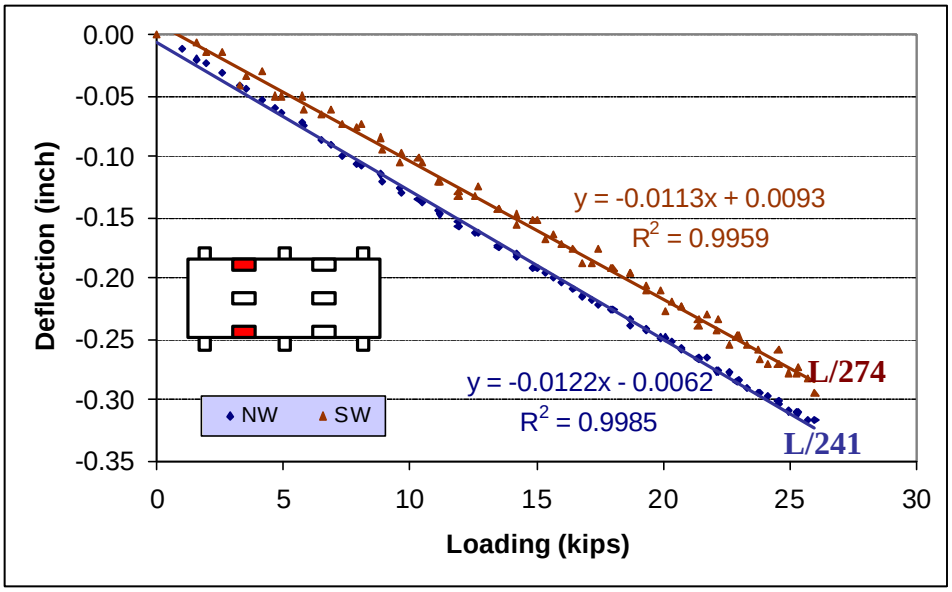


**Figure 2.13** Deflection-load curve with northwest (WP1) and southwest (WP3) loaded

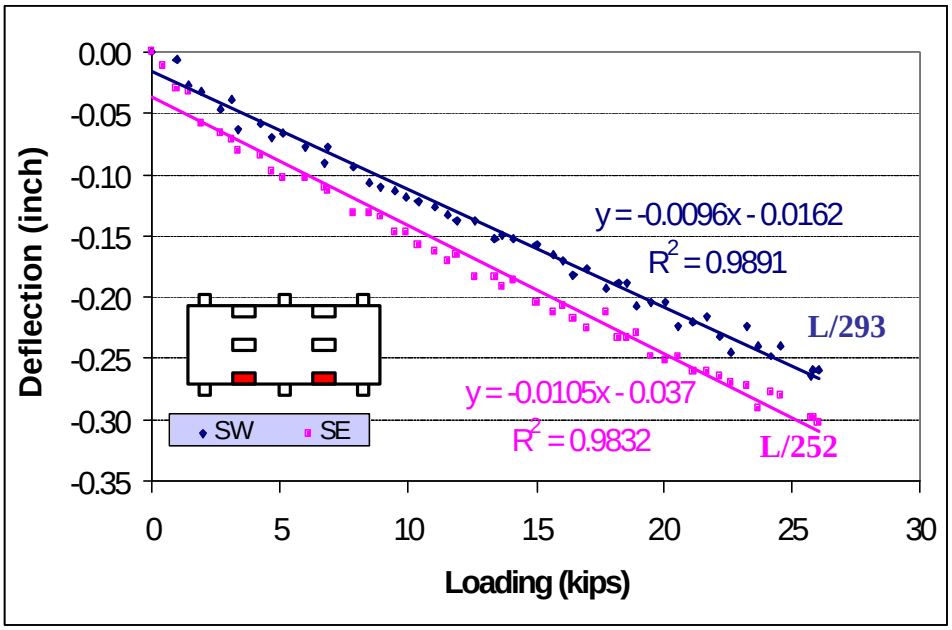


**Figure 2.14** Deflection-load curve with southwest (WP3) and southeast (WP6) loaded

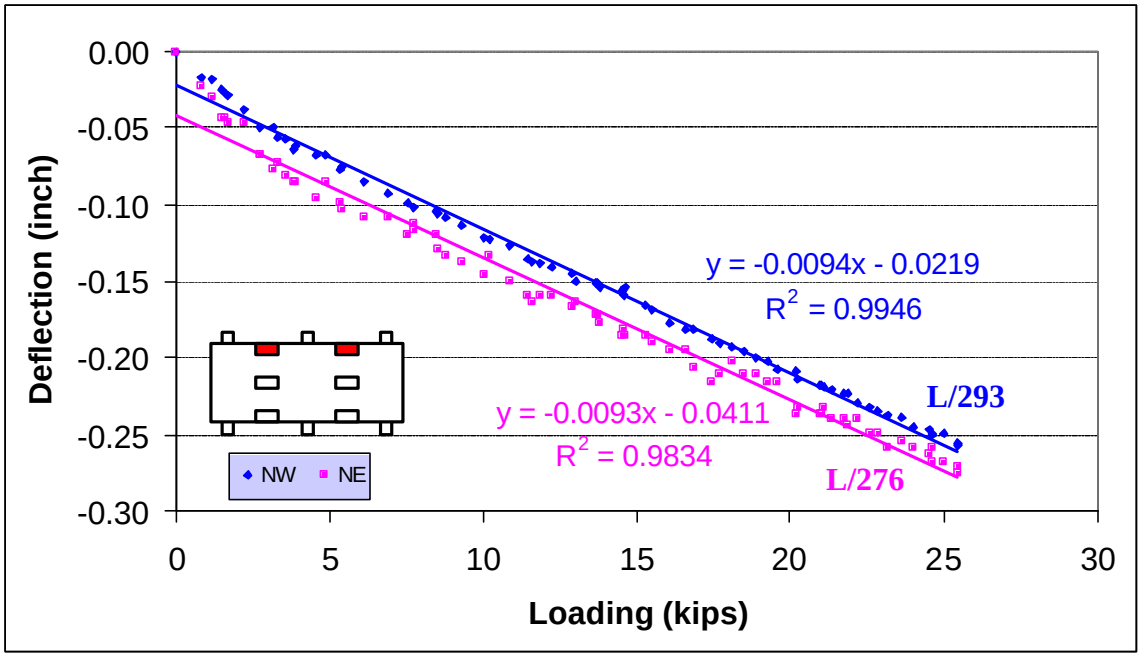


**Figure 2.15** Deflection-load curve with northwest (WP1) and northeast (WP4) loaded

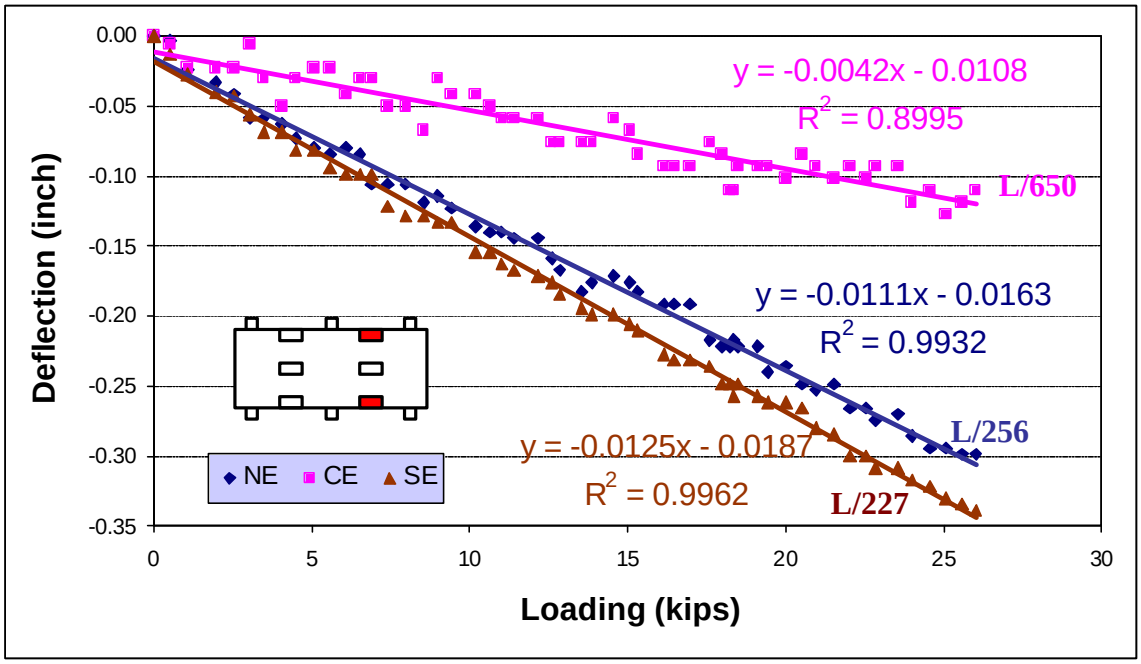


**Figure 2.16** Deflection-load curve with northeast (WP4) and southeast (WP6) loaded

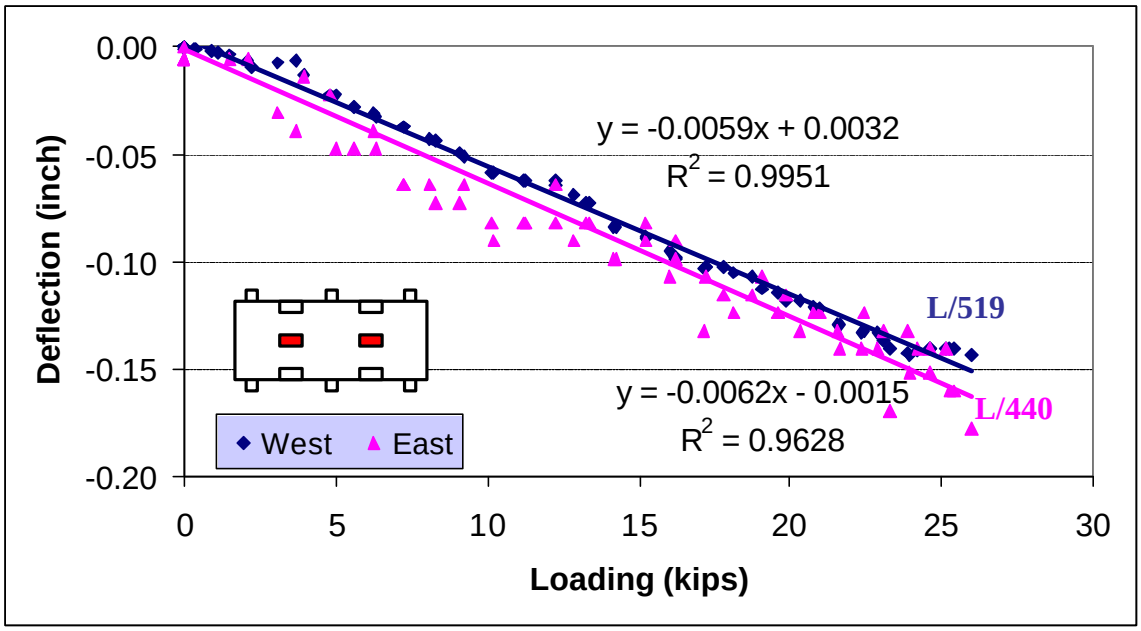


**Figure 2.17** Deflection-load curve with central west (WP2) and central east (WP5) loaded

**TABLE 2.1** Span-to-deflection ratios (deflection index)

| Loading Case | | Maximum Deflection (inch) | Deflection Index |
|---|---|---|---|
| WP2 (West Span) | Steel | 0.173 (Fig. 2.11) | L/452 |
| | Rubber | 0.246 (Fig. 2.11) | L/317 |
| WP5 (East Span) | Steel | 0.207 (Fig. 2.12) | L/378 |
| | Rubber | 0.358 (Fig. 2.12) | L/218 |
| WP1-WP3 (West Span) | North | 0.323 (Fig. 2.13) | L/241 |
| | South | 0.285 (Fig. 2.13) | L/274 |
| WP3-WP6 (South) | West | 0.266 (Fig. 2.14) | **L/293** |
| | East | 0.310 (Fig. 2.14) | L/252 |
| WP1-WP4 (North) | West | 0.266 (Fig. 2.15) | **L/293** |
| | East | 0.283 (Fig. 2.15) | L/276 |
| WP4-WP6 (East Span) | North | 0.305 (Fig. 2.16) | L/256 |
| | South | 0.344 (Fig. 2.16) | L/227 |
| WP2-WP5 (Central) | West | 0.150 (Fig. 2.17) | **L/519** |
| | East | 0.177 (Fig. 2.17) | L/440 |

The span-to-deflection ratio (deflection index) for each tested case is also shown with the corresponding line in the above plots. All these ratios are summarized in Table 2.1 (the

shadowed loading cases in the 1st column are those in which the loading is applied at the unsupported edge). The lowest span-to-deflection ratio for central loading is L/218 for a simulate tire loading patch in the east span; while the lowest span-to-deflection ratio for the unsupported edges loading is L/227 in east span under WP4-WP6 loading. The highest span-to-deflection ratio for central loading is L/519 for west span under WP2-WP5 loading; the highest span-to-deflection ratio for the free edges loading is L/293 for west span under WP3-WP6 and WP1-WP4 loadings.

The above results also highlight details about deck support conditions: when the deck is loaded at the unsupported edges (or free edges), such as WP1-WP3, WP1-WP4, WP3-WP6 and WP4-WP6, the corresponding maximum deflections are generally larger than the deflections loaded at the deck centers (WP2, WP5 and WP2-WP5 loadings). For example, for steel loading patch, the lowest central span-to-deflection ratio is L/378 in the east span while the highest edge span-to-deflection ratio is L/293 in the west span (see Table 2.1). In practical bridge deck design, the free edge effects on maximum bending deflection shall be considered.

Another observation from the above table is that, generally, the west span (with only one transverse rod) is stiffer than the east span (with 5 transverse rods). Both lowest central span-to-deflection ratio (L/218) and edge span-to-deflection ratio (L/227) are in the east span (see Table 2.1), however, the highest central span-to-deflection ratio (L/519) and edge span-to-deflection ratio (L/293) are in the west span. One possible reason for this is that the west span had much less holes (to hold transverse rods) than the east span where the integrity is seriously damaged by drilling too many holes. This indicates that in deck fabrication process, the integrity of the deck system shall be reserved.

The above tested results give us the following important information about FRP deck testing and design:

(1) The tire contact area will affect the tested maximum deflection; the smaller the contacting area, the larger the maximum deflection.

(2) Under the same loading level, the free edge (or unsupported edge) maximum deflection is generally larger than the central maximum deflection. This indicates that failure may occur at the free (or unsupported) edges, though unsupported edges are not normally used in practice. The larger deflection at the unsupported edges may also raise concerns related to the durability of the deck, i.e., the unsupported edges are weak regions, and will have less durability capability.

(3) Deck span with less holes and transverse rods is stiffer than a span that has more holes and transverse rods. The integrity of the deck system should be reserved in deck fabrication.

## 2.5 Strains Testing Results and Discussions

Some of the tested strains using the steel patch are shown in Figures 2.18 to 2.24. The following nomenclatures is used in the figures: T – top, B – Bottom, I – Internal, E – East, W – West, NE – Northeast, NW- Northwest, SE – Southeast, SW – Southwest. These strains are all longitudinal strains. Depending on the state of compression or tension, internal strains refer to the strains recorded from the gauges between the top plate and the top tube flange (compression, negative strain), and strains recorded from the gauges between the bottom plate and the bottom tube flange (tension, positive strain).

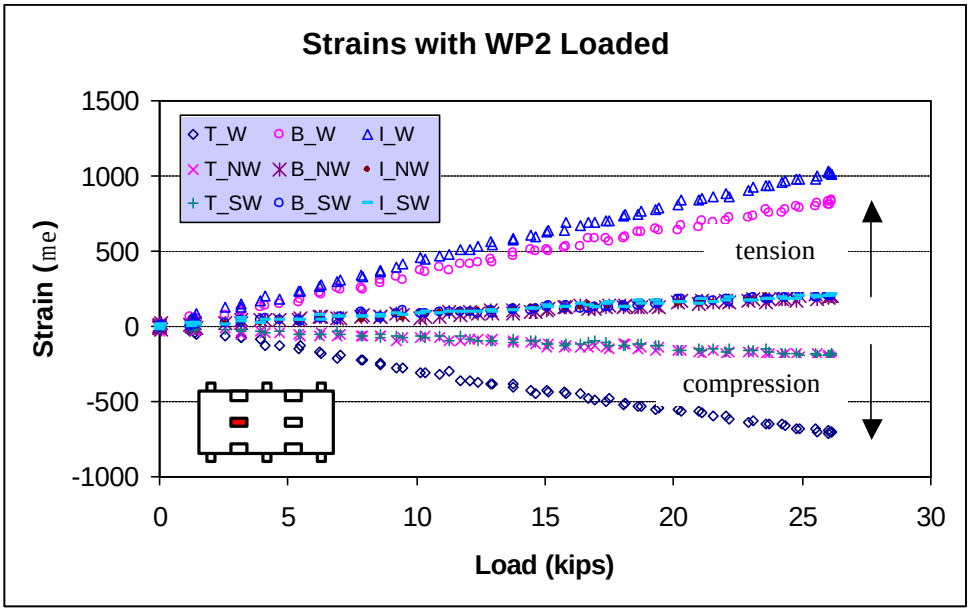


**Figure 2.18** Strain-Load curve with central west (WP2) loaded

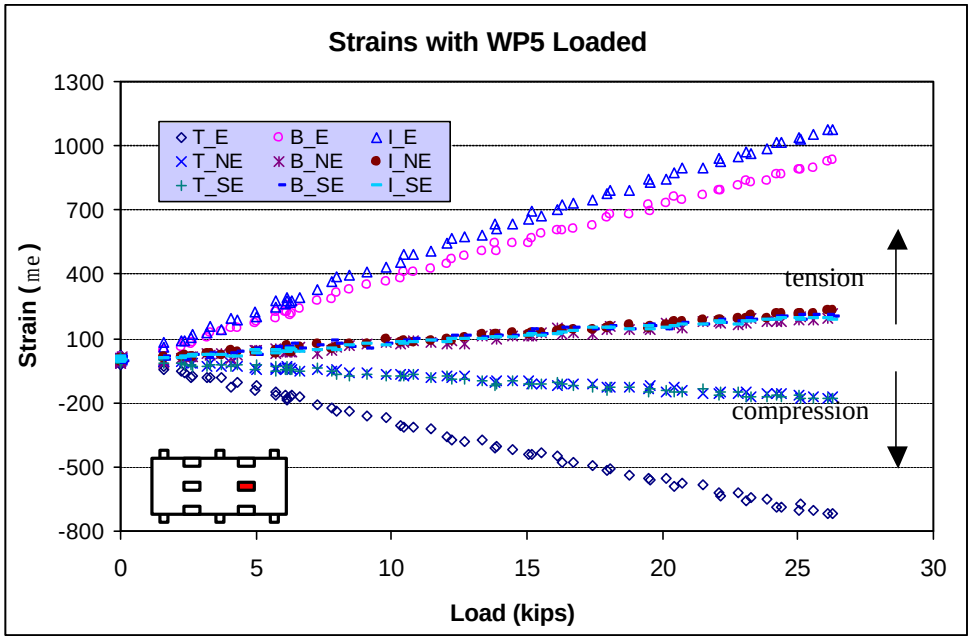


**Figure 2.19** Strain-Load curve with central east (WP5) loaded

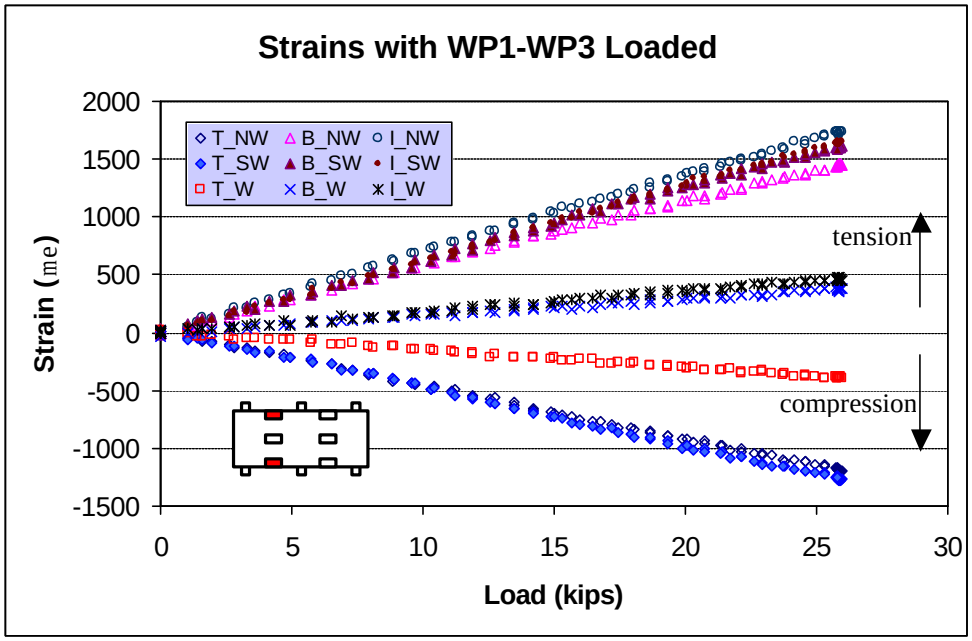


**Figure 2.20** Strain-Load curve with northwest (WP1) and southwest (WP3) loaded

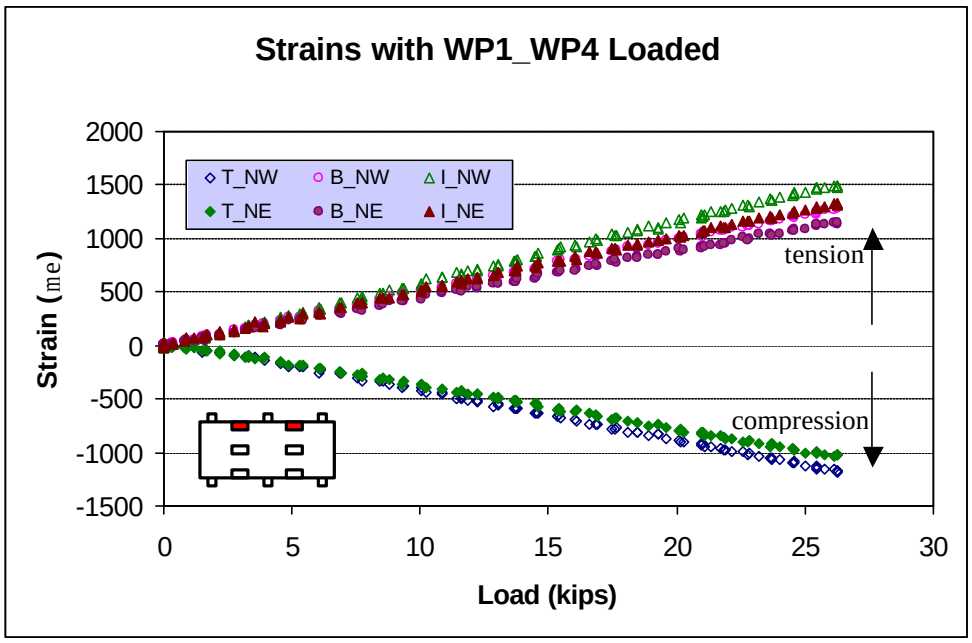


**Figure 2.21** Strain-Load curve with northwest (WP1) and northeast (WP4) loaded

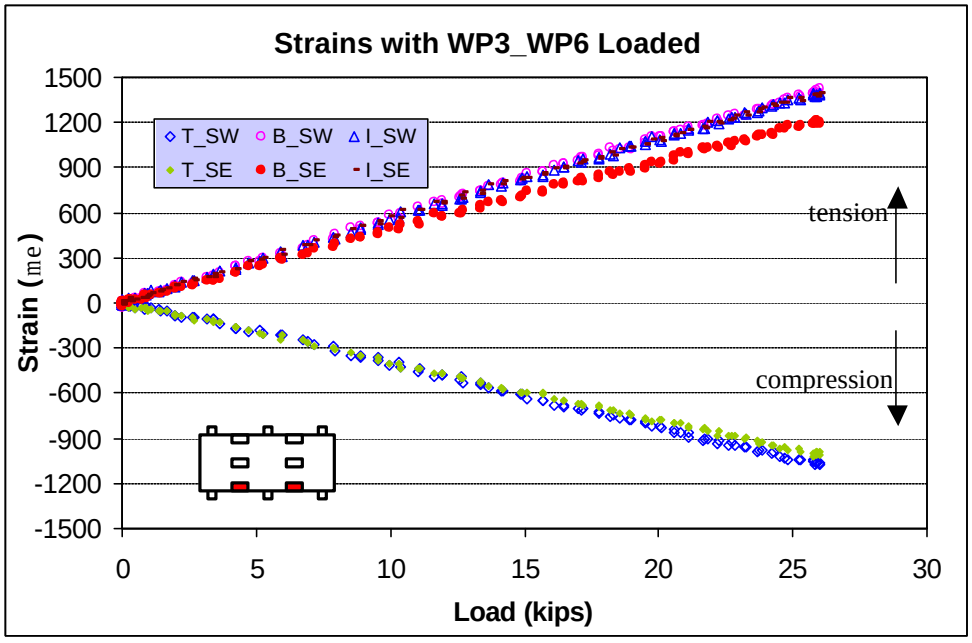


**Figure 2.22** Strain-Load curve with southwest (WP3) and southeast (WP6) loaded

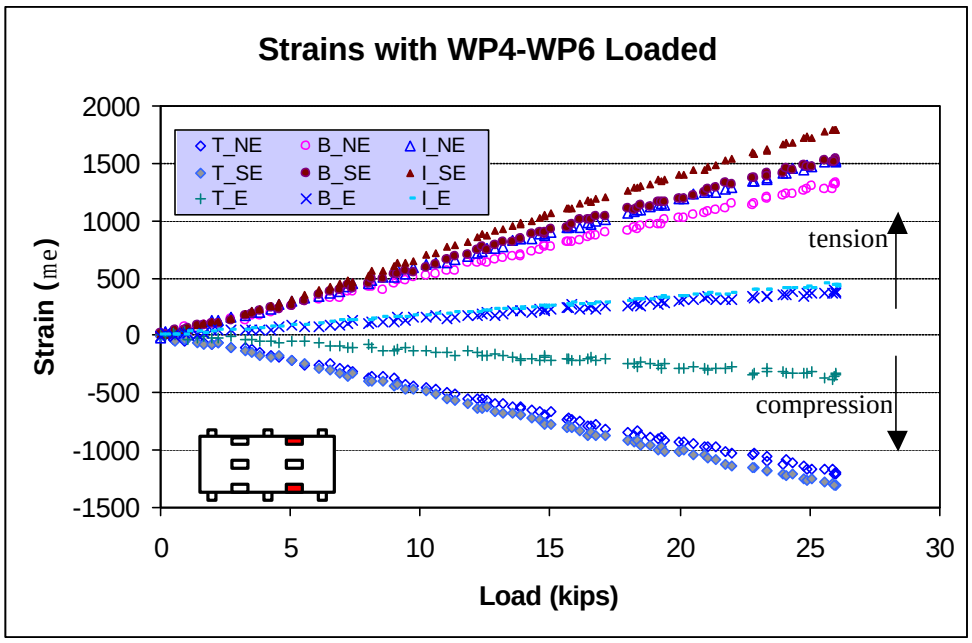


**Figure 2.23** Strain-Load curve with northeast (WP4) and southeast (WP6) loaded

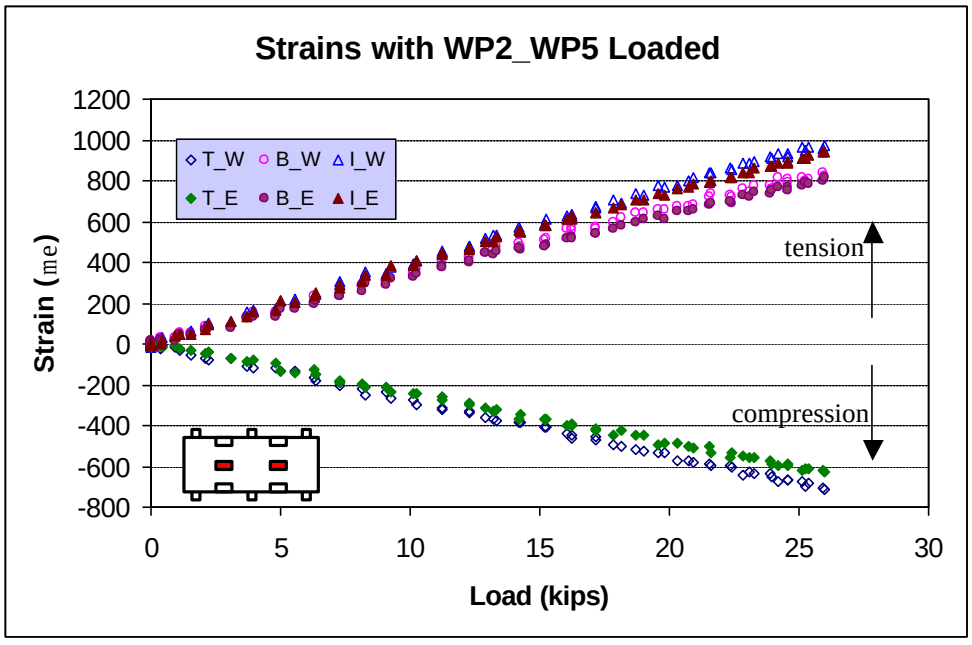


**Figure 2.24** Strain-Load curve with central west (WP2) and central east (WP5) loaded

From Figure 2.18, Figure 2.19, and Figure 2.24, the recorded strains were very close for both spans. This differs from the tested deflections, where we observed that the west span (with one transverse rod) is stiffer than the east span (with 5 transverse rods).

**TABLE 2.2** Maximum strains comparisons

| **Loading** | **Maximum Strain (*me*)** (tension/compression) | **Location** |
|---|---|---|
| WP2 | 1027 / -717 (Fig. 2.18) | I_W / T_W |
| WP5 | 1075 / -717 (Fig. 2.19) | I_E / T_E |
| WP2_WP5 | 974 / -714 (Fig. 2.24) | I_W / T_W |
| WP1-WP3 | 1738 / -1278 (Fig. 2.20) | I_NW / T_SW |
| WP1-WP4 | 1498 / -1180 (Fig. 2.21) | I_NW / T_SW |
| WP3-WP6 | 1422 / -1077 (Fig. 2.22) | B_SW / T_SW |
| WP4-WP6 | 1794 / -1311 (Fig. 2.23) | I_SE / T_SE |

Table 2.2 summaries the recorded maximum strain for each loading case. All these strains are recorded at the same loading level, i.e., 26 kips. It's observed that: when the load is applied at the span center (WP2, WP5 and WP2-WP5), the maximum tension strain ranges from 975 *me* at I_W to 1075 *me* with the average value of 1025.3 *me*, and its maximum compression strain ranges from –714 *me* to –717 *me* with the average value of –716 *me*; when the load is applied at the free edges (WP1-WP3, WP1-WP4, WP3-WP6, WP4-WP6), the maximum strain ranges from 1422 *me* to 1794 *me* with the average value of 1613 *me*, and its maximum compression strain ranges from –1077 *me* to –1311 *me* with the average value of –1211.5 *me*. Also, the third column in Table 2.2 shows that the maximum strains occur at the free edges when load applied at these edges, while the maximum strains occur at the span center when load applied at the center. However, all these maximum strains are much lower than the estimated components ultimate failure strains (see Table 2.3 [Coleman, 2002]).

**TABLE 2.3** Estimated deck components ultimate strains

| Ultimate Strain | Square Tube | ¼" Plate | ½" Plate |
|---|---|---|---|
| Tensile, LW ( $me$ ) | 12,000 | 11,100 | NA |
| Tensile, CW ( $me$ ) | 8,750 | 11,100 | NA |
| Compressive, LW ( $me$ ) | 12,000 | 13,300 | NA |
| Compressive, CW ( $me$ ) | 15,000 | 16,500 | NA |

Planning and results for field tests for this FRP deck system are also available; one should refer to Temeles [2001] and Coleman [2002] for more information.

# CHAPTER III

# ELASTIC EQUIVALENT MODELING OF FRP DECKS

Previous research showed that the design of FRP composite bridge decks were stiffness driven [Henry 1985, Ahmad and Plecnik 1989, Plecnik and Azar 199, Temeles 2001, Karbhari 2001 etc.]. In designing FRP decks, a deflection limit was chosen as the primary design criteria in most previous FRP bridge deck projects. Therefore, the calculation of the maximum deflection of FRP deck systems under design loading and boundary conditions is important. The deflection analysis approach for FRP deck systems should be easily implemented and also provide relatively accurate predictions of the behavior of the deck system. In the following two chapters, a systematic plate (two-way) bending deflection analysis procedure will be developed using the Method of Elastic Equivalent (MEE). To develop this analysis procedure, the following detailed research is conducted: (a) Develop easy and practical methods for predicting FRP deck's structural level, overall equivalent plate properties; (b) Develop solving procedures for bending analysis of FRP decks; and (c) Compare the results with experimental data and complete FEA results.

In this chapter, a simplified method, i.e., MEE, for obtaining structural level FRP deck properties (Modulus of elasticity, Poisson's ratio, flexural and torsional stiffness etc.) from its components (tubes and plates, etc.) will be developed and evaluated. After the equivalent FRP deck properties have been obtained from their components, engineering analytical models for global two way bending deflection/stiffness analysis will be proposed and evaluated in Chapter IV. This procedure is different from Brown [1998], where only one-way (longitudinal) deflection was modeled and verified without the modeling of plate edge effects on its performance. This

procedure is a general method for modeling cellular decks as orthotropic plates with two way (longitudinal and transverse) bending, and can be used for other cellular deck systems though some minor changes to consider specific deck geometries may be required.

## 3.1 Assumptions and Steps for MEE Development

The geometric model of the deck system is shown in Figure 3.1. To develop global analysis method for the deck system, the following assumptions were made: a.) All components are completely bonded together; b.) The effects of the deck's transverse steel rods and adhesives are neglected; c.) Each deck component has orthotropic material properties and will be modeled as flaw free and uniform orthotropic continuum; d.) The behavior of each deck component as well as the deck system is linear elastic, no creep and no time-dependent evaluation will be modeled.

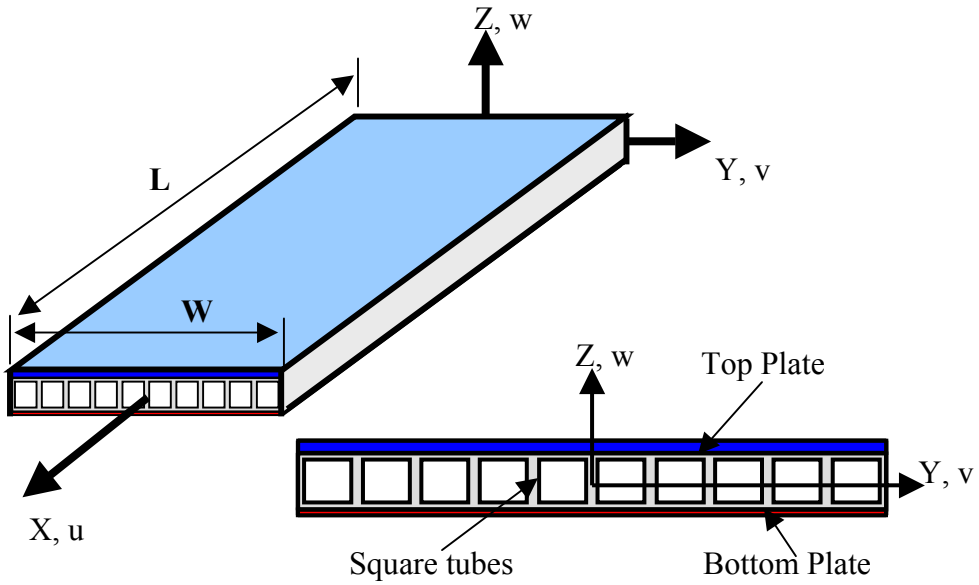


**Figure 3.1** Coordinates of the proposed FRP deck

As shown in Figure 3.2, the sandwiched tube panel will be modeled as an elastically equivalent plate (Step I), and the whole deck panel system, including top plate, internal equivalent plate and bottom plate, will then be modeled as an equivalent plate (Step II) for the

whole deck panel. This method involves two important issues: a.) The deck will be eventually represented by an equivalent orthotropic plate with the same length, width and thickness dimensions as the deck panel; b.) The deck's equivalent plate properties can be reasonably obtained from the deck components, i.e., the top plate, the internal tubes, and the bottom plate. By using this procedure, the designer can calculate the equivalent deck properties and conduct bending, thermal, vibration and other analyses of the deck system using available composite plate theories.

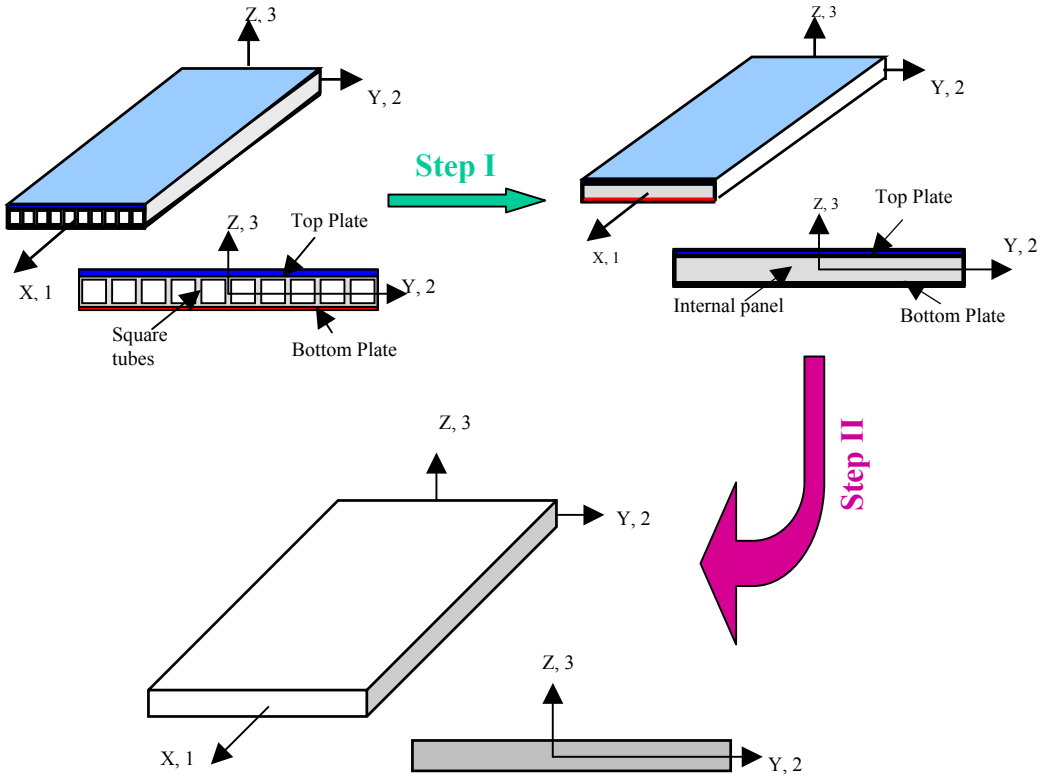


**Figure 3.2** Equivalent Plate Modeling Steps

The deck panel can also be modeled as a laminated sandwich plate using available sandwich plate analysis methods after Step I. The sandwich plate consists of a top plate, a bottom

plate and an equivalent sandwich plate representing the internal tube panel of the deck. However, this analysis requires the development of laminated sandwich plate theories. It will be easier for bridge designers to use single-layer laminated composite plate theories, since they are fully developed at the present time (even in undergraduate level courses). For this consideration, single-layer laminated composite plate theory will be used in this research.

To achieve the above goals, we must prove that the deck system can be reasonably modeled as an equivalent orthotropic plate, and show how we obtain the equivalent plate properties from its components. In the following, we will develop a simplified method to obtain equivalent plate properties from the deck's components, and then verify the proposed method.

## 3.2 Properties of The Deck Components

According to the steps in Fig.3.2, we will obtain the equivalent plate properties for the internal tube assembly first, and then obtain the overall equivalent plate properties of the whole deck system. The verification will be made by orthotropic composite plate analysis, 3-D finite element analysis as well as experimental data.

### 3.2.1 Equivalent Tube Assembly Properties

In equivalent modeling of internal tube assembly, we have the following assumptions: (1) The tube assembly will be modeled as of an equivalent orthotropic plate with the same length, width, and thickness as the panel; (2) All tubes are completely bonded together to form the panel; (3) The effects of the transverse steel rods are neglected.

The cross-section of a single square tube is shown in Fig.3.3. We assume that the X (or 1) direction of the coordinate system is perpendicular to the tube cross-section, and the Y (or 2) and Z (or 3 ) axis are presented as shown in Fig3.3. Where $a$ and $b$ are width and depth of the tube, $h$ is the depth of the tube's central lines on the top and bottom flanges, $H_t$ and $H_b$ are thickness for top and bottom flanges respectively, $H_w$ is the thickness of the tube web. For fabrication purpose,

the outer and inner corners of the tube are curved. For modeling simplicity, we assume that the tube has pure square dimensions as the dashed lines shown in the figure.

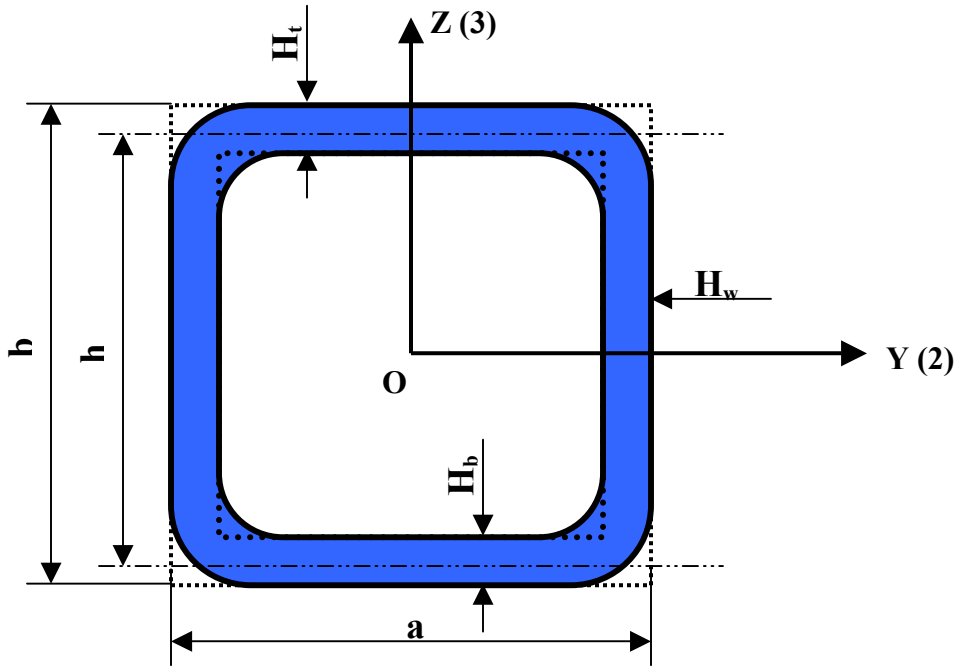


**Figure 3.3** Cross-section of a single square tube

According to the manufacturer's design manual [Strongwell, 1998], the following properties are given: $a = b = 6 \cdot in$ (152.4mm); $H_b = \frac{3}{8} \cdot in$ (9.5mm); $H_t = \frac{3}{8} \cdot in$ (9.5mm); $I_{xx} = 38.44 \cdot in^4$ (1600cm$^4$); $J_{xy} = 66.74 \cdot in^4$ (2778cm$^4$); $H_w = \frac{3}{8} \cdot in$ (9.5mm); $E_{xx} = 2.5 \times 10^6\ psi$ (17.2 GPa); $E_{yy} = 0.8 \times 10^6\ psi$ (5.5 GPa); $G_{xy} = 0.425 \times 10^6\ psi$ (2.9 GPa); and $\nu_{xy} = 0.33$.

The equivalent method works in the following way: (1) Obtain global stiffnesses of the tube assembly through its tubes; (2) Consider the tube assembly as a single-layered special orthotropic plate with the same length, width and thickness dimensions as the tube assembly; (3) Calculate equivalent orthotropic stiffness coefficients of the equivalent plate.

### 3.2.2 Tube Stiffnesses

In the longitudinal direction (or X direction), we assume that the tube assembly stiffness is the same as an individual tube, i.e., $D_{xx} = E_{xx} \cdot i_{xx}$, where $D_{xx}$ is the longitudinal stiffness, $E_{xx}$ is the Young's modulus in longitudinal direction, and $i_{xx}$ is the second moment of area per unit length (units: [length]$^3$, or $in^3$). Following this assumption, we have

$$D_{xx} = E_{xx} \cdot i_{xx} = E_{xx} \cdot \frac{I_{xx}}{b} \tag{3.1}$$

The transverse direction (or Y direction) stiffness $D_{yy}$ is not as simple as the longitudinal stiffness, since the tube assembly is a thin-walled FRP system and the stiffness in the transverse direction is much lower than the longitudinal stiffness. Equivalent modeling for thin-walled cellular panel also requires we consider the distortion of the cross-section. We will consider both effects. The second moment of area per unit length in transverse direction $i_{yy}$ for a thin-walled cellular panel can be obtained as [O'brein and Keogh, 1999]

$$i_{yy} = \frac{(H_t + H_b) \times h^2}{4} + \frac{H_t^{\,3} + H_b^{\,3}}{12} \tag{3.2-a}$$

with the following equivalent stiffness

$$D_{yy}^{'} = E_{yy} \cdot i_{yy} \tag{3.2-b}$$

We use the following factor to consider possible distortion of the panel because of shear effects [O'Brein and Keogh 1999, Hambly 1976];

$$GA_s = \frac{2 \cdot E_{yy} \cdot (2H_w)^3 \cdot H_t^3 \cdot H}{h \cdot b \cdot [h \cdot H_t^3 + b \cdot (2H_w)^3]} \tag{3.2-c}$$

The overall transverse stiffness can be obtained as [Cusens and Pama, 1975]:

$$D_{yy} = \frac{D_{yy}^{'} \cdot GA_s \cdot (W - H_w)^2}{GA_s \cdot (W - H_w)^2 + 18 \cdot D_{yy}^{'}} \tag{3.2-d}$$

Other tube panel stiffnesses can be obtained as

$$D_{xy} = \nu_{xy} \cdot D_{yy} \tag{3.2-e}$$

and the torsion stiffness $D_{66}$ can be calculated as:

$$D_{66} = \frac{GJ}{4 \cdot b} = \frac{G_{xy} \cdot J_{xy}}{4 \cdot b} \tag{3.3}$$

where $\nu_{xy}$ is the Poisson's ratio which is assumed to be the same as the tube; $G_{xy}$ is the shear modulus of the tube and $J_{xy}$ is the torsional stiffness. Substituting the available material properties of the tube, we have the stiffnesses for the tube assembly as shown in Table 3.1. In the transverse direction (-Y direction), the tubes behave like series springs in the tube assembly, therefore, low stiffness is obtained because of the series connection of the tube in the transverse direction. While, in the longitudinal direction, the tubes are bonded together and behave like parallel springs while leads to high stiffness in this direction.

**TABLE 3.1 Stiffnesses for the investigated tube assembly**

| Stiffness | Calculated Value ($lbs \cdot in^2$) | Formulations Used |
|---|---|---|
| $D_{xx}$ | $17.08 \times 10^6$ | $D_{xx} = E_{xx} \cdot i_{xx} = E_{xx} \cdot \frac{I_{xx}}{b}$ |
| $D_{yy}$ | $0.452 \times 10^6$ | $D_{yy} = \frac{D_{yy}^{'} \cdot GA_s \cdot (W - H_w)^2}{GA_s \cdot (W - H_w)^2 + 18 \cdot D_{yy}^{'}}$ |
| $D_{xy}$ | $0.149 \times 10^6$ | $D_{xy} = \nu_{xy} \cdot D_{yy}$ |
| $D_{66}$ | $1.261 \times 10^6$ | $D_{66} = \frac{GJ}{4 \cdot b} = \frac{G_{xy} \cdot J_{xy}}{4 \cdot b}$ |

### 3.2.3 Equivalent plate properties:

Now, we assume that the tube assembly is an elastic, single-layer special orthotropic plate with the same length, width and thickness dimensions as the tube assembly, whose material coordinates coincide with the system coordinates. The equivalent material properties can be obtained as followings [Reddy, 1997]:

$$E_{xx}^{e} = \frac{12 \cdot D_{xx} \cdot (1 - \nu_{xy}^{e} \cdot \nu_{yx}^{e})}{H^{3}} \tag{3.4-a}$$

$$E_{yy}^{e} = \frac{12 \cdot D_{yy} \cdot (1 - \nu_{xy}^{e} \cdot \nu_{yx}^{e})}{H^{3}} \tag{3.4-b}$$

$$G_{xy}^{e} = \frac{12 \cdot D_{66}}{H^{3}} \tag{3.4-c}$$

For the Young's modulus in the vertical direction, we assume that

$$E_{zz}^{e} = E_{zz} \tag{3.4-d}$$

The Poisson's ratios can be obtained as:

$$\nu_{xy}^{e} = \nu_{xy};\ \nu_{yx}^{e} = \frac{D_{yy}}{D_{xx}} \cdot \nu_{xy}^{e};\ \nu_{xz}^{e} = \nu_{xy}^{e}. \tag{3.4-e}$$

The equivalent shear moduli are obtained as

$$G_{yz}^{e} = \frac{D_{yz}}{H} = \frac{G \cdot J}{H \cdot L};\ G_{xz}^{e} = \frac{D_{xz}}{H} = \frac{G \cdot J}{H \cdot H}. \tag{3.4-f}$$

For a real material, the stress-strain matrix must be positive definite [ANSYS, 2002]. Sometimes we will get the equivalent material properties that will not satisfy this condition. We choose some minor properties, whose values don't affect the overall behavior of the plate too much, and modify these properties such that the positive definite stress-strain matrix is satisfied. For example, $\nu_{yz}^{e}$ will be determined such that the stress-strain matrix to be positive definite for

the equivalent tube panel. Being positive definite means the following formula must hold for the plate:

$$1-(\nu_{xy}^{e})^{2}\cdot\frac{E_{yy}^{e}}{E_{xx}^{e}}-(\nu_{yz}^{e})^{2}\cdot\frac{E_{zz}^{e}}{E_{yy}^{e}}-(\nu_{xz}^{e})^{2}\cdot\frac{E_{zz}^{e}}{E_{xx}^{e}}-2\cdot\nu_{xy}^{e}\cdot\nu_{xz}^{e}\cdot\nu_{yz}^{e}\cdot\frac{E_{zz}^{e}}{E_{xx}^{e}}>0 \qquad \text{(3.4-g)}$$

**TABLE 3.2 Equivalent Material Properties Obtained for the Tube Assembly**

| Property | Value | Method used |
|---|---|---|
| $E_{xx}^{e}\,(psi)$ | $0.95\times10^{6}$ | $E_{xx}^{e}=\dfrac{12\cdot D_{xx}\cdot(1-\nu_{xy}^{e}\cdot\nu_{yx}^{e})}{H^{3}}$ |
| $E_{yy}^{e}\,(psi)$ | $0.025\times10^{6}$ | $E_{yy}^{e}=\dfrac{12\cdot D_{yy}\cdot(1-\nu_{xy}^{e}\cdot\nu_{yx}^{e})}{H^{3}}$ |
| $E_{zz}^{e}\,(psi)$ | $0.8\times10^{6}$ | Assumption $E_{zz}^{e}=E_{zz}$ |
| $G_{xy}^{e}\,(psi)$ | $0.07\times10^{6}$ | $G_{xy}^{e}=\dfrac{12\cdot D_{66}}{H^{3}}$ |
| $G_{xz}^{e}\,(psi)$ | $0.79\times10^{6}$ | $G_{xz}^{e}=\dfrac{D_{xz}}{H}=\dfrac{G\cdot J}{H\cdot H}$ |
| $G_{yz}^{e}\,(psi)$ | $0.05\times10^{6}$ | $G_{yz}^{e}=\dfrac{D_{yz}}{H}=\dfrac{G\cdot J}{H\cdot L}$ |
| $\nu_{xy}^{e}$ | 0.33 | Assumption: $\nu_{xy}^{e}=\nu_{xy}$ |
| $\nu_{xz}^{e}$ | 0.33 | Assumption: $\nu_{xz}^{e}=\nu_{xy}^{e}$ |
| $\nu_{yz}^{e}$ | 0.10 | Determined via stress-strain matrix positive definite requirement for a real material |

The equivalent properties of the tube assembly are summarized in Table 3.2. Because of the low stiffness in the transverse direction (-Y direction), low equivalent modulus is obtained. The low stiffness in the Y direction also produces low XY and YZ shear moduli. We will verify these plate properties from equivalent modeling by comparing the bending behavior of the tube panel using the results obtained from Finite Element Analysis (FEA). The FEA software, ANSYS, will be used for the analysis.

### 3.2.4. FEA Verifications

To verify if the above procedure works for the tube assembly, we will use FEA to calculate and compare the bending deflection of the assembly. In the following, a complete FEA model, and an equivalent FEA model will be used for analysis and comparison. In the complete FEA model, the tube panel will be modeled as 10 individual square tubes completely bonded together with properties provided in Table 3.3. In the equivalent model, the tube panel will modeled as an equivalent plate with the same geometric dimension, loading conditions and boundary conditions as the complete tube panel, but with the equivalent material properties calculated from the above equivalent method (Table 3.2).

**TABLE 3.3 Material Properties Used in Complete Tube Model**

| Property | Value | Method used |
|---|---|---|
| $E_{xx}\,(psi)$ | $2.5\times10^{6}$ | From manual, testing |
| $E_{yy}\,(psi)$ | $0.8\times10^{6}$ | From manual, testing |
| $E_{zz}\,(psi)$ | $0.8\times10^{6}$ | Assumption $E_{zz}=E_{yy}$ for a square tube |
| $G_{xy}\,(psi)$ | $0.425\times10^{6}$ | From manual, testing |
| $G_{xz}\,(psi)$ | $0.425\times10^{6}$ | Assumption $G_{xz}=G_{xy}$ for a square tube |
| $G_{yz}\,(psi)$ | $0.364\times10^{6}$ | Approximation $G_{yz}=\dfrac{\sqrt{E_{yy}\cdot E_{zz}}}{2\cdot(1-\sqrt{\nu_{yz}\cdot\nu_{zy}})}$ |
| $\nu_{xy}$ | 0.33 | From manual, testing |
| $\nu_{xz}$ | 0.33 | Assumption $\nu_{xz}=\nu_{xy}$ for a square tube |
| $\nu_{yz}$ | 0.10 | Determined via stress-strain matrix positive definite requirement for a real material |

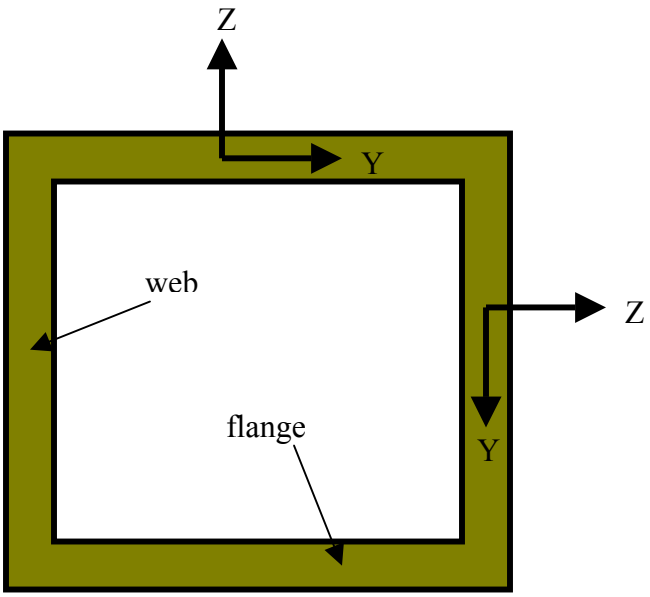


**Figure 3.4** Local coordinate system for the square tube's web and flange

Using FEA, we will make the deflection comparisons for the tube assembly with all edges simply supported (SSSS), two opposite edges are simply supported and other two edges are free (SSFF). The loading conditions are uniformly distributed load (UDL), Central Point Load (CPL) and Rectangular Patch Load (RPL). Also we will compare the deflection for Cantilevered tube assembly. Two models were used for comparison: Complete Tube Panel Model (CTPM) and Equivalent Orthotropic Plate Model (EOPM). In CTPM, the individual tube was modeled separately, with all tubes completely bonded together. For each individual tube (Fig.3.3) the material coordinate systems are different for the webs (the vertical walls in Fig.3.4) and the flanges (horizontal walls in Fig.3.4).

The CTPM geometry model in ANSYS is shown in Figure 3.5. For this tube assembly, ten identical tubes are completely bonded together, the bending neutral axis is at the center of the tube webs. The boundary conditions will be specified at the plane where the neutral axes are located. The overall length of the modeled tube panel is 90", about half of the deck length, and the total width is 60", the same width as the deck.

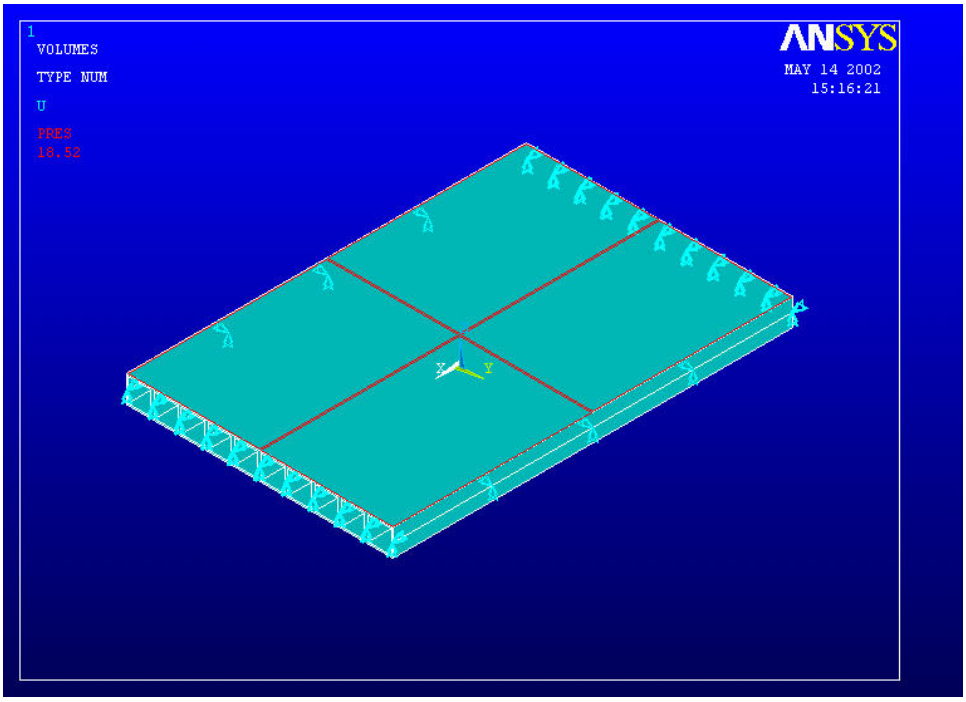


**Figure 3.5** Geometric Model of the tube panel in ANSYS

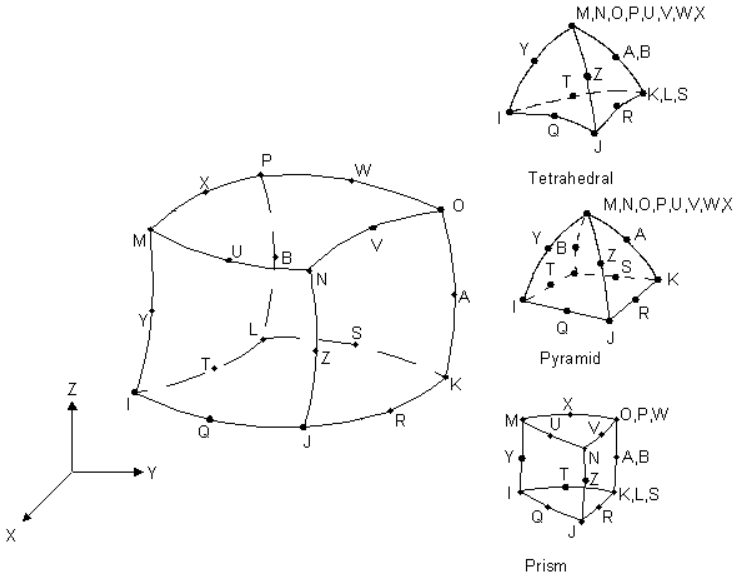


**Figure 3.6** Element SOLID 95 and its variations

[ANSYS, 2002]

The element used in the complete model is SOLID 95, a 3-D, 20-node structural solid element, as shown in Fig. 3.6 [ANSYS 2002]. For each node, there are three degrees of freedom: nodal translations in x, y, and z directions. If some nodes are defined to be the same, several degenerated element shapes can be formed (Figure 3.6). Also, because of the curved element boundaries and high-order nodes displacement field, this element can tolerate irregular shapes and entities with curved boundaries without much loss of accuracy. Another important capability of the Solid elemt is its ability to model orthotropic material properties. When modeling orthotropic materials, the orthotropic material directions in SOLID 95 correspond to the element coordinate directions. In ANSYS, it is possible to verify the element material coordinate systems after meshing the whole tube panel. A meshed panel model is shown in Figure 3.7. Totally, about 96,000 nodes were used in the CTPM modeling.

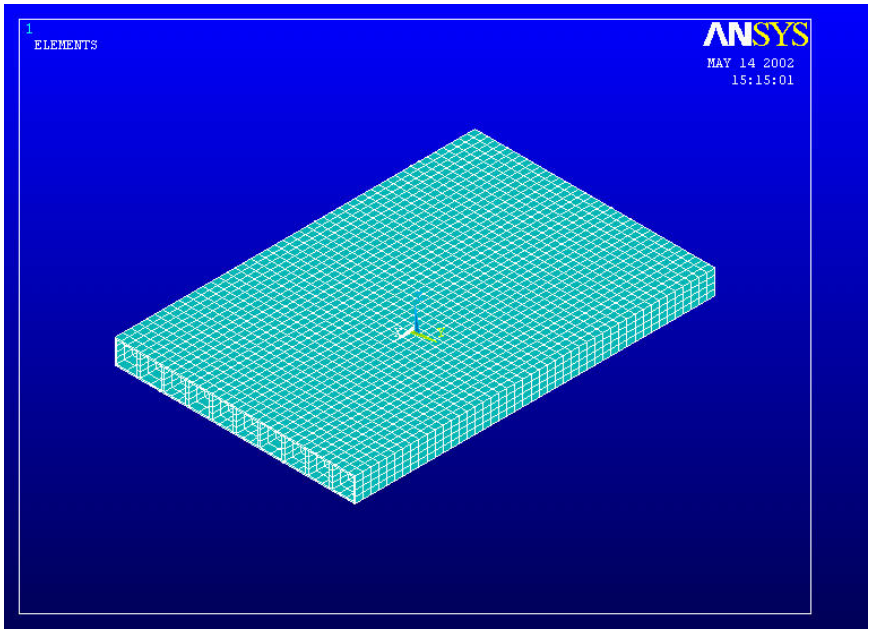


**Figure 3.7** Meshed CTPM tube panel model

The geometry of the 2-D equivalent plate model is shown in Figure 3.8. Because we have rectangular loading patch at the plate's center, the equivalent plate was subdivided into several parts, which were ideally bonded together using the GLUE command in the ANSYS pre-processor. By subdividing the plate as shown in Figure 3.8, a regularly meshed plate could be obtained. The element used in 2-D equivalent modeling is SHELL 93. SHELL 93 is a 8-node structural shell element [ANSYS, 2002], with the six degrees of freedom at each node: translations in the nodal x, y, and z directions and rotations about the nodal x, y, and z-axes. This element has quadratic deformation shape functions in both in-plane directions (x- and y-directions). SHELL 93 has the ability to model orthotropic materials, where orthotropic material directions correspond to the element coordinate directions. Shear deflections are included in SHELL 93. The out-of-plane (normal, or z- direction) stress for this element varies linearly through the thickness. The transverse shear stresses ($S_{yz}$ and $S_{xz}$) are assumed to be constant through the thickness. A meshed model for the 2-D EOPM analysis is shown in Figure 3.10. There were about 1,2000 nodes were used in this model.

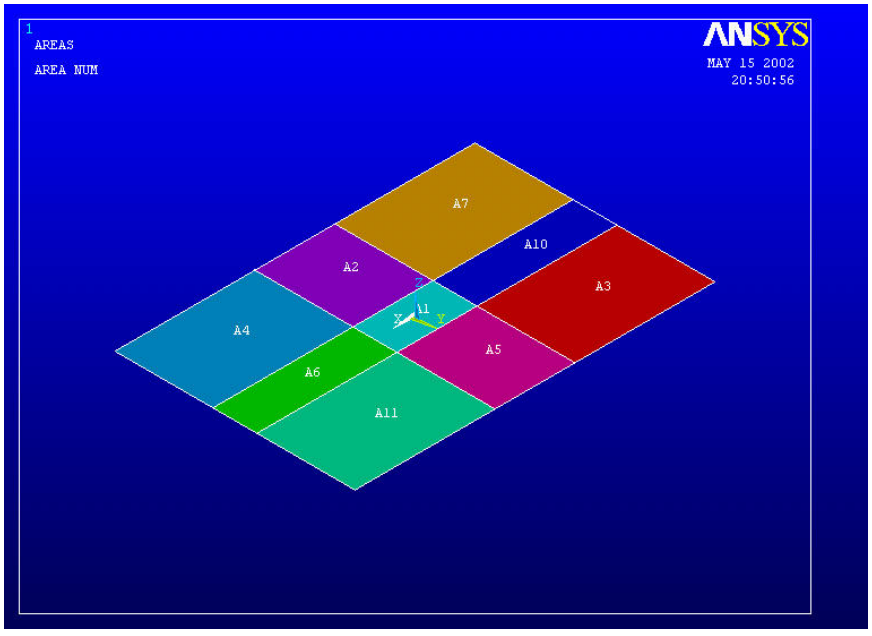


**Figure 3.8** Geometric model for 2-D equivalent plate analysis in ANSYS

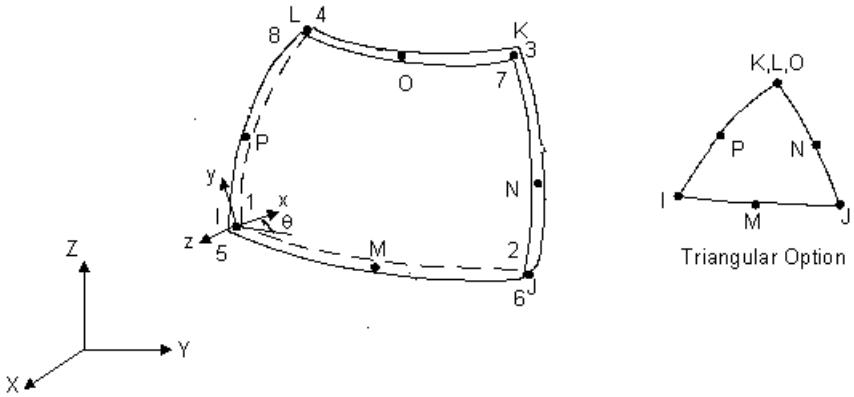


**Figure 3.9** Element SHELL 93 for EOPM modeling

[ANSYS, 2002]

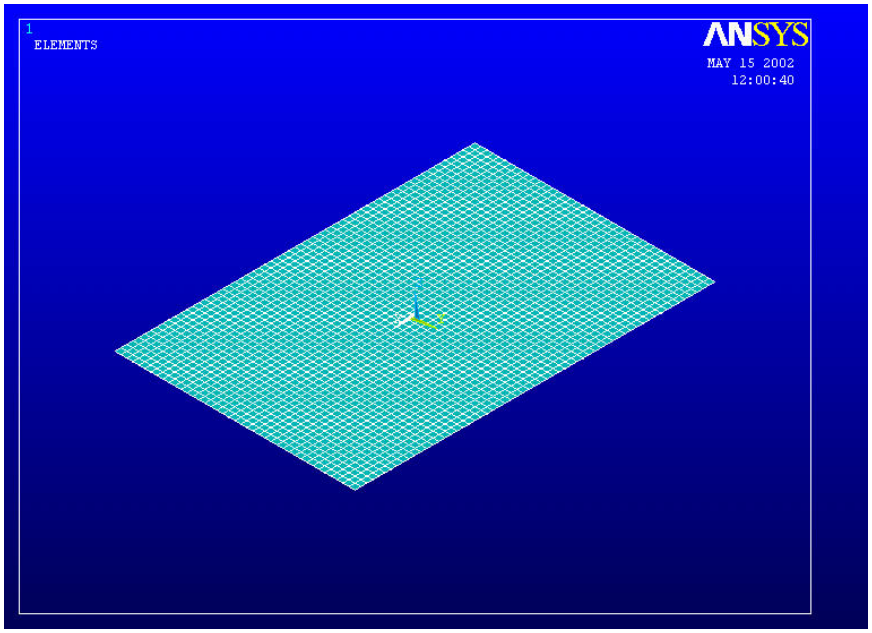


**Figure 3.10** Meshed EOPM model in ANSYS

### 3.2.5. FEA Results and Discussion

Figures (3.11) to (3.19) are plots and results related to SSSS case. In this case, all four edges of the neutral plane in CTPL modeling, and all four edges in the plate of EOPM modeling are specified as simply supported. To simplify the analysis and calculation only half of the tube panel's length was modeled, i.e., a 90" (2286mm) long, 60" (1524mm) wide and 6" (152.4mm) thick panel was modeled. For UDL, a 100 kips (445 kN) force was uniformly distributed over the 90"-60" (2286×1524mm) area, which gives 18.5 psi (127.7 kPa) pressure. The results in Figures (3.11) and (3.12) show very good agreement: the maximum deflection obtained from EOPM is –0.6543" (16.6mm) is 4% less than –0.6824" (17.3mm), the maximum deflection obtained from CTPM. For RPL loading case, a 100 kip (445 kN) force over a 20"×11" (508×279.4mm) rectangular loading area was used in the analysis. Figures (3.13) and (3.14) show the contours of vertical bending deflection for both models. While the numerical results are shown in Figures (3.15) and (3.16). The top surface, mid-plane (or neutral plane), and bottom surface in CTPM have very close deflection pattern. The maximum deflection from EOPM is –1.846" (46.9mm), which is about 11% less than –2.087" (53mm), the maximum deflection from CTPM.

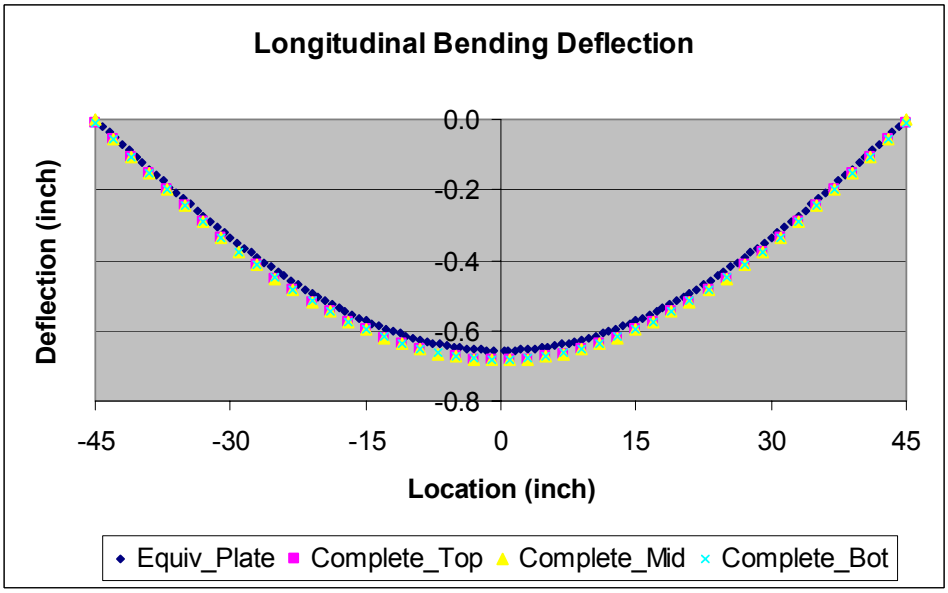


**Figure 3.11** Longitudinal bending deflection comparison for SSSS case under UDL

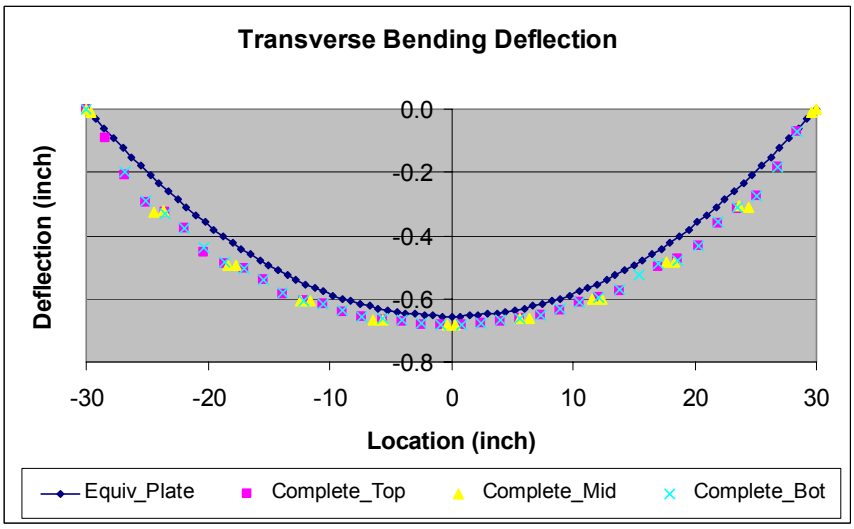


**Figure 3.12** Transverse bending deflection comparison for SSSS case under UDL

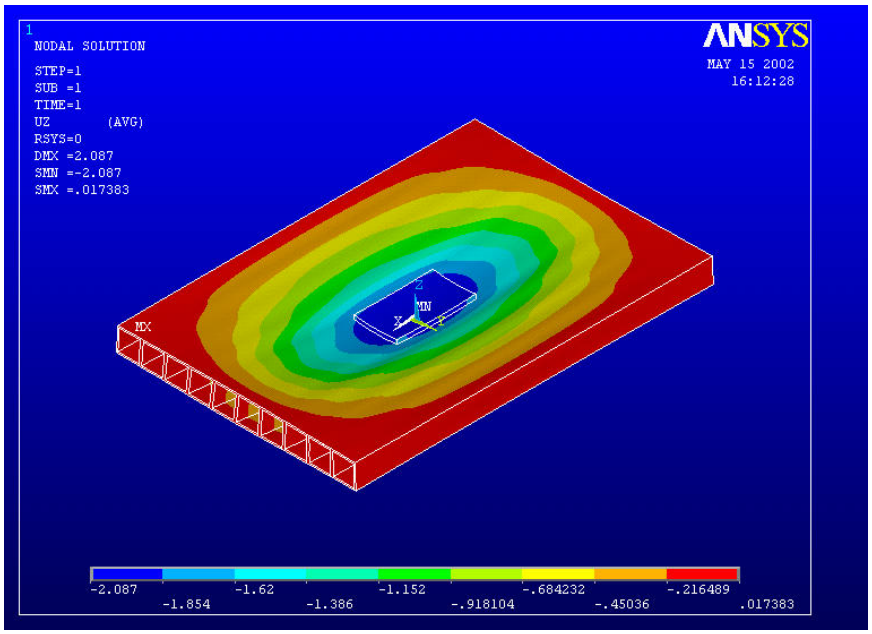


**Figure 3.13** Deflection contour of a SSSS tube panel under RPL from CTPM

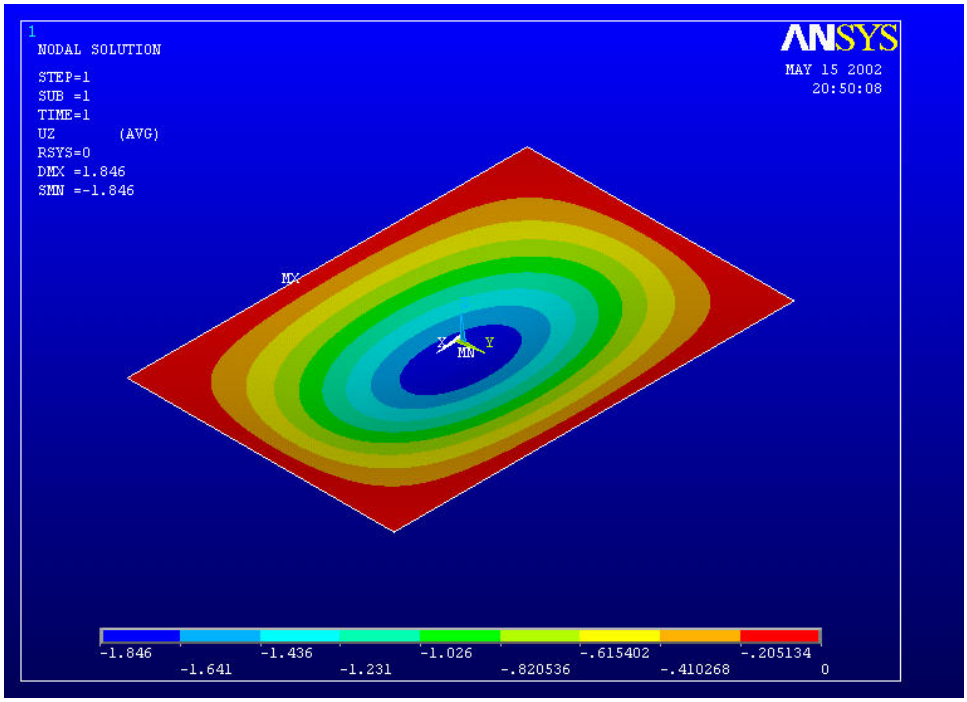


**Figure 3.14** Deflection contour of a SSSS plate under RPL load from EOPM

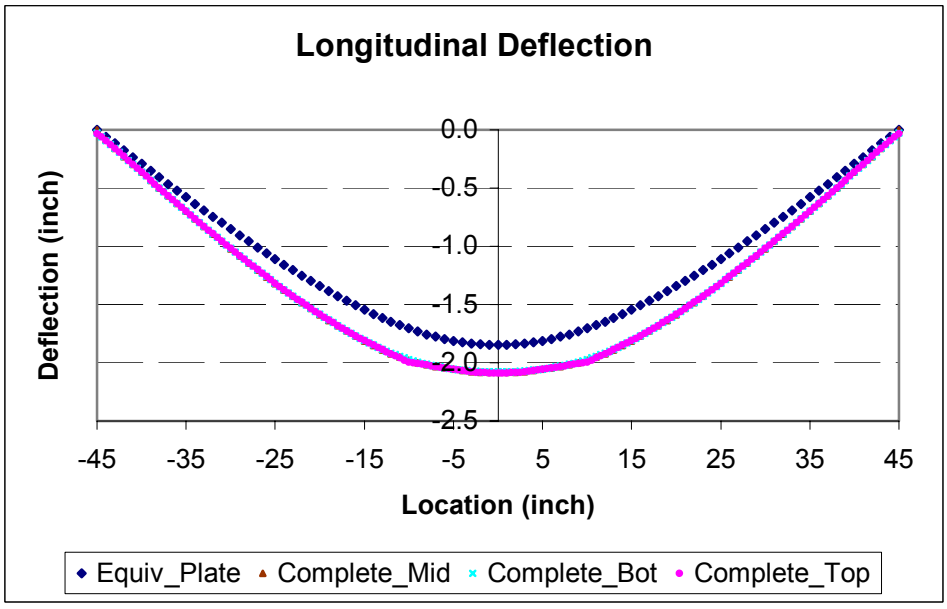


**Figure 3.15** Longitudinal bending deflection comparison for SSSS case under RPL

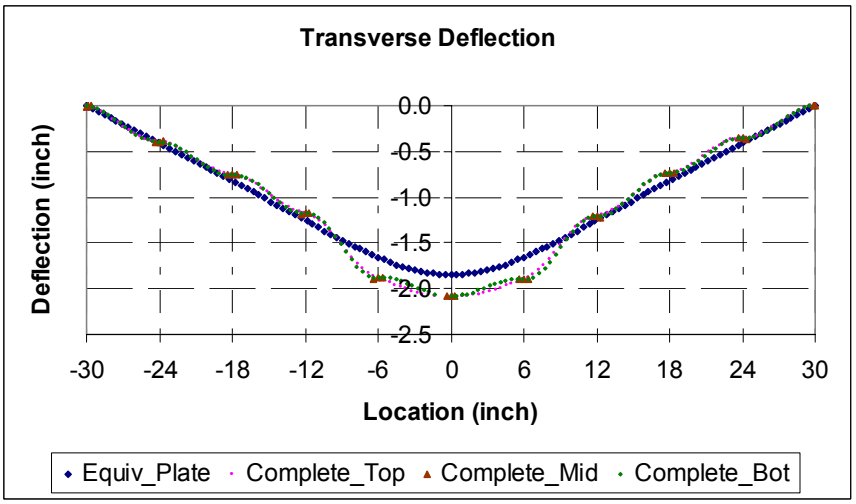


**Figure 3.16** Transverse bending deflection comparison for SSSS case under RPL

A 100 kip (445 kN) force was applied at the center of the tube panel for both models for CPL loading analysis. The bending deflection contours for CTPM and EOPM are shown in Fig. (3.17) and Fig. (3.18) respectively. It is obvious from these figures that the local bending of the deck can be represented in CTPM, but can not be predicted through EOPM. Figure (3.19) shows the numerical deflection results in the transverse direction. Obviously, the region within the width of two inner tubes (-6"- 6" width) is the region where local behavior occurs, and the maximum deflection of the top plane is bigger than the bottom plane in CTPM. Out side this region, the deflection predictions are very close for both methods. For example, at $\pm 6"$ locations, the maximum deflection from EOPM is –1.72" (43.7mm), while the maximum deflection from CTPM is –2.03" (51.6mm), the former is about 15% less than the latter; while at $\pm 12"$, the maximum deflections are almost the same for both models.

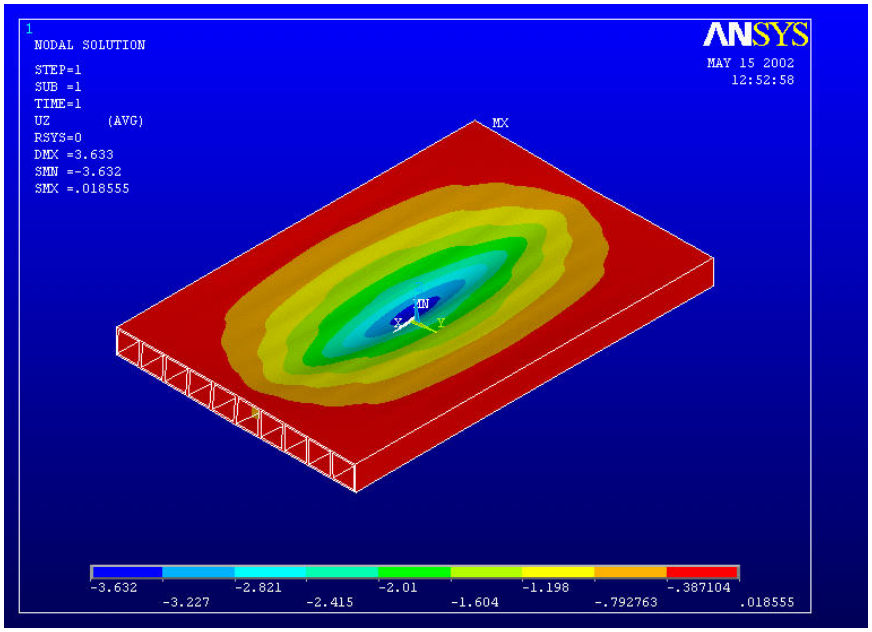


**Figure 3.17** Deflection contour of a SSSS tube panel under CPL from CTPM

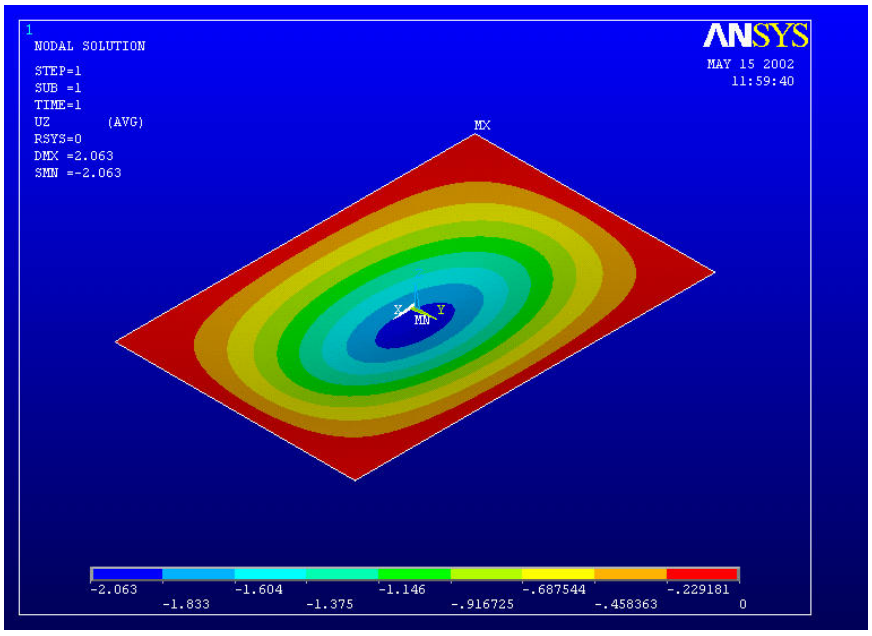


**Figure 3.18** Deflection contour of a SSSS plate under CPL load from EOPM

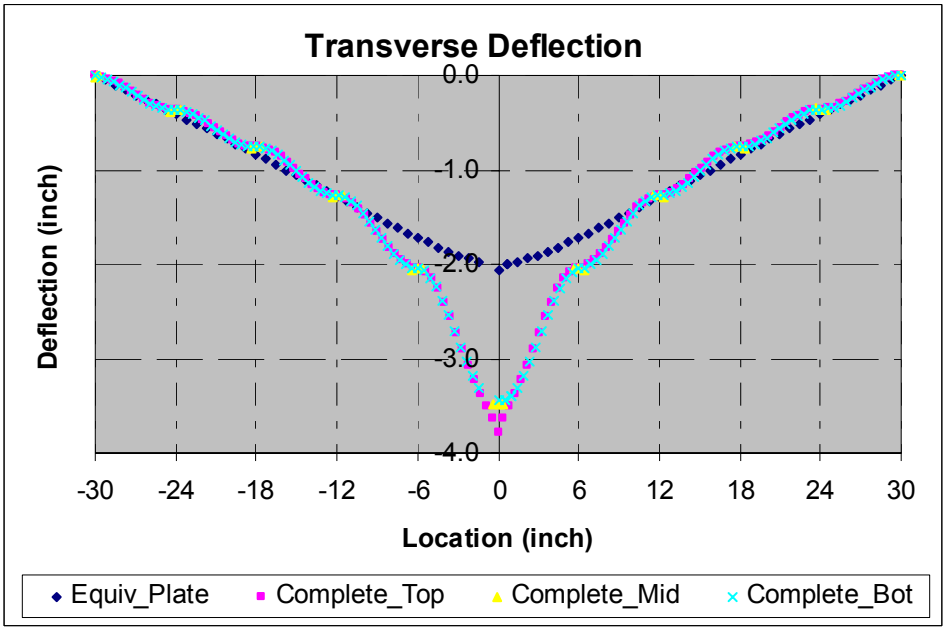


**Figure 3.19** Transverse bending deflection comparison for SSSS case under CPL

For the SSFF case, the two 60" (1524mm) opposite edges on the neutral plane were specified as simply supported, while the other 90" (2286mm) edges were free. A UDL load was applied by a 100 kips (445kN) force uniformly distributed on the 90"×60" (2286×1524mm) area. The deflection contours are shown in Fig. (3.20) and Fig. (3.21) respectively. And Fig. (3.22) and (3.23) represent their numerical comparisons. The top plane, mid-plane, and bottom plane in CTPM have very close deflection pattern and values. Both methods give very close predictions for this case while the CTPM model predicts wave pattern variation of deflections of the tube flanges. This deflection can be defined as second bending: the bending of the tube's top flange to the flange's neutral plane. The first bending is the plate's bending to the neutral plane of the whole plate (or tube assembly). The EOPM model can only predict first bending.

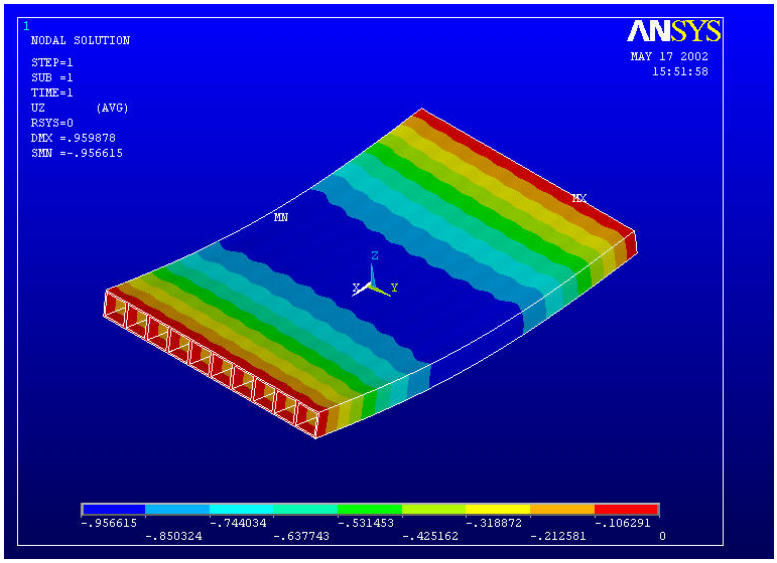


**Figure 3.20** Deflection contour of a SSFF tube panel under UDL from CTPM

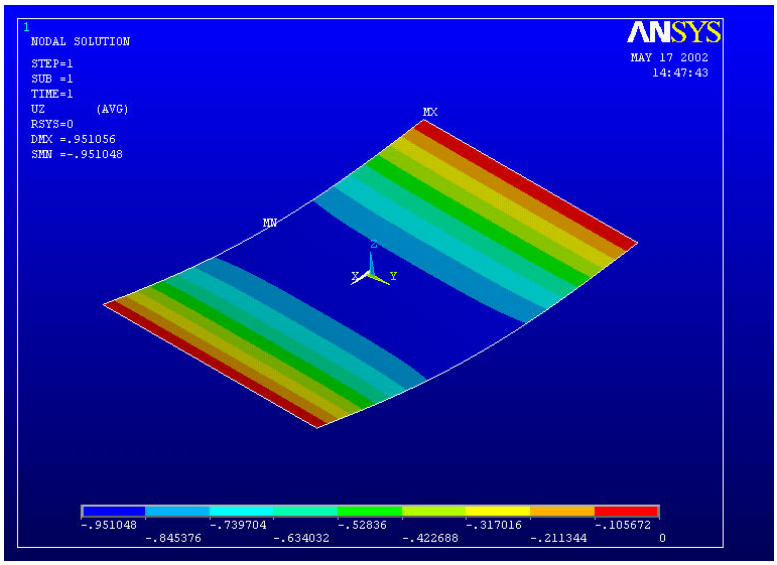


**Figure 3.21** Deflection contour of a SSFF tube panel under UDL from EOPM

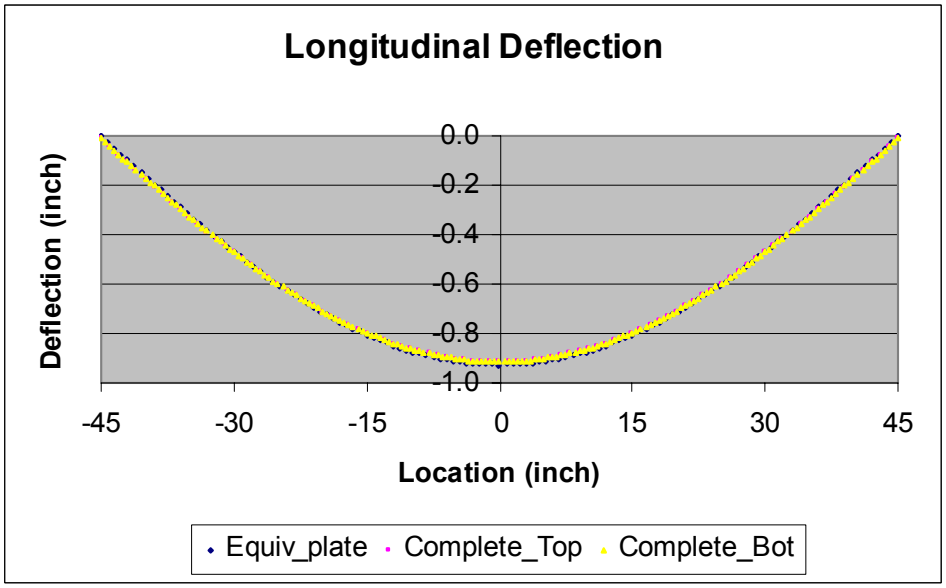


**Figure 3.22** Longitudinal bending deflection comparison for SSFF case under UDL

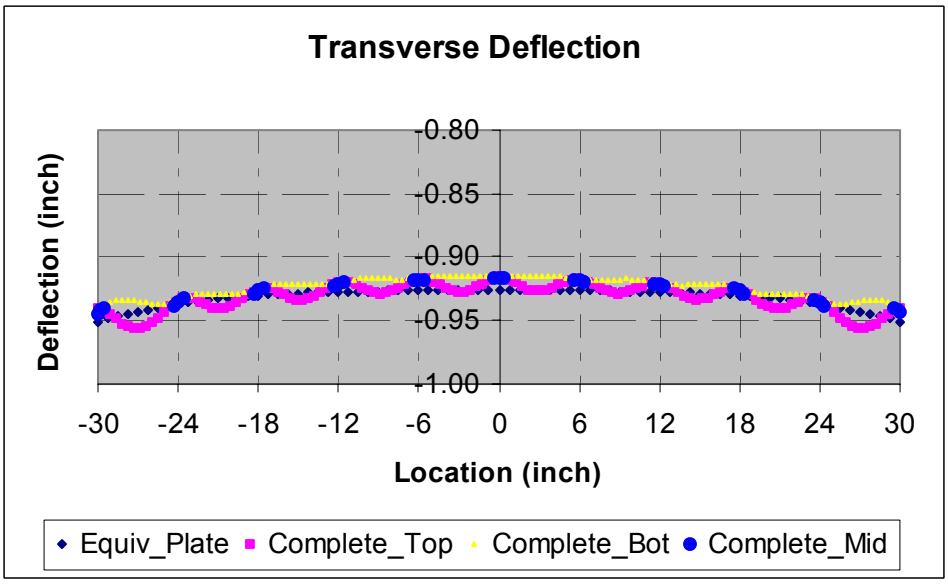


**Figure 3.23** Transverse bending deflection comparison for SSFF case under UDL

A 100 kip (445 kN) force was uniformly distributed on the 20”×11” (508×279.4mm) loading patch area for the RPL loading. The deflection contour obtained from CTPM is shown in Figure 3.24. The numerical results are shown in Figures (3.25) to (3.26). The transverse deflection obtained from CTPM in Figure 3.26 predicts the internal tube web’s effects on the tube panel’s bending behavior. Also, the CTPM curves indicate a localized bending pattern of the tube panel, which can be observed from the slopes of these curves. The top plane, mid-plane, and bottom plane in CTPM have very close deflection pattern. The maximum deflection obtained from EOPM is –2.0829” (53mm) at the deck center, while –2.201” (56mm) is observed from CTPM. The maximum deflections obtained from both models are within 5.4% difference.

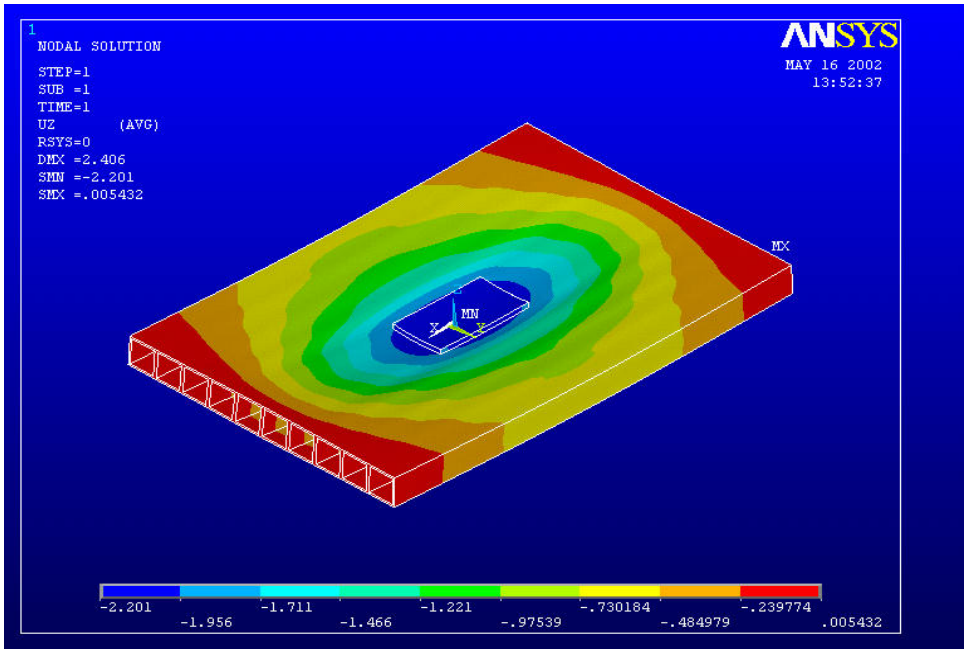


**Figure 3.24** Deflection contour of a SSFF tube panel under RPL from CTPM

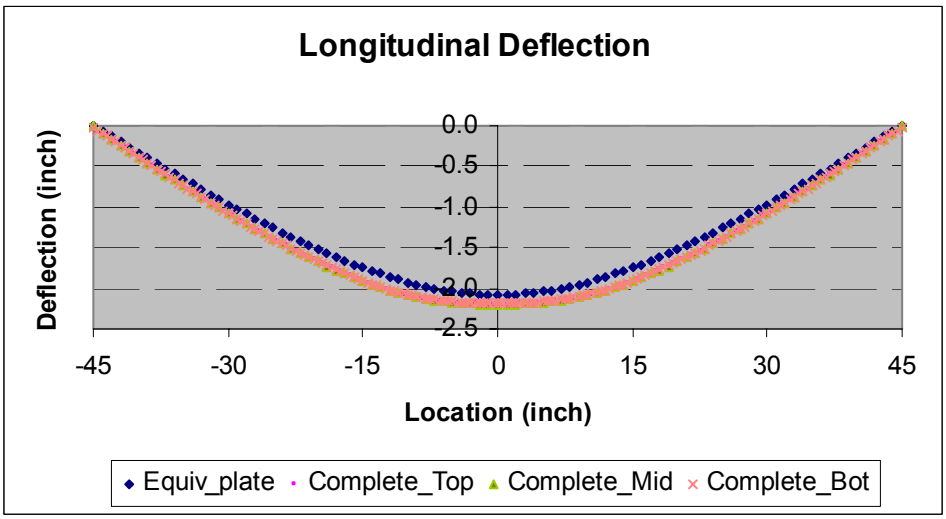


**Figure 3.25** Longitudinal bending deflection comparison for SSFF case under RPL

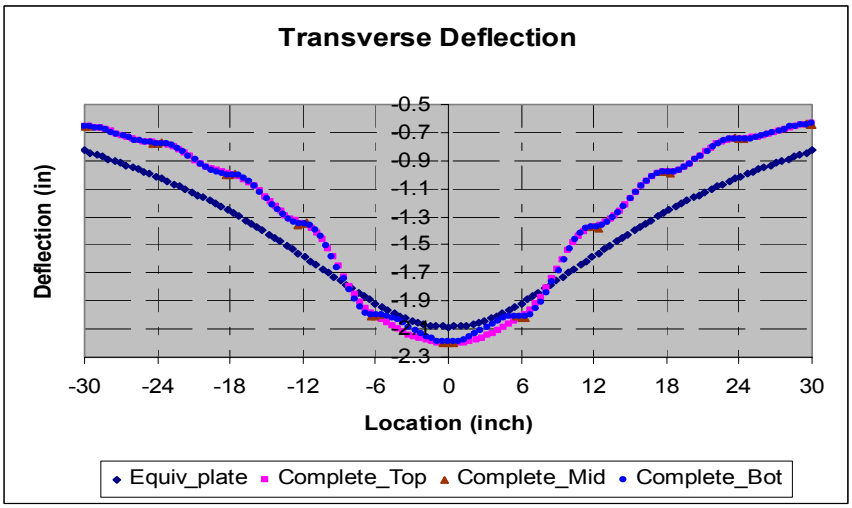


**Figure 3.26** Transverse bending deflection comparison for SSFF case under RPL

For CPL loading, a 100 kips (445 kN) force was applied at the central point for both models. The contours and numerical comparisons are shown in Figures (3.27) – (3.29). Again, the local bending of the –6"-6" region is observed in CTPM (Fig. 3.29), but the EOPM could not predict highly localized bending for point loading.

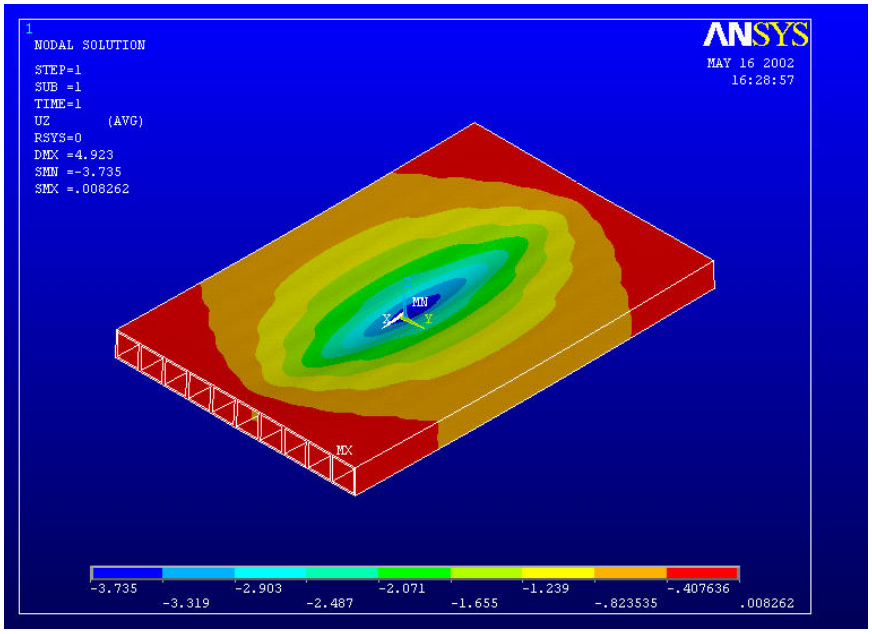


**Figure 3.27** Deflection contour of a SSFF tube panel under CPL from CTPM

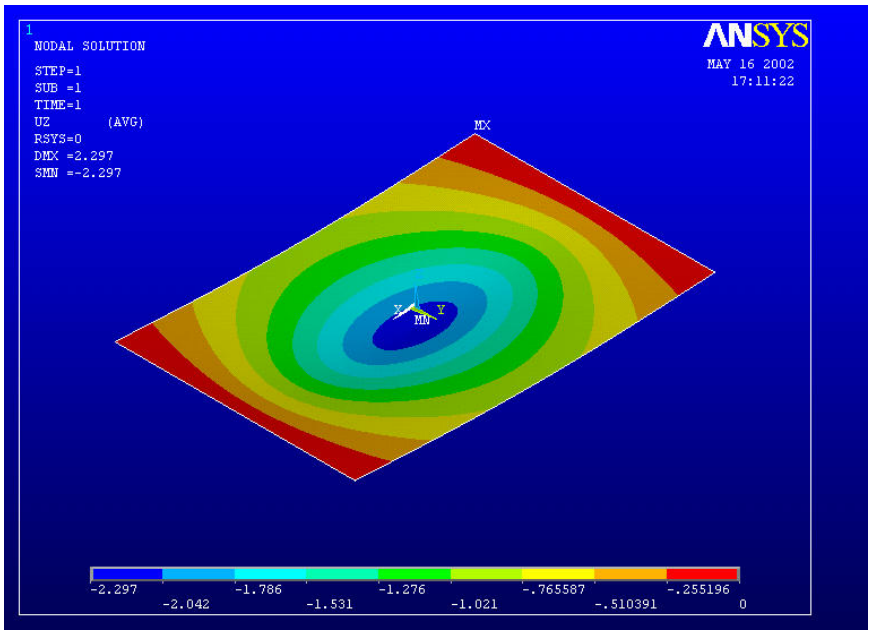


**Figure 3.28** Deflection contour of a SSFF tube panel under CPL from EOPM

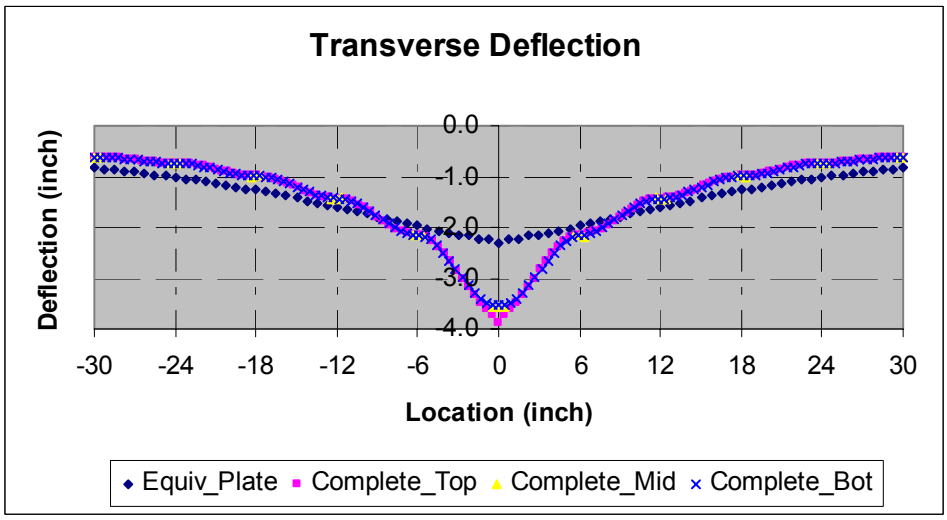


**Figure 3.29** Transverse bending deflection comparison for SSFF case under CPL

The Cantilever Bending of the tube panel was also modeled using booth methods. In the models, one end was clamped, and a 100 kips (445 kN) force was uniformly applied over the 60" (1524mm) edge line. The numerical comparisons are shown in Figures (3.30) and (3.31). Both models give very close predictions for this case. The maximum deflection difference is 10% at the loaded edge, and 9% at the span center.

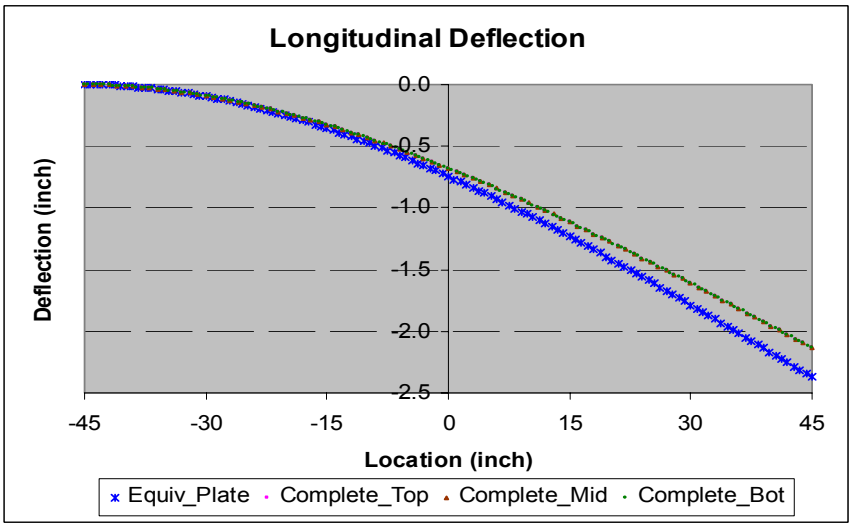


**Figure 3.30** Longitudinal bending deflection comparison for a cantilever panel

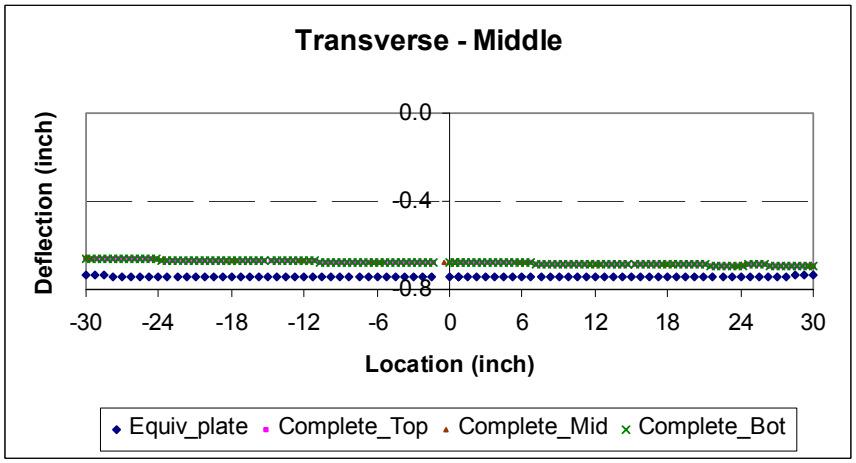


**Figure 3.31** Transverse bending deflection comparison for a cantilever panel

The above results from FEA showed very good agreement of CTPM and EOPM, except for CPL case. For CPL, the equivalent model could not predict a close deflection for the two central tubes, i.e., $(-6"-+6"\ )$ range in Figures (3.19) and (3.29), while it can give very close prediction to CTPM out of this region. The CTPM results indicate the local bending of the thin-walled cellular panel under point loading (or small contacting area loading) are significant.

By now, we have finished Step I in Figure 3.2. In the next section, we will explore Step II and obtain the equivalent orthotropic plate properties for the whole deck panel.

## 3.3 Equivalent Plate Properties of the FRP deck panel

Let $L$ be the deck length (*X-/1-* direction), $W$ be the deck width (*Y-/2-* direction), and $H$ be the deck depth (*Z-/3-* direction). $H_T$, $H_I$, and $H_B$ are thickness of the top plate, internal tube assembly and bottom plate respectively (Figure 3.32). We will develop a procedure to predict the equivalent orthotropic plate properties of the whole deck from the top plate, internal tube assembly and bottom plate.

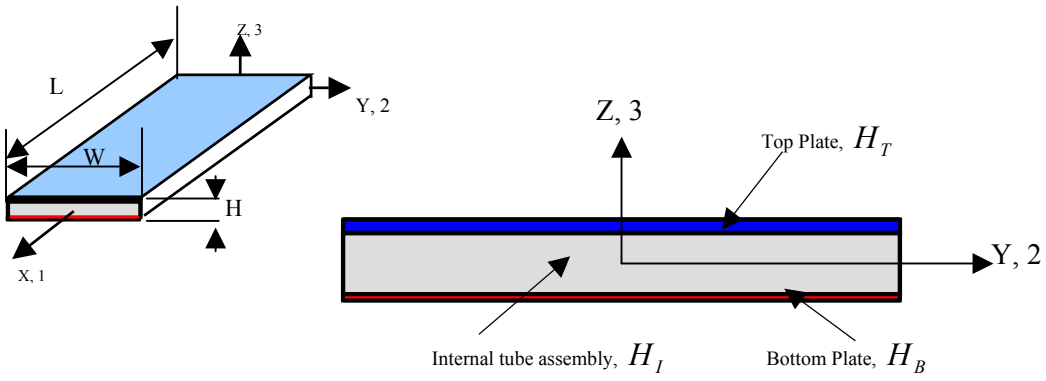


**Figure 3.32** Equivalent plate modeling step II

### 3.3.1 Moduli of Elasticity

When a tensile or compressive load $P_{11}$ is applied parallel to 1-direction (Fig.3.32), it's assumed that the strains on the top plate, internal panel and the bottom plate in direction 1 are equal, which is denoted as $\varepsilon_{11}$. The resultant axial force $P_{11}$ of the deck is shared among the top plate load $P_{11}^T$, internal panel load $P_{11}^I$, and bottom plate load $P_{11}^B$.

$$P_{11} = P_{11}^T + P_{11}^I + P_{11}^B \tag{3.5-a}$$

which can be written as:

$$\sigma_{11} \cdot A_{11} = \sigma_{11}^T \cdot A_{11}^T + \sigma_{11}^I \cdot A_{11}^I + \sigma_{11}^B \cdot A_{11}^B \text{ or } \sigma_{11} = \sigma_{11}^T \cdot \frac{A_{11}^T}{A_{11}} + \sigma_{11}^I \cdot \frac{A_{11}^I}{A_{11}} + \sigma_{11}^B \cdot \frac{A_{11}^B}{A_{11}} \tag{3.5-b}$$

With

$$A_{11} = W \cdot H\ ,\ A_{11}^T = H_T \cdot W\ ,\ A_{11}^I = H_I \cdot W\ ,\ A_{11}^B = H_B \cdot W \tag{3.5-c}$$

Let

$$\alpha_T = \frac{H_T}{H},\ \alpha_I = \frac{H_I}{H},\ \alpha_B = \frac{H_B}{H} \tag{3.5-d}$$

Substituting (3.5-c) and (3.5-d) into (3.5-b), we have,

$$\sigma_{11} = \sigma_{11}^T \cdot \alpha_T + \sigma_{11}^I \cdot \alpha_I + \sigma_{11}^B \cdot \alpha_B$$

Dividing both sides of the above equation by $\varepsilon_{11}$, we have

$$\frac{\sigma_{11}}{\varepsilon_{11}} = \frac{\sigma_{11}^T}{\varepsilon_{11}} \cdot \alpha_T + \frac{\sigma_{11}^I}{\varepsilon_{11}} \cdot \alpha_I + \frac{\sigma_{11}^B}{\varepsilon_{11}} \cdot \alpha_B$$

Since we assumed the strains are the same for each component, we have,

$$E_{11} = \alpha_T \cdot E_{11}^T + \alpha_I \cdot E_{11}^I + \alpha_B \cdot E_{11}^B \tag{3.5-e}$$

Using the same procedure, we can get the equivalent value of $E_{22}$ as the following,

$$E_{22} = \alpha_T \cdot E_{22}^T + \alpha_I \cdot E_{22}^I + \alpha_B \cdot E_{22}^B \tag{3.5-f}$$

Considering the deck under tensile or compressive load $P_{33}$ in 3- direction. This load is distributed over the top and bottom surface. Therefore, the stress in 3-direction is uniform and can be obtained as $\sigma_{33} = \frac{P_{33}}{A_{33}}$. It's obvious that:

$$\sigma_{33} = \sigma_{33}^T = \sigma_{33}^I = \sigma_{33}^B \tag{3.5-g}$$

The strain in direction 3 in each component can be expressed as,

$$\varepsilon_{33}^{T} = \frac{\sigma_{33}^{T}}{E_{33}^{T}},\ \varepsilon_{33}^{I} = \frac{\sigma_{33}^{I}}{E_{33}^{I}},\ \varepsilon_{33}^{B} = \frac{\sigma_{33}^{B}}{E_{33}^{B}} \tag{3.5-h}$$

Displacement for each component,

$$\delta_{33}^{T} = \varepsilon_{33}^{T} \cdot H_T,\ \delta_{33}^{I} = \varepsilon_{33}^{I} \cdot H_I,\ \delta_{33}^{B} = \varepsilon_{33}^{B} \cdot H_B \tag{3.5-i}$$

Total displacement of the deck in 3-direction,

$$\delta_{33} = \delta_{33}^{T} + \delta_{33}^{I} + \delta_{33}^{B} = \varepsilon_{33}^{T} \cdot H_T + \varepsilon_{33}^{I} \cdot H_I + \varepsilon_{33}^{B} \cdot H_B$$

The total strain for the deck in direction 3 can be obtained as,

$$\varepsilon_{33} = \frac{\delta_{33}}{H} = \varepsilon_{33}^{T} \cdot \frac{H_T}{H} + \varepsilon_{33}^{I} \cdot \frac{H_I}{H} + \varepsilon_{33}^{B} \cdot \frac{H_B}{H}$$

Recalling Eq.(3.5-d), we have,

$$\varepsilon_{33} = \varepsilon_{33}^{T} \cdot \alpha_T + \varepsilon_{33}^{I} \cdot \alpha_I + \varepsilon_{33}^{B} \cdot \alpha_B$$

Dividing both sides of the above equation by $\sigma_{33}$, we have,

$$\frac{\varepsilon_{33}}{\sigma_{33}} = \frac{\varepsilon_{33}^{T}}{\sigma_{33}} \cdot \alpha_T + \frac{\varepsilon_{33}^{I}}{\sigma_{33}} \cdot \alpha_I + \frac{\varepsilon_{33}^{B}}{\sigma_{33}} \cdot \alpha_B$$

Substituting (3.5-g) and (3.5-h) in to the above equation, we get,

$$\frac{1}{E_{33}} = \frac{\alpha_T}{E_{33}^{T}} + \frac{\alpha_I}{E_{33}^{I}} + \frac{\alpha_B}{E_{33}^{B}} \quad \text{or} \quad E_{33} = 1/(\frac{\alpha_T}{E_{33}^{T}} + \frac{\alpha_I}{E_{33}^{I}} + \frac{\alpha_B}{E_{33}^{B}}) \tag{3.5-j}$$

### 3.3.2 Moduli of Rigidity

The full derivation of $G_{12}$ is analogous to that for $E_{11}$, and it can be shown that,

$$G_{12} = \alpha_T \cdot G_{12}^T + \alpha_I \cdot G_{12}^I + \alpha_B \cdot G_{12}^B \tag{3.6-a}$$

Similar to $E_{33}$, for $G_{13}$ and $G_{23}$ we have,

$$\frac{1}{G_{13}} = \frac{\alpha_T}{G_{13}^T} + \frac{\alpha_I}{G_{13}^I} + \frac{\alpha_B}{G_{13}^B} \text{ or } G_{13} = 1/(\frac{\alpha_T}{G_{13}^T} + \frac{\alpha_I}{G_{13}^I} + \frac{\alpha_B}{G_{13}^B}) \tag{3.6-b}$$

$$\frac{1}{G_{23}} = \frac{\alpha_T}{G_{23}^T} + \frac{\alpha_I}{G_{23}^I} + \frac{\alpha_B}{G_{23}^B} \text{ or } G_{23} = 1/(\frac{\alpha_T}{G_{23}^T} + \frac{\alpha_I}{G_{23}^I} + \frac{\alpha_B}{G_{23}^B}) \tag{3.6-c}$$

### 3.3.3 Poisson's Ratios

The Poisson's Ratio $\nu_{12}$ is defined as $\nu_{12} = -\frac{\varepsilon_{22}}{\varepsilon_{11}}$ under stress $\sigma_{11}$ only. Suppose we have $\sigma_{11}$ in direction 1, the displacement of each component in direction 2 can be expressed as,

$$\delta_2^T = -\nu_{12}^T \cdot \varepsilon_{11}^T \cdot W,\ \delta_2^I = -\nu_{12}^I \cdot \varepsilon_{11}^I \cdot W,\ \delta_2^B = -\nu_{12}^B \cdot \varepsilon_{11}^B \cdot W \tag{3.6-d}$$

We assume that the total displacement in 2-direction can be obtained from the displacement of each component with the following form,

$$\delta_2 = \alpha_T \cdot \delta_2^T + \alpha_I \cdot \delta_2^I + \alpha_B \cdot \delta_2^B$$

From (3.6-d) we have,

$$\delta_2 = -\alpha_T \cdot \nu_{12}^T \cdot \varepsilon_{11}^T \cdot W - \alpha_I \cdot \nu_{12}^I \cdot \varepsilon_{11}^I \cdot W - \alpha_B \cdot \nu_{12}^B \cdot \varepsilon_{11}^B \cdot W$$

The total displacement in direction 2 can also be expressed as $\delta_2 = -\nu_{12} \cdot \varepsilon_{11} \cdot W$ . Therefore,

$$-\nu_{12} \cdot \varepsilon_{11} \cdot W = -\alpha_T \cdot \nu_{12}^T \cdot \varepsilon_{11}^T \cdot W - \alpha_I \cdot \nu_{12}^I \cdot \varepsilon_{11}^I \cdot W - \alpha_B \cdot \nu_{12}^B \cdot \varepsilon_{11}^B \cdot W \qquad (3.6\text{-e})$$

Dividing both sides of eq.(3.6-e) by $-\varepsilon_{11} \cdot W$ , we have,

$$\nu_{12} = \alpha_T \cdot \nu_{12}^T \cdot \frac{\varepsilon_{11}^T}{\varepsilon_{11}} + \alpha_I \cdot \nu_{12}^I \cdot \frac{\varepsilon_{11}^I}{\varepsilon_{11}} + \alpha_B \cdot \nu_{12}^B \cdot \frac{\varepsilon_{11}^B}{\varepsilon_{11}}$$

Considering $\nu_{11}^i = \varepsilon_{11}$ (where *i = T, I, B*), the above equation can be rewritten as,

$$\nu_{12} = \alpha_T \cdot \nu_{12}^T + \alpha_I \cdot \nu_{12}^I + \alpha_B \cdot \nu_{12}^B \qquad (3.6\text{-f})$$

$\nu_{13} = -\dfrac{\varepsilon_{33}}{\varepsilon_{11}}$ under $\sigma_{11}$ only. The displacements in direction-3 for each component,

$$\delta_3^T = -\nu_{13}^T \cdot \varepsilon_{11}^T \cdot H_T,\ \delta_3^I = -\nu_{13}^I \cdot \varepsilon_{11}^I \cdot H_I,\ \delta_3^B = -\nu_{13}^B \cdot \varepsilon_{11}^B \cdot H_B$$

The total displacement in the 3- direction can be obtained as,

$$\delta_3 = \delta_3^T + \delta_3^I + \delta_3^B = -\nu_{13}^T \cdot \varepsilon_{11}^T \cdot H_T - \nu_{13}^I \cdot \varepsilon_{11}^I \cdot H_I - \nu_{13}^B \cdot \varepsilon_{11}^B \cdot H_B$$

The total displacement can also be expressed as $\delta_3 = -\nu_{13} \cdot \varepsilon_{11} \cdot H$ . Hence, we have,

$$\nu_{13} \cdot \varepsilon_{11} \cdot H = \nu_{13}^T \cdot \varepsilon_{11}^T \cdot H_T + \nu_{13}^I \cdot \varepsilon_{11}^I \cdot H_I + \nu_{13}^B \cdot \varepsilon_{11}^B \cdot H_B$$

From the above equation**,** we have

$$\nu_{13} = \nu_{13}^{T} \cdot \frac{\varepsilon_{11}^{T} \cdot H_T}{\varepsilon_{11} \cdot H} + \nu_{13}^{I} \cdot \frac{\varepsilon_{11}^{I} \cdot H_I}{\varepsilon_{11} \cdot H} + \nu_{13}^{B} \cdot \frac{\varepsilon_{11}^{B} \cdot H_B}{\varepsilon_{11} \cdot H}$$

Recalling that $\alpha_i = \frac{H_i}{H}$ ($i = T, I, B$), we can rearrange the above equation as,

$$\nu_{13} = \alpha_T \cdot \nu_{13}^{T} + \alpha_I \cdot \nu_{13}^{I} + \alpha_B \cdot \nu_{13}^{B} \tag{3.6-g}$$

Similarly, $\nu_{23}$ can be obtained as,

$$\nu_{23} = \alpha_T \cdot \nu_{23}^{T} + \alpha_I \cdot \nu_{23}^{I} + \alpha_B \cdot \nu_{23}^{B} \tag{3.6-h}$$

The stress-strain matrix is required to be positive definite for real materials. Being positive definite means that the following formulation holds

$$1 - (\nu_{23})^2 \cdot \frac{E_{33}}{E_{22}} - (\nu_{13})^2 \cdot \frac{E_{33}}{E_{11}} - (\nu_{12})^2 \cdot \frac{E_{22}}{E_{11}} - 2 \cdot \nu_{12} \cdot \nu_{23} \cdot \nu_{13} \cdot \frac{E_{33}}{E_{11}} \geq 0 \tag{3.7}$$

Tables (3.4) – (3.7) show all material properties for each deck component and the equivalent orthotropic plate properties of the deck using the above proposed method. In the following section, the comparisons for the bending behavior of the deck using Finite Element Analysis will be presented. Also, when testing results are available, both modeling results will be compared with the test data.

**TABLE 3.4 Material Properties of Deck Components –Top Skin Plate**

| Property | Value | Method used |
|---|---|---|
| $E_{xx}\ (psi)$ | $2.42\times10^{6}$ | From manual, testing |
| $E_{yy}\ (psi)$ | $1.39\times10^{6}$ | From manual, testing |
| $E_{zz}\ (psi)$ | $1.39\times10^{6}$ | Assumption: $E_{zz}=E_{yy}$ |
| $G_{xy}\ (psi)$ | $0.743\times10^{6}$ | Approximation $G_{xy}=\dfrac{\sqrt{E_{xx}\cdot E_{yy}}}{2\cdot(1-\sqrt{\nu_{xy}\cdot\nu_{yx}})}$ |
| $G_{xz}\ (psi)$ | $0.706\times10^{6}$ | Approximation $G_{xz}=\dfrac{\sqrt{E_{xx}\cdot E_{zz}}}{2\cdot(1-\sqrt{\nu_{xz}\cdot\nu_{zx}})}$ |
| $G_{yz}\ (psi)$ | $0.539\times10^{6}$ | Approximation $G_{yz}=\dfrac{\sqrt{E_{yy}\cdot E_{zz}}}{2\cdot(1-\sqrt{\nu_{yz}\cdot\nu_{zy}})}$ |
| $\nu_{xy}$ | 0.31 | From manual, testing |
| $\nu_{xz}$ | 0.31 | Assumption $\nu_{xz}=\nu_{xy}$ |
| $\nu_{yz}$ | 0.29 | From manual [Strongwell, 1998] |

**TABLE 3.5 Material Properties of Deck Components – Internal Tube Panel**

| Property | Value | Method used |
|---|---|---|
| $E_{xx}\ (psi)$ | $0.95\times10^{6}$ | $E^{e}_{xx}=\dfrac{12\cdot D_{xx}\cdot(1-\nu^{e}_{xy}\cdot\nu^{e}_{yx})}{H^{3}}$ |
| $E_{yy}\ (psi)$ | $0.025\times10^{6}$ | $E^{e}_{yy}=\dfrac{12\cdot D_{yy}\cdot(1-\nu^{e}_{xy}\cdot\nu^{e}_{yx})}{H^{3}}$ |
| $E_{zz}\ (psi)$ | $0.8\times10^{6}$ | Assumption $E^{e}_{zz}=E_{zz}$ |
| $G_{xy}\ (psi)$ | $0.07\times10^{6}$ | $G^{e}_{xy}=\dfrac{12\cdot D_{66}}{H^{3}}$ |
| $G_{xz}\ (psi)$ | $0.79\times10^{6}$ | $G^{e}_{xz}=\dfrac{D_{xz}}{H}=\dfrac{G\cdot J}{H\cdot H}$ |
| $G_{yz}\ (psi)$ | $0.05\times10^{6}$ | $G^{e}_{yz}=\dfrac{D_{yz}}{H}=\dfrac{G\cdot J}{H\cdot L}$ |
| $\nu_{xy}$ | 0.33 | Assumption: $\nu^{e}_{xy}=\nu_{xy}$ |
| $\nu_{xz}$ | 0.33 | Assumption: $\nu^{e}_{xz}=\nu^{e}_{xy}$ |
| $\nu_{yz}$ | 0.10 | Determined via stress-strain matrix positive definite requirement for a real material |

**TABLE 3.6 Material Properties of Deck Components - Bottom Skin Plate**

| Property | Value | Method used |
|---|---|---|
| $E_{xx}\ (psi)$ | $1.8\times10^{6}$ | From manual [Strongwell, 1998] |
| $E_{yy}\ (psi)$ | $0.9\times10^{6}$ | From manual [Strongwell, 1998] |
| $E_{zz}\ (psi)$ | $0.9\times10^{6}$ | Assumption: $E_{zz}=E_{yy}$ |
| $G_{xy}\ (psi)$ | $0.522\times10^{6}$ | Approximation $G_{xy}=\dfrac{\sqrt{E_{xx}\cdot E_{yy}}}{2\cdot(1-\sqrt{\nu_{xy}\cdot\nu_{yx}})}$ |
| $G_{xz}\ (psi)$ | $0.490\times10^{6}$ | Approximation $G_{xz}=\dfrac{\sqrt{E_{xx}\cdot E_{zz}}}{2\cdot(1-\sqrt{\nu_{xz}\cdot\nu_{zx}})}$ |
| $G_{yz}\ (psi)$ | $0.349\times10^{6}$ | Approximation $G_{yz}=\dfrac{\sqrt{E_{yy}\cdot E_{zz}}}{2\cdot(1-\sqrt{\nu_{yz}\cdot\nu_{zy}})}$ |
| $\nu_{xy}$ | 0.31 | From manual [Strongwell, 1998] |
| $\nu_{xz}$ | 0.31 | Assumption $\nu_{xz}=\nu_{xy}$ |
| $\nu_{yz}$ | 0.29 | From manual [Strongwell, 1998] |

**TABLE 3.7 Equivalent Bridge Deck Properties**

| Property | Value | Method used |
|---|---|---|
| $E^{e}_{xx}\ (psi)$ | $1.087\times10^{6}$ | $E_{11}=\alpha_T\cdot E^{T}_{11}+\alpha_I\cdot E^{I}_{11}+\alpha_B\cdot E^{B}_{11}$ |
| $E^{e}_{yy}\ (psi)$ | $0.1585\times10^{6}$ | $E_{22}=\alpha_T\cdot E^{T}_{22}+\alpha_I\cdot E^{I}_{22}+\alpha_B\cdot E^{B}_{22}$ |
| $E^{e}_{zz}\ (psi)$ | $0.8295\times10^{6}$ | $\dfrac{1}{E_{33}}=\dfrac{\alpha_T}{E^{T}_{33}}+\dfrac{\alpha_I}{E^{I}_{33}}+\dfrac{\alpha_B}{E^{B}_{33}}$ |
| $G^{e}_{xy}\ (psi)$ | $0.1366\times10^{6}$ | $G_{12}=\alpha_T\cdot G^{T}_{12}+\alpha_I\cdot G^{I}_{12}+\alpha_B\cdot G^{B}_{12}$ |
| $G^{e}_{xz}\ (psi)$ | $0.7641\times10^{6}$ | $\dfrac{1}{G_{13}}=\dfrac{\alpha_T}{G^{T}_{13}}+\dfrac{\alpha_I}{G^{I}_{13}}+\dfrac{\alpha_B}{G^{B}_{13}}$ |
| $G^{e}_{yz}\ (psi)$ | $0.0582\times10^{6}$ | $\dfrac{1}{G_{23}}=\dfrac{\alpha_T}{G^{T}_{23}}+\dfrac{\alpha_I}{G^{I}_{23}}+\dfrac{\alpha_B}{G^{B}_{23}}$ |
| $\nu^{e}_{xy}$ | 0.328 | $\nu_{12}=\alpha_T\cdot\nu^{T}_{12}+\alpha_I\cdot\nu^{I}_{12}+\alpha_B\cdot\nu^{B}_{12}$ |
| $\nu^{e}_{xz}$ | 0.328 | $\nu_{13}=\alpha_T\cdot\nu^{T}_{13}+\alpha_I\cdot\nu^{I}_{13}+\alpha_B\cdot\nu^{B}_{13}$ |
| $\nu^{e}_{yz}$ | 0.05 | Determined via stress-strain matrix positive definite requirement for a real material |

## 3.4 FEA Structural Analysis Comparisons

Two different models were used in the analysis: the Complete Deck Model (CDM) and the Equivalent Deck Model (EDM). In CDM, the deck was modeled as the following: ten identical tubes completely bonded together to form the tube panel sandwich; the sandwich is then completely bonded with a top plate and a bottom plate. Since previous research [Zhou et al, 2001] showed the contribution of transverse steel rods to the bending of the deck system can be neglected in FEA analysis, no transverse rods effects were modeled, and this model represents the real FRP deck system. To reduce calculation time, only half of the deck was modeled, which leaded to a 91.5" (2324mm) long, 60" (1524mm) wide and 6.75" (171.5mm) thick model. The element used for this model is SOLID 95, which is the same as for 3-D tube assembly modeling in previous section.

The meshed CDM deck model is shown in Figure 3.33, where about 10,000 elements and 51,000 nodes were used. For each component, we need to check the element coordinates in the model. Special attention should be made to the element coordinates of internal tube webs, since their Z-direction is the normal web direction. A local coordinate system with the Z-direction parallel to the web's normal direction is required for these webs. The element normals reorientation can be done in ANSYS when the meshed elements normals are not initially correct.

The EDM was modeled as a 91.5" (2324mm) long, 60" (1524mm) wide plate, which was meshed by SHELL 93 with a 6.75" (171.5mm) thick element real constant. The meshed model is shown in Figure 3.34. In this model, about 4,400 nodes and 1,400 elements were used.

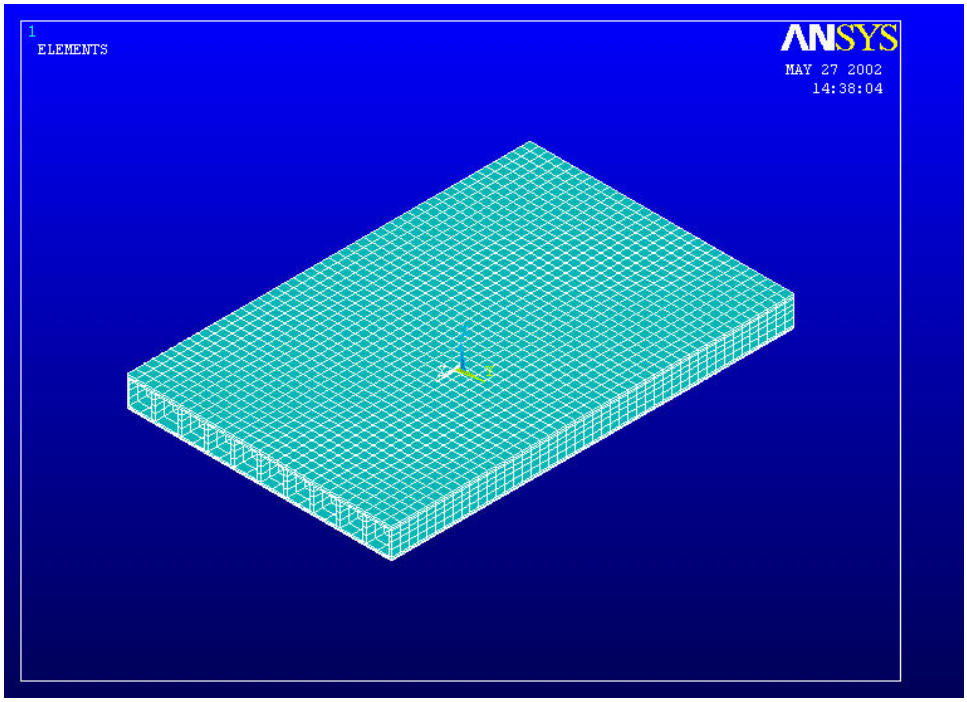


**Figure 3.33** Meshed CDM deck model in ANSYS

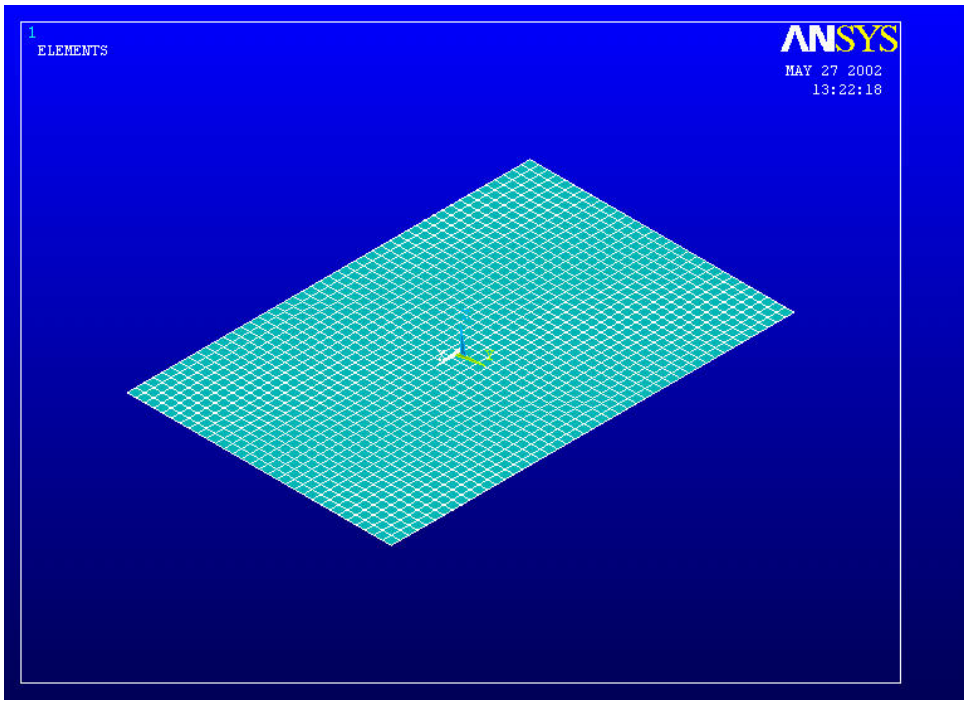


**Figure 3.34** 2-D Meshed EDM model in ANSYS

Three cases of plates were modeled: CFSS, SSFF, and SSSS. The CFSS case was chosen to compare the numerical results from both models to the tested data from laboratory testing. For CFSS case, three loading conditions were modeled and compared with the tested data: The RPL loading at the center of the edge using steel loading patch (WP1-WP4, or WP3-WP6); RPL loading at the center of a single span (WP2 and WP5) using rubber-stuffed tire patch; and RPL loading at the center of a single span (WP2 and WP5) using steel patch. For the loading, a 26 kips (115.6 kN) force was modeled as uniformly distributed over the steel patch and the tire patch areas, which leads to a 118.2 psi (815 kPa) pressure and 216.7 psi (1.5 Mpa) pressure over the 20"×11" (508×279.4mm) area (steel patch) and the 15"×8" area (381× 203.2mm) (tire patch) respectively. For this non-symmetric cross-section deck system, the neutral bending axis can be calculated using the plot in Figure 3.35.

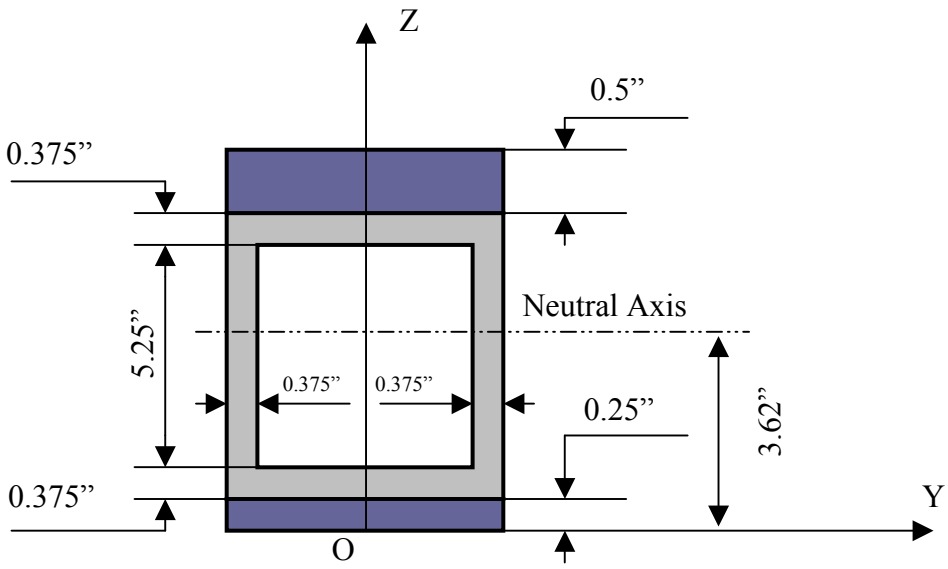


**Figure 3.35** Calculation of neutral bending plane for the deck

For the investigated deck system, the neutral bending plane can be found at $z = 3.62"$ (92 mm). The CSFF, SSFF and SSSS boundary conditions should be specified at this neutral plane. For example, Figure 3.36 shows pictures with specified boundary conditions in ANSYS, where central RPL loading was applied in Fig. (3.36-a) and a RPL load was applied at the edge center in Fig. (3.36-b). In the following, FEA results and comparisons will be presented. In CDM, deflections results obtained from the top plate, the bottom plate and the neutral plane were

collected and exported to plot comparison curves. The results and comparisons are shown through Figures (3.37) to Figures (3.49) for different loading case and boundary conditions.

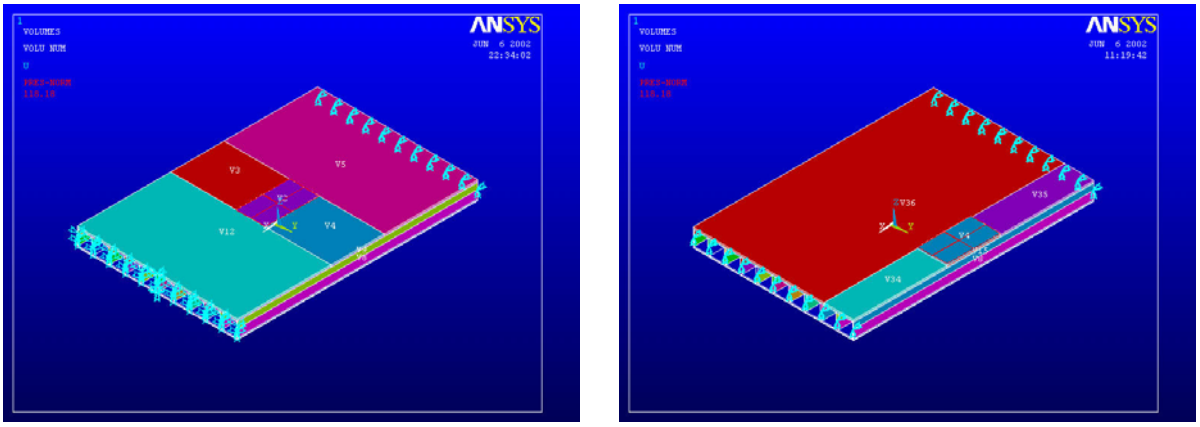


(a) CSFF with central RPL loading (b) SSFF with RPL central edge

**Figure 3.36** Boundary Conditions for CDM decks

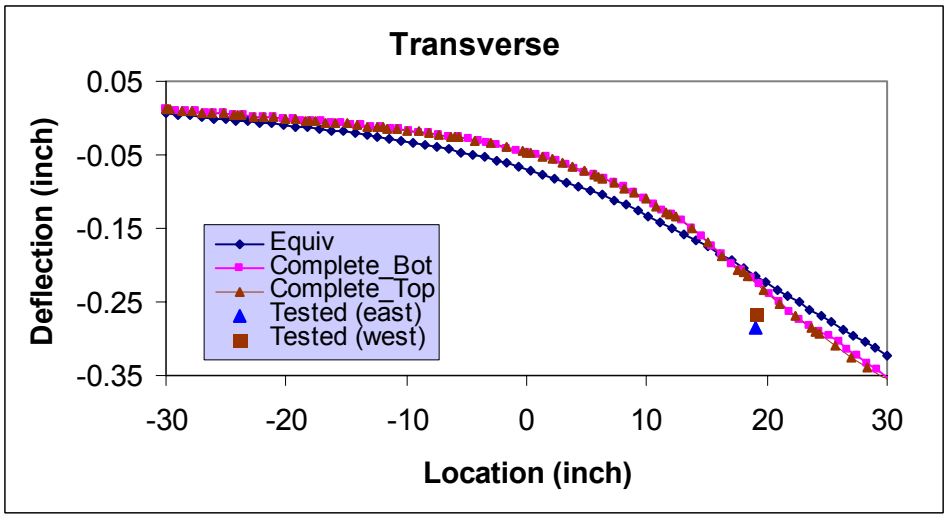


**Figure 3.37** Transverse bending deflection comparisons with CSFF case under RPL at single span's edge center (WP1-WP4, or WP3-WP6) using steel patch

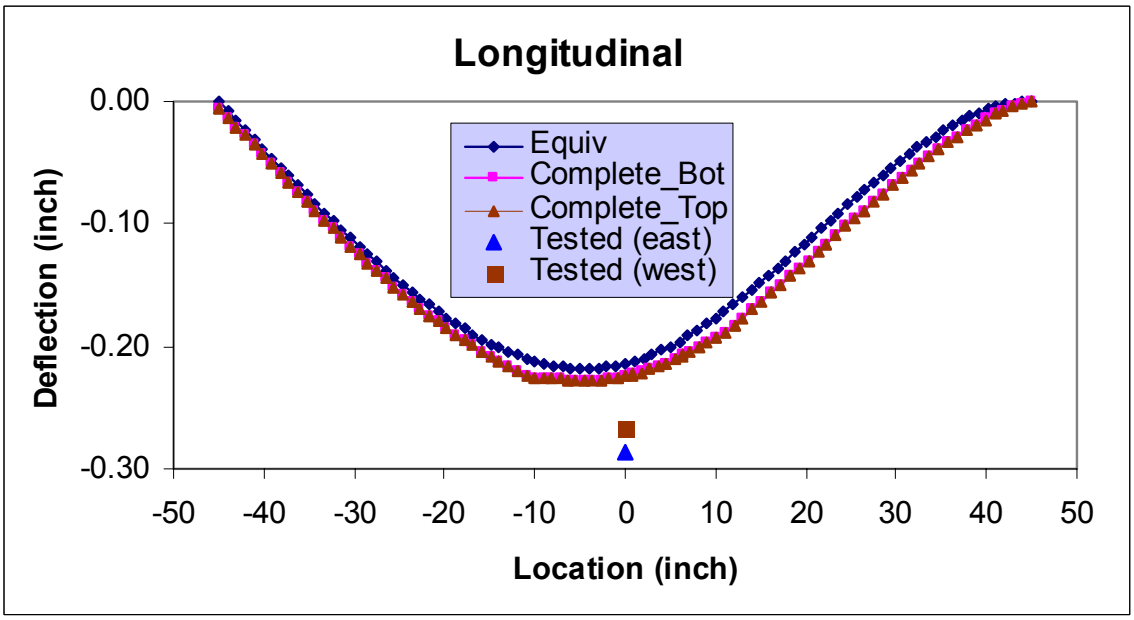


**Figure 3.38** Longitudinal bending deflection comparisons with CSFF case under RPL at single span's edge center (WP1-WP4, or WP3-WP6) using steel patch

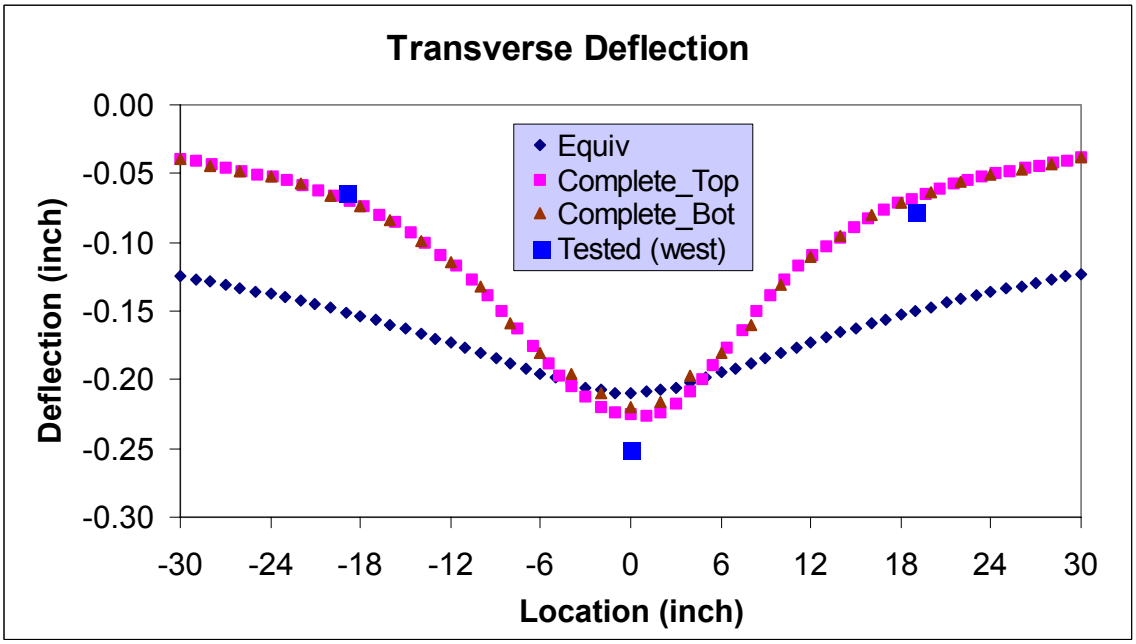


**Figure 3.39** Transverse bending deflection comparisons with CSFF case under RPL at single span's center (WP2 or WP5) using simulated tire patch

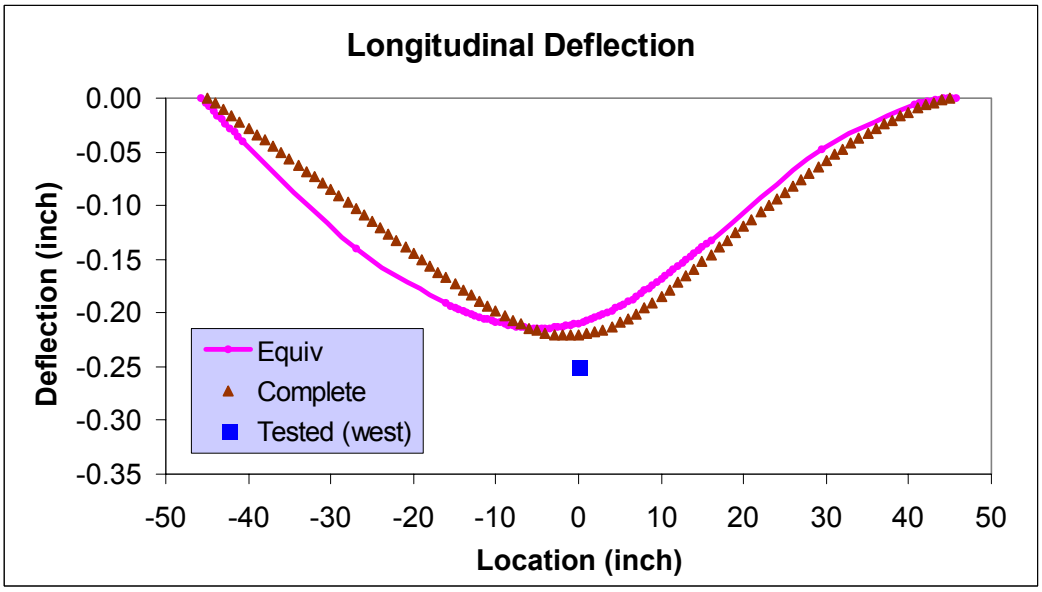


**Figure 3.40** Longitudinal bending deflection comparisons with CSFF case under RPL at single span's center (WP2 or WP5) using simulated tire patch

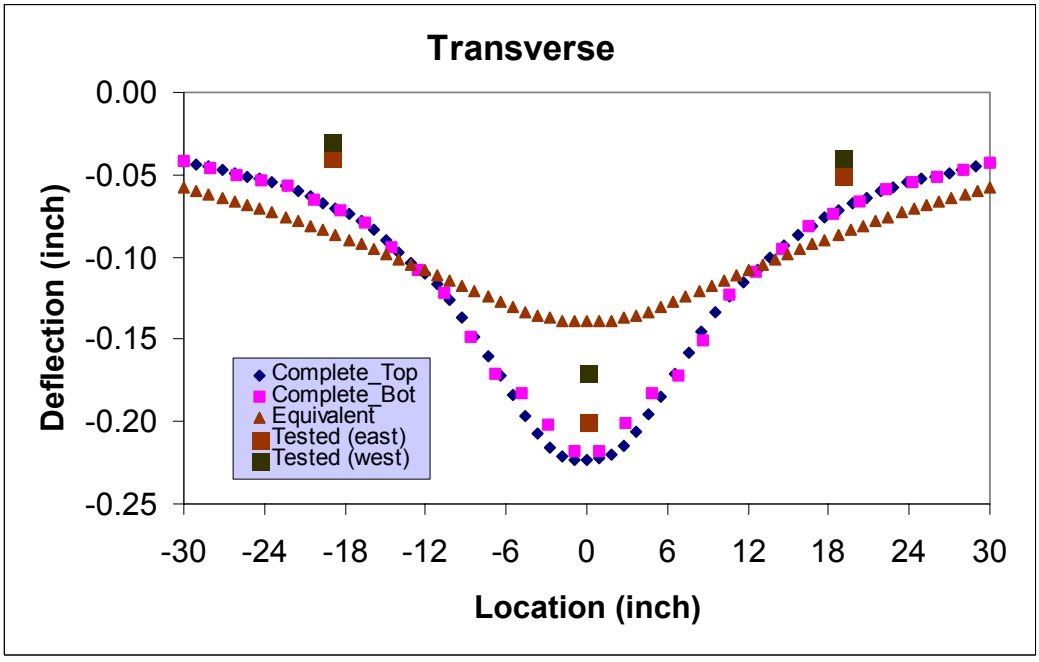


**Figure 3.41** Transverse bending deflection comparisons with CSFF case under RPL at single span's center (WP2 or WP5) using steel patch

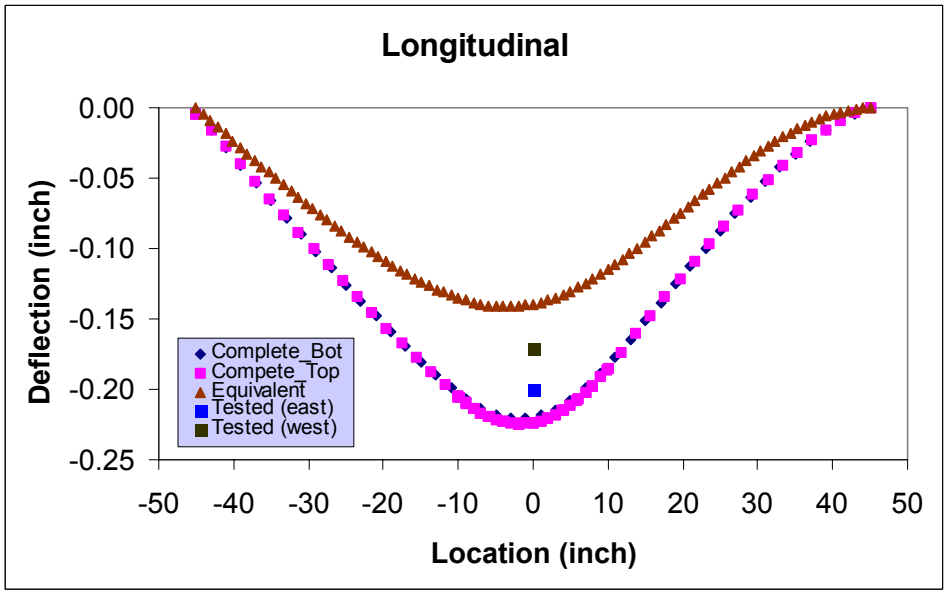


**Figure 3.42** Longitudinal bending deflection comparisons with CSFF case under RPL at single span's center (WP2 or WP5) using steel patch

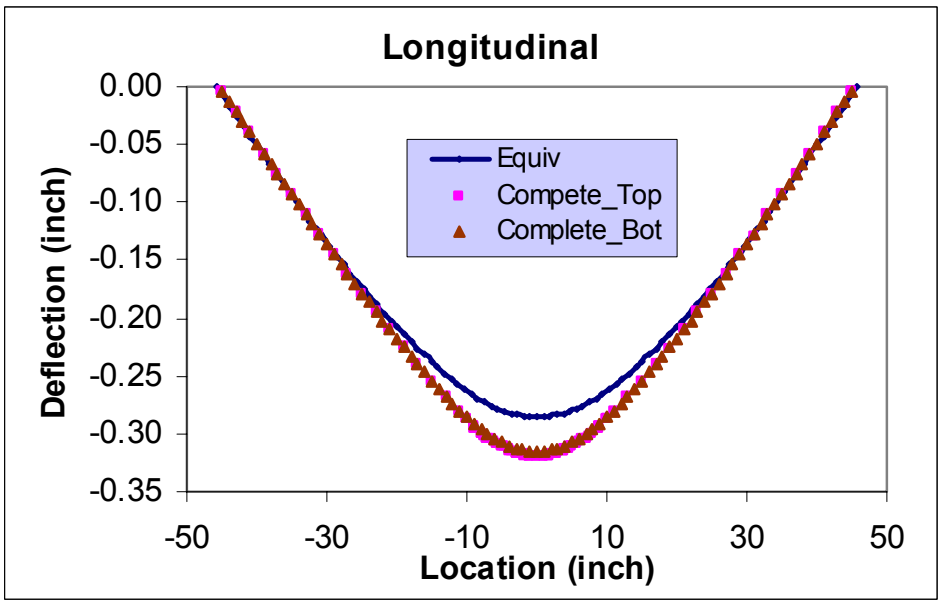


**Figure 3.43** Longitudinal bending deflection comparisons with SSFF case under RPL at single span's center (WP2 or WP5) using steel patch

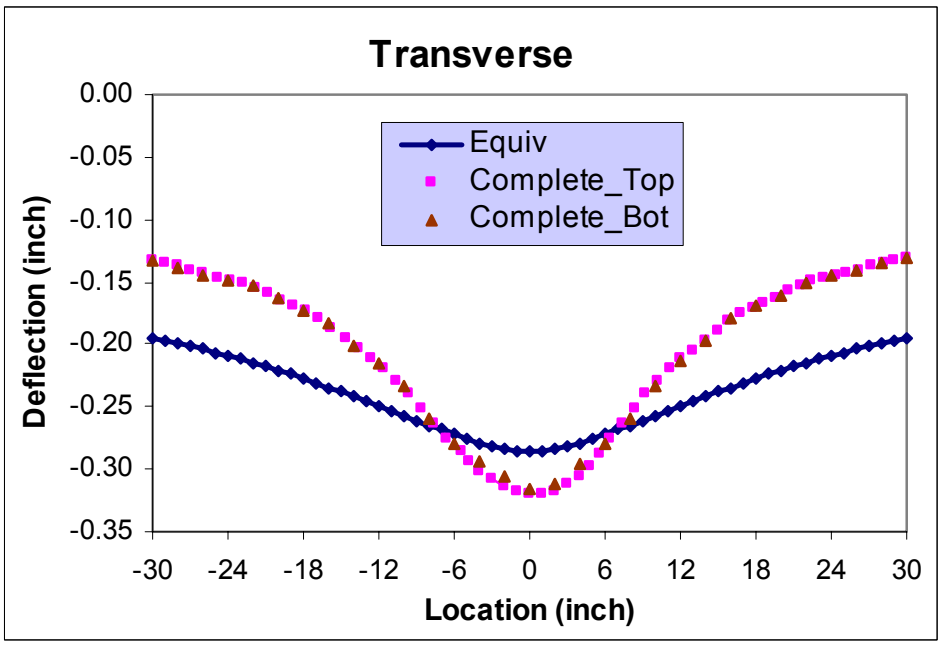


**Figure 3.44** Transverse bending deflection comparisons with SSFF case under RPL at single span's center (WP2 or WP5) using steel patch

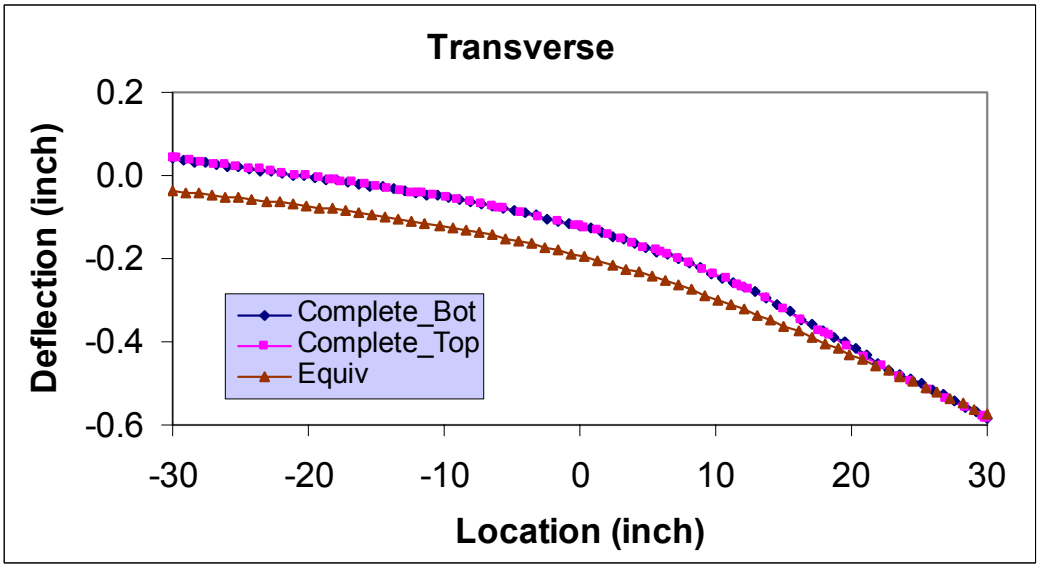


**Figure 3.45** Transverse bending deflection comparisons with SSFF case under RPL at single span's edge center (WP1-WP4 or WP3-WP6) using steel patch

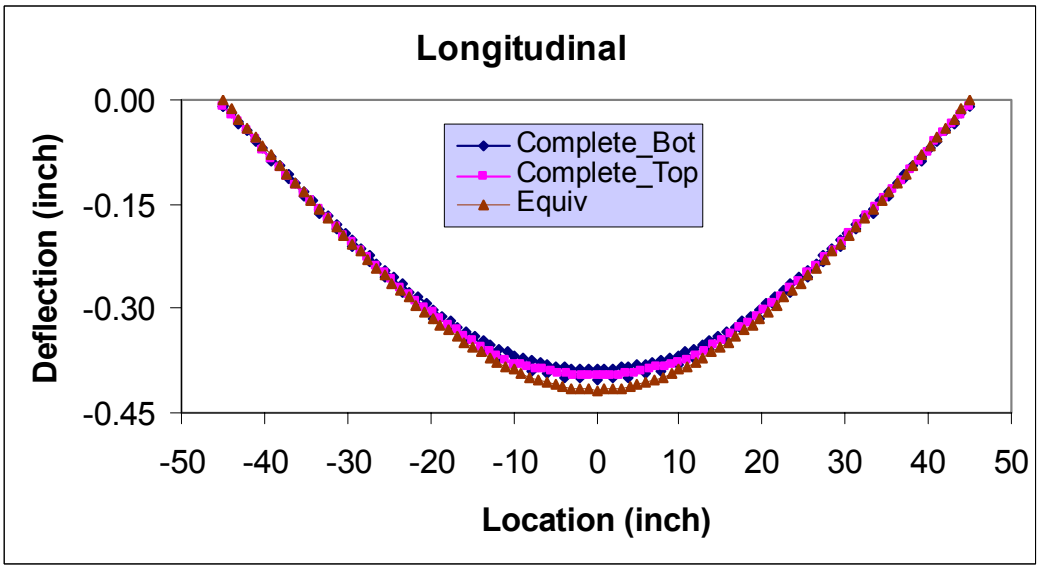


**Figure 3.46** Longitudinal bending deflection comparisons with SSFF case under RPL at single span's edge center (WP1-WP4 or WP3-WP6) using steel patch

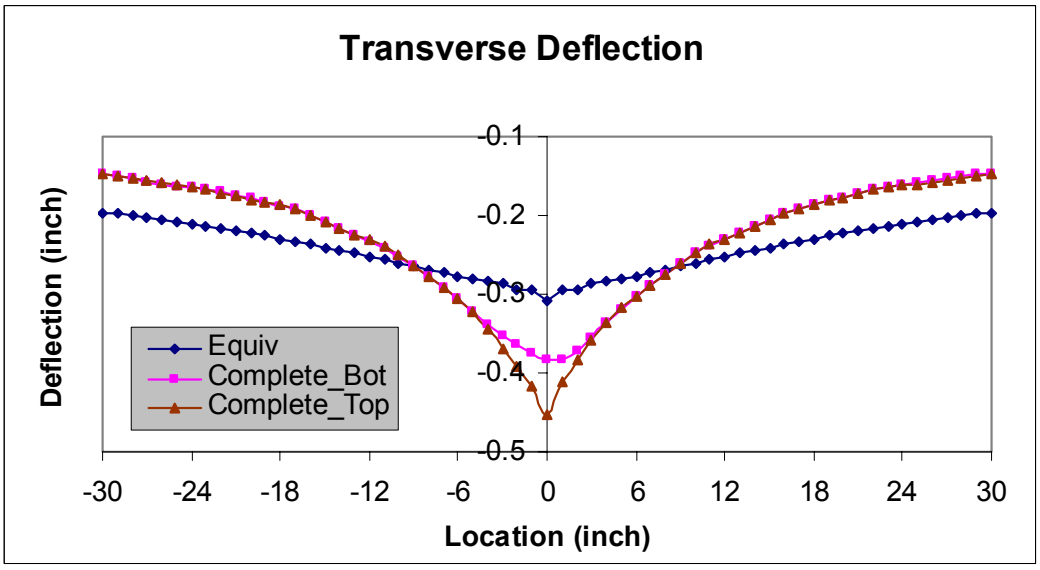


**Figure 3.47** Transverse bending deflection comparisons with SSFF case under CPL (26 kips) loading at single span's center (WP2 or WP5) using steel patch

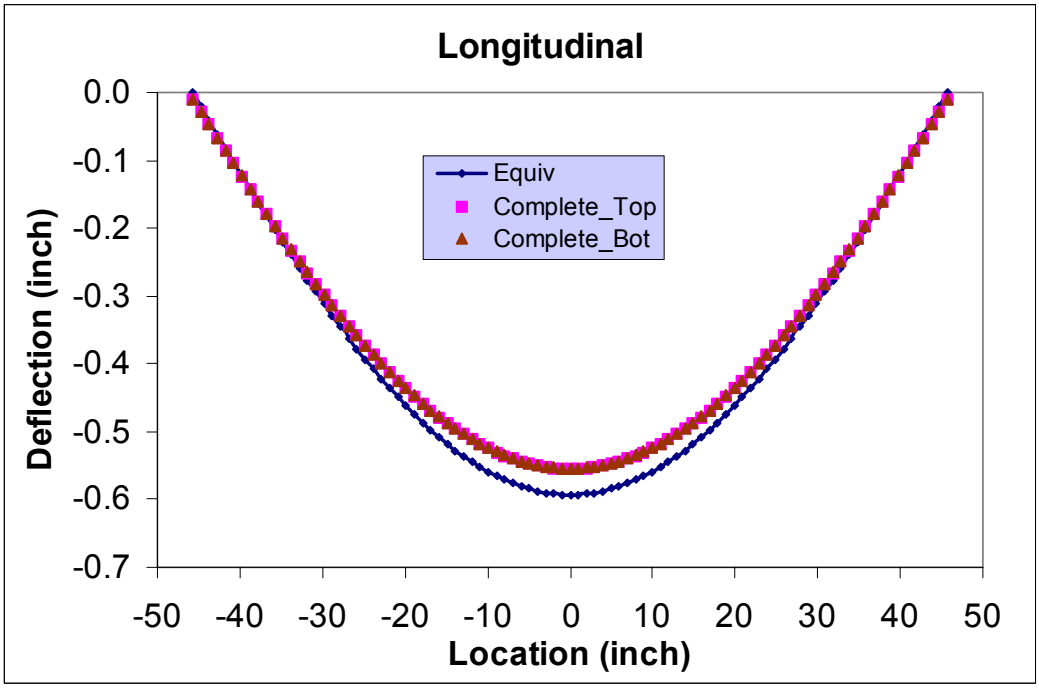


**Figure 3.48** Transverse bending deflection comparisons with SSFF case under UDL

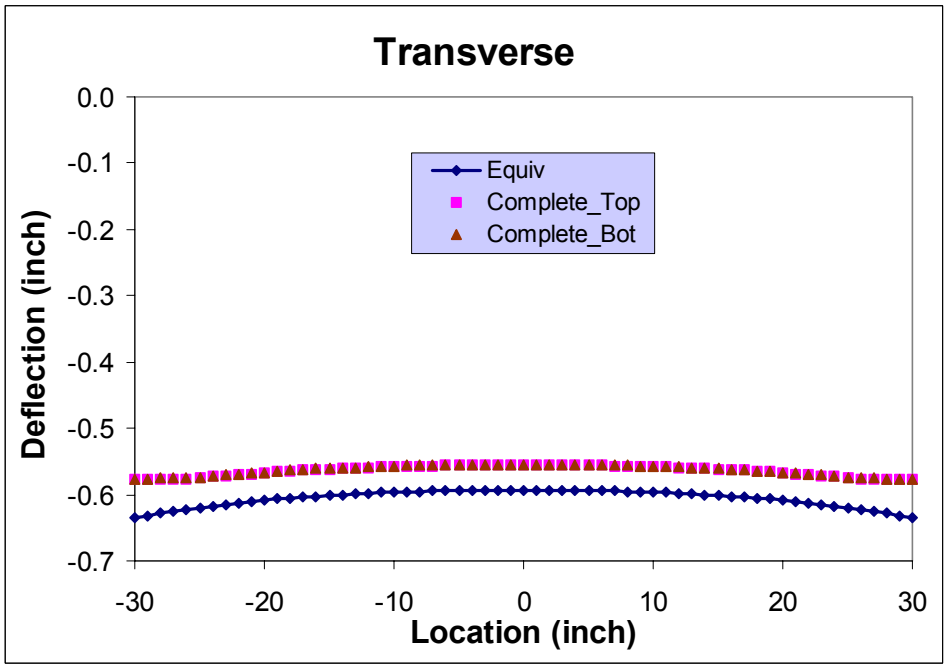


**Figure 3.49** Longitudinal bending deflection comparisons with SSFF case under UDL

The deflection comparisons of the deck under RPL at the edge center (WP1-WP4 and WP3-WP6) are shown in Figures (3.37) and (3.38). The predicted maximum deflections are –0.3521" (-8.9mm) and –0.3218" (-8.2mm) respectively for CDM and EDM, a 8.6% differences. At 19" (482.6mm) location in Figure 3.37, the average tested deflections are –0.2663" (-6.8mm) and –0.2855" (-7.3mm) for west and east spans respectively. The calculated deflections are –0.2266" (-5.8mm) from CDM and –0.2165" (-5.5) from EDM. The difference ranges from 15-20 % for CDM and 18-24 % for EDM compared to tested data. The recorded deflection for east span and west span has about 8% difference. However, the deflections obtained from the two models are within 4.5% difference.

The deflection comparisons for a simulated tire loading patch loaded at the span center are shown in Figures (3.39) and (3.40). The difference of maximum deflection to the tested data is 12% for EDM and 6% for CDM. Both models predict lower maximum deflections. The maximum deflection difference between CDM and EDM prediction is 6.4%, the CDM predicts larger maximum deflection than EDM. The situation is a little different for steel loading patch loaded at the span center (see Fig. 3.41 and 3.42): the CDM prediction gives 12% larger maximum deflection for west span and 38% lager for east span, while the EDM gives 12% less for east span and 40% less for west span. The tested maximum deflection for east span and west span differs about 27%. The CDM and EDM don't match well for steel patch loaded at the center for CSFF boundary conditions (Fig. 3.41 and 3.42) with about 38% difference. However, a better agreement can be observed for SSFF boundary conditions from Fig. (3.43) and (3.44), where only 12% difference in predicting the maximum deflection. The predicted maximum deflections are almost the same from CDM and EDM for SSFF boundary conditions under RPL loading at the span's edge center (see Fig. 3.45 and 3.46). The data in Figure 3.47 indicates that the EDM gives much lower maximum deflections than CDM for point loading within the –6" - +6" region. For SSFF boundary conditions under UDL loading, the predictions from both models are very close, the maximum difference is less than 8%.

## 3.5 Comparisons for Beam Analysis, Plate Analysis and Complete FEA

Most previous research pertaining to the bending of FRP decks used beam theory to calculate bending deflection [Brian, 1998]. Here we will compare the maximum bending deflections among the results from beam analysis, equivalent plate analysis and complete Finite Element Analysis. We will consider three beam bending cases shown in Figure (3.50) – Figure (3.52): Simply supported Three-point Bending (Fig. 3.50), Simply supported Uniform Pressure Bending (Fig. 3.51), and Cantilever Bending (Fig. 3.52). For all beams, the length is 90 inches.

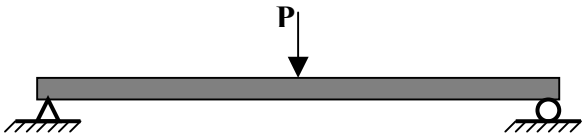


**Figure 3.50** Three-point Bending Beam

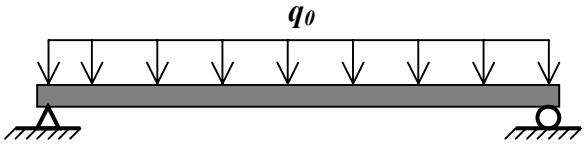


**Figure 3.51** Uniform Pressure SS Bending Beam


**Figure 3.52** Cantilever Bending Beam

From Timoshenko's beam theory, the maximum bending deflection for a Simply supported Three-point Bending beam (Fig. 3.50) can be obtained as [Brown, 1998]

$$\delta^{a}_{\max} = \frac{PL^3}{48EI} + \frac{PL}{4kF} \tag{3.8}$$

where $EI$ is the beam's bending stiffness with the unit of [force]-[length]$^2$, $k$ is the shear correction factor, (for this calculation, we choose $k = 1$), $F$ is the beam's shear stiffness. The bending stiffness can be obtained as $EI_{x,y} = D_{x,y} L_{x,y}$ , and the shear stiffness can be calculated as $F_{x,y} = G_{(x,y)z} h L_{x,y}$ , where $x, y$ refer to the longitudinal direction ($x$-direction) and transverse direction ($y$-direction ) respectively. An SSFF deck is chosen for comparison. The results are summarized in Table 3.8.

**TABLE 3.8 Maximum Deflections under CPL loading**

| Cases | Beam Analysis (inch) | | Equivalent Plate Analysis (inch) | Complete FEA (inch) |
|---|---|---|---|---|
| SSFF* | Longitudinal | 0.171 | 0.308 | 0.452 |

**: 26 kips force ;*

The local behavior for CPL is significant for this thin-walled cellular structure (see Fig. 3.47). The complete FEA gives much larger maximum deflection than the equivalent plate analysis and the beam analysis. However, the maximum deflection obtained from plate analysis is larger than from the beam analysis, and is closer to the complete FEA prediction.

For Simply supported Uniform Pressure Bending (Fig. 3.51), we have

$$\delta^{b}_{\max} = \frac{5q_0 L^3}{384EI} + \frac{q_0 L}{8kF} \tag{3.9}$$

**TABLE 3.9 Maximum Deflections under UDL loading**

| Cases | Beam Analysis (inch) | | Equivalent Plate Analysis (inch) | Complete FEA (inch) |
|---|---|---|---|---|
| SSFF* | Longitudinal | 0.558 | 0.593 (Fig. 3.48) | 0.554 (Fig. 3.48) |
| SSSS** | Longitudinal | 0.145 | 0.257 | 0.354 |

**: 454.55 PSI pressure (100 kips force); **: 118.18 PSI pressure (26 kips force).*

The Cantilever Bending beam's (Fig. 3.52) maximum deflection can be found as

$$\delta^{d}_{\max} = \frac{PL^3}{3EI} + \frac{PL}{kF} \tag{3-10}$$

**TABLE 3.10 Cantilever Maximum Deflections for the tube panel***

| Beam Analysis** (inch) | Equivalent Plate Analysis (inch) [Fig. 3.30-31] | | Complete FEA (inch) [Fig. 3.30-31] | |
|---|---|---|---|---|
| 4.11 | Center | 2.375 | Center | 2.133 |
| | Edge | 2.378 | Edge | 2.217 |

**: $D_{xx} = 17.08 \times 10^6$ **: No shear effect considered, load P=26 kips*

From the above comparisons one can find that the beam analysis only gives close maximum deflection prediction for SSFF deck under UDL (see Table 3.9). For any other cases compared above, the beam analysis cannot provide a reasonable bending deflection prediction.

The above FEA results show that the EDM modeling and the CDM modeling give very close deflection predictions in longitudinal and transverse directions for UDL loading and central

edge RPL loadings. For a central RPL loading, EDM gives close predictions to CDM for the simulated tire patch. For CPL loading the local behavior of the thin-walled deck system cannot be accurately predicted by EDM. Either higher order plate theories or complete FEA should be conducted to predict the local behavior of the thin-walled cellular deck system. However, EDM can still be used as a method to calculate maximum deflections under these loading conditions if a correction factor is implemented. This correction factor can be determined using the results from EDM and CDM or testing. For example, referring to Figure (3.40) and Figure (3.46), the correction factor for this deck is about 2 for both cases. The actual deck maximum deflection under these loading conditions would be the maximum deflection obtained from EDM multiplied by that correction factor.

In the following chapter, we will develop detailed analysis procedures for orthotropic plate analysis for various boundary conditions. The bridge designer can directly follow these procedures and calculate maximum bending deflection.

# CHAPTER IV

# STRUCTURAL ANALYSIS OF FRP DECKS USING PLATE THEORIES

This chapter will address the applications of the equivalent method developed in Chapter III. Using the equivalent properties obtained from previous chapter, the structural analytical analysis procedures of FRP composite bridge decks will be developed based on orthotropic composite plate analysis. Comparisons among equivalent plate theory, FEA, and tested data will be presented regarding to the bending behavior of FRP decks. Finally, stiffness design principles will be proposed for FRP bridge deck systems. Currently, we will focus on the bending behavior of a single span FRP deck. We will also discuss the application of single span analysis to continuous multi-span decks.

## 4.1 Single Span Analysis

A single span FRP bridge deck is the simplest form of structural analysis using composite laminated plate theories. The analysis of composite plates in the past have been based on one of the following approaches (Reddy, 1997): (1) 2-D equivalent single-layer theories: Classical laminate theory and shear deformation laminate theories; (2) 3-D elasticity theory: Traditional 3-D elasticity formulations and layer-wise theories; and (3) Other 2-D and 3-D multiple model methods. In the 3-D elasticity theory or in a layer-wise theory, each layer of the laminate is modeled as a 3-D solid. While the equivalent single-layer (ESL) theories are derived from the 3-D elasticity theory by making suitable assumptions concerning the kinematics of deformation or the stress state through the laminate. These assumptions allow the reduction of a relatively complicated 3-D problem to a simpler 2-D problem. The ESL theories are developed by

assuming the displacement (or stress) field as a linear combination of thickness coordinate and unknown functions:

$$\varphi_i(x,y,z,t) = \sum_{j=0}^{N} z^j \cdot \phi_i^j(x,y,t) \tag{4.1}$$

where $\varphi_i$ is the *i*th component of the displacement (or stress), *z* is the thickness coordinate, *(x, y)* are in-plane coordinates, *t* is time, and $\phi_i^j$ are functions to be determined.

The classical laminate plate theory (CLPT) and the first-order shear deformation theory (FSDT) are the simplest ESL theories, and they adequately describe the kinematic behavior of most composite laminated plates. The CLPT is an extension of the Kirchhoff (classical) plate theory to laminate composite plates, with the following displacement field:

$$\begin{aligned} u(x,y,z,t) &= u_0(x,y,t) - z \cdot \frac{\partial w_0}{\partial x} \\ v(x,y,z,t) &= v_0(x,y,t) - z \cdot \frac{\partial w_0}{\partial y} \\ w(x,y,z,t) &= w_0(x,y,t) \end{aligned} \tag{4.2}$$

where $(u_0, v_0, w_0)$ are displacement components of a point on the mid-plane (where $z = 0$). When conducting bending analysis, it is convenient to express the equations of motion in terms of displacements $(u_0, v_0, w_0)$. We assume that the equivalent plate representing the deck is homogeneous and we are only interested in the vertical bending $(w_0)$ of the deck. To simplify the analysis, no extension-bending coupling will be considered, the deck will be treated as a single and specially orthotropic plate. Therefore, the bending-extensional coupling stiffnesses $B_{ij}$ are considered to be zero. In terms of vertical bending $w_0$, the equation of motion can be expressed as:

$$-[D_{11}\frac{\partial^4 w_0}{\partial x^4}+2(D_{12}+2D_{66})\frac{\partial^4 w_0}{\partial x^2\partial y^2}+D_{22}\frac{\partial^4 w_0}{\partial y^4}]+q(x,y)-(\frac{\partial^2 M_{xx}^T}{\partial x^2}+2\frac{\partial^2 M_{xy}^T}{\partial x\partial y}+\frac{\partial^2 M_{yy}^T}{\partial y^2})$$
$$+\hat{N}_{xx}\frac{\partial^2 w_0}{\partial x^2}+2\hat{N}_{xy}\frac{\partial^2 w_0}{\partial x\partial y}+\hat{N}_{yy}\frac{\partial^2 w_0}{\partial y^2}=I_0\ddot{w}_0-I_2(\frac{\partial^2 \ddot{w}_0}{\partial x^2}+\frac{\partial^2 \ddot{w}_0}{\partial y^2}) \tag{4.3}$$

where $q(x,y)$ is the distributed force at the mid-plane, $(M_{xx}^T, M_{xy}^T, M_{yy}^T)$ are thermal moment resultants, $(\hat{N}_{xx}, \hat{N}_{xy}, \hat{N}_{yy})$ are in-plane force resultants specified at the plate boundaries, $I_0$ and $I_2$ are the mass moments of inertia with $I_0=\int_{-\frac{h}{2}}^{\frac{h}{2}}\rho_0 dz$, and $I_2=\int_{-\frac{h}{2}}^{\frac{h}{2}}z^2\rho_0 dz$. For static problems in the absence of thermal effects and in-plane forces, the above equation can be reduced to

$$D_{11}\frac{\partial^4 w_0}{\partial x^4}+2(D_{12}+2D_{66})\frac{\partial^4 w_0}{\partial x^2\partial y^2}+D_{22}\frac{\partial^4 w_0}{\partial y^4}=q(x,y) \tag{4.4}$$

In FSDT, the transverse shear strains $(\varepsilon_{xz}, \varepsilon_{yz}, \varepsilon_{zz})$ are included in the theory, which does not require the transverse normals to be perpendicular to the mid-surface after deformation. The displacement filed of FSDT takes the form:

$$\begin{aligned} u(x,y,z,t)&=u_0(x,y,t)+z\cdot\phi_x(x,y,t)\\ v(x,y,z,t)&=v_0(x,y,t)+z\cdot\phi_y(x,y,t)\\ w(x,y,z,t)&=w_0(x,y,t)\end{aligned} \tag{4.5}$$

The quantities $(u_0, v_0, w_0, \phi_x, \phi_y)$ are called generalized displacements. Again, the deck will be treated as a single and specially orthotropic plate: $B_{ij}=0$, $D_{16}=D_{26}=0$, and $A_{45}=0$. For static problems without considering thermal and in-plane forces, the equation of motion for FSDT related to $w_0, \phi_x, \phi_y$ can be expressed as:

$$KA_{55}(\frac{\partial^2 w_0}{\partial x^2}+\frac{\partial \phi_x}{\partial x})+KA_{44}(\frac{\partial^2 w_0}{\partial y^2}+\frac{\partial \phi_y}{\partial y})+q(x,y)=0$$

$$D_{11}\frac{\partial^2 \phi_x}{\partial x^2}+D_{12}\frac{\partial^2 \phi_y}{\partial x\partial y}+D_{66}(\frac{\partial^2 \phi_x}{\partial y^2}+\frac{\partial^2 \phi_y}{\partial x\partial y})-KA_{55}(\frac{\partial w_0}{\partial x}+\phi_x)=0 \quad (4.6)$$

$$D_{12}\frac{\partial^2 \phi_x}{\partial x\partial y}+D_{22}\frac{\partial^2 \phi_y}{\partial x^2}+D_{66}(\frac{\partial^2 \phi_x}{\partial x\partial y}+\frac{\partial^2 \phi_y}{\partial x^2})-KA_{44}(\frac{\partial w_0}{\partial y}+\phi_y)=0$$

Since CLPT does not require the determination the shear correction factor [Reddy, 1997] and is much easier than FSDT, we will use CLPT to analyze the bending behavior of FRP decks. However, the analysis can be extended to FSDT or other higher order plate theories. We will consider three categories of boundary conditions for the single span deck: (1) All four edges are simply supported (SSSS); (2) The Levy plates: two opposite edges are simply supported and other two opposite edges have varied boundary conditions, clamped, simply supported, or free; and (3) Other boundary conditions. The Navier method will be used to analyze case (1), and the Levy method will be used to investigate case (2). For case (3), an approximation method, the Reyleigh-Ritz method, will be used to do the analysis. The results for the above cases from orthotropic plate analysis will be used to compare deflection predictions equivalent finite element analysis. The deflection analysis in this chapter will serve as deflection calculation guidelines for deflection design.

For a single-layer specially orthotropic plate, the stiffnesses can be expressed in terms of the reduced stiffnesses $Q_{ij}$ and its thickness *h* [Reddy, 1997]. The non-zero stiffnesses in Eq. ( 4-4) and Eq.( 4-6) are:

$$D_{11}=\frac{Q_{11}h^3}{12}=\frac{h^3}{12}\cdot\frac{E_{xx}}{1-\nu_{xy}\nu_{yx}},\ \text{and}\ D_{22}=\frac{Q_{22}h^3}{12}=\frac{h^3}{12}\cdot\frac{E_{yy}}{1-\nu_{xy}\nu_{yx}}$$

$$D_{12}=\frac{Q_{12}h^3}{12}=\frac{h^3}{12}\cdot\frac{\nu_{yx}E_{xx}}{1-\nu_{xy}\nu_{yx}}\ \text{or}\ =\frac{h^3}{12}\cdot\frac{\nu_{xy}E_{yy}}{1-\nu_{xy}\nu_{yx}} \quad (4.7)$$

$$D_{66}=\frac{Q_{66}h^3}{12}=\frac{G_{12}h^3}{12},\ A_{44}=KQ_{44}h=KG_{23}h,\ A_{55}=KQ_{55}h=KG_{13}h$$

For the investigated deck, the equivalent plate stiffnesses are obtained as in Table 4.1:

**TABLE 4.1 Equivalent Plate Stiffnesses of Deck IV**

| Stiffness | Calculated Value $(lbs \cdot in^2)$ | Formulation used for calculation |
|---|---|---|
| $D_{11}$ | $2.83884 \times 10^7$ | $D_{11} = \frac{h^3}{12} \cdot \frac{E_{xx}}{1 - \nu_{xy}\nu_{yx}}$ |
| $D_{12}$ | $1.35278 \times 10^6$ | $D_{12} = \frac{h^3}{12} \cdot \frac{\nu_{yx}E_{xx}}{1 - \nu_{xy}\nu_{yx}}$ |
| $D_{22}$ | $4.12712 \times 10^6$ | $D_{22} = \frac{h^3}{12} \cdot \frac{E_{yy}}{1 - \nu_{xy}\nu_{yx}}$ |
| $D_{66}$ | $3.50072 \times 10^6$ | $D_{66} = \frac{G_{12}h^3}{12}$ |
| $A_{44}$ | $0.37456 \times 10^6$ | $A_{44} = KG_{23}h, K = 1$ |
| $A_{55}$ | $5.16971 \times 10^6$ | $A_{55} = KG_{13}h, K = 1$ |

### 4.1.1 Bending Analysis for SSSS Single Span Bridge Deck Using CLPT

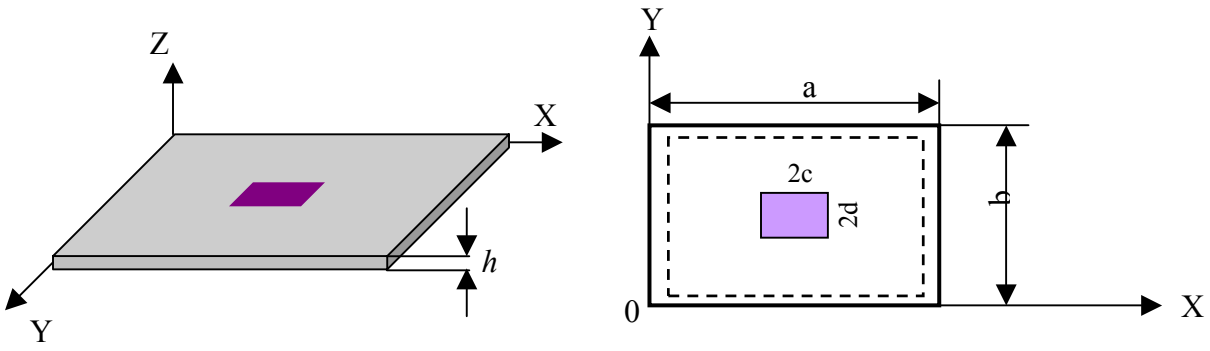


**Figure 4.1** A Plate with All Edges Simply Supported (SSSS Plate)

Let $a$ be the plate length, $b$ be the width, and $h$ be the thickness, as shown in Figure 4.1. First, the CLPT will be used for bending analysis. We will consider three loading cases: Uniformly Distributed Load (UDL), Central Point Load (CPL), and Rectangular Patch Load (RPL) with a uniformly distributed load on a $2c \times 2d$ central rectangular loading patch. For this case, the boundary conditions can be expressed as:

$$\begin{aligned} &\text{At edges } x = 0, a: \quad w_0(0,y) = w_0(a,y) = 0 \text{, and } M_{xx}(0,y) = M_{xx}(a,y) = 0 \\ &\text{At edges } y = 0, b: \quad w_0(x,0) = w_0(x,b) = 0 \text{, and } M_{yy}(x,0) = M_{yy}(x,b) = 0 \end{aligned} \tag{4.8}$$

The solution to Eq. (4-4) for a rectangular plate with all edges simply supported can be obtained using available method – the Navier method, which can be found in many elastic plate analysis books [Hyer 1998, Jones, 1999 Lekhniskii 1968, Reddy 1999]. In this method, the unknown displacement $w_0$, the applied load $q(x,y)$ (and also possible thermal load) are expanded in trigonometric series. The trigonometric functions are chosen to satisfy the SSSS boundary conditions of the problem. The SSSS conditions are met by choosing the following double sine series form of transverse deflection $w_0$ [Reddy 1999]:

$$w_0(x,y)=\sum_{n=1}^{\infty}\sum_{m=1}^{\infty}W_{mn}\cdot\sin\frac{m\pi x}{a}\cdot\sin\frac{n\pi y}{b} \tag{4.9}$$

Where $W_{mn}$ are coefficients to be determined such that Eq. (4-4) hold everywhere within the plate domain. The applied load, the right-hand side of Eq.( 4-4), can also be expanded in double sine series as

$$q(x,y)=\sum_{n=1}^{\infty}\sum_{m=1}^{\infty}q_{mn}\cdot\sin\frac{m\pi x}{a}\cdot\sin\frac{n\pi y}{b} \tag{4.10-a}$$

And the coefficients $q_{mn}$ can be calculated from the following formulation

$$q_{mn}=\frac{4}{ab}\int_0^b\int_0^a q(x,y)\cdot\sin\frac{m\pi x}{a}\cdot\sin\frac{n\pi y}{b}dxdy \tag{4.10-b}$$

For UDL with $q(x,y)=q_0$, we find from the above equation that

$$q_{mn}=\frac{16}{mn\pi^2},\ \text{for}\ m,n=1,3,5,... \tag{4.11-a}$$

For a point load of $Q_0$ applied at $x=x_0, y=y_0$, we have $q(x,y)=Q_0\delta(x-x_0)\delta(y-y_0)$, (where $\delta(\cdot)$ is the Dirac Delta Function), and find

$$q_{mn}=\frac{4Q_0}{ab}\cdot\sin\frac{m\pi x_0}{a}\cdot\sin\frac{n\pi y_0}{b},\ \text{for}\ m,n=1,2,3... \tag{4.11-b}$$

For CPL, we have $q_{mn}=\frac{4Q_0}{ab}$, with $m,n=1,3,5,....$, where $x_0=\frac{a}{2}, y_0=\frac{b}{2}$.

For a uniform load of intensity $q_0$ on a $2c\times 2d$ rectangular loading patch with the center of $(x_0,y_0)$, from (10-b), we have,

$$q_{mn} = \frac{16q_0}{mn\pi^2} \cdot \sin\frac{m\pi x_0}{a} \cdot \sin\frac{n\pi y_0}{b} \cdot \sin\frac{m\pi c}{a} \cdot \sin\frac{n\pi d}{b} \qquad (4.11\text{-c})$$

Following the Navier solution procedures [Reddy 1999 and Lekhnitskii 1968], we can find the coefficients $W_{mn}$ in Eq.( 4.9) for UDL, CPL, and RPL.

(1) Plates with Uniformly Distributed Load $q_0$,

$$w_0(x,y) = \frac{16q_0}{\pi^2} \sum_{n=1,3,5}^{\infty} \sum_{m=1,3,5}^{\infty} \frac{1}{mnd_{mn}} \cdot \sin\frac{m\pi x}{a} \cdot \sin\frac{n\pi y}{b} \qquad (4.12\text{-a})$$

(2) Plates with Central Point Load $Q_0$ at $(x_0 = a/2, y_0 = b/2)$

$$w_0(x,y) = \frac{4Q_0}{ab} \sum_{n=1}^{\infty}\sum_{m=1}^{\infty} \frac{1}{d_{mn}} \cdot \sin\frac{m\pi x}{a} \cdot \sin\frac{n\pi y}{b} \cdot \sin\frac{m\pi}{2} \cdot \sin\frac{n\pi}{2} \qquad (4.12\text{-b})$$

(3) Plates with uniform load $q_0$applied on a rectangular patch of 2c × 2d centered at $(\frac{a}{2}, \frac{b}{2})$:

$$w_0(x,y) = \frac{16q_0}{\pi^2} \sum_{n=1}^{\infty}\sum_{m=1}^{\infty} \frac{1}{mnd_{mn}} \cdot \sin\frac{m\pi x}{a} \cdot \sin\frac{n\pi y}{b} \cdot \sin\frac{m\pi x_0}{a} \cdot \sin\frac{n\pi y_0}{b} \cdot \sin\frac{m\pi c}{a} \cdot \sin\frac{n\pi d}{b} \qquad (4.12\text{-c})$$

where $d_{mn} = \frac{\pi^4}{b^4}(D_{11}m^4s^4 + 2(D_{12} + 2D_{66})m^2n^2s^2 + D_{22}n^4$, and $s = \frac{b}{a}$ in (4.12-a) –(4.12-c).

Substituting the equivalent stiffnesses, $D_{11}, D_{12}, D_{22}, D_{66}$, into (4-12-a), (4-12-b) and (4-12-c), we can obtain the mid-plane deflection $w_0$ for UDL, CPL, and RPL loading cases respectively. The longitudinal direction is the direction with 90" (2286mm) length and is stiffer (has larger bending stiffness), while the transverse direction is the direction with 60" (1524mm) length with smaller bending stiffness. Mathematica® is used for analytical solution.

Numerical comparisons are shown in Figures 4.2 and 4.3 for a SSSS plate under UDL loading with the pressure of 18.2 psi (125.5 kPa). The analytical solution using CLPT predicts 9.7% lower maximum deflection for this case.

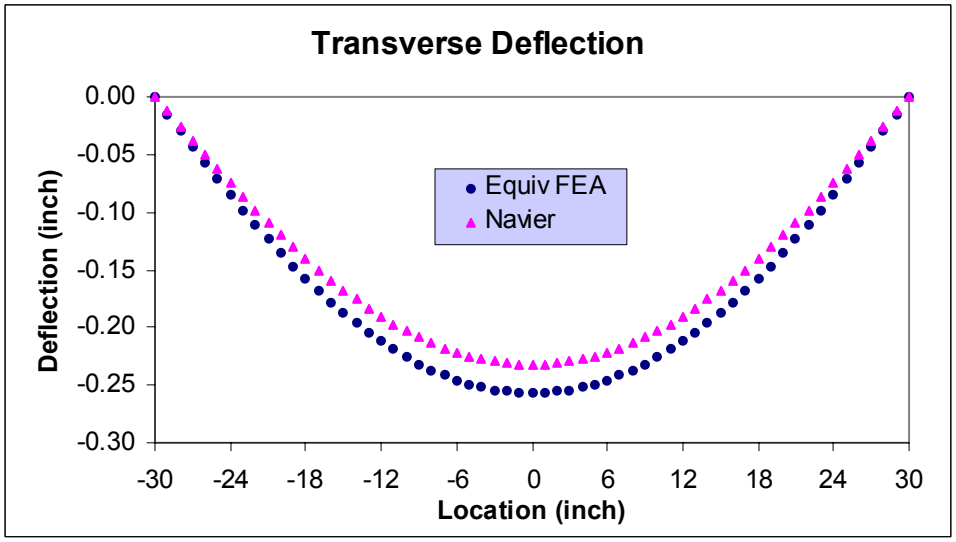


**Figure 4.2** Transverse deflection comparison of a SSSS plate under UDL

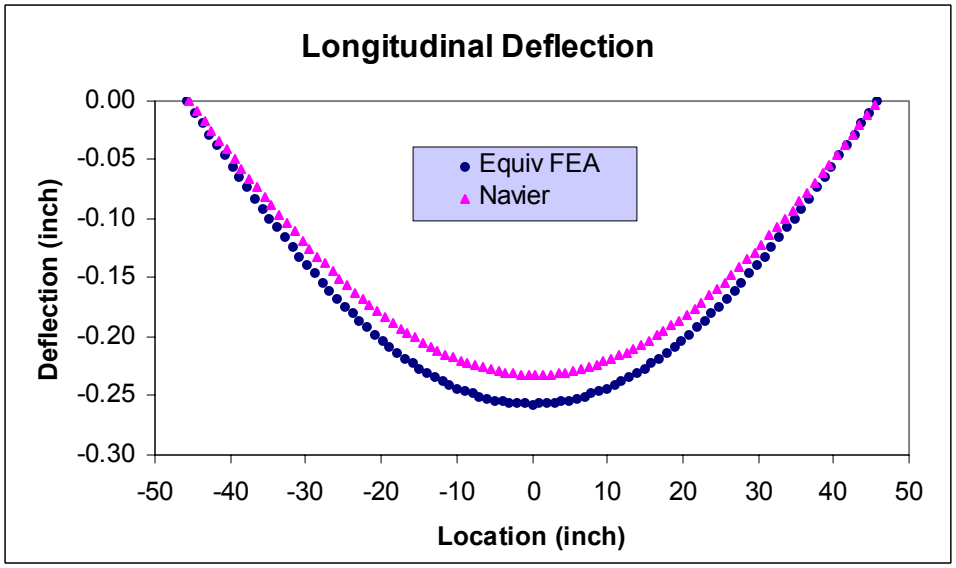


**Figure 4.3** Longitudinal deflection comparison of a SSSS plate under UDL

For CPL, a 100 kips (444.5kN) force was applied at the plate center. The numerical results are shown in Figures 4.4 and 4.5. For this case, the Navier solution using CLPT gives 15% lower maximum deflection prediction than the FEA.

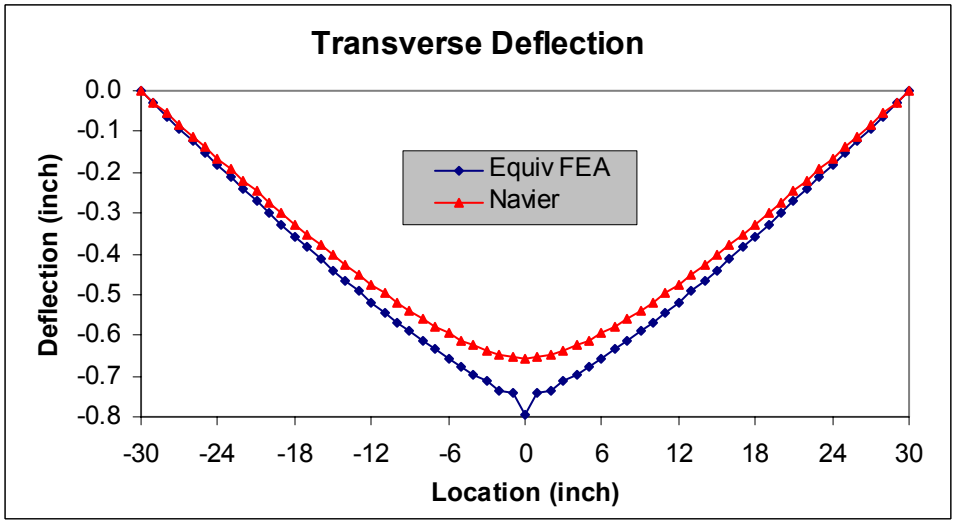


**Figure 4.4** Transverse deflection comparison of a SSSS plate under CPL

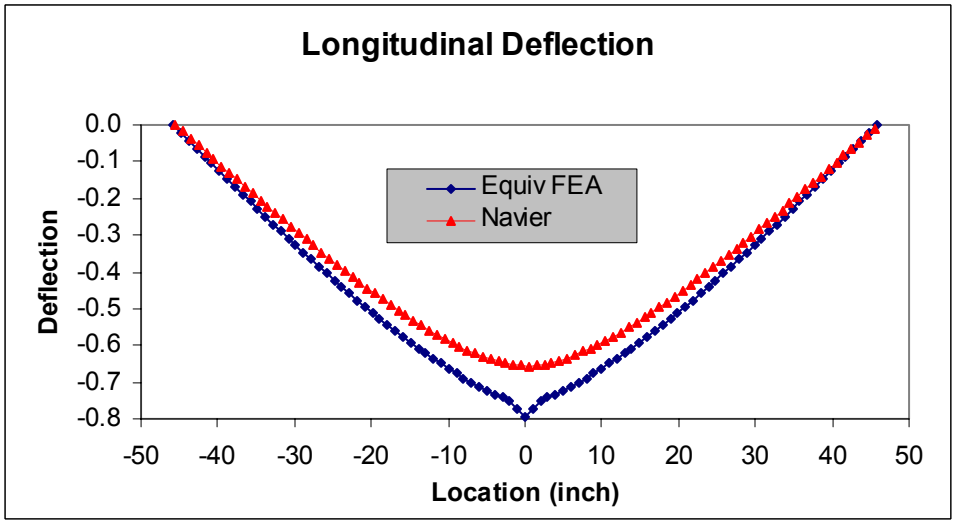


**Figure 4.5** Longitudinal deflection comparison of a SSSS plate under CPL

For a SSSS plate under RPL, a 26 kips (115.6 kN) force was uniformly distributed on a 20"×11" (508×279.4mm) rectangular loading patch at the plate center. The numerical results are shown in Figure 4.6. The analytical solution using CLPT predicts about 17% lower maximum deflection compared to FEA.

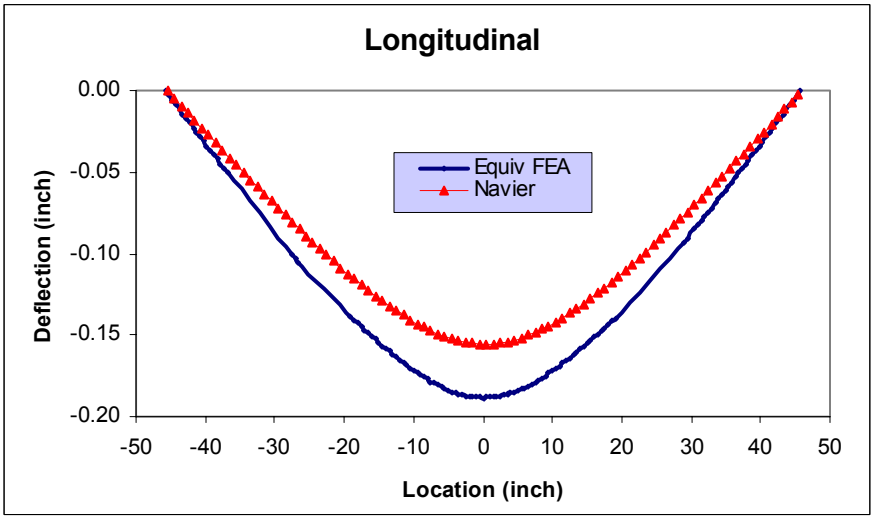


**Figure 4.6** Longitudinal deflection comparison of a SSSS plate under RPL

It is known that the CLPT under-estimates deflection more than FSDT [Reddy 1997]. The shell element used in the equivalent modeling is an element considering first order shear deformation. If FSDT or higher order plate theory was used, the analytical maximum deflection prediction will be closer to the FEA prediction.

### 4.1.2 Bending Analysis for Levy Type Single Span Bridge Deck Using CLPT

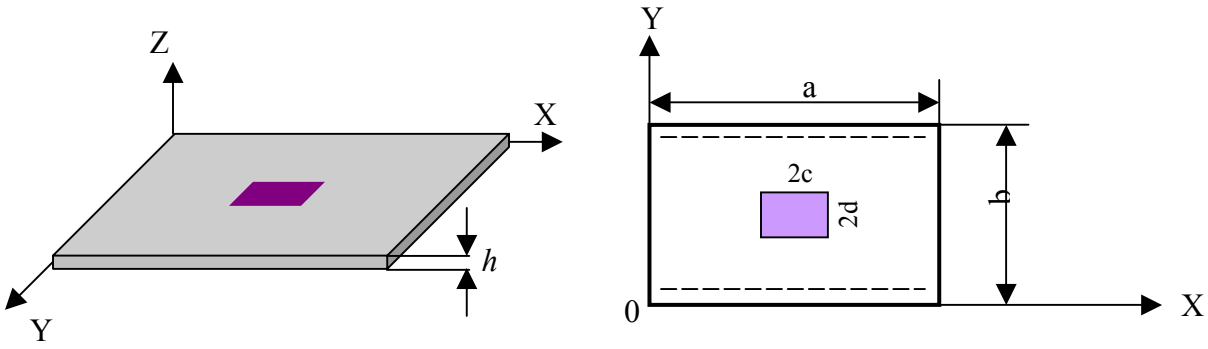


**Figure 4.7** A Plate with Two Opposite Edges Simply Supported (Levy Plate)

Plates with two opposite edges simply supported and other two edges having arbitrary boundary conditions can be solved using Levy method. There are six possible cases for Levy type plates (Figure 3.7): SSCC, SSCF, SSCS, SSFF, SSFS, and SSSS, where C means Clamped, F refers to Free. The Levy solutions for several cases (such as SSSS, SSCC, SSFF etc.) are available in some literatures [Reddy 1997, Reddy 1999 etc.] However, most available results from these published literatures are not compared with FEA solutions. In this section, we will provide detailed and comprehensive solution procedures to all Levy plates, including SSSC, SSCF, and SSSF plates not completely detailed in previous literatures. All the Levy solutions will be compared with equivalent FEA analysis using ANSYS®. Also, some results will be compared with the available test data. The solution procedure is not necessarily limited to bridge deck analysis, it can also for FRP wall or floor analysis, or any analysis that investigate the Levy type orthotropic plate.

According to the Levy method, the solution to the problem that satisfies SS boundary conditions on edges $y = 0, b$ can be represented in terms of single Fourier series as

$$w_0(x,y) = \sum_{n=1}^{\infty} W_n(x) \cdot \sin\frac{n\pi y}{b} \tag{4.13}$$

The applied mechanical load $q$ can also be represented as

$$q(x,y)=\sum_{n=1}^{\infty} q_n(x)\cdot\sin\frac{n\pi y}{b} \tag{4.14-a}$$

where $q_n(x)$ is defined as

$$q_n(x)=\frac{2}{b}\int_0^b q(x,y)\cdot\sin\frac{n\pi y}{b}dy \tag{4.14-b}$$

The coefficients for UDL and CPL loading cases can be obtained as: (1) UDL: $q_n=\frac{4q_0}{n\pi}$, $n=1,3,5,...$; and (2) CPL: $q_n=\frac{2Q_0}{b}\cdot\sin\frac{n\pi y_0}{b}\cdot\delta(x-x_0)$, $n=1,2,3,...$.

The substitution of Eq. (13) and Eq. (14-a) into Eq. (4) leads to the following ordinary differential equation for $W_n(x)$:

$$D_{11}\frac{d^4W_n}{dx^4}-2\beta^2(D_{12}+2D_{66})\frac{d^2W_n}{dx^2}+\beta^4D_{22}W_n=q_n \tag{4.15-a}$$

The solution of the above equation has two parts with the form of $W_n(x)=W_n^h(x)+W_n^p(x)$, where $W_n^h(x)$ is the homogeneous solution and $W_n^p(x)$ is the particular solution of Eq. (4-15-a) respectively. The form of the homogeneous solution, $W_n^h(x)$, is determined from the nature of the roots $\lambda$ of the following characterization equation:

$$D_{11}\lambda^4-2\beta^2(D_{12}+2D_{66})\lambda^2+\beta^4D_{22}=0 \tag{4.15-b}$$

From (4.15-b), we have, $\lambda_{1,2}^2=\frac{\beta^2}{D_{11}}[(D_{12}+2D_{66})\pm\sqrt{(D_{12}+2D_{66})^2-D_{11}D_{22}}]$. The following three cases need to be considered for roots $\lambda$:

**Case I:** $(D_{12}+2D_{66})^2 > D_{11}D_{22}$, roots of $\lambda$ are real and distinct, $\lambda_1$, $-\lambda_1$, $\lambda_2$, $-\lambda_2$. The homogeneous solution $W_n^h(x)$ is

$$W_n^h(x) = A_n \cosh \lambda_1 x + B_n \sinh \lambda_1 x + C_n \cosh \lambda_2 x + D_n \sinh \lambda_2 x \tag{4.16-a}$$

where $\lambda_{1,2}^2 = \frac{\beta^2}{D_{11}}[(D_{12}+2D_{66}) \pm \sqrt{(D_{12}+2D_{66})^2 - D_{11}D_{22}}]$.

**Case II:** $(D_{12}+2D_{66})^2 = D_{11}D_{22}$, roots of $\lambda$ are real and equal. The homogeneous solution $W_n^h(x)$ is

$$W_n^h(x) = (A_n + B_n x)\cosh \lambda x + (C_n + D_n x)\sinh \lambda x \tag{4.16-b}$$

**Case III:** $(D_{12}+2D_{66})^2 < D_{11}D_{22}$, roots of $\lambda$ are complex in complex conjugate pairs: $\lambda_1 \pm i\lambda_2$, and $-\lambda_1 \pm i\lambda_2$, where $(\lambda_{1,2})^2 = \frac{\beta^2}{2D_{11}}[\sqrt{D_{11}D_{22}} \pm (D_{12}+2D_{66})]$. The homogeneous solution $W_n^h(x)$ is

$$W_n^h(x) = (A_n \cos \lambda_2 x + B_n \sin \lambda_2 x)\cosh \lambda_1 x + (C_n \cos \lambda_2 x + D_n \sin \lambda_2 x)\sinh \lambda_1 x \tag{4.16-c}$$

The constants $A_n, B_n, C_n,$ and $D_n$ will be determined from the boundary conditions on other two edges of the plate. In practical engineering applications, Case II usually applies for isotropic plates, where $D_{11} = D_{22} = D$, and $(D_{12}+2D_{66}) = D$. For most orthotropic plates, either Case I or Case III applies. In the followings, Case I and Case III will be discussed.

The particular solution $W_n^p(x)$ of Eq. (15-a) can be determined by expanding the solution and the load in Fourier series, which takes the form

$$W_n^p(x) = \sum_{m=1}^{\infty} \frac{q_{mn}}{d_{mn}} \sin \frac{m\pi x}{a} \tag{4.17-a}$$

where $d_{mn}$ is the same as in Eq. (12-a). If the applied loads are constants or linear functions of $x$, the particular solution $W_n^p(x)$ is also a constant or a linear function of $x$, and is given by

$$W_n^p(x) = \frac{q_n}{D_{22}\beta^4} \equiv \hat{q}_n \tag{4.17-b}$$

In the following discussion, detailed solution procedures for all Levy type plate will be provided with specific boundary conditions. We will also present a calculation example for each case under Uniformly Distributed Load (dead load or snow load etc. in bridge design) using the equivalent deck properties. A calculation of the equivalent deck indicates that this deck is a Case III plate ($(D_{12}+2D_{66})^2 < D_{11}D_{22}$). The complete solution of Eq. (4.4) for UDL loading becomes:

$$w_0(x,y) = \sum_{n=1}^{\infty}[W_n^h(x) + \hat{q}_n]\cdot \sin\frac{n\pi y}{b} \tag{4.18}$$

In the following six sections, we will find constants $A_n, B_n, C_n,$ and $D_n$ for each Levy orthotropic plate.

#### *4.1.2.1 SSCC Plate*

This case can be found in practice where a single span of a continuous simply supported deck is analyzed. The two clamped boundaries represent the cut boundaries from the continuous deck. The Boundary conditions can be represented as:

(i) At the SS edges *( $y = 0, b$ )*: $w_0(x,0) = w_0(x,b) = 0$, and $M_{yy}(x,0) = M_{yy}(x,b) = 0$

(ii) At the clamped edges ( $x = 0, a$ ): $w_0(0,y) = w_0(a,y) = 0$, and

$$\frac{\partial w_0}{\partial x}(0,y) = \frac{\partial w_0}{\partial x}(a,y) = 0$$

For Case I, when $(D_{12}+2D_{66})^2 > D_{11}D_{22}$, the substitution of the clamped boundary conditions leads to the following algebraic equations for $A_n, B_n, C_n,$ and $D_n$:

$$\begin{aligned}
&A_n + C_n + \hat{q}_n = 0\\
&B_n\lambda_1 + D_n\lambda_2 = 0\\
&A_n \cosh a\lambda_1 + B_n \sinh a\lambda_1 + C_n \cosh a\lambda_2 + D_n \sinh a\lambda_2 + \hat{q}_n = 0\\
&A_n\lambda_1 \sinh a\lambda_1 + B_n\lambda_1 \cosh a\lambda_1 + C_n\lambda_2 \sinh a\lambda_2 + D_n\lambda_2 \cosh a\lambda_2 = 0
\end{aligned} \tag{4.19-a}$$

where $\lambda_{1,2}^2 = \dfrac{\beta^2}{D_{11}}[(D_{12}+2D_{66}) \pm \sqrt{(D_{12}+2D_{66})^2 - D_{11}D_{22}}]$.

For Case III, when $(D_{12}+2D_{66})^2 < D_{11}D_{22}$, constants $A_n, B_n, C_n,$ and $D_n$ can be determined from the following algebraic equations:

$$\begin{aligned}
&A_n + \hat{q}_n = 0\\
&B_n\lambda_2 + C_n\lambda_1 = 0\\
&A_n \cosh a\lambda_1 \cos a\lambda_2 + B_n \cosh a\lambda_1 \sin a\lambda_2 + C_n \sinh a\lambda_1 \cos a\lambda_2 + D_n \sinh a\lambda_1 \sin a\lambda_2 + \hat{q}_n = 0\\
&A_n(\lambda_1 \sinh a\lambda_1 \cos a\lambda_2 - \lambda_2 \cosh a\lambda_1 \sin a\lambda_2) + B_n(\lambda_1 \sinh a\lambda_1 \sin a\lambda_2 + \lambda_2 \cosh a\lambda_1 \cos a\lambda_2)\\
&+ C_n(\lambda_1 \cosh a\lambda_1 \cos a\lambda_2 - \lambda_2 \sinh a\lambda_1 \sin a\lambda_2) + D_n(\lambda_1 \cosh a\lambda_1 \sin a\lambda_2 + \lambda_2 \sinh a\lambda_1 \cos a\lambda_2) = 0
\end{aligned} \tag{4.19-b}$$

where $(\lambda_{1,2})^2 = \dfrac{\beta^2}{2D_{11}}[\sqrt{D_{11}D_{22}} \pm (D_{12}+2D_{66})]$.

The longitudinal direction is the direction with 90" (2286mm) length and is stiffer (has larger bending stiffness), while the transverse direction is the direction with 60" (1524mm) length with smaller bending stiffness. These definitions hold for other five cases.

The numerical deflection comparisons with the FEA results using ANSYS® are shown in Figure (4.8) and Figure (4.9). 30 terms are used in the series expansion in the analytical solution.

The maximum deflection predicted from Levy method using CLPT is 15% lower than the FEA prediction. This difference will be smaller with more expansion terms, or using higher order plate theory considering shear effects.

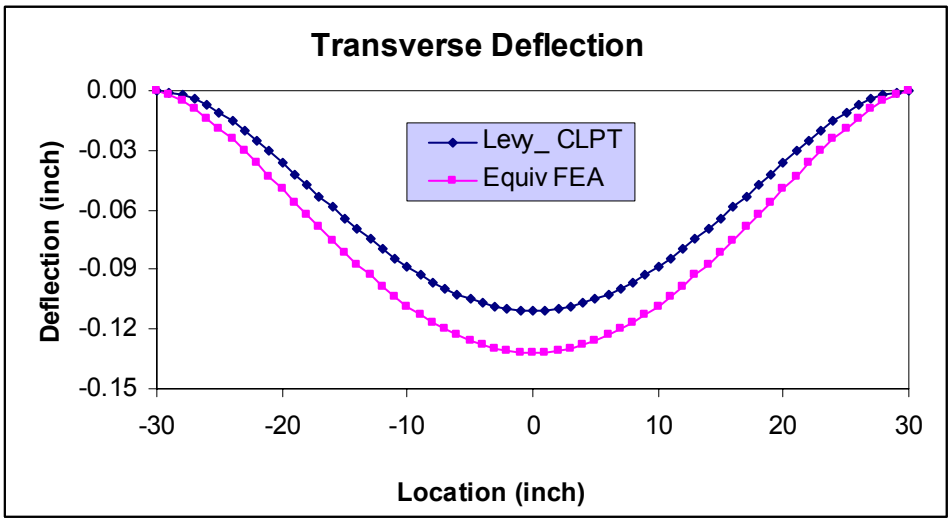


**Figure 4.8** Transverse deflection comparison for a SSCC plate under UDL

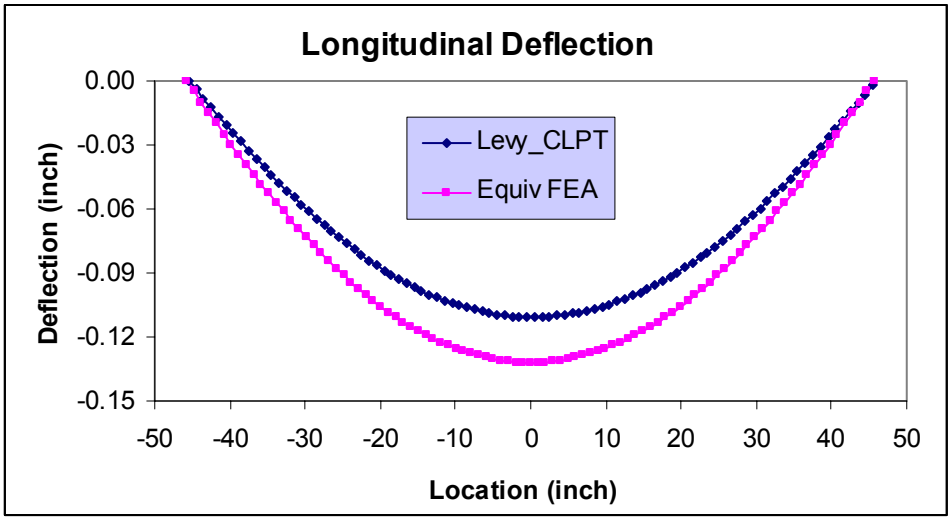


**Figure 4.9** Longitudinal deflection of a SSCC plate under UDL

### *4.1.2.2 SSCF Plate*

Though it is rare to have this case in practice of designing bridge decks, an FRP floor may be categorized to this case. Primarily because of the rarity of practical use of this case, previous literature did not give detailed solution for a SSCF plate. The boundary conditions can be represented as:

(i) At the clamped edge ( $x = 0$ ): $w_0(0, y) = 0$ , and $\frac{\partial w_0}{\partial x}(0, y) = 0$

(ii) At the free edge ( $x = a$ ): $M_{xx}(a, y) = 0$, and $N_{xx}(a, y) + \frac{\partial M_{xy}(a, y)}{\partial y} = 0$

where $N_{xx} = \int_{-\frac{h}{2}}^{\frac{h}{2}} \tau_{zx} dz$ ( Lekhnitskii, SG, Anisotropic Plates. pp.276). For orthotropic plates, we have

$$N_{xx}(a, y) + \frac{\partial M_{xy}(a, y)}{\partial y} = -\frac{\partial}{\partial x}(D_{11}\frac{\partial^2 w_0}{\partial x^2} + D_{12}\frac{\partial^2 w_0}{\partial y^2} + 4D_{66}\frac{\partial^2 w_0}{\partial y^2} = 0$$

The above equation can be represented by

$$D_{11}\frac{\partial^3 w_0}{\partial x^3} + \overline{D}_{12}\frac{\partial^3 w_0}{\partial x \partial y^2} = 0 \text{, where } \overline{D}_{12} = D_{12} + 4D_{66}$$

For Case I, when $(D_{12} + 2D_{66})^2 > D_{11}D_{22}$ , the substitution of boundary conditions (i) and (ii) leads to the following equations for $A_n, B_n, C_n,$ and $D_n$ :

$$A_n + C_n + \hat{q}_n = 0$$

$$B_n\lambda_1 + D_n\lambda_2 = 0$$

$$A_n(\lambda_1^2 D_{11} - \beta^2 D_{12})\cosh a\lambda_1 + B_n(\lambda_1^2 D_{11} - \beta^2 D_{12})\sinh a\lambda_1$$
$$+ C_n(\lambda_2^2 D_{11} - \beta^2 D_{12})\cosh a\lambda_2 + D_n(\lambda_2^2 D_{11} - \beta^2 D_{12})\sinh a\lambda_2 - \beta^2 D_{12}\hat{q}_n = 0$$

$$A_n[\lambda_1(\lambda_1^2 D_{11} - \beta^2 \overline{D}_{12})\sinh a\lambda_1] + B_n[\lambda_1(\lambda_1^2 D_{11} - \beta^2 \overline{D}_{12})\cosh a\lambda_1]$$
$$+ C_n[\lambda_2(\lambda_2^2 D_{11} - \beta^2 \overline{D}_{12})\sinh a\lambda_2] + D_n[\lambda_2(\lambda_2^2 D_{11} - \beta^2 \overline{D}_{12})\cosh a\lambda_2] = 0$$

(4.20-a)

where $\lambda_{1,2}^2 = \dfrac{\beta^2}{D_{11}}[(D_{12} + 2D_{66}) \pm \sqrt{(D_{12} + 2D_{66})^2 - D_{11}D_{22}}]$.

For Case III, when $(D_{12} + 2D_{66})^2 < D_{11}D_{22}$, constants $A_n, B_n, C_n,$ and $D_n$ can be determined from the following algebraic equations:

$$A_n + \hat{q}_n = 0$$

$$B_n\lambda_2 + C_n\lambda_1 = 0$$

$$A_n[D_{11}(\lambda_1^2 \cosh a\lambda_1 \cos a\lambda_2 - 2\lambda_1\lambda_2 \sinh a\lambda_1 \sin a\lambda_2 - \lambda_2^2 \cosh a\lambda_1 \cos a\lambda_2) - \beta^2 D_{12} \cosh a\lambda_1 \cos a\lambda_2] +$$
$$B_n[D_{11}(\lambda_1^2 \cosh a\lambda_1 \sin a\lambda_2 + 2\lambda_1\lambda_2 \sinh a\lambda_1 \cos a\lambda_2 - \lambda_2^2 \cosh a\lambda_1 \sin a\lambda_2) - \beta^2 D_{12} \cosh a\lambda_1 \sin a\lambda_2] +$$
$$C_n[D_{11}(\lambda_1^2 \sinh a\lambda_1 \cos a\lambda_2 - 2\lambda_1\lambda_2 \cosh a\lambda_1 \sin a\lambda_2 - \lambda_2^2 \sinh a\lambda_1 \cos a\lambda_2) - \beta^2 D_{12} \sinh a\lambda_1 \cos a\lambda_2] +$$
$$D_n[D_{11}(\lambda_1^2 \sinh a\lambda_1 \sin a\lambda_2 + 2\lambda_1\lambda_2 \cosh a\lambda_1 \cos a\lambda_2 - \lambda_2^2 \sinh a\lambda_1 \sin a\lambda_2) - \beta^2 D_{12} \sinh a\lambda_1 \sin a\lambda_2] -$$
$$\beta^2 D_{12}\hat{q}_n = 0$$

$$A_n[D_{11}(\lambda_1^3 \sinh a\lambda_1 \cos a\lambda_2 - 3\lambda_1^2\lambda_2 \cosh a\lambda_1 \sin a\lambda_2 - 3\lambda_1\lambda_2^2 \sinh a\lambda_1 \cos a\lambda_2 + \lambda_2^3 \cosh a\lambda_1 \sin a\lambda_2)$$
$$- \beta^2 \overline{D}_{12}(\lambda_1 \sinh a\lambda_1 \cos a\lambda_2 - \lambda_2 \cosh a\lambda_1 \sin a\lambda_2)] +$$
$$B_n[D_{11}(\lambda_1^3 \sinh a\lambda_1 \sin a\lambda_2 + 3\lambda_1^2\lambda_2 \cosh a\lambda_1 \cos a\lambda_2 - 3\lambda_1\lambda_2^2 \sinh a\lambda_1 \sin a\lambda_2 - \lambda_2^3 \cosh a\lambda_1 \cos a\lambda_2)$$
$$- \beta^2 \overline{D}_{12}(\lambda_1 \sinh a\lambda_1 \sin a\lambda_2 + \lambda_2 \cosh a\lambda_1 \cos a\lambda_2)] +$$
$$C_n[D_{11}(\lambda_1^3 \cosh a\lambda_1 \cos a\lambda_2 - 3\lambda_1^2\lambda_2 \sinh a\lambda_1 \sin a\lambda_2 - 3\lambda_1\lambda_2^2 \sinh a\lambda_1 \sin a\lambda_2 + \lambda_2^3 \sinh a\lambda_1 \sin a\lambda_2)$$
$$- \beta^2 \overline{D}_{12}(\lambda_1 \cosh a\lambda_1 \cos a\lambda_2 - \lambda_2 \sinh a\lambda_1 \sin a\lambda_2)] +$$
$$D_n[D_{11}(\lambda_1^3 \cosh a\lambda_1 \sin a\lambda_2 + 3\lambda_1^2\lambda_2 \sinh a\lambda_1 \cos a\lambda_2 - 3\lambda_1\lambda_2^2 \cosh a\lambda_1 \sin a\lambda_2 - \lambda_2^3 \sinh a\lambda_1 \cos a\lambda_2)$$
$$- \beta^2 \overline{D}_{12}(\lambda_1 \cosh a\lambda_1 \sin a\lambda_2 + \lambda_2 \sinh a\lambda_1 \cos a\lambda_2)] = 0$$

(4.20-b)

where $(\lambda_{1,2})^2 = \dfrac{\beta^2}{2D_{11}}[\sqrt{D_{11}D_{22}} \pm (D_{12} + 2D_{66})]$.

The numerical deflection comparisons with the FEA results are shown in Figure (4.10) and Figure (4.11). The two methods give very close predictions for this case. The maximum

deflection obtained from the analytical solution with 30 expanded terms is –0.52" (-13.2mm); while the equivalent FEA gives a –0.55" (-14mm) maximum deflection. The difference is 5.5%.

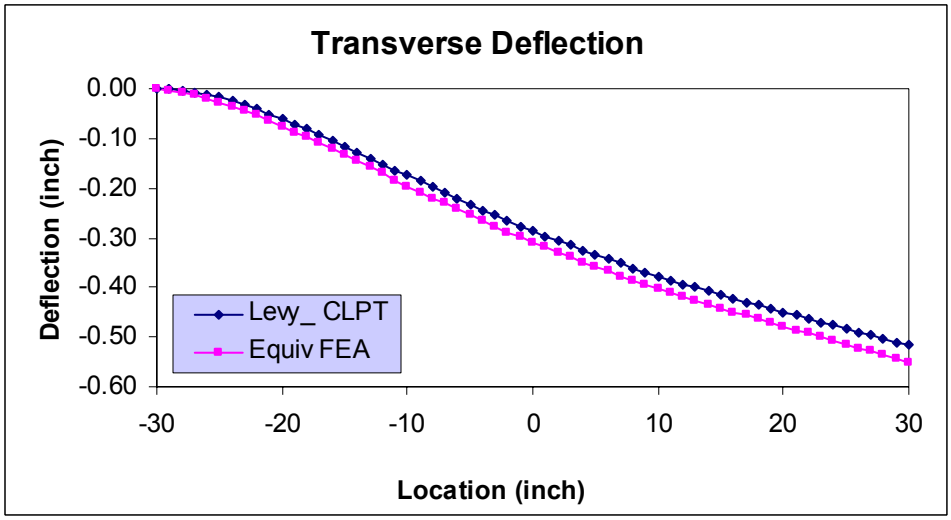


**Figure 4.10** Transverse deflection comparison for a SSCF plate under UDL

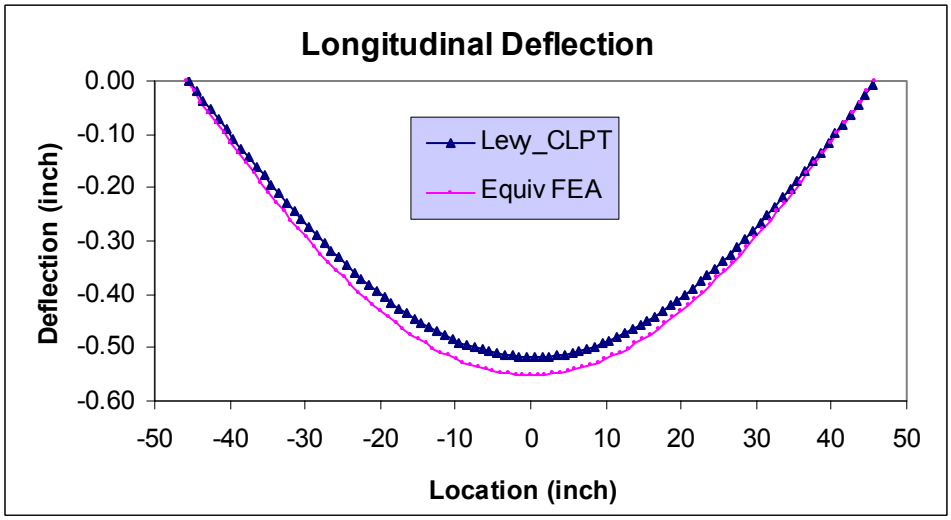


**Figure 4.11** Longitudinal deflection of a SSCF plate under UDL

### *4.1.2.3 SSCS Plate*

When analyzing a single span cut from a 2-span continuous simply supported bridge deck, one can use this case to do the analysis. Where the clamped edge represents the cutting edge. The Boundary conditions can be represented as:

(i) At the clamped edge ( $x = 0$ ): $w_0(0, y) = 0$ , and $\frac{\partial w_0}{\partial x}(0, y) = 0$

(ii) At the simply supported edge ( $x = a$ ): $w_0(a, y) = 0$ , and $M_{xx}(a, y) = 0$

For Case I, when $(D_{12} + 2D_{66})^2 > D_{11}D_{22}$ , the substitution of boundary conditions (i) and (ii) leads to the following equations for $A_n, B_n, C_n,$ and $D_n$ :

$$A_n + C_n + \hat{q}_n = 0$$

$$B_n\lambda_1 + D_n\lambda_2 = 0$$

$$A_n \cosh a\lambda_1 + B_n \sinh a\lambda_1 + C_n \cosh a\lambda_2 + D_n \sinh a\lambda_2 + \hat{q}_n = 0$$

$$A_n(\lambda_1^2 D_{11} - \beta^2 D_{12})\cosh a\lambda_1 + B_n(\lambda_1^2 D_{11} - \beta^2 D_{12})\sinh a\lambda_1$$
$$+ C_n(\lambda_2^2 D_{11} - \beta^2 D_{12})\cosh a\lambda_2 + D_n(\lambda_2^2 D_{11} - \beta^2 D_{12})\sinh a\lambda_2 - \beta^2 D_{12}\hat{q}_n = 0 \qquad (4.21\text{-a})$$

where $\lambda_{1,2}^2 = \frac{\beta^2}{D_{11}}[(D_{12} + 2D_{66}) \pm \sqrt{(D_{12} + 2D_{66})^2 - D_{11}D_{22}}]$.

For Case III, when $(D_{12} + 2D_{66})^2 < D_{11}D_{22}$, constants $A_n, B_n, C_n,$ and $D_n$ can be determined from the following algebraic equations:

$$A_n + \hat{q}_n = 0$$

$$B_n\lambda_2 + C_n\lambda_1 = 0$$

$$A_n \cosh a\lambda_1 \cos a\lambda_2 + B_n \cosh a\lambda_1 \sin a\lambda_2 + C_n \sinh a\lambda_1 \cos a\lambda_2 + D_n \sinh a\lambda_1 \sin a\lambda_2 + \hat{q}_n = 0$$

$$A_n[D_{11}(\lambda_1^2\cosh a\lambda_1\cos a\lambda_2 - 2\lambda_1\lambda_2\sinh a\lambda_1\sin a\lambda_2 - \lambda_2^2\cosh a\lambda_1\cos a\lambda_2) - \beta^2 D_{12}\cosh a\lambda_1\cos a\lambda_2] +$$
$$B_n[D_{11}(\lambda_1^2\cosh a\lambda_1\sin a\lambda_2 + 2\lambda_1\lambda_2\sinh a\lambda_1\cos a\lambda_2 - \lambda_2^2\cosh a\lambda_1\sin a\lambda_2) - \beta^2 D_{12}\cosh a\lambda_1\sin a\lambda_2] +$$
$$C_n[D_{11}(\lambda_1^2\sinh a\lambda_1\cos a\lambda_2 - 2\lambda_1\lambda_2\cosh a\lambda_1\sin a\lambda_2 - \lambda_2^2\sinh a\lambda_1\cos a\lambda_2) - \beta^2 D_{12}\sinh a\lambda_1\cos a\lambda_2] +$$
$$D_n[D_{11}(\lambda_1^2\sinh a\lambda_1\sin a\lambda_2 + 2\lambda_1\lambda_2\cosh a\lambda_1\cos a\lambda_2 - \lambda_2^2\sinh a\lambda_1\sin a\lambda_2) - \beta^2 D_{12}\sinh a\lambda_1\sin a\lambda_2] -$$
$$\beta^2 D_{12}\hat{q}_n = 0 \qquad (4.21\text{-b})$$

where $(\lambda_{1,2})^2 = \dfrac{\beta^2}{2D_{11}}[\sqrt{D_{11}D_{22}} \pm (D_{12} + 2D_{66})]$.

The numerical deflection comparisons with the FEA results are shown in Figure (4.12) and Figure (4.13). The Levy solution gives reasonably close predictions compared to equivalent FEA. However, it is still liberal: The maximum deflection obtained from the Levy CLPT solution with 30 terms is –0.165" (-4.2mm) ; the maximum deflection predicted from the FEA is –0.187" (-4.7mm). The difference is about 12%.

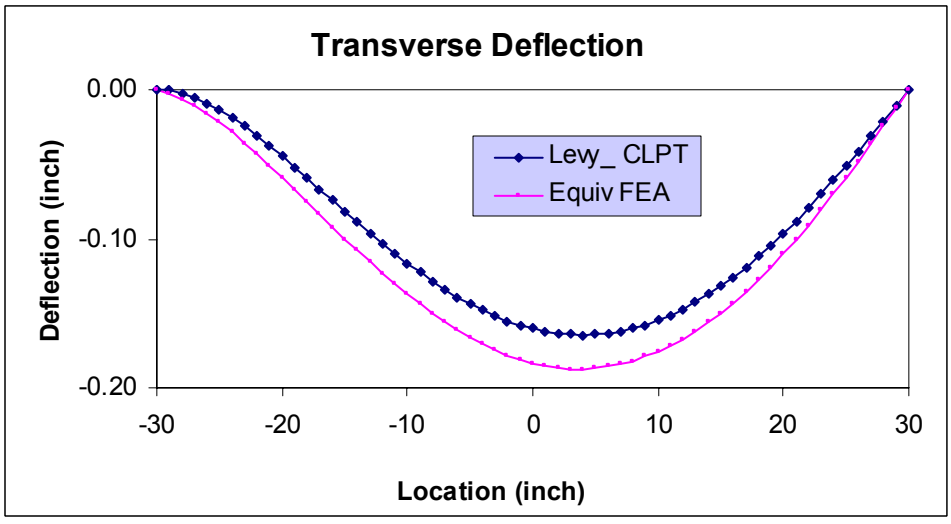


**Figure 4.12** Transverse deflection comparison for a SSCS plate under UDL

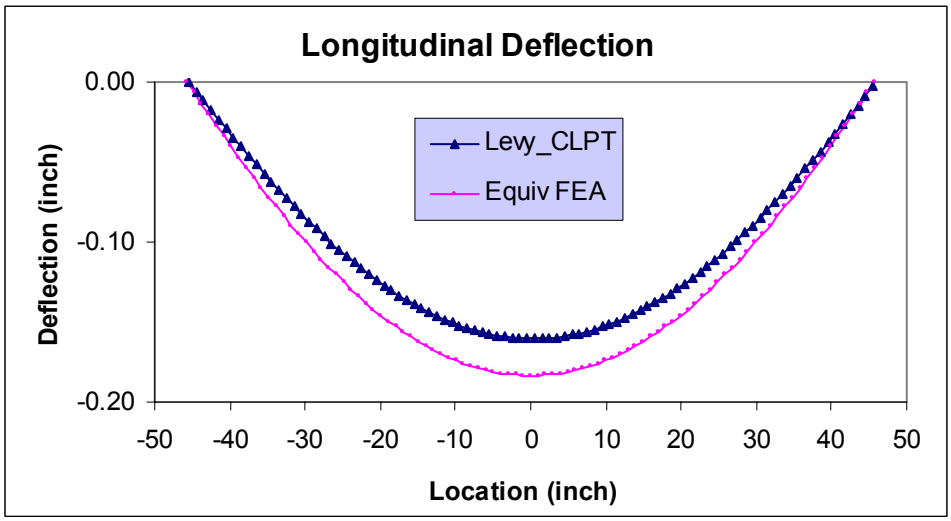


**Figure 4.13** Longitudinal deflection of a SSCS plate under UDL

#### *4.1.2.4 SSFF Plate*

This is a common case in lab testing when two opposite edges of a bridge deck are simply supported, while the other two opposite edges are unsupported. The free edges ($x = 0, a$) Boundary conditions can be represented as:

$$M_{xx}(0,y) = 0,\ M_{xx}(a,y) = 0, \text{and}\ N_{xx}(0,y) + \frac{\partial M_{xy}(0,y)}{\partial y} = 0,$$

$$N_{xx}(a,y) + \frac{\partial M_{xy}(a,y)}{\partial y} = 0, \text{or}\ D_{11}\frac{\partial^3 w_0}{\partial x^3} + \overline{D}_{12}\frac{\partial^3 w_0}{\partial x \partial y^2} = 0 \ \text{at}\ x = 0, a$$

For Case I, when $(D_{12} + 2D_{66})^2 > D_{11}D_{22}$, the substitution of boundary conditions (i) and (ii) leads to the following equations for $A_n, B_n, C_n,$ and $D_n$:

$$A_n(\lambda_1^2 D_{11} - \beta^2 D_{12}) + C_n(\lambda_2^2 D_{11} - \beta^2 D_{12}) - \beta^2 D_{12}\hat{q}_n = 0$$

$$B_n(\lambda_1^3 D_{11} - \lambda_1 \beta^2 \overline{D}_{12}) + D_n(\lambda_2^3 D_{11} - \lambda_2 \beta^2 \overline{D}_{12}) = 0$$

$$A_n(\lambda_1^2 D_{11} - \beta^2 D_{12})\cosh a\lambda_1 + B_n(\lambda_1^2 D_{11} - \beta^2 D_{12})\sinh a\lambda_1$$
$$+ C_n(\lambda_2^2 D_{11} - \beta^2 D_{12})\cosh a\lambda_2 + D_n(\lambda_2^2 D_{11} - \beta^2 D_{12})\sinh a\lambda_2 - \beta^2 D_{12}\hat{q}_n = 0$$

$$A_n[\lambda_1(\lambda_1^2 D_{11} - \beta^2 \overline{D}_{12})\sinh a\lambda_1] + B_n[\lambda_1(\lambda_1^2 D_{11} - \beta^2 \overline{D}_{12})\cosh a\lambda_1]$$
$$+ C_n[\lambda_2(\lambda_2^2 D_{11} - \beta^2 \overline{D}_{12})\sinh a\lambda_2] + D_n[\lambda_2(\lambda_2^2 D_{11} - \beta^2 \overline{D}_{12})\cosh a\lambda_2] = 0 \quad \text{(4.22-a)}$$

where $\lambda_{1,2}^2 = \dfrac{\beta^2}{D_{11}}[(D_{12} + 2D_{66}) \pm \sqrt{(D_{12} + 2D_{66})^2 - D_{11}D_{22}}]$.

For Case III, when $(D_{12} + 2D_{66})^2 < D_{11}D_{22}$, constants $A_n, B_n, C_n,$ and $D_n$ can be determined from the following algebraic equations:

$$A_n[D_{11}(\lambda_1^2 - \lambda_2^2) - \beta^2 D_{12}) + D_n(2\lambda_1\lambda_2 D_{11}) - \beta^2 D_{12}\hat{q}_n = 0$$

$$B_n(3\lambda_1^2\lambda_2 D_{11} - \lambda_2^3 D_{11} - \lambda_1\beta^2 \overline{D}_{12}) + C_n(\lambda_1^3 D_{11} - 3\lambda_1\lambda_2^2 D_{11} - \lambda_1\beta^2 \overline{D}_{12}) = 0$$

$$A_n[D_{11}(\lambda_1^2 \cosh a\lambda_1 \cos a\lambda_2 - 2\lambda_1\lambda_2 \sinh a\lambda_1 \sin a\lambda_2 - \lambda_2^2 \cosh a\lambda_1 \cos a\lambda_2) - \beta^2 D_{12} \cosh a\lambda_1 \cos a\lambda_2] +$$
$$B_n[D_{11}(\lambda_1^2 \cosh a\lambda_1 \sin a\lambda_2 + 2\lambda_1\lambda_2 \sinh a\lambda_1 \cos a\lambda_2 - \lambda_2^2 \cosh a\lambda_1 \sin a\lambda_2) - \beta^2 D_{12} \cosh a\lambda_1 \sin a\lambda_2] +$$
$$C_n[D_{11}(\lambda_1^2 \sinh a\lambda_1 \cos a\lambda_2 - 2\lambda_1\lambda_2 \cosh a\lambda_1 \sin a\lambda_2 - \lambda_2^2 \sinh a\lambda_1 \cos a\lambda_2) - \beta^2 D_{12} \sinh a\lambda_1 \cos a\lambda_2] +$$
$$D_n[D_{11}(\lambda_1^2 \sinh a\lambda_1 \sin a\lambda_2 + 2\lambda_1\lambda_2 \cosh a\lambda_1 \cos a\lambda_2 - \lambda_2^2 \sinh a\lambda_1 \sin a\lambda_2) - \beta^2 D_{12} \sinh a\lambda_1 \sin a\lambda_2] -$$
$$\beta^2 D_{12}\hat{q}_n = 0$$

$$A_n[D_{11}(\lambda_1^3 \sinh a\lambda_1 \cos a\lambda_2 - 3\lambda_1^2\lambda_2 \cosh a\lambda_1 \sin a\lambda_2 - 3\lambda_1\lambda_2^2 \sinh a\lambda_1 \cos a\lambda_2 + \lambda_2^3 \cosh a\lambda_1 \sin a\lambda_2)$$
$$- \beta^2 \overline{D}_{12}(\lambda_1 \sinh a\lambda_1 \cos a\lambda_2 - \lambda_2 \cosh a\lambda_1 \sin a\lambda_2)] +$$
$$B_n[D_{11}(\lambda_1^3 \sinh a\lambda_1 \sin a\lambda_2 + 3\lambda_1^2\lambda_2 \cosh a\lambda_1 \cos a\lambda_2 - 3\lambda_1\lambda_2^2 \sinh a\lambda_1 \sin a\lambda_2 - \lambda_2^3 \cosh a\lambda_1 \cos a\lambda_2)$$
$$- \beta^2 \overline{D}_{12}(\lambda_1 \sinh a\lambda_1 \sin a\lambda_2 + \lambda_2 \cosh a\lambda_1 \cos a\lambda_2)] +$$
$$C_n[D_{11}(\lambda_1^3 \cosh a\lambda_1 \cos a\lambda_2 - 3\lambda_1^2\lambda_2 \sinh a\lambda_1 \sin a\lambda_2 - 3\lambda_1\lambda_2^2 \sinh a\lambda_1 \sin a\lambda_2 + \lambda_2^3 \sinh a\lambda_1 \sin a\lambda_2)$$
$$- \beta^2 \overline{D}_{12}(\lambda_1 \cosh a\lambda_1 \cos a\lambda_2 - \lambda_2 \sinh a\lambda_1 \sin a\lambda_2)] +$$
$$D_n[D_{11}(\lambda_1^3 \cosh a\lambda_1 \sin a\lambda_2 + 3\lambda_1^2\lambda_2 \sinh a\lambda_1 \cos a\lambda_2 - 3\lambda_1\lambda_2^2 \cosh a\lambda_1 \sin a\lambda_2 - \lambda_2^3 \sinh a\lambda_1 \cos a\lambda_2)$$
$$- \beta^2 \overline{D}_{12}(\lambda_1 \cosh a\lambda_1 \sin a\lambda_2 + \lambda_2 \sinh a\lambda_1 \cos a\lambda_2)] = 0 \quad \text{(4.22-b)}$$

where $(\lambda_{1,2})^2 = \dfrac{\beta^2}{2D_{11}}[\sqrt{D_{11}D_{22} \pm (D_{12} + 2D_{66})}]$.

The deformed shape of an SSFF plate under UDL loading (18.2 psi) is shown in Figure (4.14). The numerical deflection comparisons with FEA results are shown in Figure (4.15) and Figure (4.16). The Levy solution gives reasonably close predictions compared to equivalent FEA. The maximum deflection at the free edge obtained from the Levy solution is –0.617" (-

16.7mm); while the maximum deflection is –0.635" (-16.1mm) from equivalent FEA. The difference is less than 3%. Also given in Figures 4.21 and 4.22 are deflections from complete 3-D FEA. It's observed from the three methods (see Figure 4.16) that, for a SSFF plate, deflections at the free edges are larger than at the center.

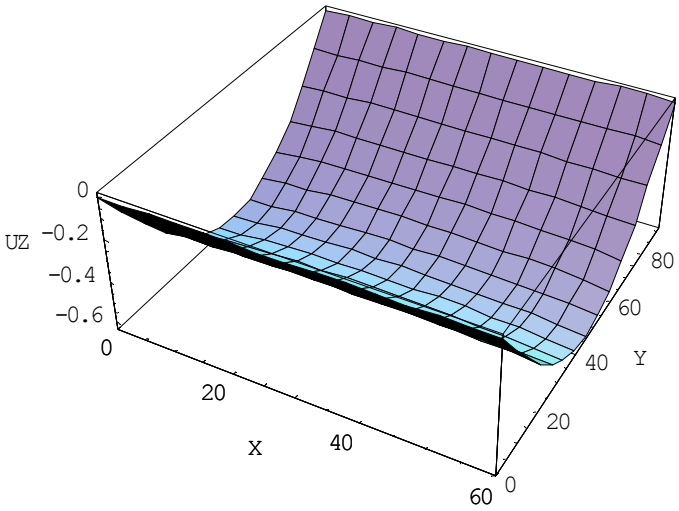


**Figure 4.14** Deformed shape of a SSFF plate under UDL

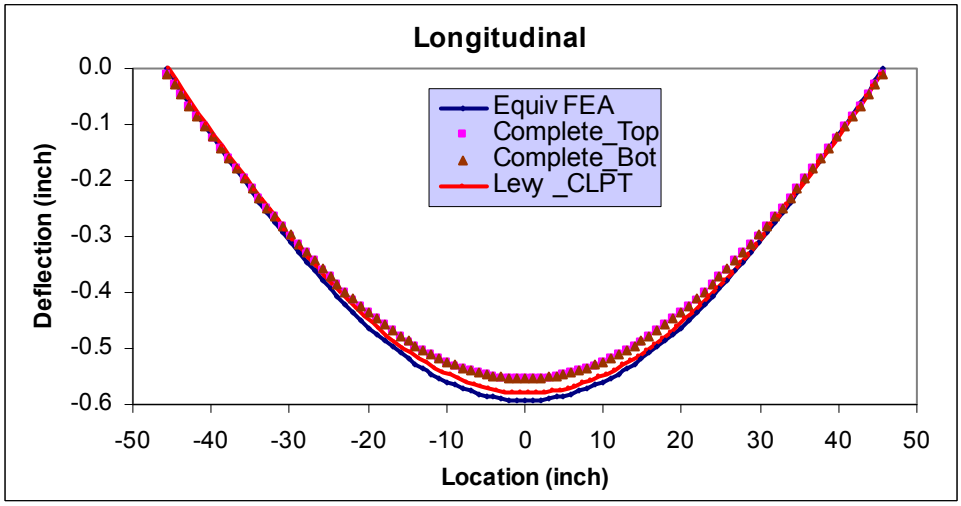


**Figure 4.15** Transverse deflection comparison for a SSFF plate under UDL

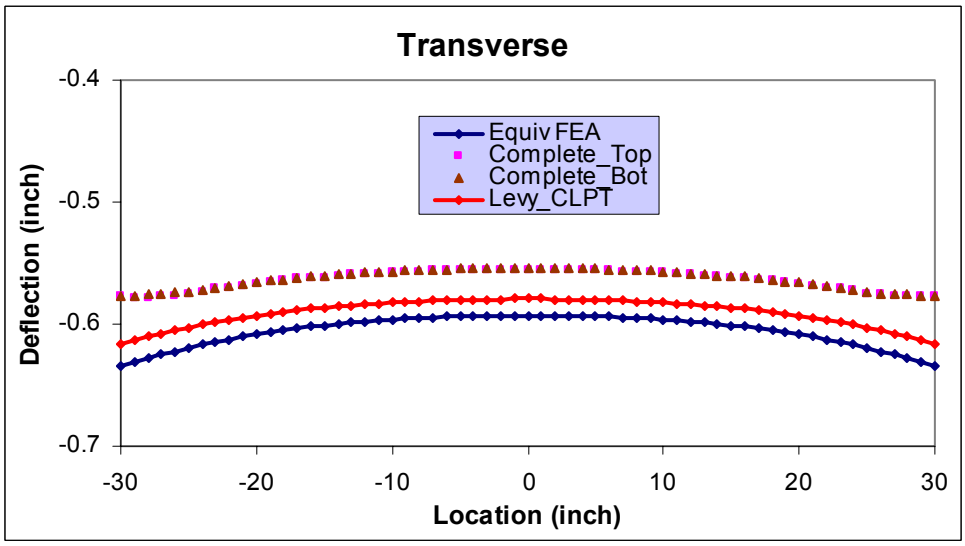


**Figure 4.16** Longitudinal deflection of a SSFF plate under UDL

#### *4.1.2.5 SSSF Plate*

Similar to the SSCF case, it is rare to have an SSSF deck design and construction in practice. No previous literature gave complete and detailed solution for an SSSF plate. The boundary conditions for this plate can be expressed as

(i) At the simply supported edge ( $x = 0$ ): $w_0(0, y) = 0$, and $M_{xx}(0, y) = 0$

(ii) At the free edge ( $x = a$ ): $M_{xx}(a, y) = 0$, and $N_{xx}(a, y) + \dfrac{\partial M_{xy}(a, y)}{\partial y} = 0$ ( or

$$D_{11}\frac{\partial^3 w_0}{\partial x^3} + \overline{D}_{12}\frac{\partial^3 w_0}{\partial x \partial y^2} = 0 \text{ at } x = a$$ )

For Case I, when $(D_{12} + 2D_{66})^2 > D_{11}D_{22}$, the substitution of boundary conditions (i) and (ii) leads to the following equations for $A_n, B_n, C_n,$ and $D_n$:

$$A_n + C_n + \hat{q}_n = 0$$

$$A_n(\lambda_1^2 D_{11} - \beta^2 D_{12}) + C_n(\lambda_2^2 D_{11} - \beta^2 D_{12}) - \beta^2 D_{12}\hat{q}_n = 0$$

$$A_n(\lambda_1^2 D_{11} - \beta^2 D_{12})\cosh a\lambda_1 + B_n(\lambda_1^2 D_{11} - \beta^2 D_{12})\sinh a\lambda_1$$
$$+ C_n(\lambda_2^2 D_{11} - \beta^2 D_{12})\cosh a\lambda_2 + D_n(\lambda_2^2 D_{11} - \beta^2 D_{12})\sinh a\lambda_2 - \beta^2 D_{12}\hat{q}_n = 0$$

$$A_n[\lambda_1(\lambda_1^2 D_{11} - \beta^2 \overline{D}_{12})\sinh a\lambda_1] + B_n[\lambda_1(\lambda_1^2 D_{11} - \beta^2 \overline{D}_{12})\cosh a\lambda_1]$$
$$+ C_n[\lambda_2(\lambda_2^2 D_{11} - \beta^2 \overline{D}_{12})\sinh a\lambda_2] + D_n[\lambda_2(\lambda_2^2 D_{11} - \beta^2 \overline{D}_{12})\cosh a\lambda_2] = 0$$

(4.23-a)

where $\lambda_{1,2}^2 = \dfrac{\beta^2}{D_{11}}[(D_{12} + 2D_{66}) \pm \sqrt{(D_{12} + 2D_{66})^2 - D_{11}D_{22}}]$.

For Case III, when $(D_{12} + 2D_{66})^2 < D_{11}D_{22}$, constants $A_n, B_n, C_n,$ and $D_n$ can be determined from the following algebraic equations:

$$A_n + \hat{q}_n = 0$$

$$A_n[D_{11}(\lambda_1^2 - \lambda_2^2) - \beta^2 D_{12}) + D_n(2\lambda_1\lambda_2 D_{11}) - \beta^2 D_{12}\hat{q}_n = 0$$

$$A_n[D_{11}(\lambda_1^2 \cosh a\lambda_1 \cos a\lambda_2 - 2\lambda_1\lambda_2 \sinh a\lambda_1 \sin a\lambda_2 - \lambda_2^2 \cosh a\lambda_1 \cos a\lambda_2) - \beta^2 D_{12} \cosh a\lambda_1 \cos a\lambda_2] +$$
$$B_n[D_{11}(\lambda_1^2 \cosh a\lambda_1 \sin a\lambda_2 + 2\lambda_1\lambda_2 \sinh a\lambda_1 \cos a\lambda_2 - \lambda_2^2 \cosh a\lambda_1 \sin a\lambda_2) - \beta^2 D_{12} \cosh a\lambda_1 \sin a\lambda_2] +$$
$$C_n[D_{11}(\lambda_1^2 \sinh a\lambda_1 \cos a\lambda_2 - 2\lambda_1\lambda_2 \cosh a\lambda_1 \sin a\lambda_2 - \lambda_2^2 \sinh a\lambda_1 \cos a\lambda_2) - \beta^2 D_{12} \sinh a\lambda_1 \cos a\lambda_2] +$$
$$D_n[D_{11}(\lambda_1^2 \sinh a\lambda_1 \sin a\lambda_2 + 2\lambda_1\lambda_2 \cosh a\lambda_1 \cos a\lambda_2 - \lambda_2^2 \sinh a\lambda_1 \sin a\lambda_2) - \beta^2 D_{12} \sinh a\lambda_1 \sin a\lambda_2] -$$
$$\beta^2 D_{12}\hat{q}_n = 0$$
$$A_n[D_{11}(\lambda_1^3 \sinh a\lambda_1 \cos a\lambda_2 - 3\lambda_1^2\lambda_2 \cosh a\lambda_1 \sin a\lambda_2 - 3\lambda_1\lambda_2^2 \sinh a\lambda_1 \cos a\lambda_2 + \lambda_2^3 \cosh a\lambda_1 \sin a\lambda_2)$$
$$- \beta^2 \overline{D}_{12}(\lambda_1 \sinh a\lambda_1 \cos a\lambda_2 - \lambda_2 \cosh a\lambda_1 \sin a\lambda_2)] +$$
$$B_n[D_{11}(\lambda_1^3 \sinh a\lambda_1 \sin a\lambda_2 + 3\lambda_1^2\lambda_2 \cosh a\lambda_1 \cos a\lambda_2 - 3\lambda_1\lambda_2^2 \sinh a\lambda_1 \sin a\lambda_2 - \lambda_2^3 \cosh a\lambda_1 \cos a\lambda_2)$$
$$- \beta^2 \overline{D}_{12}(\lambda_1 \sinh a\lambda_1 \sin a\lambda_2 + \lambda_2 \cosh a\lambda_1 \cos a\lambda_2)] +$$
$$C_n[D_{11}(\lambda_1^3 \cosh a\lambda_1 \cos a\lambda_2 - 3\lambda_1^2\lambda_2 \sinh a\lambda_1 \sin a\lambda_2 - 3\lambda_1\lambda_2^2 \sinh a\lambda_1 \sin a\lambda_2 + \lambda_2^3 \sinh a\lambda_1 \sin a\lambda_2)$$
$$- \beta^2 \overline{D}_{12}(\lambda_1 \cosh a\lambda_1 \cos a\lambda_2 - \lambda_2 \sinh a\lambda_1 \sin a\lambda_2)] +$$
$$D_n[D_{11}(\lambda_1^3 \cosh a\lambda_1 \sin a\lambda_2 + 3\lambda_1^2\lambda_2 \sinh a\lambda_1 \cos a\lambda_2 - 3\lambda_1\lambda_2^2 \cosh a\lambda_1 \sin a\lambda_2 - \lambda_2^3 \sinh a\lambda_1 \cos a\lambda_2)$$
$$- \beta^2 \overline{D}_{12}(\lambda_1 \cosh a\lambda_1 \sin a\lambda_2 + \lambda_2 \sinh a\lambda_1 \cos a\lambda_2)] = 0$$

(4.23-b)

where $(\lambda_{1,2})^2 = \dfrac{\beta^2}{2D_{11}}[\sqrt{D_{11}D_{22}} \pm (D_{12} + 2D_{66})]$.

The deformed shape of an SSSF plate under UDL loading is shown in Figure (4.17). The numerical deflection comparisons with FEA results are shown in Figure (4.18) and Figure (4.19). The maximum deflection difference is 5.2% for the two methods.

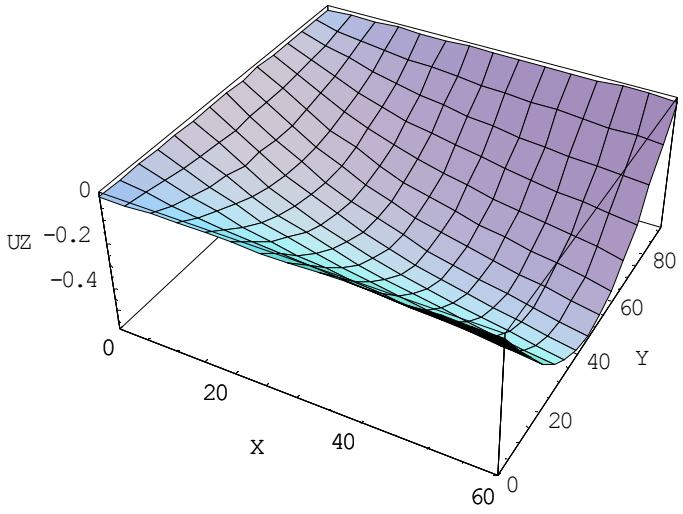


**Figure 4.17** Deformed shape of a SSSF plate under UDL

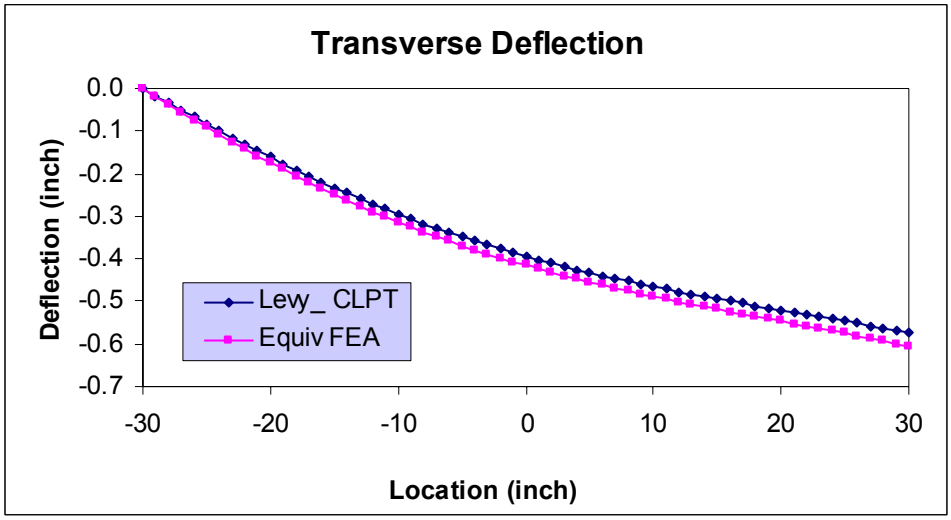


**Figure 4.18** Transverse deflection comparison for a SSSF plate under UDL

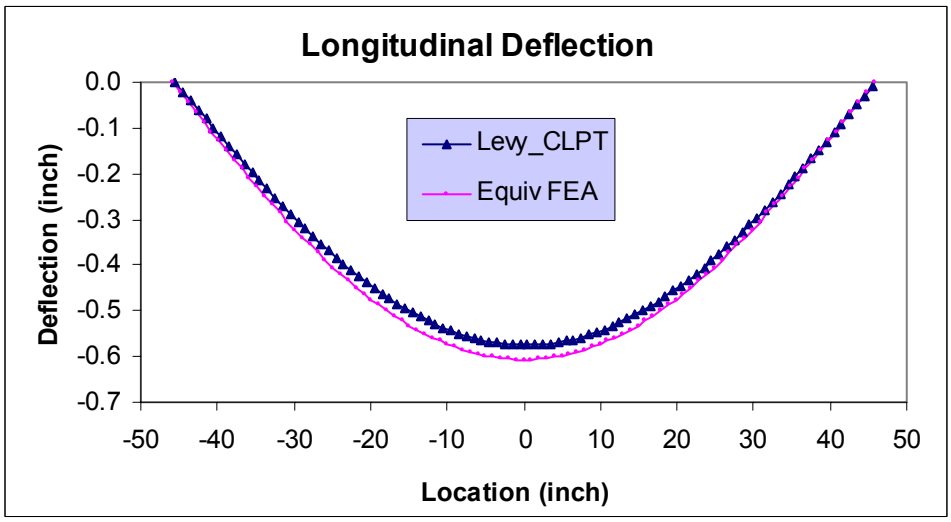


**Figure 4.19** Longitudinal deflection of a SSSF plate under UDL

#### *4.1.2.6 SSSS Plate*

At the simply supported edges ( $x = 0, a$ ):

$$w_0(0, y) = w_0(a, y) = 0 \text{, and } M_{xx}(0, y) = M_{xx}(a, y) = 0$$

For Case I, when $(D_{12} + 2D_{66})^2 > D_{11}D_{22}$, the above boundary conditions lead to the following equations for $A_n, B_n, C_n,$ and $D_n$:

$$A_n + C_n + \hat{q}_n = 0$$

$$A_n \cosh a\lambda_1 + B_n \sinh a\lambda_1 + C_n \cosh a\lambda_2 + D_n \sinh a\lambda_2 + \hat{q}_n = 0$$

$$A_n(\lambda_1^2 D_{11} - \beta^2 D_{12}) + C_n(\lambda_2^2 D_{11} - \beta^2 D_{12}) - \beta^2 D_{12}\hat{q}_n = 0$$

$$A_n(\lambda_1^2 D_{11} - \beta^2 D_{12})\cosh a\lambda_1 + B_n(\lambda_1^2 D_{11} - \beta^2 D_{12})\sinh a\lambda_1$$
$$+ C_n(\lambda_2^2 D_{11} - \beta^2 D_{12})\cosh a\lambda_2 + D_n(\lambda_2^2 D_{11} - \beta^2 D_{12})\sinh a\lambda_2 - \beta^2 D_{12}\hat{q}_n = 0$$

(4.24-a)

where $\lambda_{1,2}^2 = \frac{\beta^2}{D_{11}}[(D_{12}+2D_{66}) \pm \sqrt{(D_{12}+2D_{66})^2 - D_{11}D_{22}}]$.

For Case III, when $(D_{12}+2D_{66})^2 < D_{11}D_{22}$, constants $A_n, B_n, C_n,$ and $D_n$ can be determined from the following algebraic equations:

$$A_n + \hat{q}_n = 0$$

$$A_n[D_{11}(\lambda_1^2 - \lambda_2^2) - \beta^2 D_{12}) + D_n(2\lambda_1\lambda_2 D_{11}) - \beta^2 D_{12}\hat{q}_n = 0$$

$$A_n \cosh a\lambda_1 \cos a\lambda_2 + B_n \cosh a\lambda_1 \sin a\lambda_2 + C_n \sinh a\lambda_1 \cos a\lambda_2 + D_n \sinh a\lambda_1 \sin a\lambda_2 + \hat{q}_n = 0$$

$$\begin{aligned} &A_n[D_{11}(\lambda_1^2 \cosh a\lambda_1 \cos a\lambda_2 - 2\lambda_1\lambda_2 \sinh a\lambda_1 \sin a\lambda_2 - \lambda_2^2 \cosh a\lambda_1 \cos a\lambda_2) - \beta^2 D_{12} \cosh a\lambda_1 \cos a\lambda_2] + \\ &B_n[D_{11}(\lambda_1^2 \cosh a\lambda_1 \sin a\lambda_2 + 2\lambda_1\lambda_2 \sinh a\lambda_1 \cos a\lambda_2 - \lambda_2^2 \cosh a\lambda_1 \sin a\lambda_2) - \beta^2 D_{12} \cosh a\lambda_1 \sin a\lambda_2] + \\ &C_n[D_{11}(\lambda_1^2 \sinh a\lambda_1 \cos a\lambda_2 - 2\lambda_1\lambda_2 \cosh a\lambda_1 \sin a\lambda_2 - \lambda_2^2 \sinh a\lambda_1 \cos a\lambda_2) - \beta^2 D_{12} \sinh a\lambda_1 \cos a\lambda_2] + \\ &D_n[D_{11}(\lambda_1^2 \sinh a\lambda_1 \sin a\lambda_2 + 2\lambda_1\lambda_2 \cosh a\lambda_1 \cos a\lambda_2 - \lambda_2^2 \sinh a\lambda_1 \sin a\lambda_2) - \beta^2 D_{12} \sinh a\lambda_1 \sin a\lambda_2] - \\ &\beta^2 D_{12}\hat{q}_n = 0 \end{aligned}$$

(4.24-b)

where $(\lambda_{1,2})^2 = \frac{\beta^2}{2D_{11}}[\sqrt{D_{11}D_{22}} \pm (D_{12}+2D_{66})]$.

The deformed shape of an SSSS plate under UDL loading is shown in Figure (4.20). The numerical deflection comparisons with FEA results and results obtained from the Navier method are shown in Figure (4.21) and Figure (4.22). For this case, the results obtained from the Navier Method, the Levy Method and equivalent FEA show very good agreement, within 10% differences. The Navier Method and the Levy Method give the almost the same predictions for the deflection.

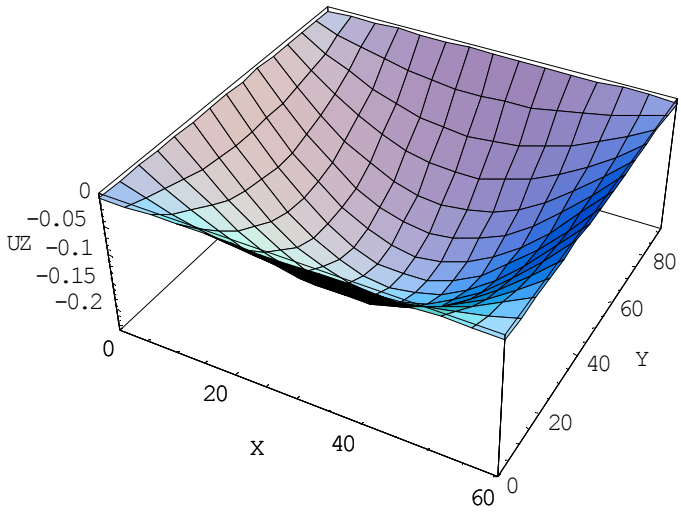


**Figure 4.20** Deformed shape of a SSSS plate under UDL (Levy Method)

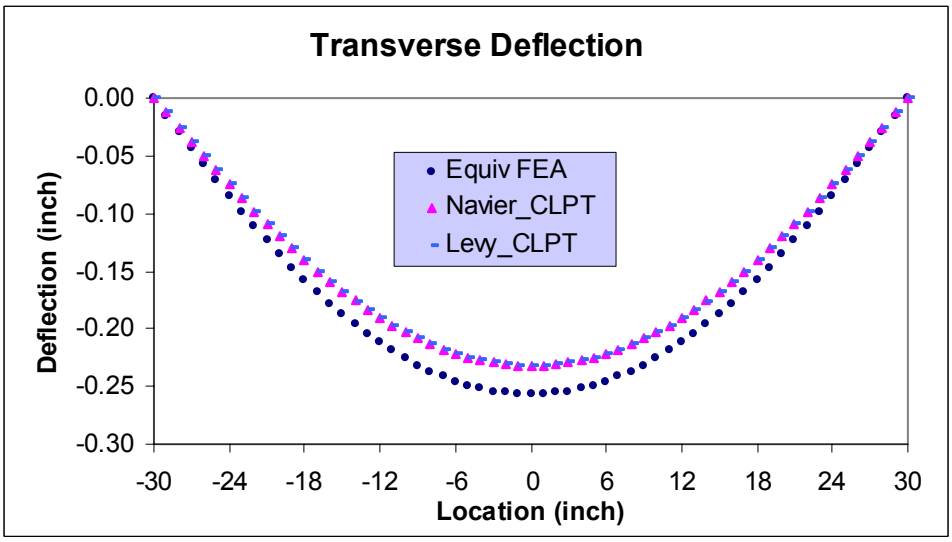


**Figure 4.21** Transverse deflection comparison for a SSSS plate under UDL

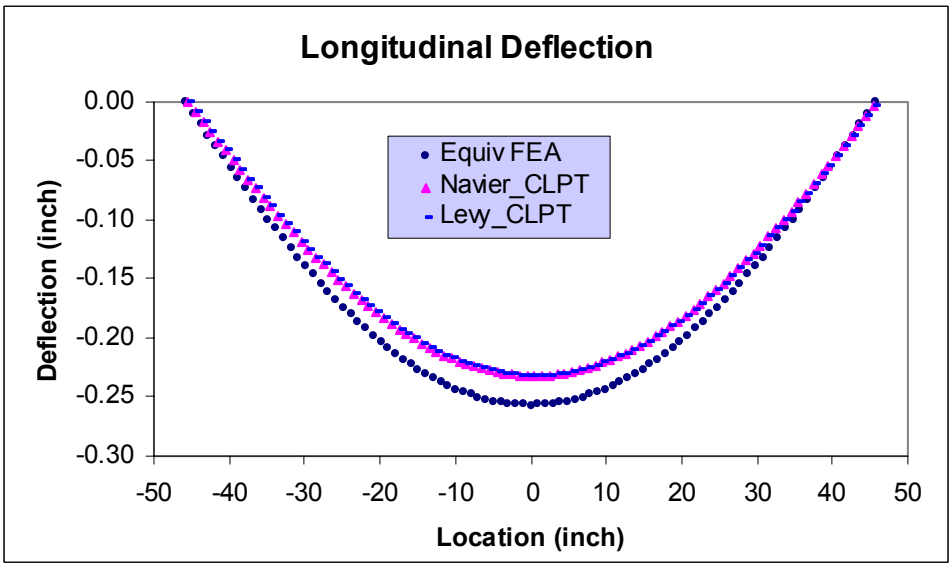


**Figure 4.22** Longitudinal deflection of a SSSS plate under UDL

### 4.1.3 Various Boundary Conditions

There are several other cases of boundary conditions that are commonly used in bridge deck applications but not covered in previous sections. For these plates, analytical methods such as the Navier Method and the Levy Method cannot be used directly; instead, approximate methods should be used to find approximate solutions. The Rayleigh-Ritz Method (RRM) will be used as the prime approximate method in this section. An alternative for RRM is the Finite Element Method (FEM) based on Galerkin's approximation. Because various commercial Finite Element Analysis software are currently available, such as ANSYS and ABAQUS etc., we will not develop any formulation for FEA. However, we will still use the ANSYS software and compare the obtained results of the CCCC and CCFF plates to the results obtained from RRM. In the followings, as examples, we will consider CCCC, and CCFF plates that most possibly occur in bridge deck applications and are not covered previous sections.

RRM starts with the virtual work statement (or weak form) and the total potential energy for the plate [Reddy 1999]. For a rectangular plate, the N-parameter Rayleigh-Ritz approximation can be expressed in the form

$$w_0(x,y) \approx W_{mn}(x,y) = \sum_{i=1}^{N}\sum_{j=1}^{N} c_{ij}\varphi_{ij}(x,y) \tag{4.25-a}$$

where the parameters $c_{ij}$ will be determined by requiring that the principle of virtual displacements hold (or the principle of virtual work is satisfied) for the approximate problem (or minimize the total potential energy functional); and $\varphi_{ij}(x,y)$ are approximate functions that are chosen to satisfy all the essential (or geometric) boundary conditions. $\varphi_{ij}(x,y)$ are usually written as a tensor product of the one-dimensional functions $X_i(x)$, and $Y_j(y)$ as $\varphi_{ij}(x,y) = X_i(x)\cdot Y_j(y)$, where $i, j = 1,2,...,N$. Therefore, an approximation to the above plates can be rewritten as [Reddy 1999],

$$w_0(x,y) \approx W_{mn}(x,y) = \sum_{i=1}^{N}\sum_{j=1}^{N} c_{ij}\cdot X_i(x)\cdot Y_j(y) \tag{4.25-b}$$

and $X_i(x), Y_j(y)$ are chosen such that all the essential boundary conditions are satisfied. There are several forms for the approximation functions $X_i(x), Y_j(y)$. The algebraic polynomials and the characteristic polynomials are commonly used for Rayleigh-Ritz approximation. For simplicity, the algebraic polynomials will be used as the approximation functions in the followings.

#### *4.1.3.1 CCCC Plate*

The boundary conditions associated with the clamped plate are,

(i) At edges $x = 0, a$: $w_0 = 0$, and $\dfrac{\partial w_0}{\partial x} = 0$

(ii) At edges $y = 0, b$: $w_0 = 0$, and $\dfrac{\partial w_0}{\partial y} = 0$

The following algebraic polynomials satisfy the essential boundary conditions for a CCCC plate [Reddy, 1999]

$$X_i(x) = \left(\frac{x}{a}\right)^{i+1}\left(1-\frac{x}{a}\right)^2 = \left(\frac{x}{a}\right)^{i+1} - 2\left(\frac{x}{a}\right)^{i+2} + \left(\frac{x}{a}\right)^{i+3} \tag{4.26-a}$$

$$Y_j(y) = \left(\frac{y}{b}\right)^{i+1}\left(1-\frac{y}{b}\right)^2 = \left(\frac{y}{b}\right)^{i+1} - 2\left(\frac{y}{b}\right)^{i+2} + \left(\frac{y}{b}\right)^{i+3} \tag{4.26-b}$$

The coefficients $c_{ij}$ of Eq. (25-b) can be found from the following $m \times n$ equations

$$\sum_{i=1}^{m}\sum_{j=1}^{n}\{\int_0^b\int_0^a [D_{11}\frac{d^2X_i}{dx^2}Y_j\frac{d^2X_p}{dx^2}Y_q + D_{22}X_i\frac{d^2Y_j}{dy^2}X_p\frac{d^2Y_q}{dy^2} + 4D_{66}\frac{dX_i}{dx}\frac{dY_j}{dy}\frac{dX_p}{dx}\frac{dY_q}{dy} + D_{12}\left(X_i\frac{d^2Y_j}{dy^2}\frac{d^2X_p}{dx^2}Y_q + \frac{d^2X_i}{dx^2}Y_jX_p\frac{d^2Y_q}{dy^2}\right)]dxdy\}c_{ij} = \int_0^b\int_0^a q(x,y)X_pY_q\,dxdy \tag{4.26-c}$$

For example, for a one-parameter Rayleigh-Ritz approximation with $m = 1 = 1$, and uniformly distributed load with $q(x, y) = q_0$, we have:

$$X_1(x) = \left(\frac{x}{a}\right)^2\left(1-\frac{x}{a}\right)^2 \tag{4.26-d}$$

$$Y_1(y) = \left(\frac{y}{b}\right)^2\left(1-\frac{y}{b}\right)^2 \tag{4.26-e}$$

with $\left[\dfrac{7}{a^4}D_{11} + \dfrac{7}{b^4}D_{22} + \dfrac{4}{a^2b^2}(D_{12}+2D_{66})\right]\cdot c_{11} = \dfrac{49}{8}q_0$ to calculate $c_{11}$.

The one-parameter Rayleigh-Ritz approximation for a CCCC plate can be expressed as [Reddy 199]:

$$w_0(x,y) \approx W_{11}(x,y) = \frac{49q_0}{8} \cdot \frac{\left(\frac{x}{a}\right)^2\left(1-\frac{x}{a}\right)^2\left(\frac{y}{b}\right)^2\left(1-\frac{y}{b}\right)^2}{\left[\frac{7}{a^4}D_{11} + \frac{7}{b^4}D_{22} + \frac{4}{a^2b^2}(D_{12}+2D_{66})\right]} \tag{4.26-f}$$

The deformed shaped in Mathematica® for a UDL load can be obtained as shown in Figure (4.23). In this analysis a 60"×60" (1524×1524mm) plate with the equivalent deck properties was modeled. The UDL is represented by a 100 kips (444.5 kN) force uniformly distributed over a 60"×60" area. The results from FEA were obtained using SHELL 93 with the thickness of 6.75" (171.5mm). The longitudinal direction is defined as the direction with larger bending stiffness and the transverse direction is the direction with smaller bending stiffness. The 1-parameter Rayleigh-Ritz formulation gives very good bending predictions in longitudinal direction compared to FEA (see Figure 4.24). As shown in Figure (4.25), the transverse deflections at the clamped boundaries do not mach very well. Because the deck is relatively thick (6.75" compare to its 60" length and width), and the transverse direction is the compliant direction, CLPT could not accurately model the plate behavior at the regions close to the clamped edges in this direction. A higher order plate theory or more parameters and terms in the Rayleigh-Ritz formulation may give a closer prediction. However, the 1-parameter Rayleigh-Ritz formulation does give very good maximum deflection prediction compared to FEA with 3% difference.

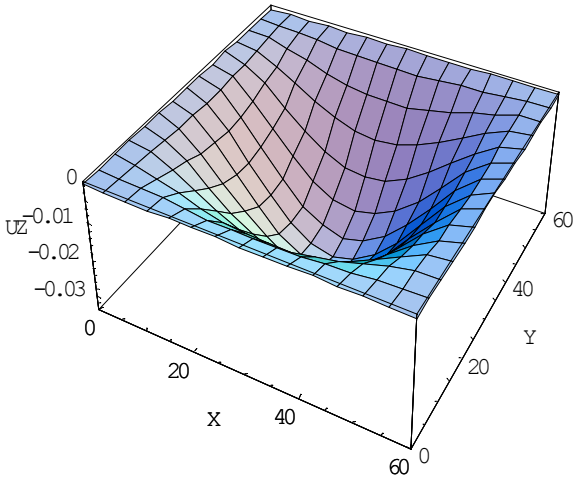


**Figure 4.23** Deformed shape of a CCCC plate under UDL

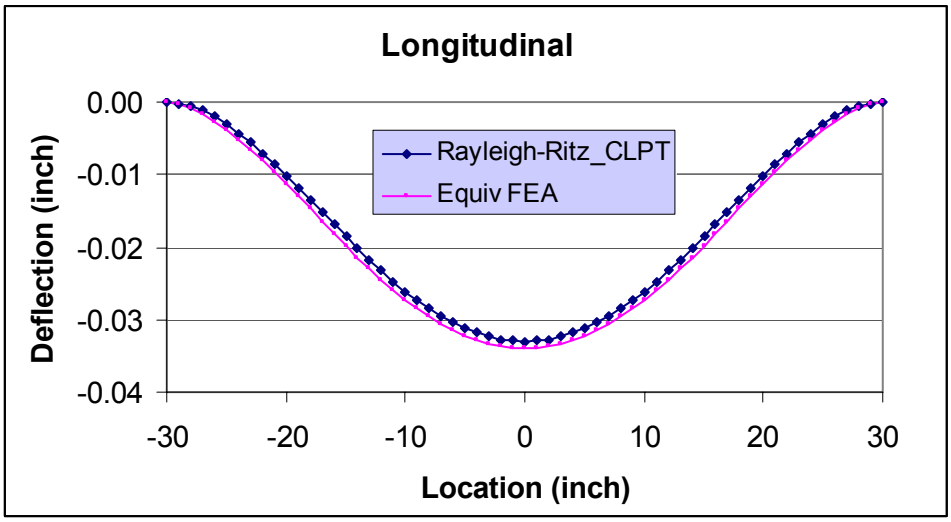


**Figure 4.24** Longitudinal deflection of a CCCC plate under UDL

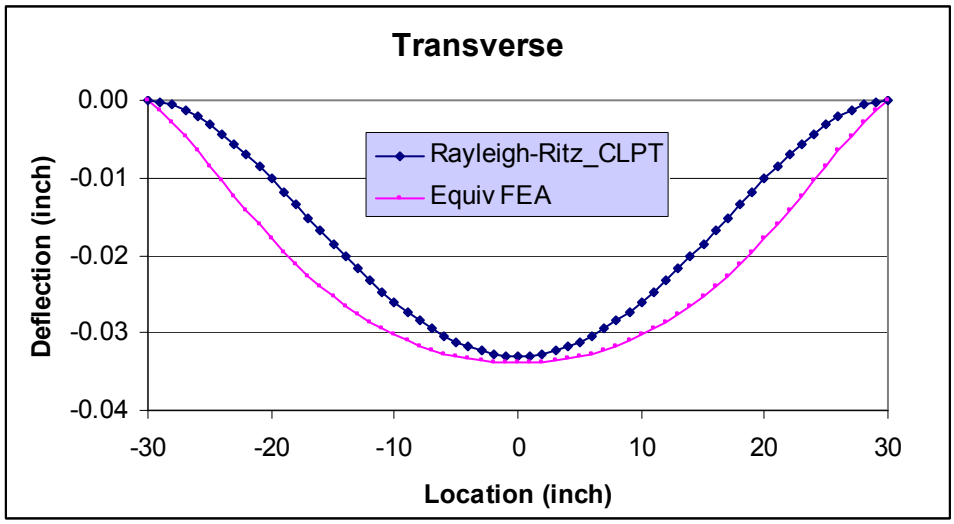


**Figure 4.25** Transverse deflection of a CCCC plate under UDL

### *4.1.3.2 CCFF Plate*

The boundary conditions for a CCFF plate are

(i) At the clamped edges $x = 0, a$: $w_0 = 0$, and $\dfrac{\partial w_0}{\partial x} = 0$

(ii) At free edges $y = 0, b$: $M_{yy}(x,0) = 0$, $M_{yy}(x,b) = 0$, and $N_{yy}(x,0) + \dfrac{\partial M_{xy}(x,0)}{\partial x} = 0$,

$N_{yy}(x,b) + \dfrac{\partial M_{xy}(x,b)}{\partial x} = 0$.

The following polynomials satisfy the essential boundary conditions for a CCFF plate

$$X_i(x) = \left(\frac{x}{a}\right)^{i+1}\left(1-\frac{x}{a}\right)^2; \text{ and } Y_j(y) = \left(\frac{y}{b}\right)^{i-1} \tag{4.27}$$

In (27), $i, j \geq 2$. For example, we choose the following 1-parameter Rayleigh-Ritz approximation for the problem: $X_1(x) = \left(\dfrac{x}{a}\right)^2\left(1-\dfrac{x}{a}\right)^2$; and $Y_1(y) = \left(\dfrac{y}{b}\right)^0$. We have $C_{11} = \dfrac{a^4 Q_0}{24 D_{11}}$, with the following 3-D deformed plot (Figure 4.26):

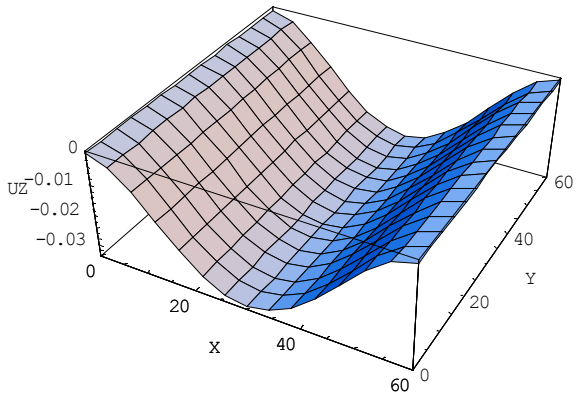


**Figure 4.26** Deformed shape of a CCFF plate under UDL

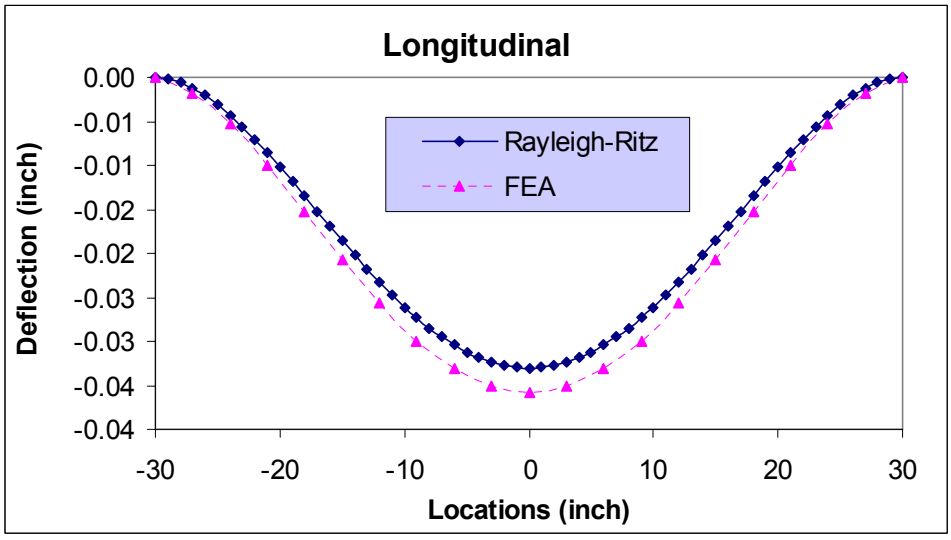


**Figure 4.27** Transverse deflection comparison for a CCFF plate under UDL

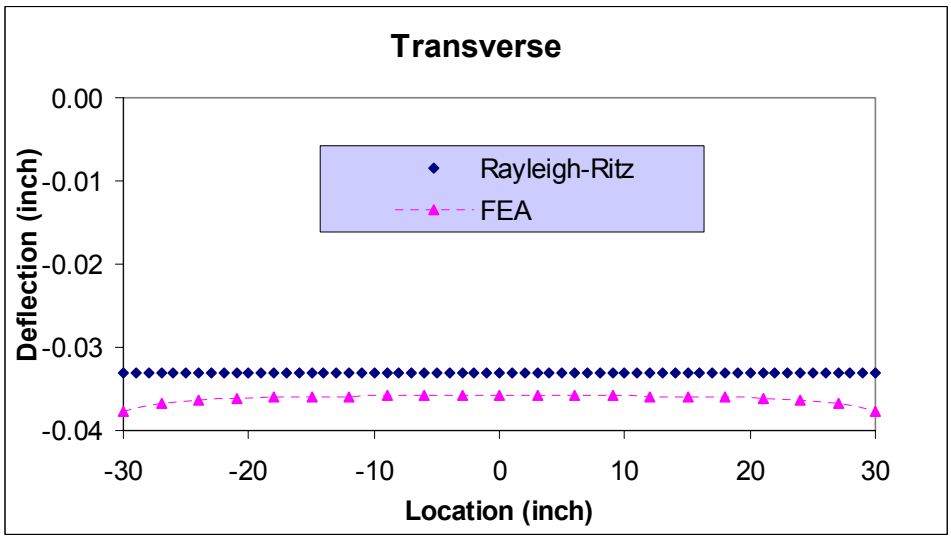


**Figure 4.28** Longitudinal deflection comparison for a CCFF plate under UDL

The numerical results are shown in Figures 4.27 and 4.28. The 1-parameter Rayleigh-Ritz formulation gives very good bending predictions in both transverse direction (the weak direction) and longitudinal direction compared to FEA. However, edge-loading effects at the free edges could not be predicted by the 1-parameter Rayleigh-Ritz formulation. A higher order plate theory or more parameters and terms in the Rayleigh-Ritz formulation may be required for better prediction.

## 4.2 Discussions

Bridge decks are usually used as continuous plates in practical bridge design and construction. Since we have developed a procedure for obtaining the equivalent plate properties from the bridge deck's components, we can use any available continuous plate analysis methods to investigate the behavior of the continuous FRP bridge decks. Another alternative method to investigate the behavior of continuous bridge decks is to subdivide the continuous deck into several single-span deck section, find the proper boundary conditions for each single-span, and used the single-span analysis method developed in this chapter to conduct the analysis of the continuous deck. For an FRP deck supported by close stringers, one should refer to the analysis developed by Salim and Davalos et al [1997, 1999], Brown [1998], and Qiao et al [2000].

The procedures presented in the previous section were developed with the assumption that the deck is located on the stiff foundation. In reality, the deck's support could be a transverse or longitudinal girder, or a foundation that not stiff enough so that the foundation's deformation cannot be neglected in the analysis. While in most cases, the specific foundation behavior is complicated and hard to model, most researchers used elastic foundation models to consider the foundation's effects on the behavior of bridge decks on its. After obtaining the equivalent plate properties of the FRP deck system, one can apply any possible elastic plate on elastic foundation model to analyze the behavior of the deck system. The dynamic behavior can also be investigated after obtaining the equivalent plate properties of the deck. However, these topics are not the interests of this dissertation.

In practical bridge deck design, a rectangular area (tire contacting area) is usually applied to consider tire effects. For an SSSS deck, a solution to this case is provided in section 4.1.1. However, for a Levy plate, it is challenging to expand the loading on a rectangular area. From Eq. (4.14-a) and (4.14-b), a Levy solution only expand a loading in one direction (say X direction). For point load, the expansion coefficient $q_n = \frac{2Q_0}{b} \cdot \sin\frac{n\pi y_0}{b} \cdot \delta(x - x_0)$, $n = 1,2,3,\ldots$. has singularity at the loading point (the Delta function), which brings mathematical difficulties.

However, because of the demanding practical applications in deck design, it will be valuable to obtain analytical solutions for rectangular patch loading and point loading for a Levy plate.

## 4.3 Stiffness Analysis and Design For FRP Bridge Decks

In analyzing a multi-cellular FRP deck, we first obtain the equivalent plate properties through its components, and then apply appropriate loading and boundary conditions to obtain maximum deflection. The calculated maximum deflection is then compared with design criteria (or Deflection Index), or with tested results.

For FRP deck design, one can follow these procedures to conduct initial stiffness design and analysis: 1.) Specify Deflection Index for a deck design according to design criteria and obtain maximum deflection of the designed deck system; 2.) Figure out appropriate loading and boundary conditions for the design for the deck system; 3.) Choose stiffness properties to calculate maximum deflection for all possible design loads until the deflection criteria is satisfied (using procedures in Chapter IV); 4.) Select FRP components and calculate equivalent plate stiffness properties to satisfy the target properties in step (3) (using the method in Chapter III, but in reverse procedure). If necessary, conduct complete FEA or lab testing to verify the design.

Flexural members of bridge structures shall be designed to have adequate stiffness to limit deflections or any deformations that may adversely affect the strength or serviceability of the structure at service load. The following recommendations are made for stiffness analysis and design for mid-span decks (10-20 ft, or 3048mm-6096mm): A.) The bending behavior of the deck should be studied as a plate instead of a beam. B.) In calculation of equivalent global deck properties, the effects of fastener holes can be neglected to simplify the analysis procedure without losing much accuracy. C.) Except for SSFF or CCFF cases, span length specification and deflection limits should be specified in two directions. Also, it is preferred to obtain both the longitudinal and transverse stiffnesses from testing. D.) The tire contacting area effects maximum deflection both in testing and analysis. E.) For better understanding of the local bending behavior of the thin-walled deck system, a complete FEA modeling is preferred.

# CHAPTER V

# STRENGTH AND FAILURE OF FRP COMPOSITE BRIDGE DECKS

Previous research showed that FRP bridge decks possess extremely high levels of strength with the levels of designed stiffness comparable to the required range for reinforced concrete decks. Therefore, many FRP bridge deck designers used deflection limit design criteria when designing FRP bridge decks. However, even with the deflection limit satisfied, there are many issues related to the strength of FRP decks that need to be considered when designing FRP decks. For example, testing results showed that the failure of the deck is highly localized for thin-walled FRP deck components, and the components' failure modes and failure mechanisms as well as ultimate strength will vary depending on the contacting element used in the testing. In addition, practical applications indicated that the fatigue cracking of FRP decks at the deck's free edges is a major damage mode under real field traffic loading conditions. Test results also showed that the delamination of FRP components is an important damage mode for adhesively bonded FRP bridge deck systems. All these issued indicate that the investigation of strength characteristics is critical in designing and analyzing FRP bridge decks. When addressing the strength of FRP decks, we need to keep these questions in mind:

a. How will we describe the strength of an FRP deck system? How will we obtain these values?

b. What are the possible failure/damage modes in adhesively bonded pultrusions? How will the different failure modes influence the ultimate strength?

c. Do the loading conditions (and also deck's boundary conditions) affect its strength and damage modes?
d. How would one go about developing a failure analysis for a bridge deck system made from laminated FRP composites?

This chapter attempts to address the above questions for adhesively bonded pultrusions. We will define local damage modes of FRP decks, discuss possible failure modes of thin-walled, multi-cellular FRP decks and explore the failure modes and failure mechanisms of the thin-walled cellular FRP bridge decks by testing and numerical analysis. We will also provide a systematic analysis procedure to investigate the strength characteristics of FRP decks.

## 5.1 Strength of an FRP deck system

The strength of a material is the material's state of being strong, or its ability to resist the applied loads before failure, or the amount of mechanical force to break it. However, it is not this quite simple for an FRP composite bridge deck system. Research has shown that the strength of FRP composite materials changes with the load history, i.e., the internal stress state and material state of the component. Therefore, FRP deck strength requires long-term investigation. However, because of the lack of long-term data for the failure of FRP bridge decks at the present time, the strength characteristic analysis and failure analysis will be primarily conducted for static or quasi-static loadings in this research.

The *failure function method* was developed as a common engineering method for proper strength description of the material. In this method, a scalar failure function $F_a = F_a(\sigma_{ij} / X_{ij})$ is defined, where $0 \le F_a \le 1$, with $F_a = 1$ defining failure, $\sigma_{ij}$ denoting applied stress, and $X_{ij}$ denoting material strength, $i, j$ are material direction indicators. For unidirectional continuous FRP composite materials, a simple choice may be to compare the stresses in the composite directions and through thickness direction to their respective strengths. Since FRP composite structures are generally anisotropic and inhomogeneous, their inner stress state is very

complicated even when a simple stress state is applied at the global level. The strength of FRP composite materials cannot be simply identified as a single stress level that cause the failure. It is known that the axial, transverse, vertical and shear failures did not independently occur in a general FRP composite structure. In fact, a simple stress applied in only one direction at the global level will result in a complex stress state at the local level, and the axial, transverse, vertical and shear failures interact. For this reason, failure functions considering complex combination of local stresses were developed for FRP composites. These functions were usually applied for each ply of the FRP composite. *Ply failure* analysis is a more typical method to investigate the strength of laminated FRP composite structures. The global failure can be defined by the failure of the critical element in a structure [Reifsnider and Case, 2002]. The scale of the critical element can be determined from the region of influence of the local process that determines final failure at the global level, such as the fiber-matrix level, the ply level, the sub-laminate level, and structural level etc.

Obviously, the answer to the question "how strong is this bridge deck" requires the definition of deck damage modes, since the amount of the mechanical load (force or stress) failing the deck depends on how we define the failure state. In our research, we define *failure* as *separation* of bridge deck components. This separation may occur between the deck's two structural components, within its components, or cross several components or even the entire deck system. According to this definition, an FRP composite bridge deck may have the following modes of failure: debonding between two components; cracking or breaking within a component; delamination within a component; and cracking (or breaking) across several components, or the whole deck. The bridge deck strength investigated in this research is *the deck's ability to resist separation* (including debonding, cracking, or delamination), which can be described as the mechanical load (force or stress) to separate (debond, crack, or delaminate) the deck components.

At this point, we are confronted with another question: How do we set the degree or level of separation so that the deck can be defined as failed? As we know, fiber fracture, flaws and micro-cracks always exist in an FRP composite material produced in the material's processing stage. These flaws and micro-cracks also separate the material, however, their existence does

not necessarily mean failure of the material or the structure. Therefore, we need to propose a degree (or level) of separation within the deck – when the separation approaches a proposed degree (or level), the deck will define failure. With the above definition and explanation, the deck strength can be obtained when defining the mechanical load (force or stress) that separates the deck or deck components. For example, if debonding (delamination) of deck components decreases the stiffness of the deck system so that the initially (deflection limit) designed lowest stiffness is approached, this state can be defined as the failure of the deck, and the load (static, dynamic, or fatigue loads) to generate the debonding (delamination) area may be reported as the strength of the deck. Another example is that: when we observe large cracks in the deck system, which may cause the break-down of the deck, we will define this state as deck failure, and the load (static, dynamic, or fatigue loads) to generate the cracks will be reported as the strength of the deck. Or when the deck is locally broken, punched or crashed (or any other local failure), and this local failure makes the deck to be structurally inefficient and to be replaced, the load (again static, dynamic, or fatigue loads) causes this local failure will be reported as the strength of the deck.

The question for us now is "How many parameters are needed to describe the strength characteristics of an FRP bridge deck?" The strength analysis and failure analysis of FRP decks can be conducted at the ply level, or even fiber-matrix level. However, when conducting strength testing and failure testing in the laboratory or field, the ply level and fiber-matrix level strength and failure testing for a whole FRP deck system is impractical. It's the author's belief that component or global level performance specifications of FRP bridge decks would be practical and easily implemented to ensure the design, safety and serviceability of these decks. Noticing that our deck system is an orthotropic system, we assume that the final deck failure is caused by the individual or the combination of longitudinal, transverse, vertical and shear failures of its components. Therefore, the strength of the deck system will be described by longitudinal strength, transverse strength, vertical strength and shear strength, at the component level or the global deck level. Using the failure function method, we define a failure function at component or global deck level as [Reifsnider and Case, 2002]:

$$F_a = F_a(\frac{\sigma_{ij}}{X_{ij}}) = k_1 \frac{\sigma_{11}}{X_{11}} + k_2 \frac{\sigma_{22}}{X_{22}} + k_3 \frac{\sigma_{33}}{X_{33}} + \zeta_1 \frac{\tau_{12}}{S_{12}} + \zeta_2 \frac{\tau_{13}}{S_{13}} + \zeta_3 \frac{\tau_{23}}{S_{23}} \quad (5.1)$$

where $0 \le F_a \le 1$, with $F_a = 1$ defining deck failure; $\sigma_{ii}$, $i = 1,2,3$ denote applied stress in 1, 2 and 3 directions, and $\tau_{ij}$ denote applied shear stress, and $X_{ii}$, $i = 1,2,3$ denote strength in 1, 2, and 3 directions, while and $S_{ij}$ denote shear strength; $k_i$ and $\zeta_i$ ($i = 1,2,3$) are factors, with values from 0 to 1, and $\sum_{i=1}^{3} k_i + \sum_{i=1}^{3} \zeta_i = 1$, indicating the role of applied stresses causing deck failure. All the above parameters at the right hand side of Eq. (1) are at component level or global deck level.

## 5.2 Failure Modes and Failure Mechanisms of Cellular FRP deck systems

### 5.2.1 Laboratory Tested Deck Failure Modes

Two FRP decks were fabricated for this research: one with a 3/8” (0.95cm) thick top plate and a 3/8” (0.95cm) thick bottom plate, as well as a 1/4" (0.635cm) thick wearing surface and 12 transverse steel rods, which is referred as Deck A for simplicity purpose (which is the third generation deck – Deck III); the other with a 1/4” (0.635cm) thick bottom plate, a 1/2" (1.27cm) thick top plate, and 7 steel rods, no wearing surface, which is referred as Deck B (which is actually the fourth generation deck – Deck IV). The transverse rods were used primarily for fabrication purpose. In Deck B, half of the deck has 5 evenly located transverse rods (east), while the other half has only one rod (west). Deck B was also designed to investigate the effects of the number and location of transverse rods on the overall behavior of the deck system. A simulated tire loading patch was specially proposed and designed (see Fig. 2.4 and and section 2.3 for details) for testing Deck B.

Detailed test data for Deck A can be found from Temeles [2001]. During the testing, debonding noise was observed during the loading cycle when the load reached about 55 kips (244.48 kN) the first time. The deck was failed at 107 kips (475.62 kN). At the center, the failure of Deck A was local punching (Figure 5.1-a) right under the steel patch. For the other side of the deck, the loading patch was located at the deck edge of the center of the span. The deck failed at the edge with shearing crack initiating from the underneath of the loading patch (Figure 5.1-b).

(a) (b)

**Figure 5.1** Failure of Deck A using steel loading patch [Temeles, 2001]

The load-deflection curves for Deck B's east span (with 5 transverse rods) and west span (with 1 transverse rod) are shown in Figure 5.2. Where, CE – Central East, NE – North East, SE – South East, CW – Central West, NW – North West, and SW – South West, they are location symbols for deflection gauges. For both spans, debonding noise was observed when the load reached about 55 kips the first time during the 60 kips (266.7 kN) loading cycle. For east span, debonding was also observed even in the last failure loading cycle (Figure 5.2-a). This span failed at 117 kips (520 kN), which is about 10 % higher than Deck A using the steel patch. For west span, the ultimate strength of 137 kips (609 kN) was recorded (Figure 5.2-b). This is 17 % higher than the east span of Deck B and 28 % higher than Deck A's failure at the center. From Figure (5.2-c), it's observed that the West Span is stiffer than the East Span.

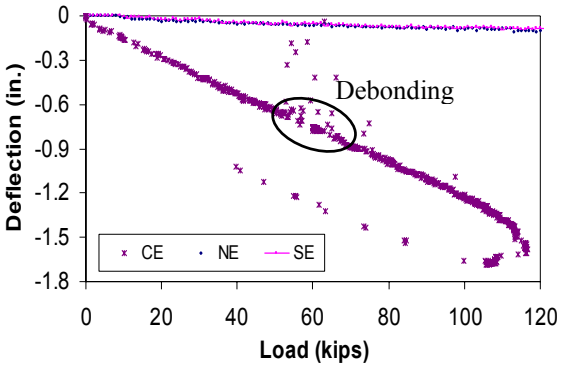


(a) East Span Deflection Gauges

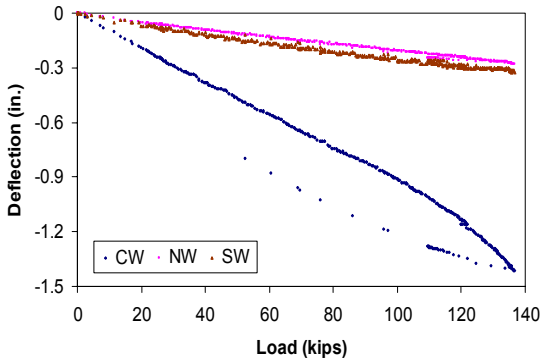


(b) West Span Deflection Gauges

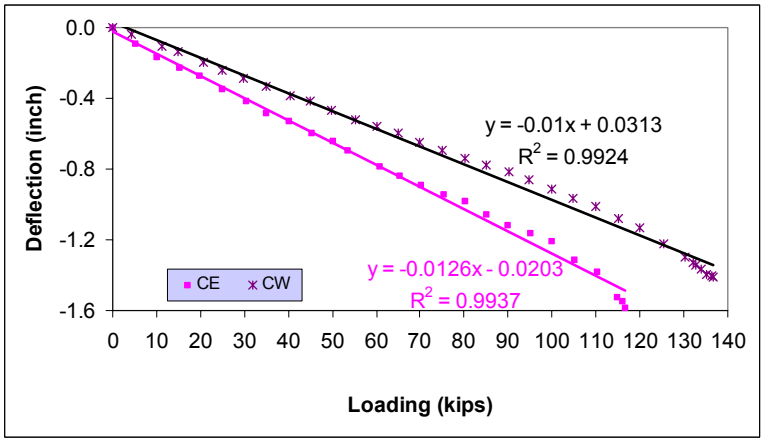


(c) Deflection at the span center for both spans

**Figure 5.2** Deflection-load curves Deck B

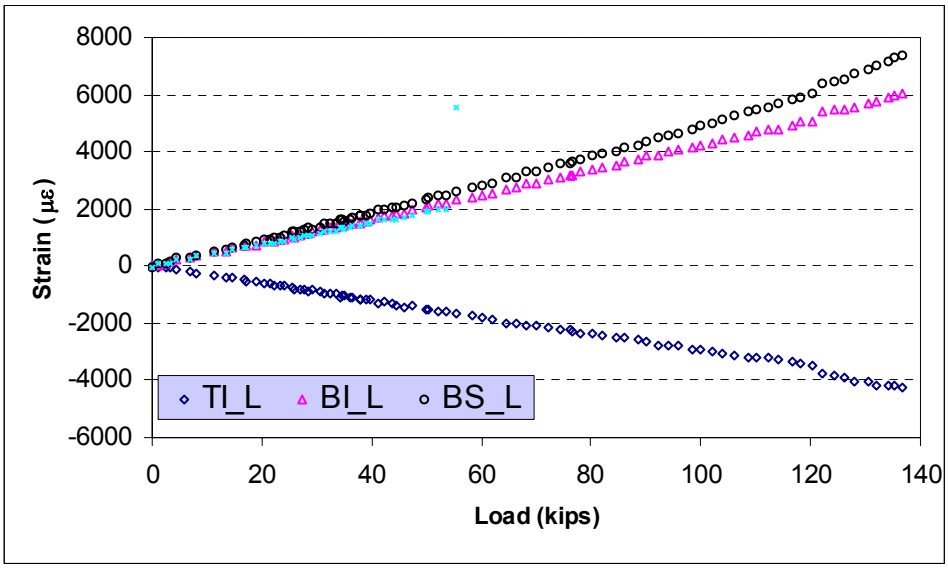


**Figure 5.3** Strains from Central West Gages

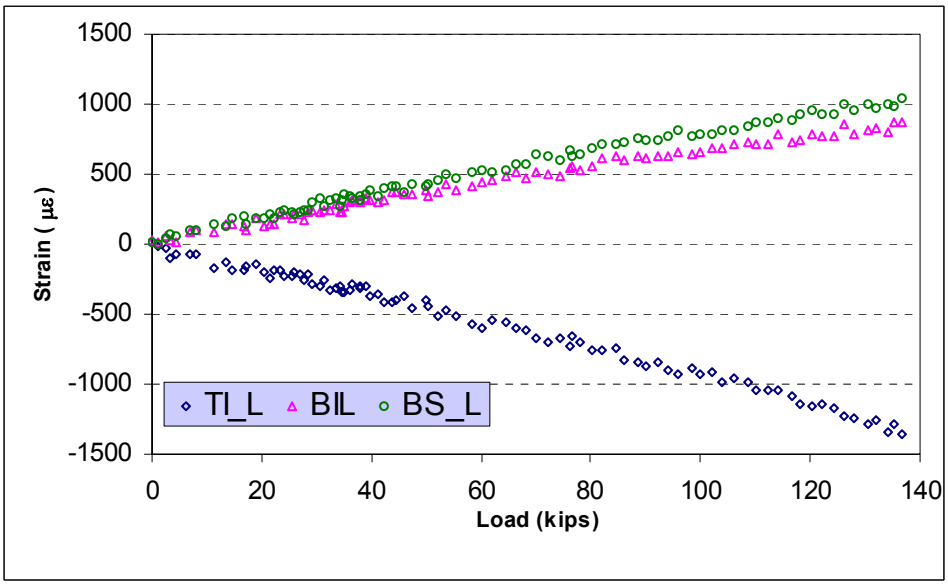


**Figure 5.4** Strains from Northwest Gages

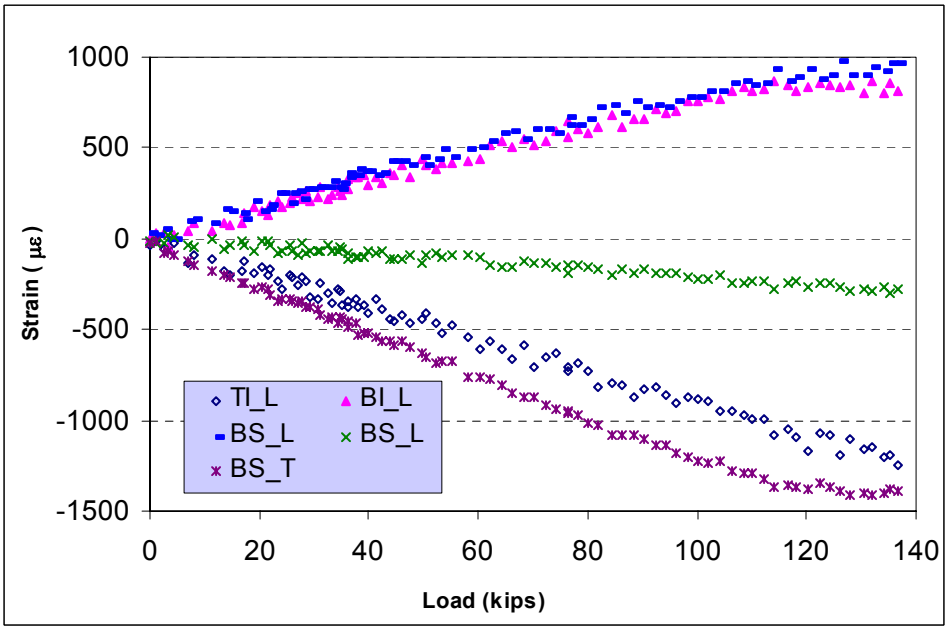


**Figure 5.5** Strains from Southwest Gages

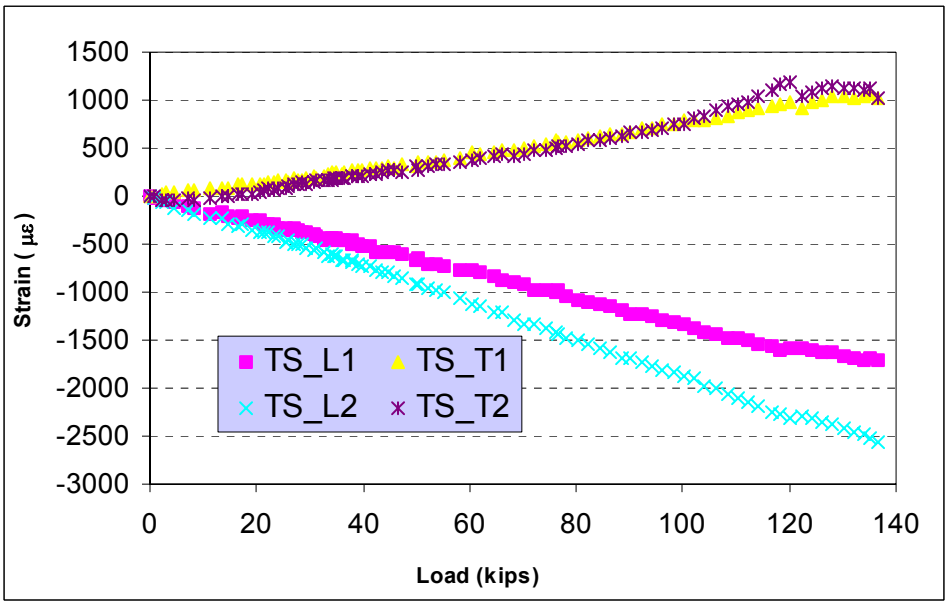


**Figure 5.6** Strains from Southwest Top Plate Gages

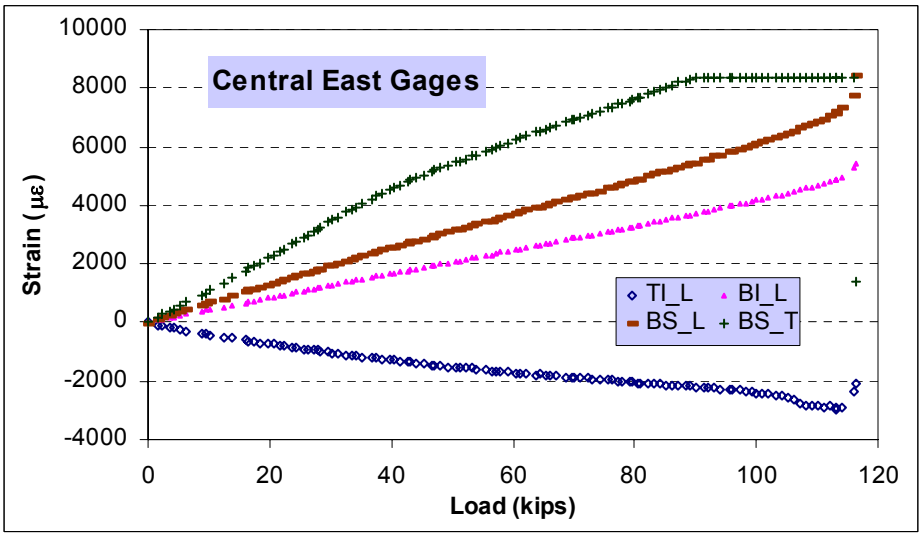


**Figure 5.7** Strains from Central East Gages

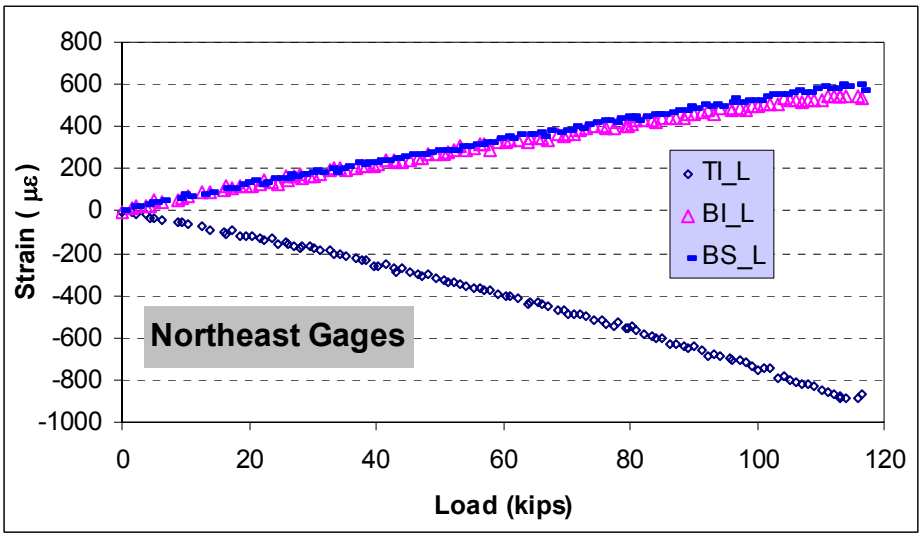


**Figure 5.8** Strains from Northeast Gages

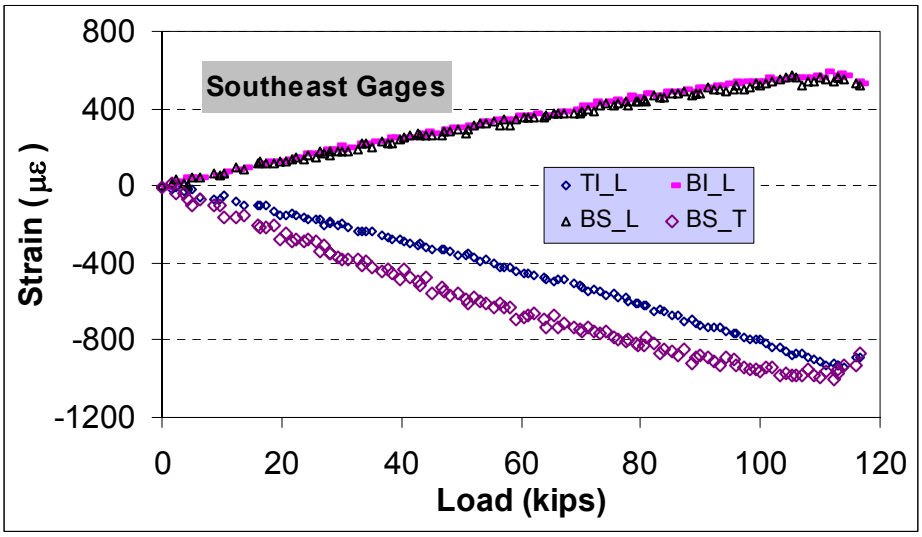


**Figure 5.9** Strains from Southeast Strain gages

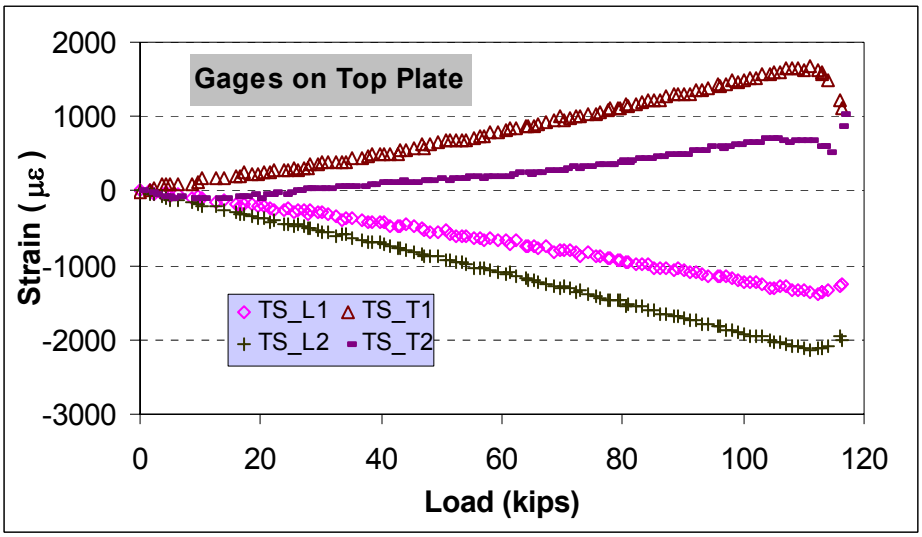


**Figure 5.10** Strains from Southeast Top plate Strain gages

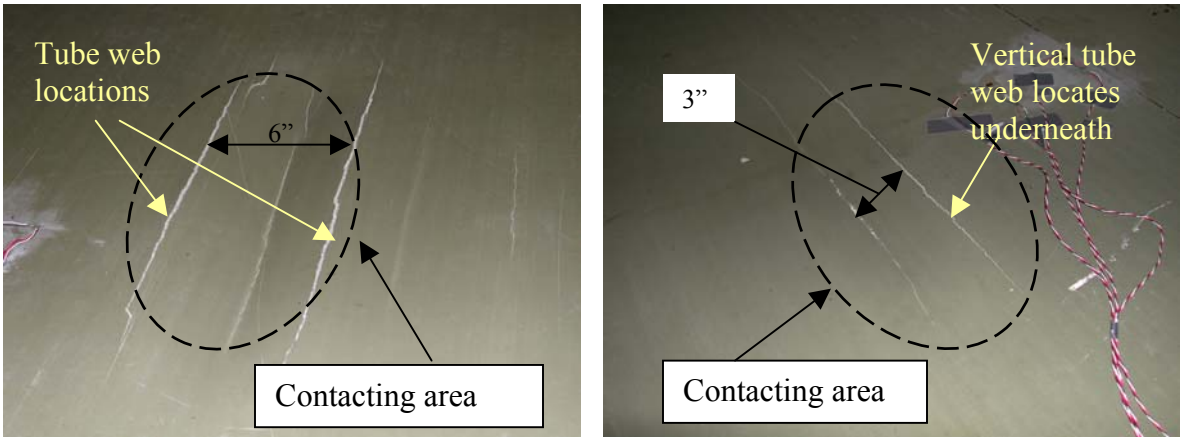


(a) Surface failure-east span (b) Surface failure-west span

**Figure 5.11** Surface failure of Deck B using real tire patches

As shown in Figure 5.11, the failure of Deck B at the span center was not punching shear as was observed in Deck A, but bending failure of the top plate. The space between two cracks is

about 3" (76mm). In Figure (5.11-a), the location of the central crack is about the center of the 6" (152.4mm) space of the tube's top flange. In Figure (5.11-b), the west span also failed as surface carking. For both spans, the failure areas were highly localized and right under the tire patch – deck contacting area.

Figure 5.12 shows the failure of Deck B's internal tubes of east span and west span. For both spans, the top flange of the tube under the tire patch contacting area was failure in bending, with the central opening cracking at the flange. Also observed was the cracking of tube webs in east span (Figure 5.12-a). The east span has 5 evenly transverse rods. The cracking of these tube webs showed that the holes in the webs holding these rods reduced the tube webs' resistance to bearing stress. No cracking was observed on the tube webs in west span (Figure 5.12-b), in which only 1 transverse rod was used in the center of the span.

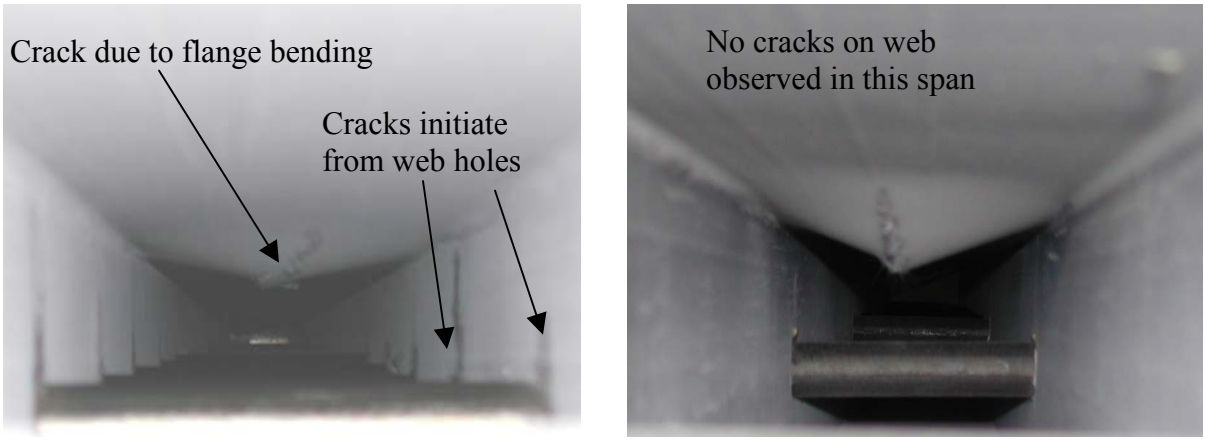


(a) Internal tube failure-east span (b) Internal tube failure-west span

**Figure 5.12** Internal tube failure of Deck B using real tire patches

Under real tire loading conditions, no punching shear was observed. The deck components, top plate and the top flange of the tube, were failed in bending, with transverse direction separation.

The failure tests revealed that, for a soft contacting entity like rubber, the failure of this thin-walled FRP deck is primarily controlled by the $k_2$ term (the weak direction, $k_2 = 1$) in Eq. 5.1, which means the transverse tensile strength of the deck components controls the local deck strength. Written in equation form, the deck failure function for the deck under soft contacting loading patch can be presented as

$$F_a^{soft} \cong \frac{\sigma_{22}}{X_{22}} \tag{5.2}$$

For stiff contacting entity like steel, the deck failure is punching shear at the deck center and cracking at the deck's free edge, which indicates that for stiff contacting patch and/or at the free edges, the deck failure function is mainly controlled by $\zeta_2$ and/or $\zeta_3$ terms:

$$F_a^{stiff} \cong \zeta_2 \frac{\tau_{13}}{S_{13}} + \zeta_3 \frac{\tau_{23}}{S_{23}} \tag{5.3}$$

The delamination and debonding failure mode is mainly controlled by $k_3$ term and the out-of-pane share terms. And the failure function can be reduced as:

$$F_a^{\text{delamination}} \cong k_3 \frac{\sigma_{33}}{X_{33}} + \zeta_2 \frac{\tau_{13}}{S_{13}} + \zeta_3 \frac{\tau_{23}}{S_{23}} \tag{5.4}$$

Therefore, the failure function of these thin-walled cellular FRP bridge decks can be reduced for specific loading situations at specific local regions. The reduced failure functions simplify the failure analysis procedures and help us concentrate on specific stresses/strains for different conditions and locations in deck design.

### 5.2.2 Failure Mechanisms Investigation by FEA

To understand the failure mode differences, contacting analyses using FEA were conducted to investigate the deck surface local stress and strain distribution characteristics under steel loading patch and simulated tire patch. A series of 2-D finite element analyses (FEA) for FRP deck cross-sections were conducted using FEA software ANSYS® 6.0 [Zhou et al, 2002].

ANSYS supports both rigid-to-flexible and flexible-to-flexible surface-to-surface contact elements. These contact elements use a "target surface" and a "contact surface" to form a contact pair. The target surface is modeled with target element (TARGE169 for a 2-D target). The contact surface is modeled with contact element. To create a contact pair, assign the same real constant number to both the target and contact elements. For the steel patch, since the patch is contacting with the deck all the time, and there is no contacting area change, no contacting analysis will be necessary. The steel patch can be modeled as completely bonded to the deck surface. The steel patch was modeled as a linear isotropic material using PLANE 82, while the rubber tire patch was modeled as hyper-elastic isotropic using a 2-D hyper-elastic element – PLANE 183, with the Yong's modulus of 409 psi (2820 kPa) and the Poisson's Ratio of 0.4999. A friction factor 0.5 was chosen to consider friction effects. The patch loadings were applied through the controlled displacements, i.e., the maximum displacements obtained through lab testing. The plane strain assumption was made in both models. According to the mechanics of the problem, the rubber tire patch-deck contacting is a surface-to-surface contact after the initial contacting. The contact pair was modeled using two elements: TARGET 169 and CONTA 172.

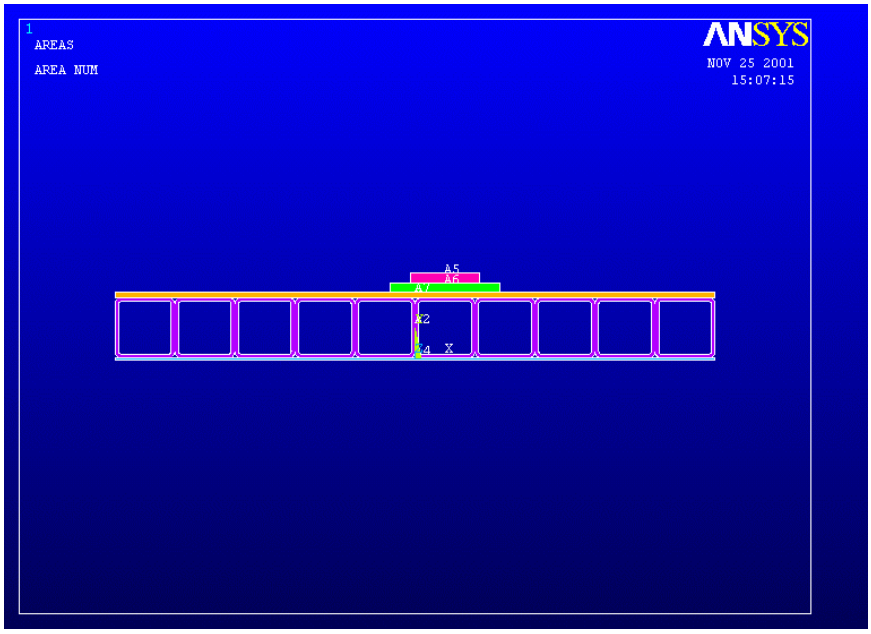


**Figure 5.13** FEA model for cross-section stress analysis under steel patch

The FEA model deck–steel patch analysis is shown in Figure (5.13). In the model, the effects of transverse rods were neglected, since the purpose of this modeling was to investigate the stress distribution of the top plate. Neglecting the rods simplified the analysis. The contour plots of transverse stress (X-stress), vertical stress (Y-stress) and shear stress within the deck cross-section (XY-stress) under steel patch loading are shown in Figure (5.14), (5.15) and (5.16) respectively. It is obvious that there are serious concentrations of transverse stress, vertical stress and shear stress at the edge areas between the top plate and the steel patch. While no serious stress concentration were observed in the middle of the plate-patch contacting area.

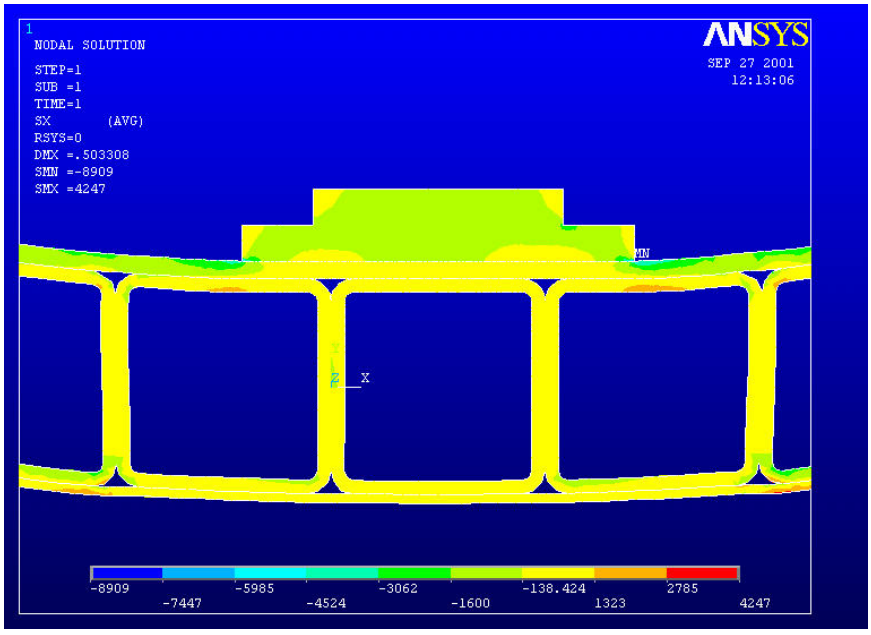


**Figure 5.14** Transverse stress distribution under steel patch (psi)

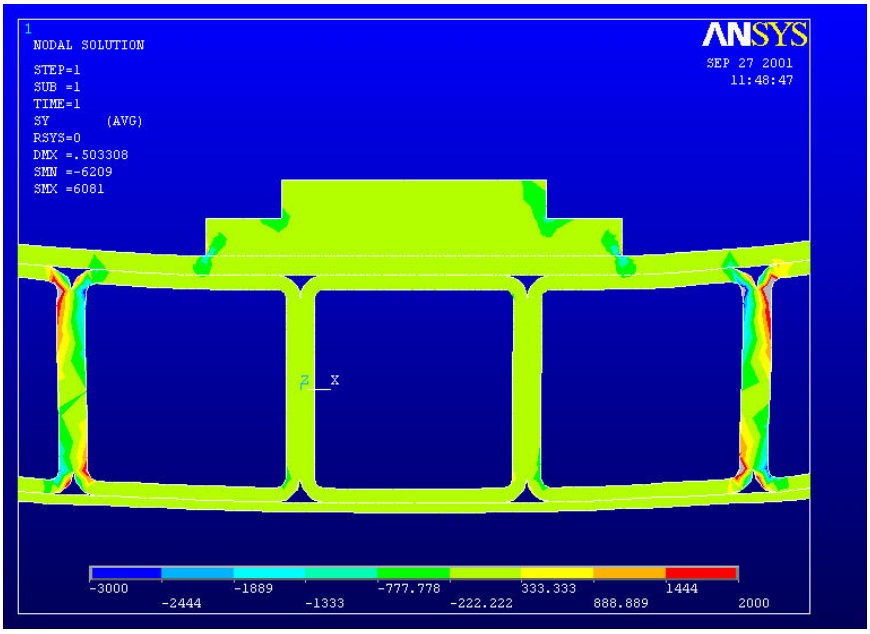


**Figure 5.15** Vertical stress distribution under steel patch (psi)

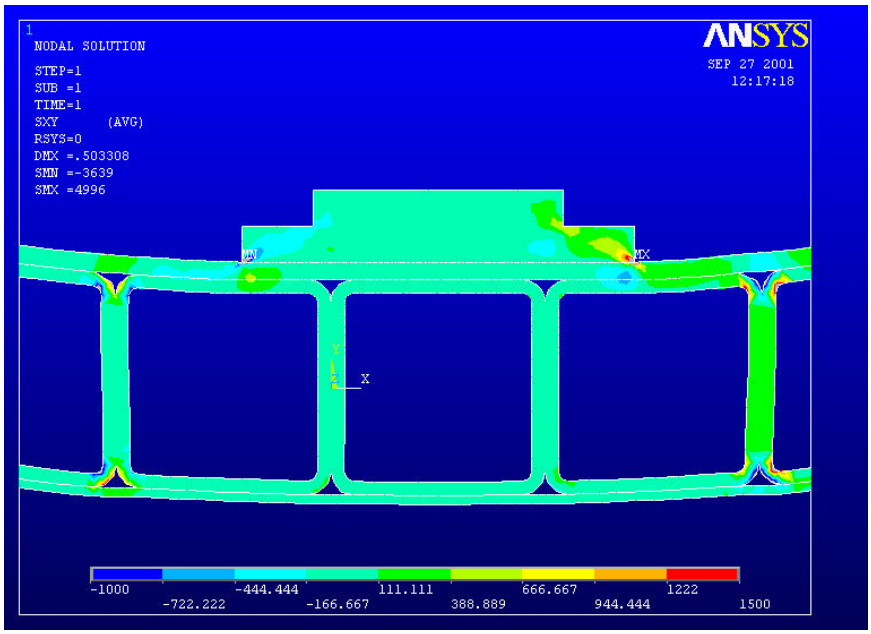


**Figure 5.16** Shear stress distribution under steel patch (psi)

The distribution of normal contacting pressure for the tire patch and the top plate surface is shown in Figure (5.17). This pattern of contacting normal pressure distribution represents a real truck tire normal pressure distribution by some tire researchers [Pottinger and McIntyre, 1999]. Contour plots of the stress distributions of the deck cross-section under tire loading patch are shown in Figures (5.18)-(5.20). Severe transverse stress concentration within the top plate and the top tube flange can be observed from Figure (5.18). The concentration occurred at the central part of the contacting area. Shear stress concentration was also observed in the top plate and the tube's top flange under the contacting area. However, no stress concentration was observed at the contacting edges.

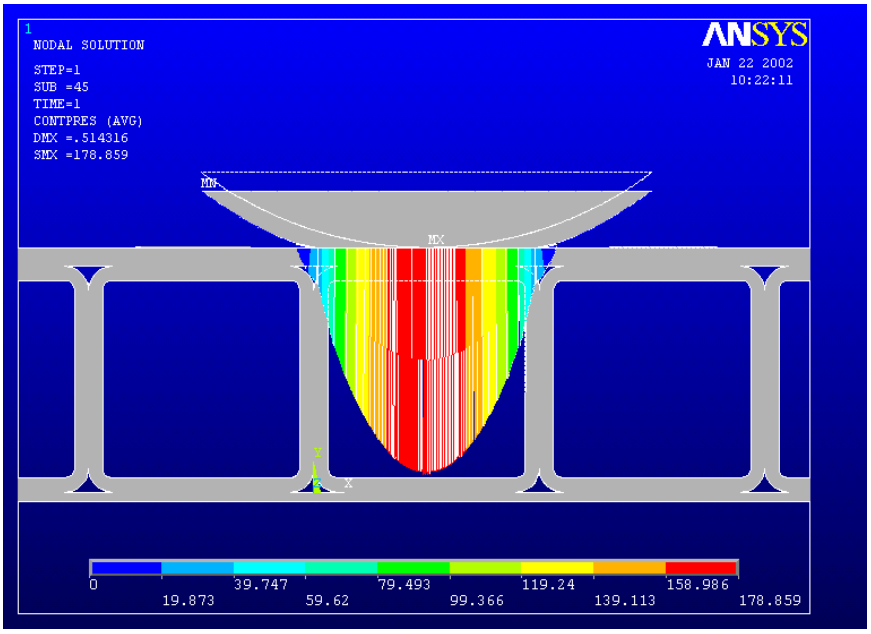


**Figure 5.17** Contacting normal stress distributions (psi)

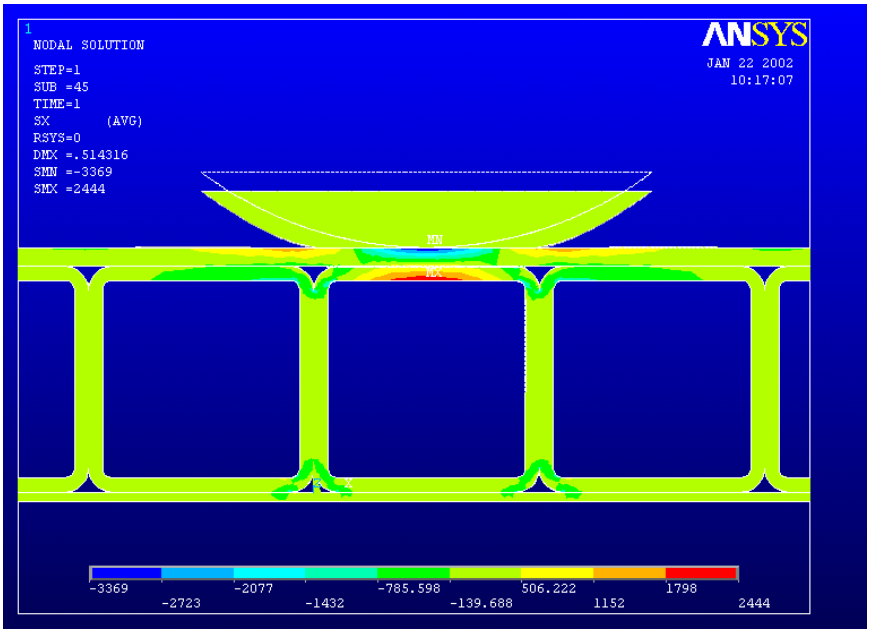


**Figure 5.18** Transverse stress distributions under tire patch (psi)

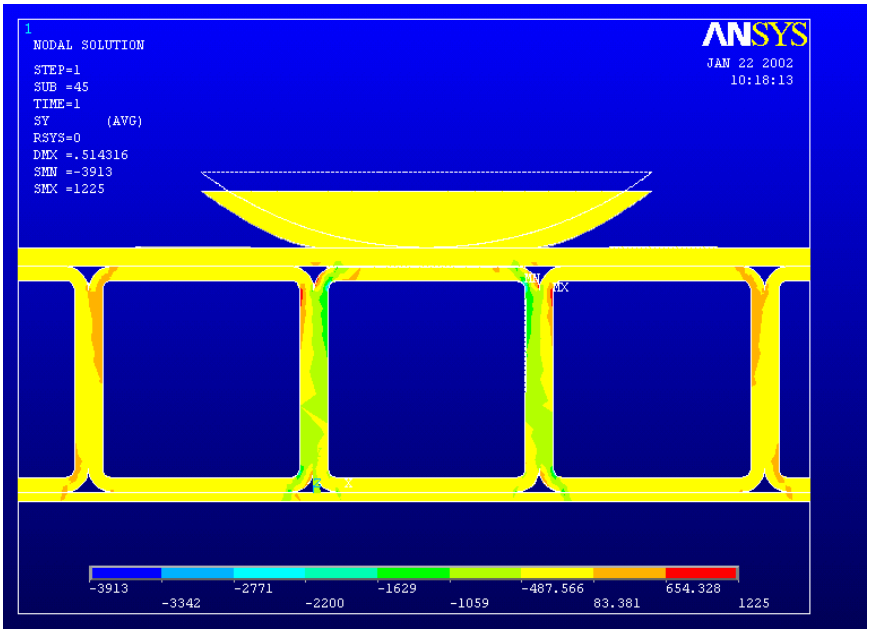


**Figure 5.19** Transverse stress distributions under tire patch (psi)

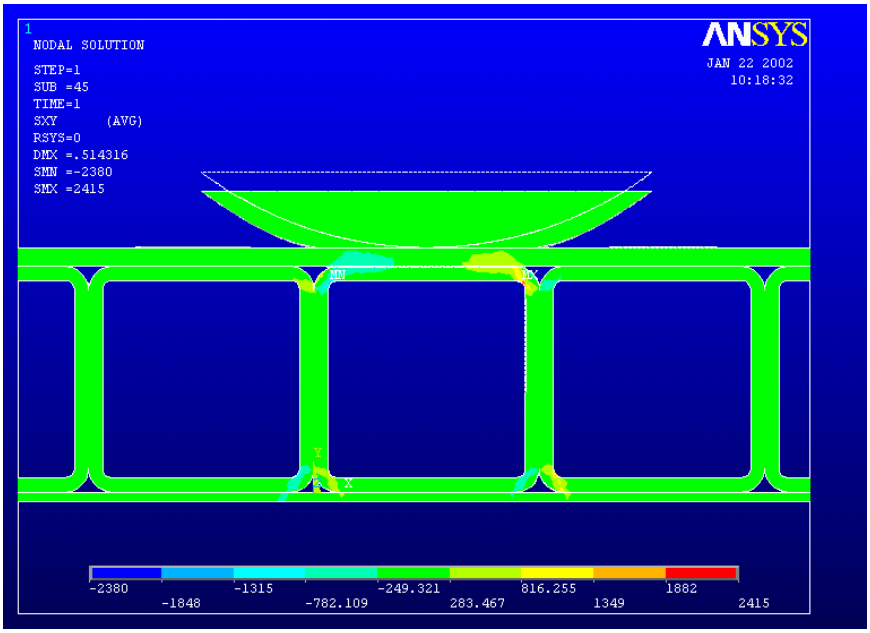


**Figure 5.20** Shear stress distributions under tire patch (psi)

The observations from the above numerical analyses and the foot-prints of normal pressure distributions in Figure 2.3 may provide an explanation of different damage modes at the span center using steel patch and simulated tire patch: In the case of steel patch, the patch was too stiff to deform, which made the transverse stress, vertical stress and the longitudinal-transverse shear stress (and therefore, transverse, vertical and shear strains) dominant around the patch-deck contacting edges before failure. The stress/strain concentration on the edge areas contributed to the punching failure at the span center using steel patch. In the case of simulated tire patch, the patch was very flexible since the patch was made from rubber. The large deformation of the tire patch in the transverse direction and the friction between the tire patch and the deck surface made the transverse stress/strain dominant before failure. The transverse stress and strain concentration contributed to the bending cracking of the top plate. Therefore, the stiffness and deformability of loading patches contributed to the deck's local failure modes.

### 5.2.3 Deck Failure through field testing

A test bed was constructed at Troutsville, Virginia in November, 1999 in-service testing of the FRP deck system [Temeles 2001]. The installed deck is shown in Figure 5.21, with the deck before installation and under service pictures on top right corner and top left corner respectively. The deck was supported by three I beams, and the south and north sides of the deck are free (see "Installing picture in Figure 5.21). The deck was routinely monitored and the data were routinely collected and analyzed at Virginia Tech [Temeles 2001, Coleman 2002].

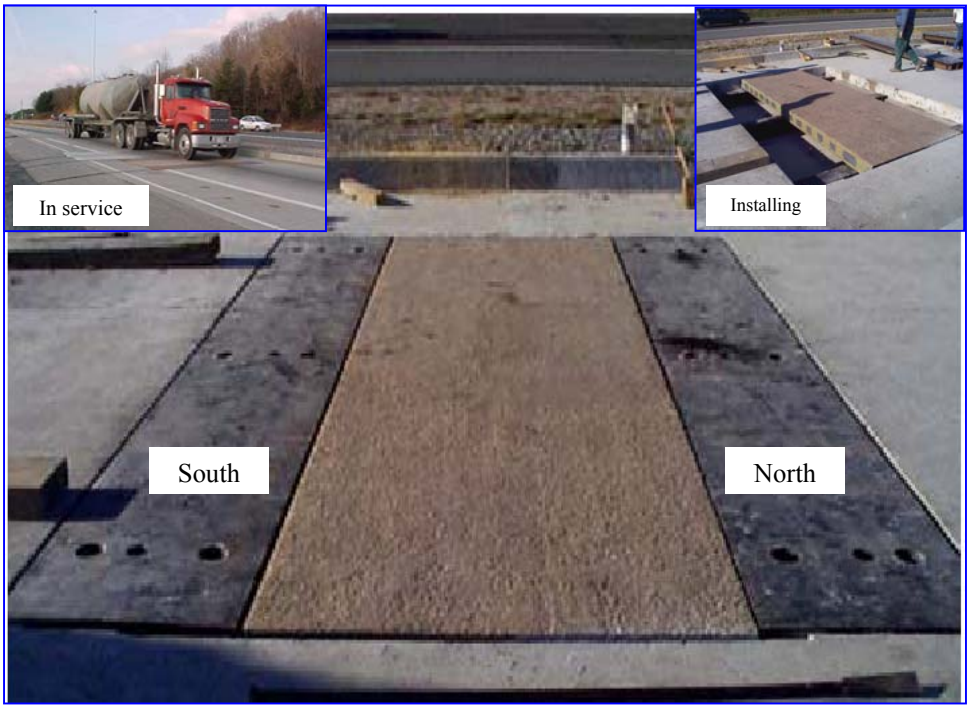


**Figure 5.21** FRP deck testing bed at Troutsville weight station

Initial surface overlay's (polymer concrete) cracking at two free edges, north edge and south edge is shown in Figure 5.22. The heavy red lines are marked cracks. These surface cracks were concentrated over the tube webs (the vertical web), and parallel to the tube running direction.

(a) South edge cracking of the surface overlay

(b) North edge cracking of the surface overlay

**Figure 5.22** Surface overlay cracking at the testing bed's free edges

In June 2002, serious damage of the deck was observed. The surface cracking is shown in Figure 5.23. These cracks are randomly orientated. Severe cracking and damage happened at the free edges. Shown in Figure 5.24 is the cracking of the free edge at the deck's supporting end, with the enlarged view of the damage at the right lower corner. The cracking at the free edge's center is shown in Figure 5.25, and a closer view provided at the right lower corner. The internal tube's web and flange corners were severely damaged and even separated, as can be seen from Figure 5.26. The damage at the free edges told us how little we knew about the behavior of the deck system at the free edges when the deck was initially designed and installed. However, a fast repair was completed, and after repair, the deck was returned to service and was monitored again in July 2002. In this research, a finite element analysis will be conducted using the ply-level composite materials information to make a better understanding of the deck's behavior at the free edges.

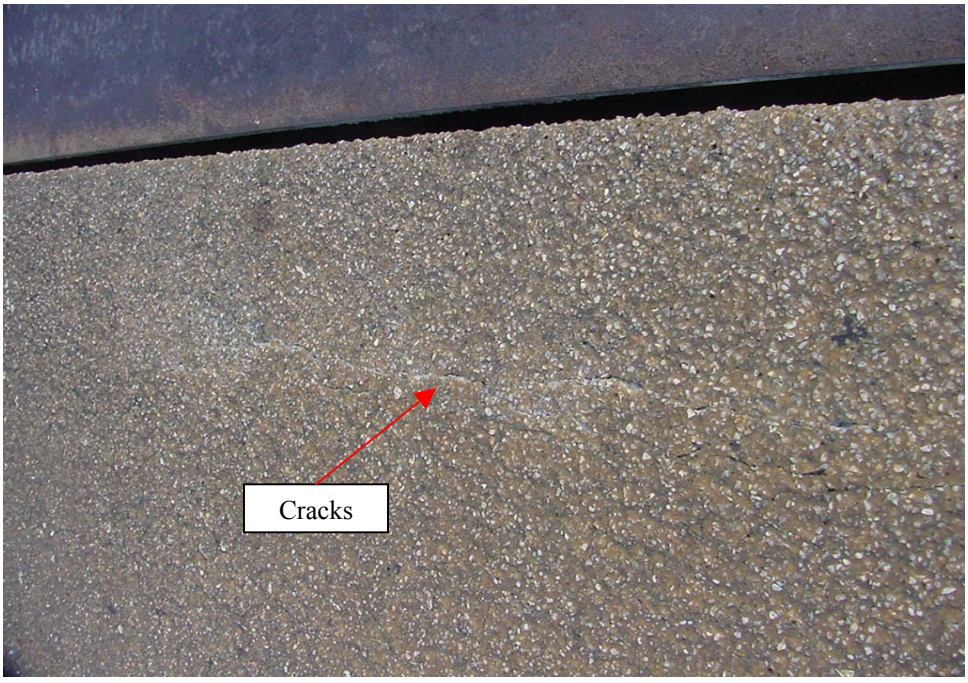


**Figure 5.23** Surface cracks observed in June 2002

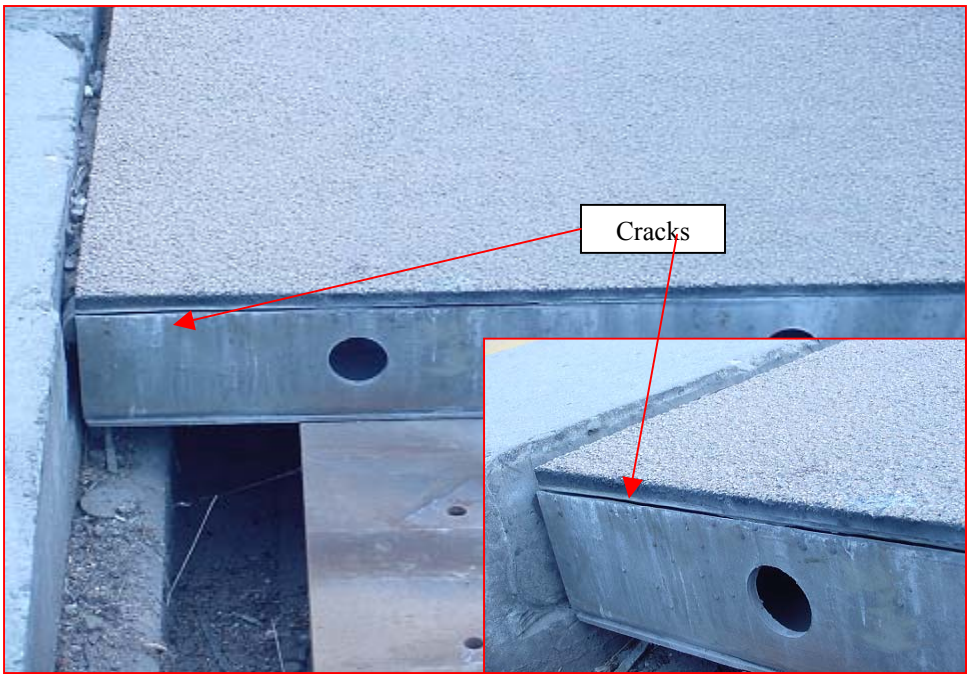


**Figure 5.24** Cracking at the free edges end support

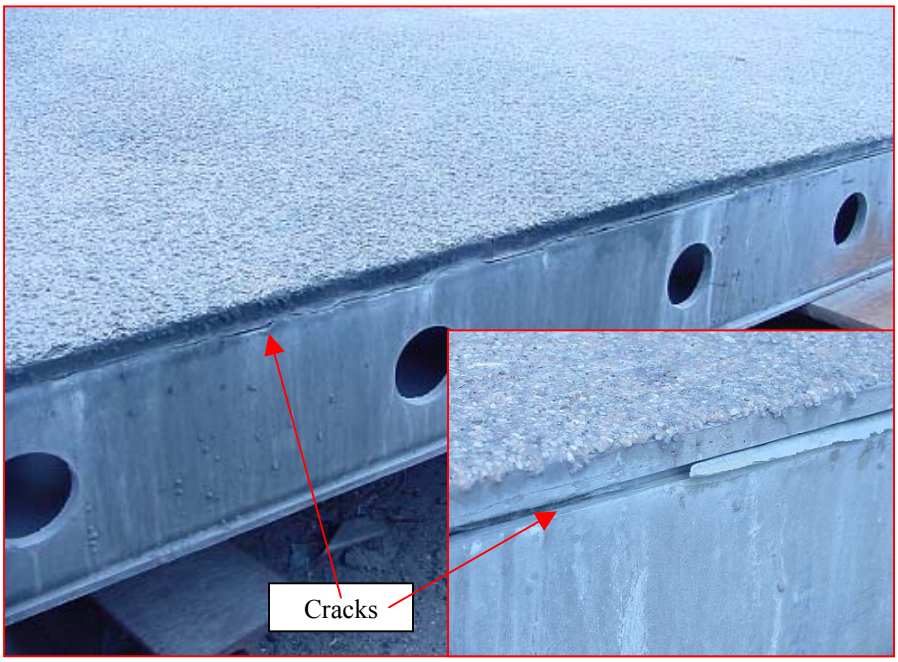


**Figure 5.25** Cracking at the free edge's center

**Figure 5.26** Damage of the internal tubes at the free edges

## 5.3 Strength Analysis Using Ply-level Properties

The philosophy of deck's strength analysis using ply-level information can be explained using the schematic plot in Figure 5.27:

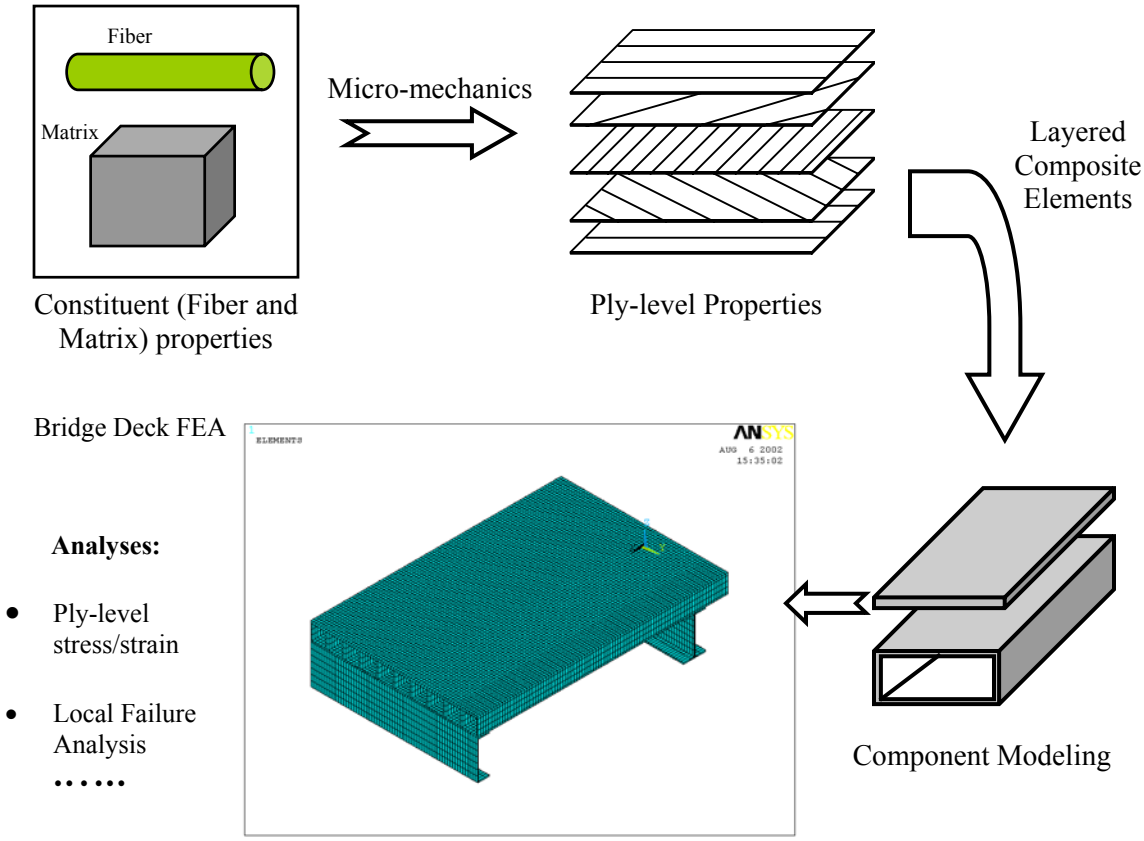


**Figure 5.27** Schematic representation of deck strength analysis philosophy

We start from the micro-mechanics of the FRP laminated composites. First, we need to know the microstructures and material constituents of each deck component. Then, using micro-mechanics models, the ply-level properties can be obtained for each deck component. These ply-level properties are then entered into the deck components FEA models using composite elements, to represent the whole deck system. After specifying appropriate boundary conditions and run the FEA model, the results can then be processed. In post-processing, more accurate

stress and strain analysis, failure analysis and other analysis with ply-level information can be conducted. In the following discussion, we will start with the microstructures of the deck components, using micro-mechanics models to obtain ply-level material properties of the components, then using ANASYS to conduct strength analysis and failure analysis using ply-level information. Using available ply-level strength prediction models and computer codes [Reifsnider & Case 2002, Case & Reifsnider 1999, etc], one can also conduct ply-level strength analysis. Also, there are a number of commercial FEA codes and software, such as GENOA [ASC, 2002], available for ply-level progressive failure analysis. However, these codes require further validation.

A comprehensive failure analysis including all ply-level damage and failure modes for the whole deck system seems impractical at the present time, since there are many undetermined parameters in the deck system, which are required in the models' prediction and analysis. For the deck system we investigate, the separation in the transverse direction is the most likely failure mode under real vehicle tire loading at the deck center. The other likely failure mode we observed is cracking at the free edges. Therefore, we are interested in investigating two cases: behavior of the deck system when loaded at the deck center and the behavior of the free (unsupported) edges.

### 5.3.1 Microstructures and Ply-level Properties for Deck Strength Analysis

The bridge deck's FRP components consist of A-glass and E-glass mats and roving. The E-glass roving, continuous E-glass mat were used as the reinforcements for these shapes. A-glass mat was also used outside of the shapes for corrosion resistance. Both E-glass and A-glass mats have randomly located fibers.

The 6"×6"×3/8" (152.4×152.4×9.5mm) square tube is made up of standard E-glass and A -glass. The structural mat and roving is E - glass. The mats toward the inside and outside are A-glass strand mats for the corrosion properties. All of the roving used is 113 yards per pound with each taking up 0.0047 $in^2$. The E - glass mat is 2 oz. per square foot and taking up 0.030 inch per

layer. The A - glass mat is 1½ oz. Per $ft^2$ with 0.033 inch. The E-glass roving runs longitudinally, i.e., along with the machine direction. The overall glass fiber volume fraction is 43.26%. The composite has 7 layers with the lay-up as following from inside out (Figure 5.28):

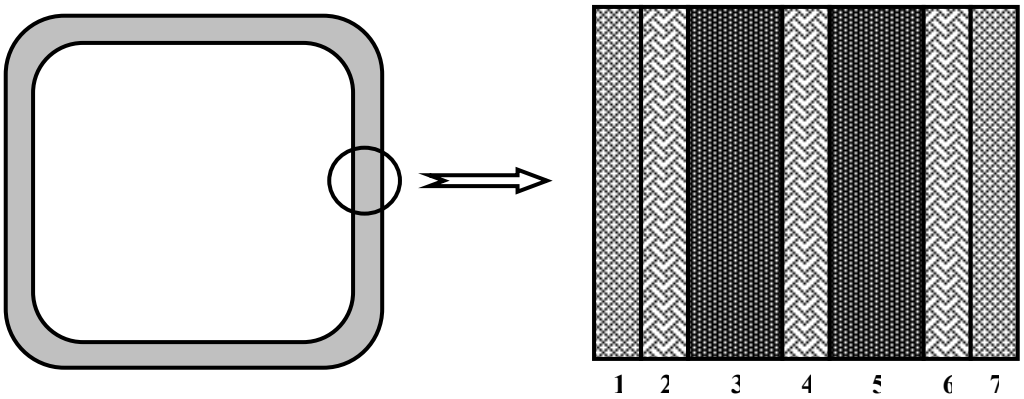


Layer 1: 0.033", 1-½ oz. A-glass mat; Layer 2: 0.03", 2 oz. E-glass mat; Layer 3: 0.109", 460 roving placed; Layer 4: 0.03", 2 oz. E-glass mat; Layer 5: 0.110", 476 roving placed; Layer 6: 0.03", 2 oz. E-glass, Layer 7: 0.033", 1-½ oz. A-glass mat; *Layer 1 and 2 have two 11" mats overlapped; Layer 4 has two 11-7/8" mats overlapped; Layer 6 and 7 have two 13" mats overlapped.*

**Figure 5.28** Microstructure of the 6"×3/8" FRP Square Tube

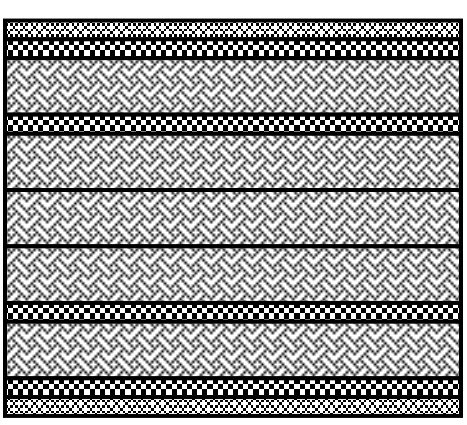


Layer 11: 0.014", ½ oz. A – glass mat
Layer 10: 0.009", roving spaced at 2/in.
Layer 9: 0.037", 2 oz. E - glass mat
Layer 8: 0.009", roving spaced at 2/in.
Layer 7: 0.037", 2 oz. E - glass mat
Layer 6: 0.037", 2 oz. E - glass mat
Layer 5: 0.037", 2 oz. E - glass mat
Layer 4: 0.009", roving spaced at 2/in.
Layer 3: 0.037", 2 oz. E – glass mat
Layer 2: 0.009", roving spaced at 2/in.
Layer 1: 0.014", ½ oz. A - glass mat

**Figure 5.29** Microstructure of the ¼ " thick FRP plate

The ¼" (6.35mm) thick flat plate is 28.72% by volume glass. Each roving is taking 0.005 $in^2$. The 2 oz. E - mat is 0.037" thick and the ½ oz. A - glass is 0.014" thick. This flat rectangular plate has 11 layers of glass fibers. From bottom to top, the fiber reinforcement lay-up is as followings (Figure 5.29):

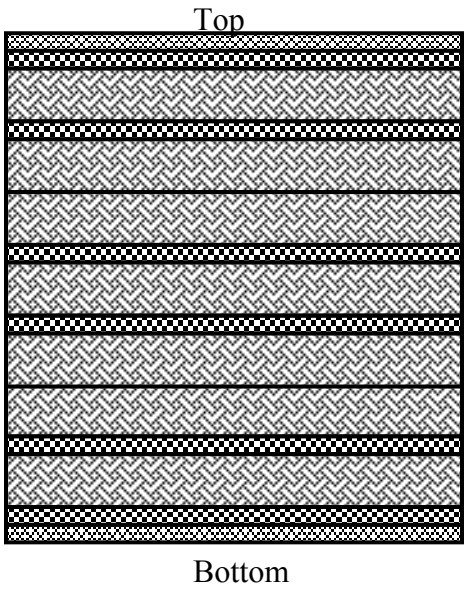


**Figure 5.30** Microstructure of the ½ " thick FRP plate

The ½" (12.7mm) thick flat plate has a overall fiber volume fraction of 29.35%. Each roving is taking 0.005 $in^2$. The 3 oz. E - mat is 0.056" thick and the ½ oz. A - mat is 0.014" thick. This flat rectangular plate has 15 layers of glass fibers. From bottom to top, the fiber reinforcement lay-up is shown in Figure 5.30.

The roving in flat plates runs in the machine direction. The plates were produced 4' (1219.2mm) wide. A 4 ft (1219.2mm) plate and a 1 ft (304.8mm) plate were bonded together to make the 5 feet (1524mm) wide plate for deck panel fabrication. Thus, the actual tensile strength and modulus in the width direction is some lower than the 4 ft (1219.4) pultruded plate. The resin used for the FRP shapes was not a simple resin for the matrix, it was by resin grade with the manufacturer's (Strongwell Corp.) own formulation to include pigments, fire retardants, mold releases, fillers, etc. Different polyester resins from two suppliers, AOC and Ashland

Chemical, were used in these FRP shapes. The application or product desired dictates the choice of resin system. Table 5.1 shows typical properties for Polyester resin used in the FRP shapes. The ply level fiber and resin information for each deck component are presented in Tables (5.2), (5.3) and (5.4).

**TABLE 5.1** Typical properties of the resin used in the FRP shapes

| Property | Polyester Resin |
|---|---|
| Tensile Strength (psi) | 10,500 |
| Tensile Modulus (psi) | 440,000 |
| Flexural Strength (psi) | 19,000 |
| Flexural Modulus (psi) | 480,000 |
| Elongation (%) | 4 |

**TABLE 5.2** Fiber and resin Properties of the Square Tubes

| *Layer* | *Thickness (inch)* | $V_f$ | *Fiber* | $E_f$ *(msi)* | $G_f$ *(msi)* | $\nu_f$ | $\rho$ *(lb/in$^3$)* | $E_m$ *(msi)* | $\nu_m$ |
|---|---|---|---|---|---|---|---|---|---|
| 1 | 0.033 | 0.20 | A mat | 10 | 4.17 | 0.2 | 0.089 | 0.44 | 0.36 |
| 2 | 0.03 | 0.30 | E mat | 10.5 | 4.375 | 0.2 | 0.094 | 0.44 | 0.36 |
| 3 | 0.109 | 0.45 | E rov | 10.5 | 4.375 | 0.2 | 0.094 | 0.44 | 0.36 |
| 4 | 0.03 | 0.30 | E mat | 10.5 | 4.375 | 0.2 | 0.094 | 0.44 | 0.36 |
| 5 | 0.11 | 0.45 | E rov | 10.5 | 4.375 | 0.2 | 0.094 | 0.44 | 0.36 |
| 6 | 0.03 | 0.30 | E mat | 10.5 | 4.375 | 0.2 | 0.094 | 0.44 | 0.36 |
| 7 | 0.033 | 0.20 | A mat | 10.5 | 4.375 | 0.2 | 0.089 | 0.44 | 0.36 |

**TABLE 5.3** Fiber and resin Properties of the ¼" Flat Plate

| *Layer* | *Thickness (inch)* | $V_f$ | *Fiber* | $E_f$ *(msi)* | $G_f$ *(msi)* | $\nu_f$ | $\rho$ *(lb/in$^3$)* | $E_m$ *(msi)* | $\nu_m$ |
|---|---|---|---|---|---|---|---|---|---|
| 1 | 0.014 | 0.16 | A mat | 10 | 4.17 | 0.2 | 0.089 | 0.44 | 0.36 |
| 2 | 0.009 | 0.55 | E rov. | 10.5 | 4.375 | 0.2 | 0.094 | 0.44 | 0.36 |
| 3 | 0.037 | 0.25 | E mat | 10.5 | 4.375 | 0.2 | 0.094 | 0.44 | 0.36 |
| 4 | 0.009 | 0.55 | E rov. | 10.5 | 4.375 | 0.2 | 0.094 | 0.44 | 0.36 |
| 5 | 0.037 | 0.25 | E mat | 10.5 | 4.375 | 0.2 | 0.094 | 0.44 | 0.36 |
| 6 | 0.037 | 0.25 | E mat | 10.5 | 4.375 | 0.2 | 0.094 | 0.44 | 0.36 |
| 7 | 0.037 | 0.25 | E mat | 10.5 | 4.375 | 0.2 | 0.094 | 0.44 | 0.36 |
| 8 | 0.009 | 0.55 | E rov. | 10.5 | 4.375 | 0.2 | 0.094 | 0.44 | 0.36 |
| 9 | 0.037 | 0.25 | E mat | 10.5 | 4.375 | 0.2 | 0.094 | 0.44 | 0.36 |
| 10 | 0.009 | 0.55 | E rov. | 10.5 | 4.375 | 0.2 | 0.094 | 0.44 | 0.36 |
| 11 | 0.014 | 0.16 | A mat | 10 | 4.17 | 0.2 | 0.089 | 0.44 | 0.36 |

**TABLE 5.4** Fiber and resin Properties of the ½" Flat Plate

| *Layer* | *Thickness (inch)* | $V_f$ | *Fiber* | $E_f$ *(msi)* | $G_f$ *(msi)* | $\nu_f$ | $\rho$ *(lb/in$^3$)* | $E_m$ *(msi)* | $\nu_m$ |
|---|---|---|---|---|---|---|---|---|---|
| 1 | 0.014 | 0.16 | A mat | 10 | 4.17 | 0.2 | 0.089 | 0.44 | 0.36 |
| 2 | 0.013 | 0.37 | E rov. | 10.5 | 4.38 | 0.2 | 0.094 | 0.44 | 0.36 |
| 3 | 0.056 | 0.25 | E mat | 10.5 | 4.38 | 0.2 | 0.094 | 0.44 | 0.36 |
| 4 | 0.014 | 0.37 | E rov. | 10.5 | 4.38 | 0.2 | 0.094 | 0.44 | 0.36 |
| 5 | 0.056 | 0.25 | E mat | 10.5 | 4.38 | 0.2 | 0.094 | 0.44 | 0.36 |
| 6 | 0.056 | 0.25 | E mat | 10.5 | 4.38 | 0.2 | 0.094 | 0.44 | 0.36 |
| 7 | 0.014 | 0.37 | E rov. | 10.5 | 4.38 | 0.2 | 0.094 | 0.44 | 0.36 |
| 8 | 0.056 | 0.25 | E mat | 10.5 | 4.38 | 0.2 | 0.094 | 0.44 | 0.36 |
| 9 | 0.014 | 0.37 | E rov. | 10.5 | 4.38 | 0.2 | 0.094 | 0.44 | 0.36 |
| 10 | 0.056 | 0.25 | E mat | 10.5 | 4.38 | 0.2 | 0.094 | 0.44 | 0.36 |
| 11 | 0.056 | 0.25 | E mat | 10.5 | 4.38 | 0.2 | 0.094 | 0.44 | 0.36 |
| 12 | 0.014 | 0.37 | E rov. | 10.5 | 4.38 | 0.2 | 0.094 | 0.44 | 0.36 |
| 13 | 0.056 | 0.25 | E mat | 10.5 | 4.38 | 0.2 | 0.094 | 0.44 | 0.36 |
| 14 | 0.013 | 0.37 | E rov. | 10.5 | 4.38 | 0.2 | 0.094 | 0.44 | 0.36 |
| 15 | 0.014 | 0.16 | A mat | 10 | 4.17 | 0.2 | 0.089 | 0.44 | 0.36 |

### 5.3.2 Ply Level Properties of FRP Shapes

The lamina with glass roving can be considered as a lamina with $0^\circ$ unidirectional continuous fiber. The lamina with randomly oriented and continuous glass mat can be modeled as a randomly oriented fiber lamina. For unidirectional continuous fiber laminae [Mallick 1993, Hyer 1998, Jones 1999]:

The elastic moduli $E_{11}$ and $E_{22}$:

$$E_{11} = E_f \cdot V_f + E_m \cdot V_m \tag{5.6}$$

$$E_{22} = \frac{E_f \cdot E_m}{E_f \cdot V_m + E_m \cdot V_f} \tag{5.7}$$

The shear modulus $G_{12}$:

$$G_{12} = \frac{G_f \cdot G_m}{G_f \cdot V_m + G_m \cdot V_f} \tag{5.8}$$

The major Poisson's ratio:

$$\nu_{12} = \nu_f \cdot V_f + \nu_m \cdot V_m \tag{5.9}$$

where $E_f$, $E_m$ are modulus of the fiber and the matrix respectively, $V_f$, $V_m$ are volume fraction of the fiber and the matrix respectively, $G_f$, $G_m$ are shear modulus of the fiber and the matrix respectively, $\nu_f$, $\nu_m$ are modulus of the fiber and the matrix respectively.

For randomly oriented fiber lamina [Mallick, 1993], the effective Yong's modulus $E_r$, effective shear modulus $G_r$ and the effective Poisson's ratio $\nu_r$ can be obtained as:

$$E_r = \frac{3}{8}E_{11} + \frac{5}{8}E_{22}; \tag{5.10-a}$$

$$G_r = \frac{1}{8}E_{11} + \frac{1}{4}E_{22}; \tag{5.10-b}$$

and

$$\nu_r = \frac{E_r}{2G_r} - 1 \tag{5.10-c}$$

Followings are summaries of calculated material properties for each deck component:

**TABLE 5.5** Ply level properties summary for square tubes

| Layer | Thickness (inch) | $E_{11}$ (msi) | $E_{22}$ (msi) | $G_{12}$ (msi) | $V_{12}$ |
|---|---|---|---|---|---|
| 1 | 0.033 | 1.222 | 1.222 | 0.430 | 0.42 |
| 2 | 0.030 | 1.683 | 1.683 | 0.587 | 0.43 |
| 3 | 0.109 | 4.97 | 0.773 | 0.287 | 0.29 |
| 4 | 0.030 | 1.683 | 0.228 | 0.587 | 0.43 |
| 5 | 0.110 | 4.97 | 0.773 | 0.287 | 0.29 |
| 6 | 0.030 | 1.683 | 1.683 | 0.587 | 0.43 |
| 7 | 0.033 | 1.222 | 1.222 | 0.430 | 0.42 |

**TABLE 5.6** Ply level properties summary for 1/4" plate

| Layer | Thickness (inch) | $E_{11}$ (msi) | $E_{22}$ (msi) | $G_{12}$ (msi) | $V_{12}$ |
|---|---|---|---|---|---|
| 1 | 0.014 | 1.063 | 1.063 | 0.376 | 0.41 |
| 2 | 0.0095 | 5.973 | 0.930 | 0.345 | 0.27 |
| 3 | 0.037 | 1.466 | 1.466 | 0.513 | 0.43 |
| 4 | 0.009 | 5.973 | 0.930 | 0.345 | 0.27 |
| 5 | 0.037 | 1.466 | 1.466 | 0.513 | 0.43 |
| 6 | 0.037 | 1.466 | 1.466 | 0.513 | 0.43 |
| 7 | 0.037 | 1.466 | 1.466 | 0.513 | 0.43 |
| 8 | 0.009 | 5.973 | 0.930 | 0.345 | 0.27 |
| 9 | 0.037 | 1.466 | 1.466 | 0.513 | 0.43 |
| 10 | 0.0095 | 5.973 | 0.930 | 0.345 | 0.27 |
| 11 | 0.014 | 1.063 | 1.063 | 0.376 | 0.41 |

**TABLE 5.7** Ply level properties summary for 1/2" plate

| Layer | Thickness (inch) | $E_{11}$ (msi) | $E_{22}$ (msi) | $G_{12}$ (msi) | $V_{12}$ |
|---|---|---|---|---|---|
| 1 | 0.014 | 1.063 | 1.063 | 0.376 | 0.41 |
| 2 | 0.014 | 4.162 | 0.682 | 0.252 | 0.30 |
| 3 | 0.056 | 1.457 | 1.457 | 0.510 | 0.43 |
| 4 | 0.013 | 4.162 | 0.682 | 0.252 | 0.30 |
| 5 | 0.056 | 1.457 | 1.457 | 0.510 | 0.43 |
| 6 | 0.056 | 1.457 | 1.457 | 0.510 | 0.43 |
| 7 | 0.013 | 4.162 | 0.682 | 0.252 | 0.30 |
| 8 | 0.056 | 1.457 | 1.457 | 0.510 | 0.43 |
| 9 | 0.013 | 4.162 | 0.682 | 0.252 | 0.30 |
| 10 | 0.056 | 1.457 | 1.457 | 0.510 | 0.43 |
| 11 | 0.056 | 1.457 | 1.457 | 0.510 | 0.43 |
| 12 | 0.013 | 4.162 | 0.682 | 0.252 | 0.30 |
| 13 | 0.056 | 1.457 | 1.457 | 0.510 | 0.43 |
| 14 | 0.014 | 4.162 | 0.682 | 0.252 | 0.30 |
| 15 | 0.014 | 1.063 | 1.063 | 0.376 | 0.41 |

### 5.3.3 Analysis for FRP Bridge Decks Using Ply-level Properties

For ply-level composite analysis, special element (composite element) will be used. ANSYS has following element types to model laminated composite materials: SHELL99, SHELL91 , SOLID46 , and SOLID191. In our analysis, SOLID191, a layered structural solid element, was used to model the ply-level deck behavior (Figure 5.31). SOLID191 is a layered version of the 20 node 3-D solid element SOLID95, with three degrees of freedom per node: translations in the nodal x, y, and z directions (UX, UY, UZ). The geometry, node locations, and the coordinate system for this element are shown in Fig. 5.31. This layered composite element is designed to model thick layered shells or layered solids and allows up to 100 layers per element.

In analysis, SOLID191 is defined by layer thicknesses, layer material direction angles, and orthotropic material properties. In modeling, sometimes we need to reorient the elements after automatic meshing make SOLID191 elements match an element whose orientation is as desired, or set the orientation to be as parallel as possible to a defined axis. With ANSYS

command EORIENT, one can set the orientation as desired. For each analysis, one needs to check the element material orientations. It's assumed that there is no sliding between the element layers, and all material orientations are parallel to the reference plane.

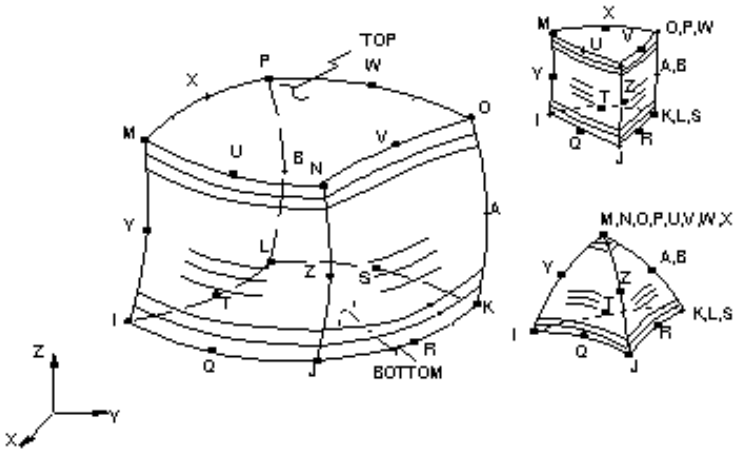


**Figure 5.31** Composite Element SOLID 191
[ANSYS 2002]

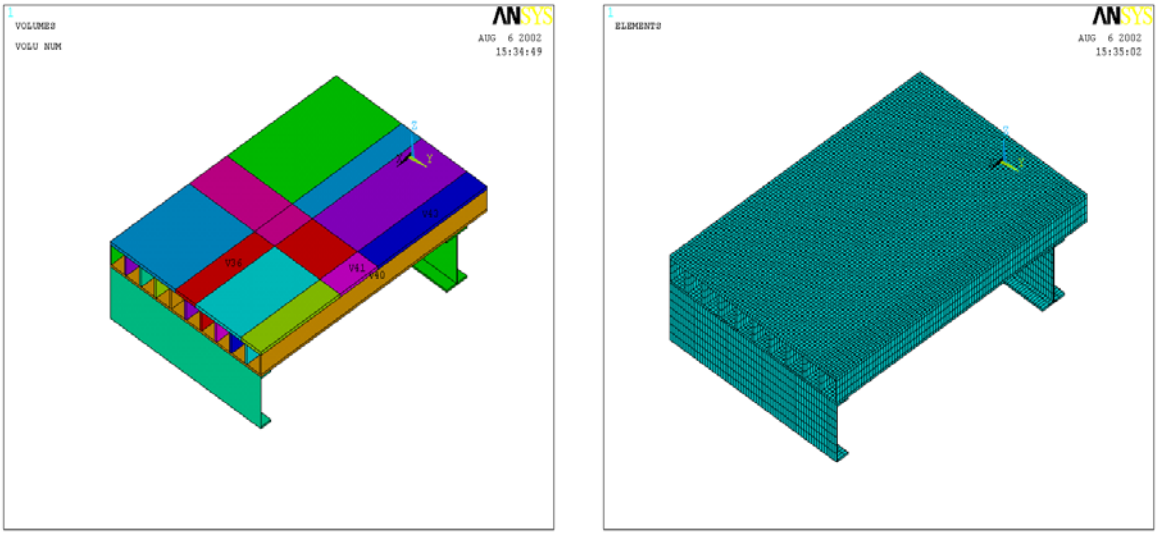

(a) Geometric Model (b) Meshed Half deck model

**Figure 5.32** FEA Model for Ply-level Strength analysis

The geometry model for analysis when the deck is loaded at the span center is shown in Figure 5.32. Because of the symmetry of the problem, only half of the deck was modeled. The two small pink rectangular areas simulate the tire contacting area for the simulated tire patch, one at the span center, one at the free edge's central part.

The ply-level material information used in the model are listed in Tables 5.5 to 5.7. The supported I beams are W14×43 steel I beams, with the modulus of 29 msi and the Poisson's ratio of 0.3. For this model, 118465 nodes and 18076 elements were used. The boundary conditions for deck system were clamped at the left hand side in Figure 5.32, and simply supported at the right hand side. For central loading, a uniform pressure of 1142 psi (7.87 Mpa) was applied through an 8"×15" (203.2×381mm) rectangular area to represent the 137 kips (609 kN) forced applied for simulated tire loading patch. The FEA results for the deck when loaded at span center will be shown in section 5.3.4.1. The FEA results for the free edge will be provided in section 5.3.1.4. In the FEA models, the X direction is the longitudinal direction (pultrusion direction), the Y direction is the transverse direction and the Z direction is the vertical (through the thickness) direction. For each case, the calculated values of deflection, stresses and strains are also shown at X=51", where the loading central line runs in the transverse direction. In these plots, the X direction is the longitudinal direction; the Y direction is the transverse direction and the Z direction is the vertical (through the thickness) direction. The symbol SX means normal stress in the X (longitudinal direction); SXY means shear stress in XY plane, and so on. The symbol EPTOX denotes normal strain in the X direction; EXPOXY denotes shear strain in XY plane, etc. The test data are shown as "Test_L" referring to tested data in the "Longitudinal" direction, or X direction in the FEA model; "Test_T" denotes test data in the "Transverse" direction, or Y direction in the FEA model. For each analysis, contour plots are provides for the overview of the stress/strain distribution; the location – deflection, location – stress and location – strain curves are presented for numerical comparisons.

### *5.3.3.1 FEA results for loadings at the span center*

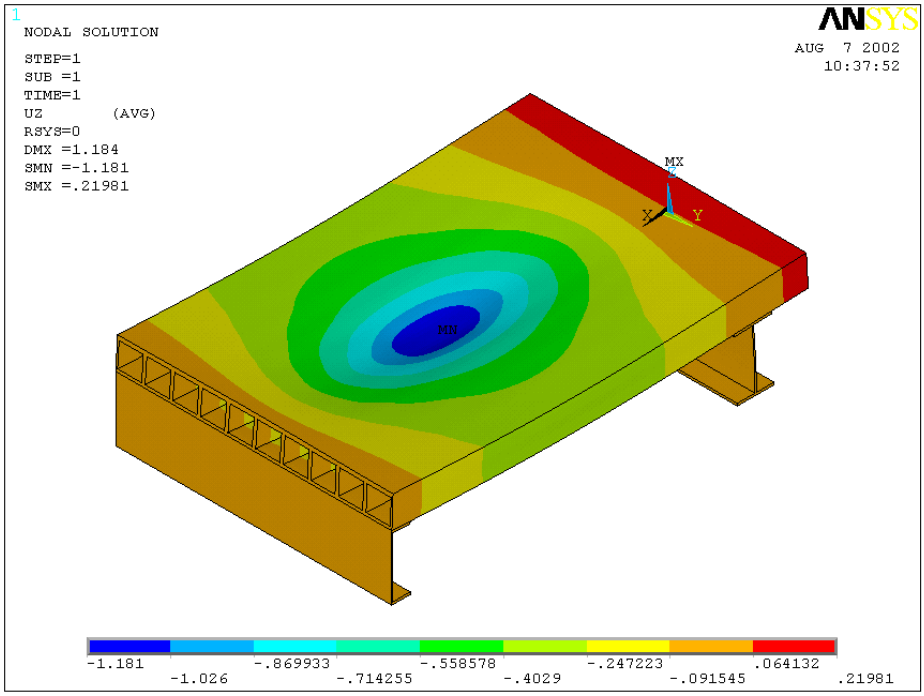


**Figure 5.33** Bending Deflection Contour from FEA

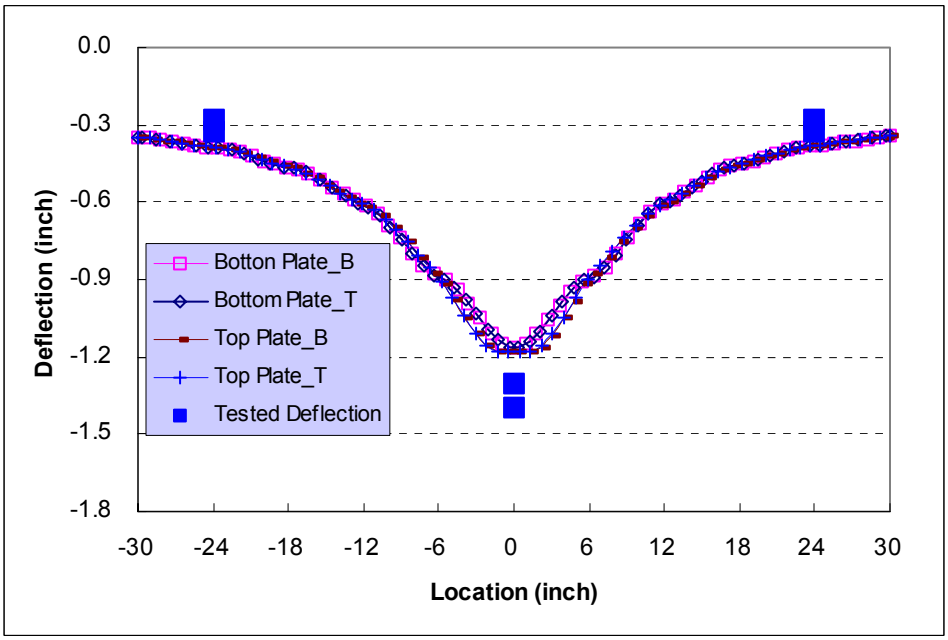


**Figure 5.34** Deflection at the Loading Patch Center – Transverse

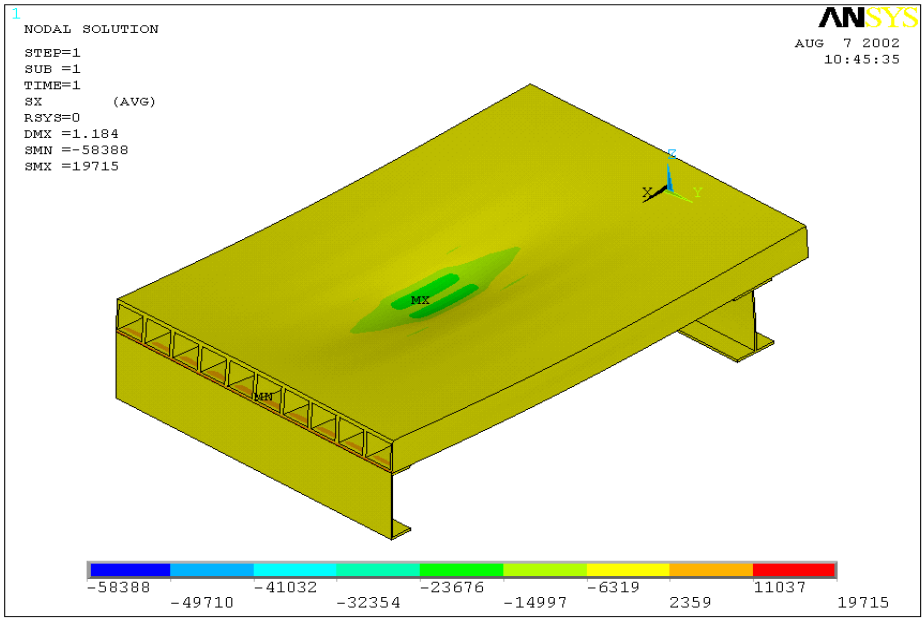


**Figure 5.35** Longitudinal Stress (X-stress) Contour from FEA

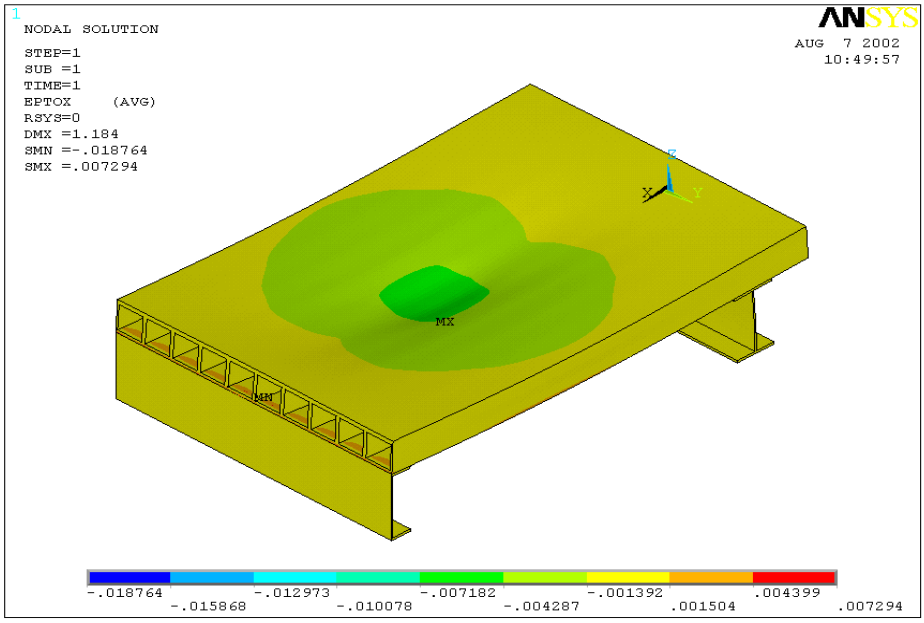


**Figure 5.36** Longitudinal Strain (X-strain) Contour from FEA

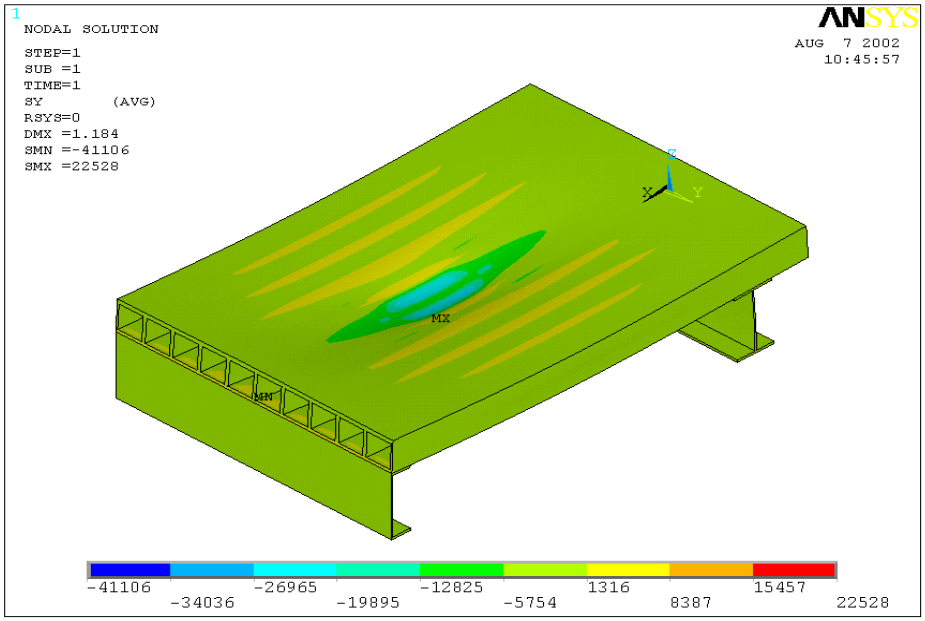


**Figure 5.37** Transverse Stress (Y-stress) Contour from FEA

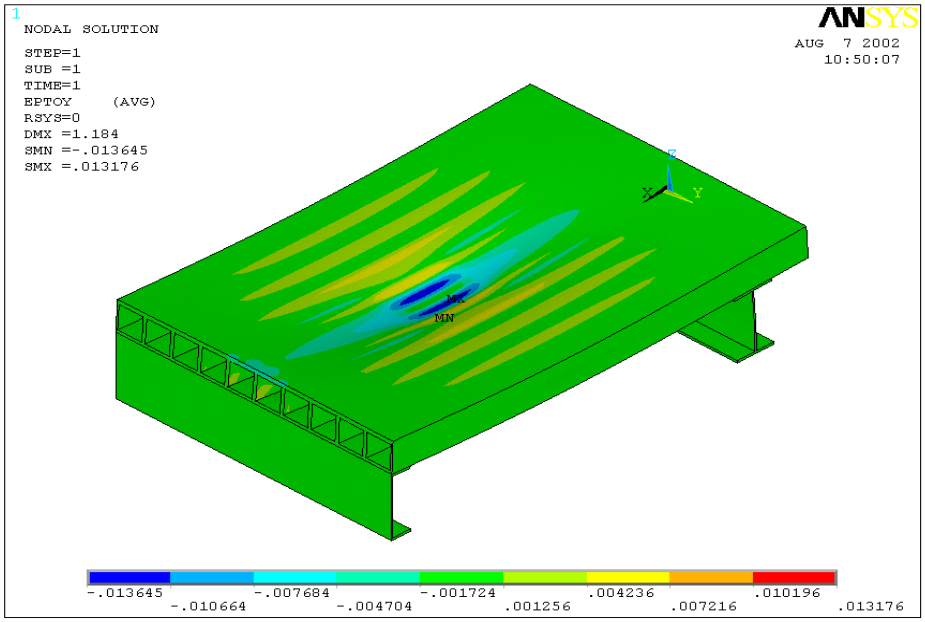


**Figure 5.38** Transverse Strain (Y-strain) Contour from FEA

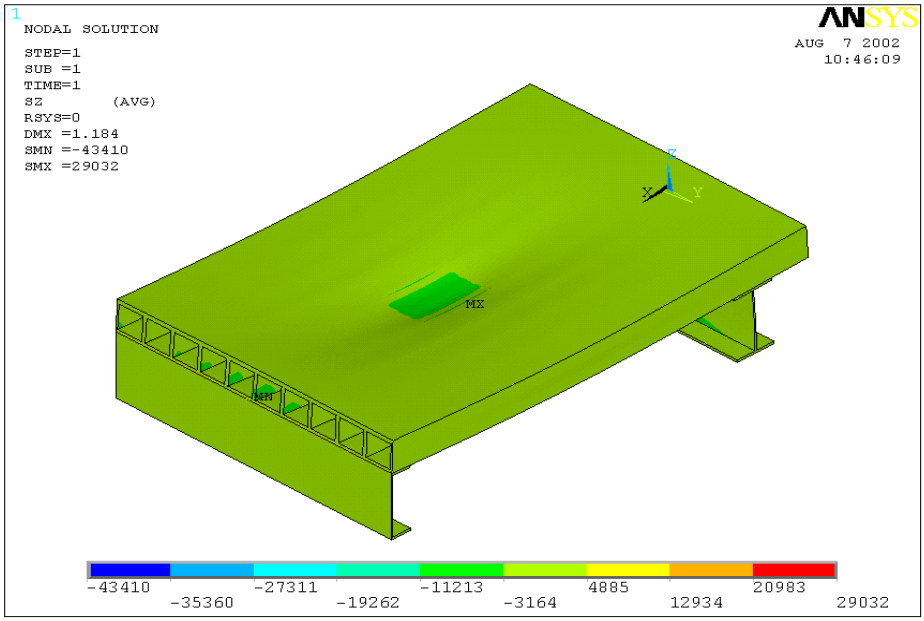


**Figure 5.39** Vertical Stress (Z-stress) Contour from FEA

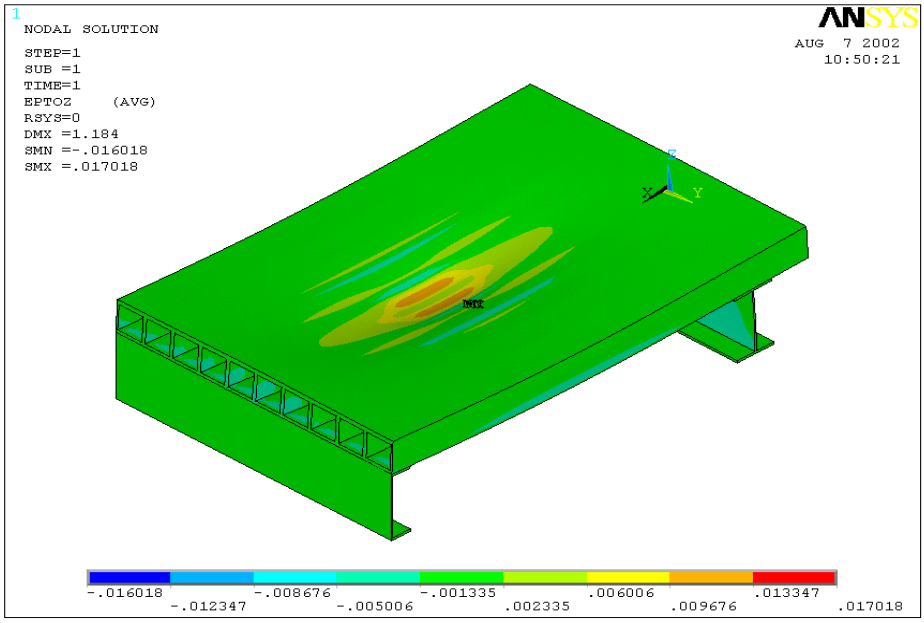


**Figure 5.40** Vertical Strain (Z-strain) Contour from FEA

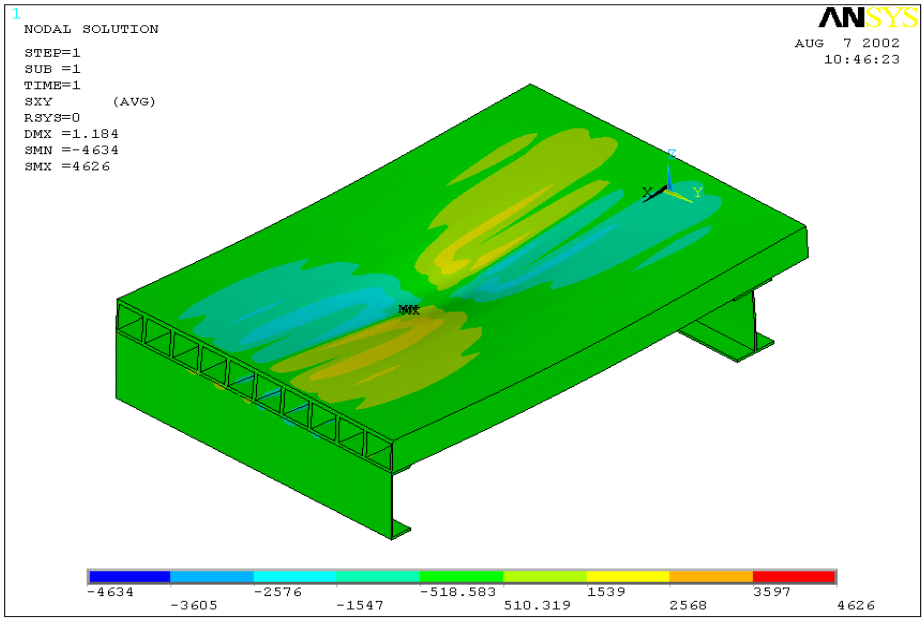


**Figure 5.41** In-plane Shear Stress (XY-stress) Contour from FEA

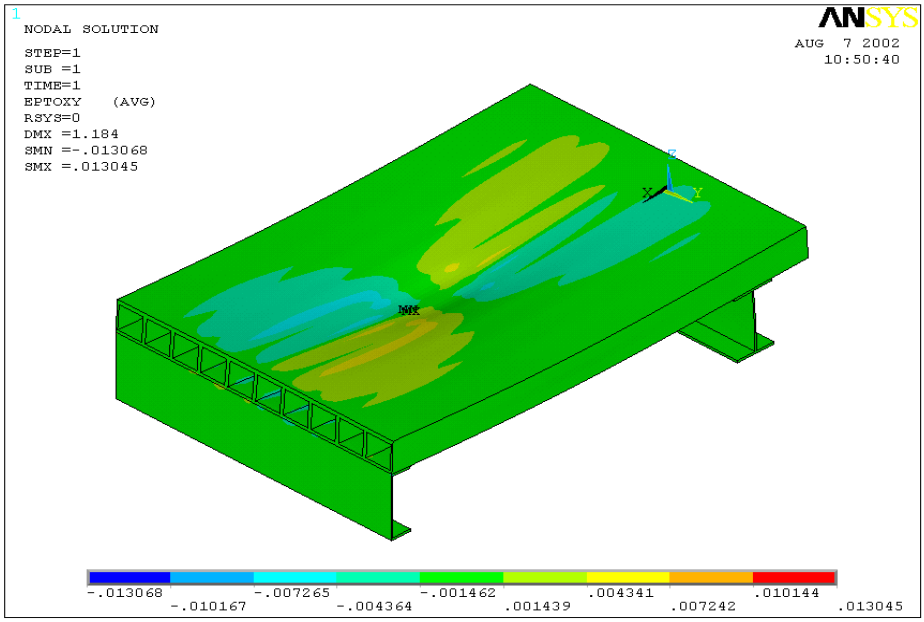


**Figure 5.42** In-plane Shear Strain (XY-strain) Contour from FEA

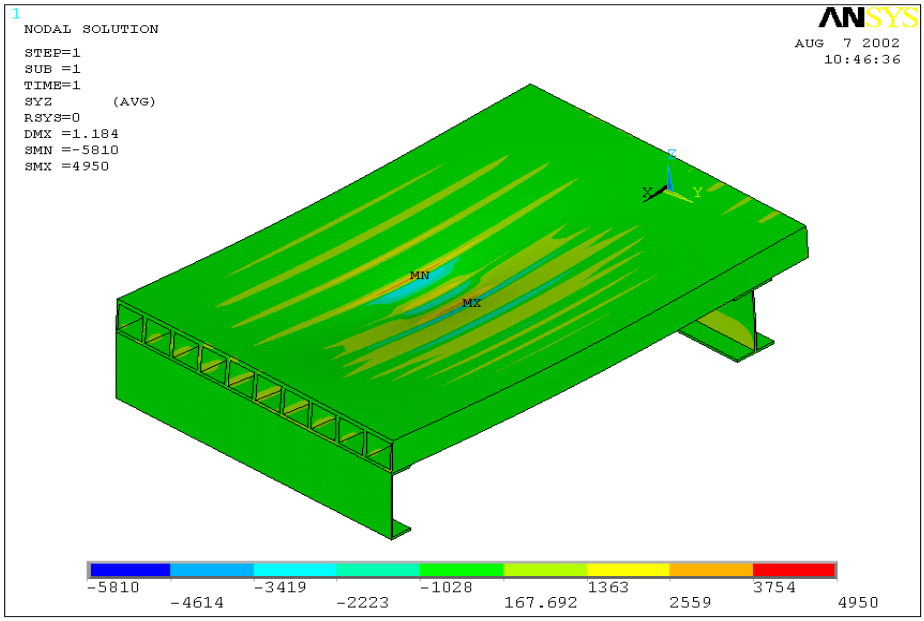


**Figure 5.43** Out-plane Shear Stress (YZ-stress) Contour from FEA

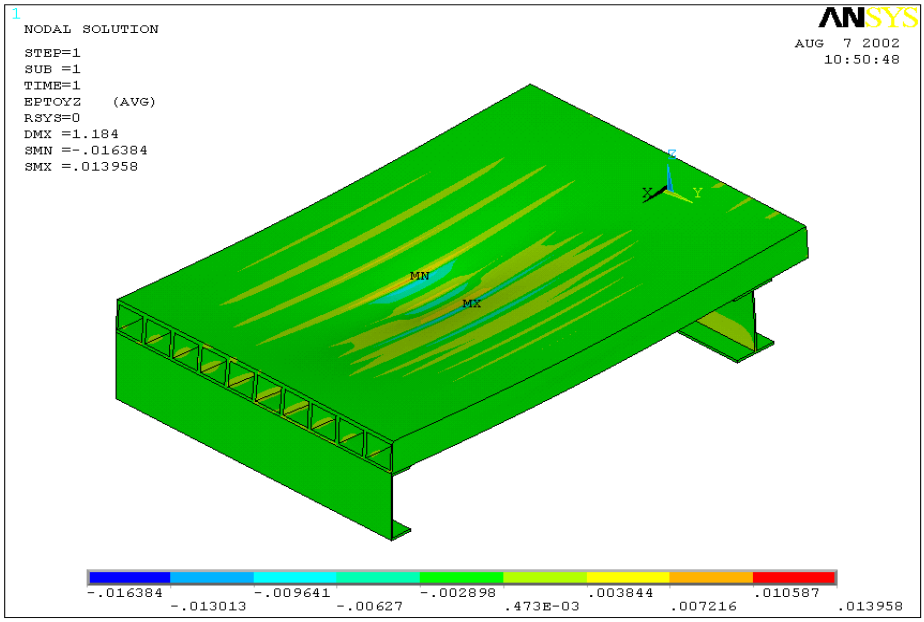


**Figure 5.44** Out-of-plane Shear Strain (YZ-strain) Contour from FEA

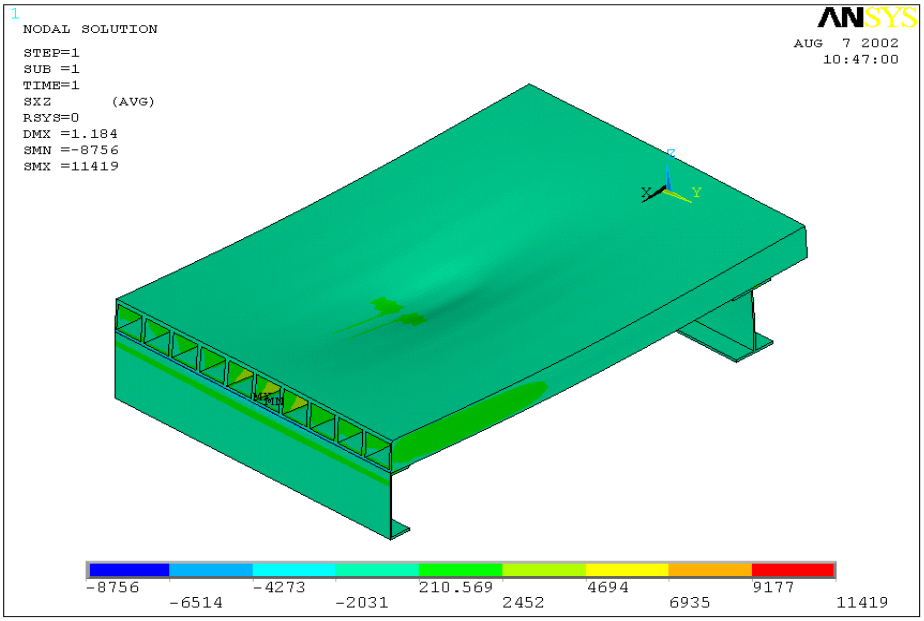


**Figure 5.45** Out-of-plane Shear Stress (XZ-stress) Contour from FEA

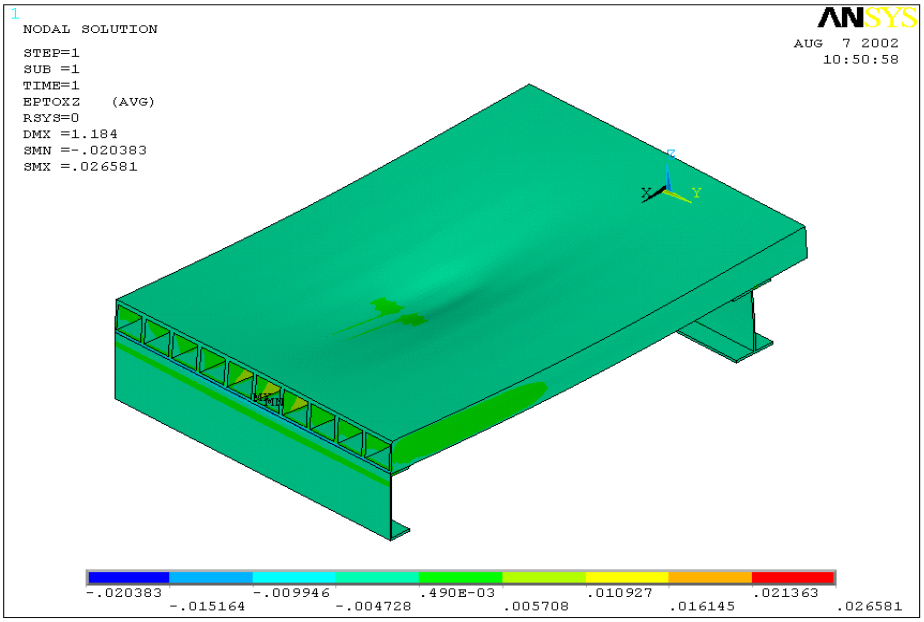


**Figure 5.46** Out-plane Shear Strain (XZ-strain) Contour from FEA

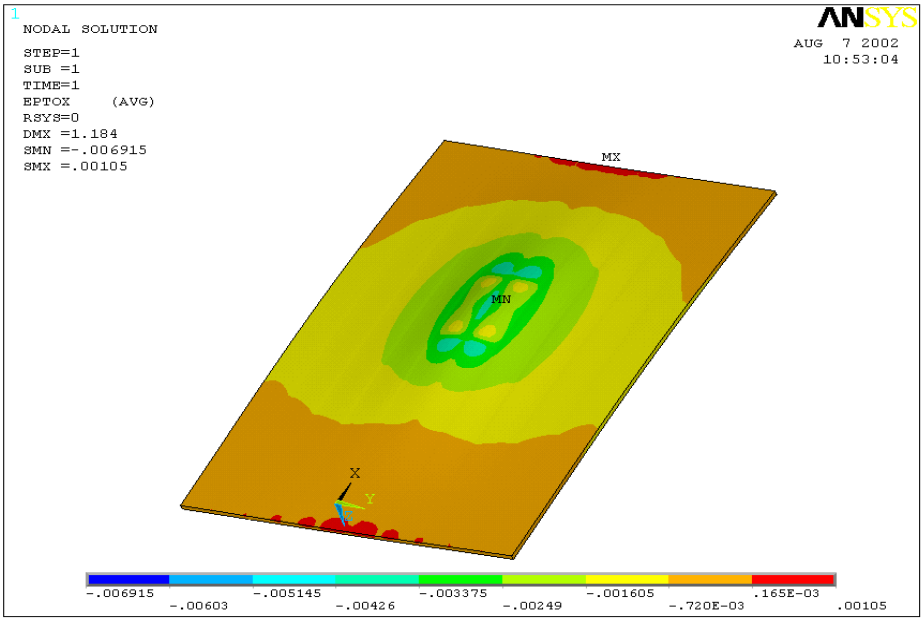


**Figure 5.47** Longitudinal Strain (X-strain) Contour for the Bottom Surface of Tube Top Flange

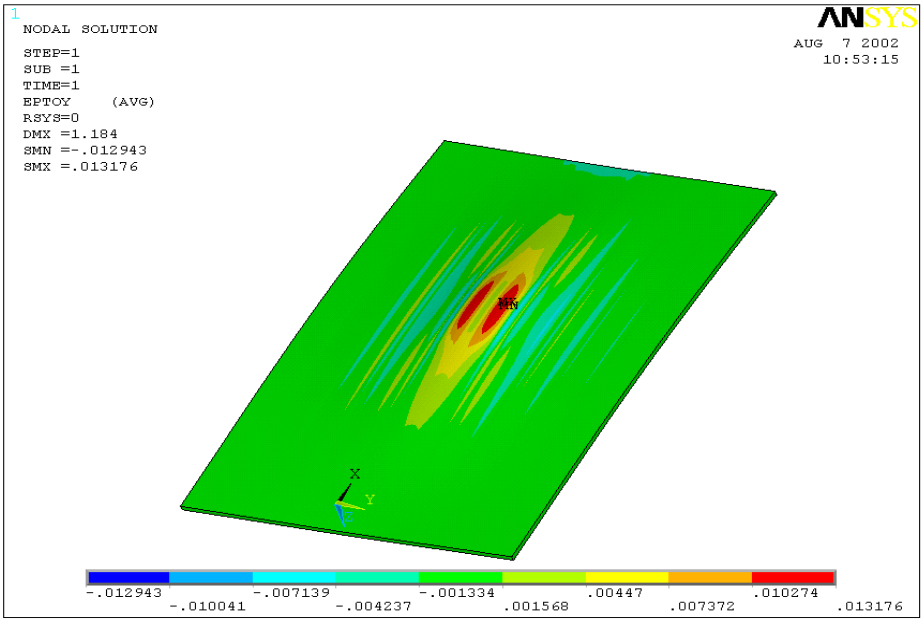


**Figure 5.48** Transverse Strain (Y-strain) Contour for the Bottom Surface of Tube Top Flange

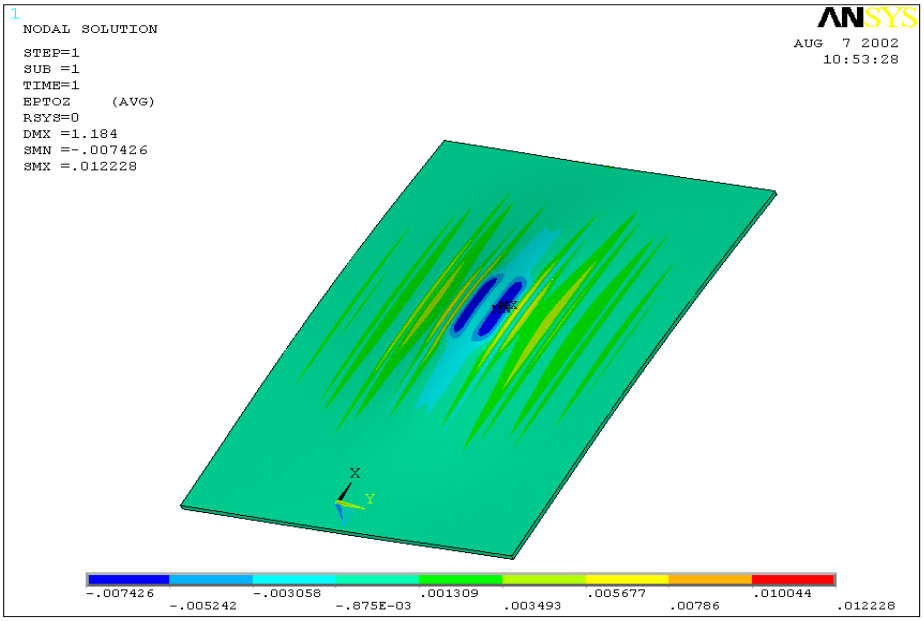


**Figure 5.49** Vertical Strain (Z-strain) Contour for the Bottom Surface of Tube Top Flange

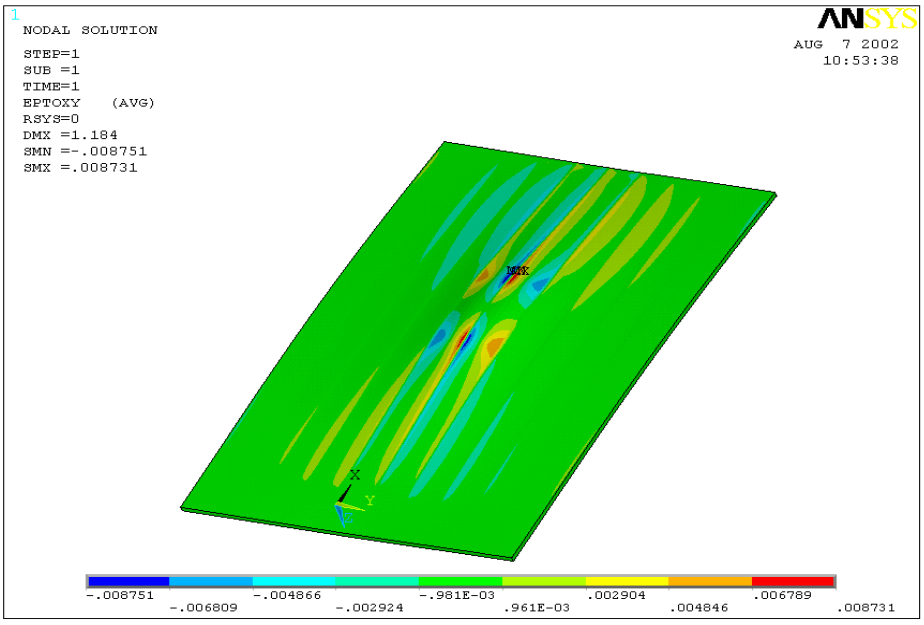


**Figure 5.50** Shear Strain (XY-strain) Contour for the Bottom Surface of Tube Top Flange

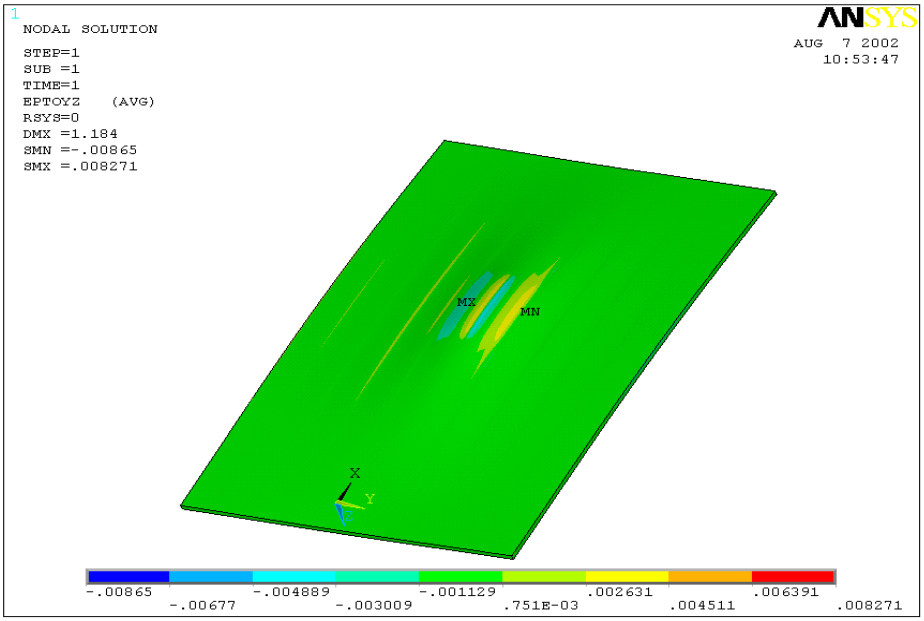


**Figure 5.51** Shear Strain (YZ-strain) Contour for the Bottom Surface of Tube Top Flange

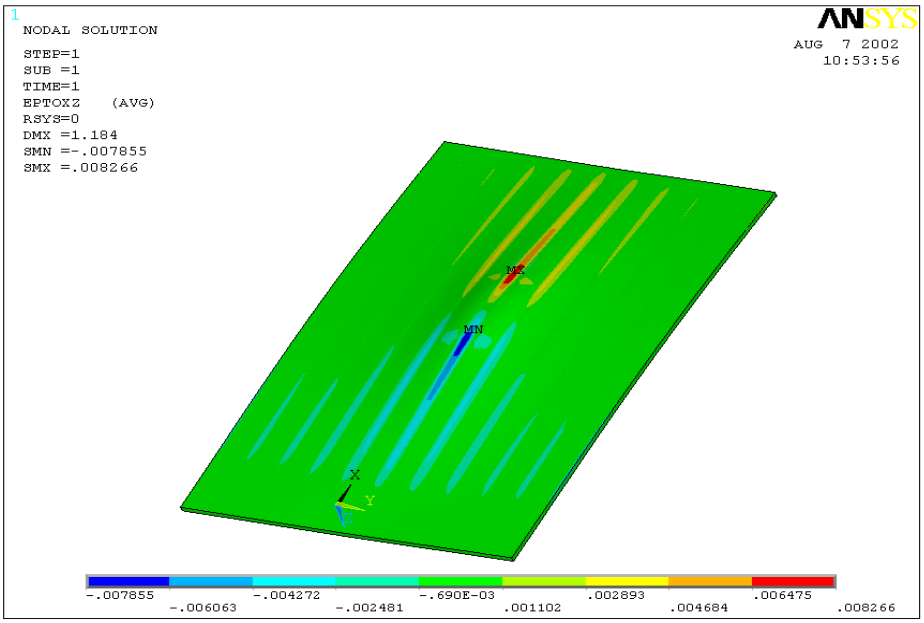


**Figure 5.52** Shear Strain (XZ-strain) Contour for the Bottom Surface of Tube Top Flange

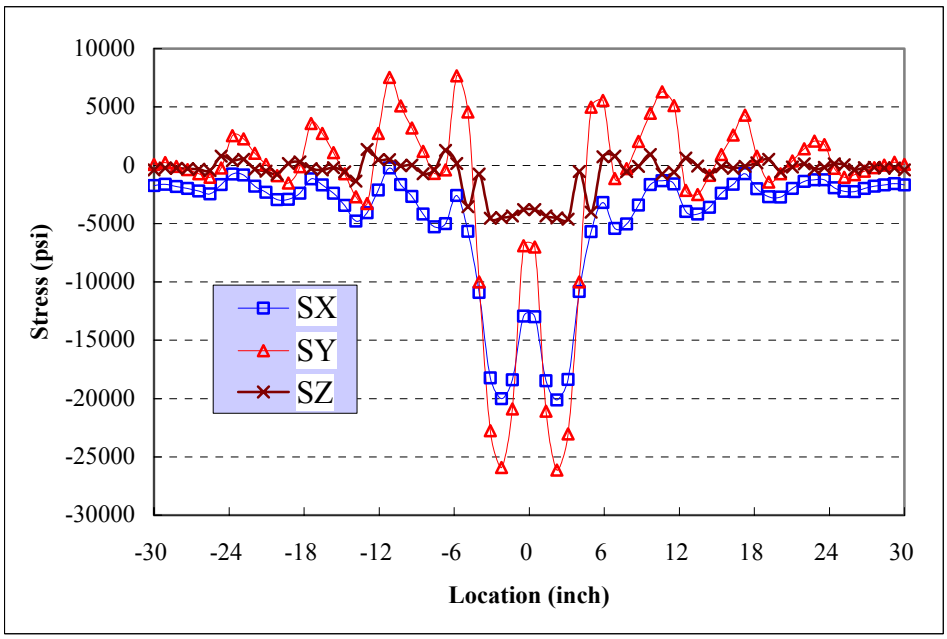


**Figure 5.53** Normal Stresses of Top plate's top surface at Loading Center

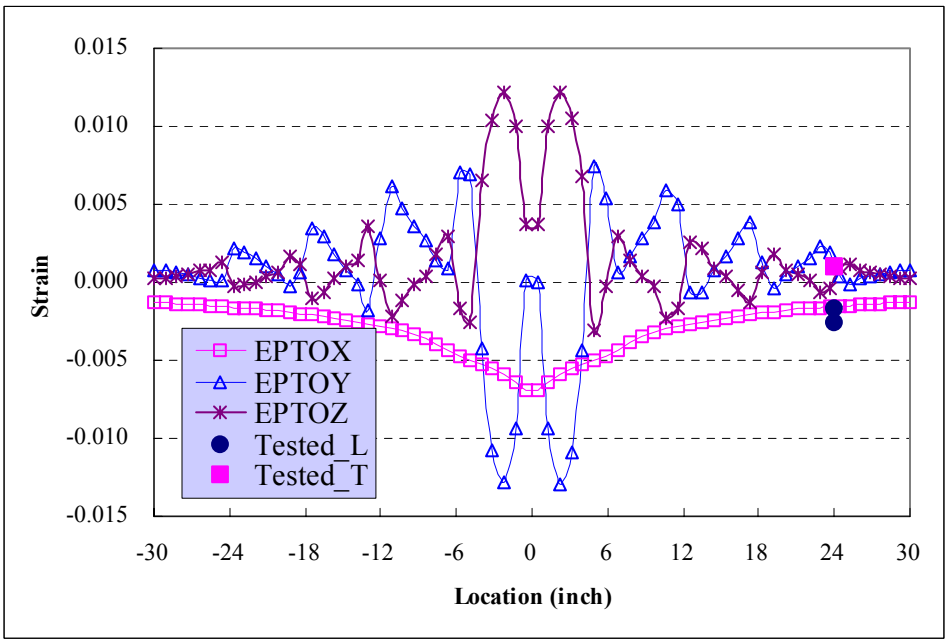


**Figure 5.54** Normal Strains of Top plate's top surface at Loading Center

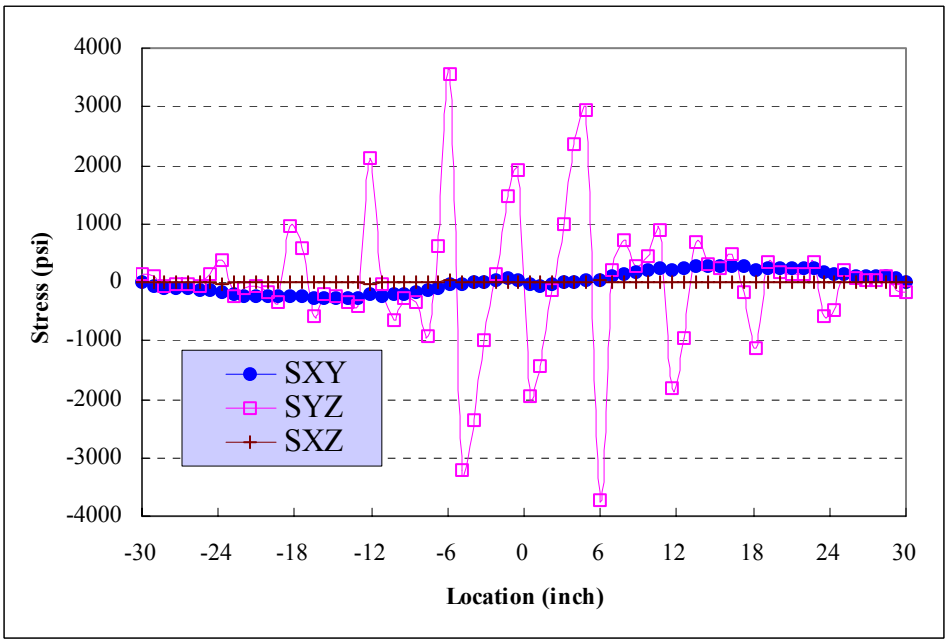


**Figure 5.55** Shear Stresses of Top plate's top surface at Loading Center

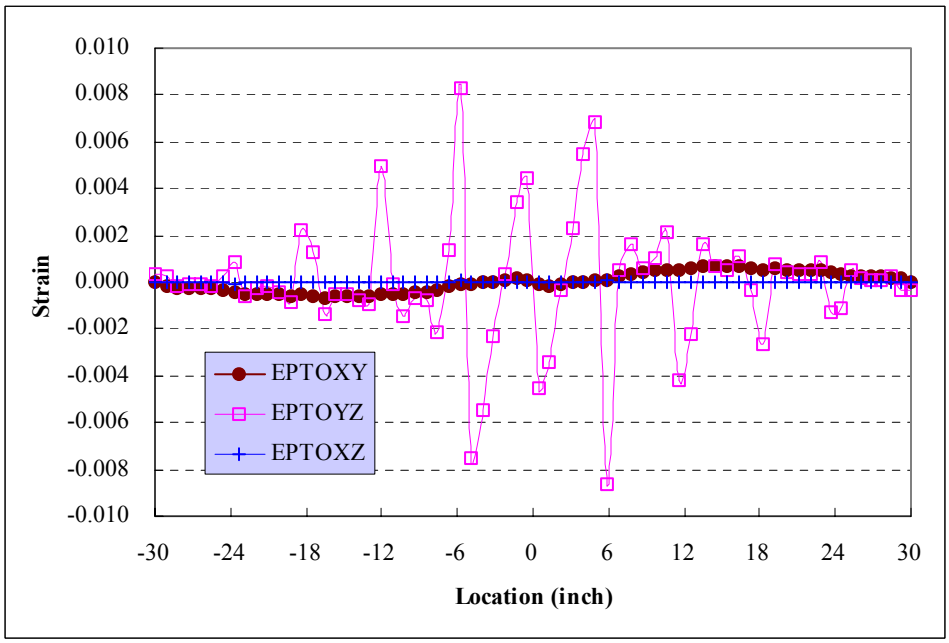


**Figure 5.56** Shear Strains of Top plate's top surface at Loading Center

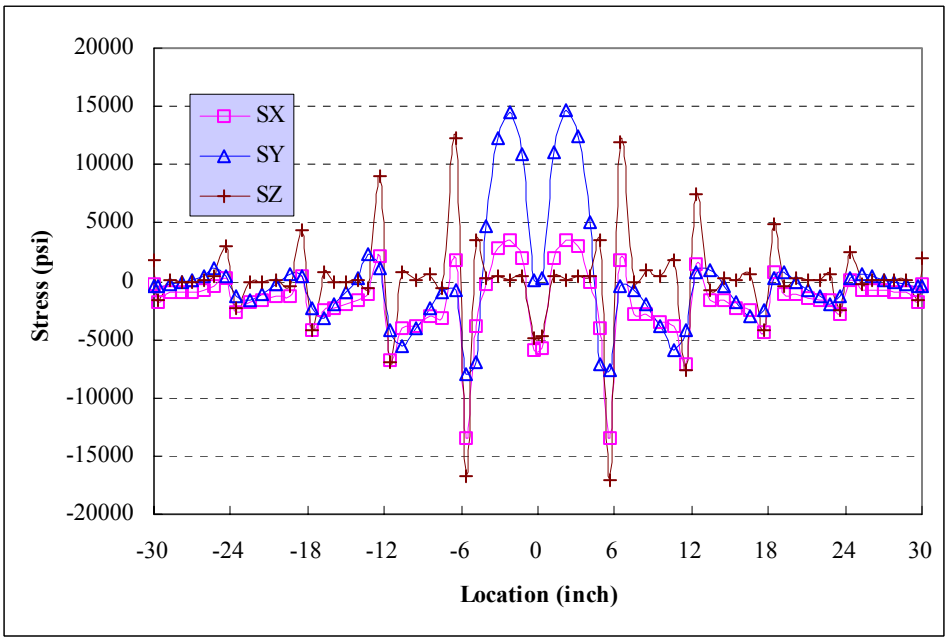


**Figure 5.57** Normal Stresses of Tube Top Flange's bottom surface at Loading Center

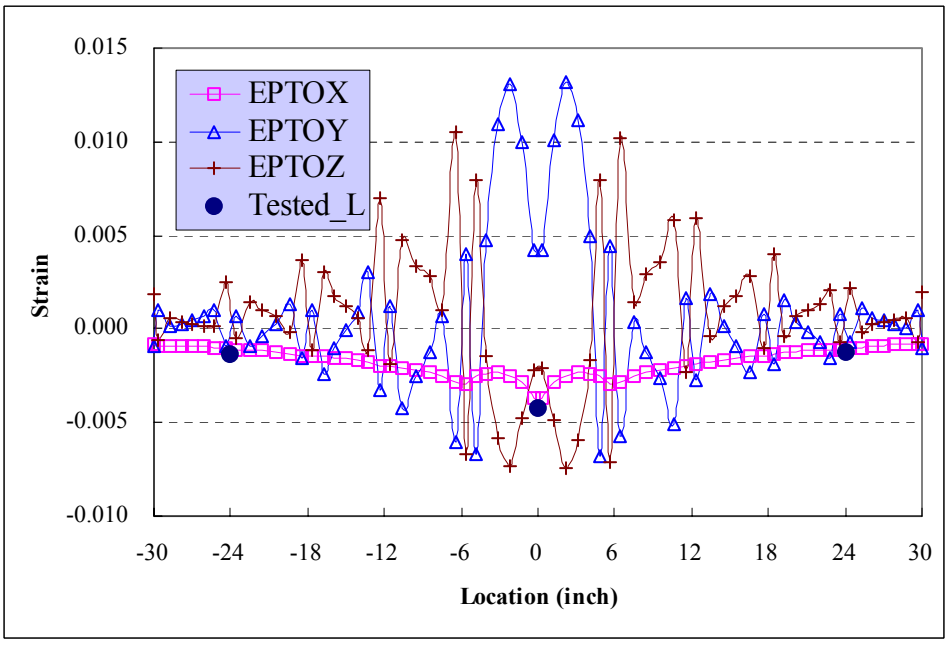


**Figure 5.58** Normal Strains of Tube Top Flange's bottom surface at Loading Center

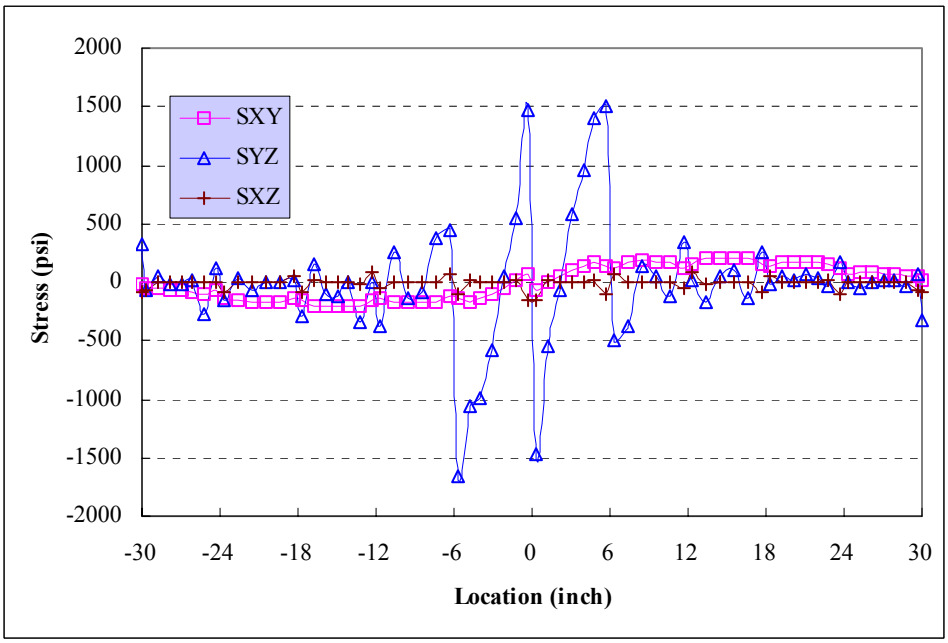


**Figure 5.59** Shear Stresses of Tube Top Flange's bottom surface at Loading Center

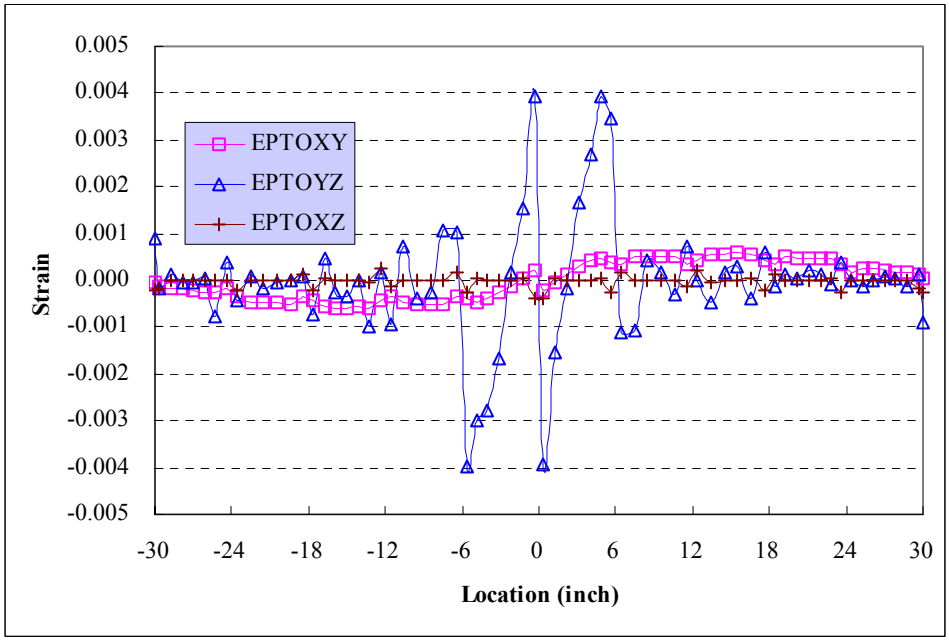


**Figure 5.60** Shear Strains of Tube Top Flange's bottom surface at Loading Center

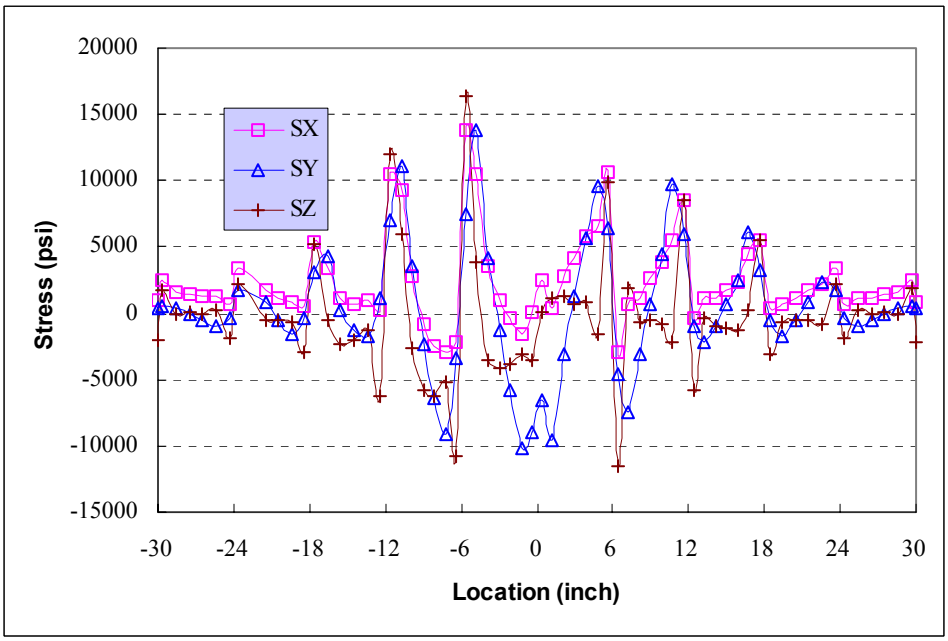


**Figure 5.61** Normal Stresses of Tube Bottom Flange's inner surface at Loading Center

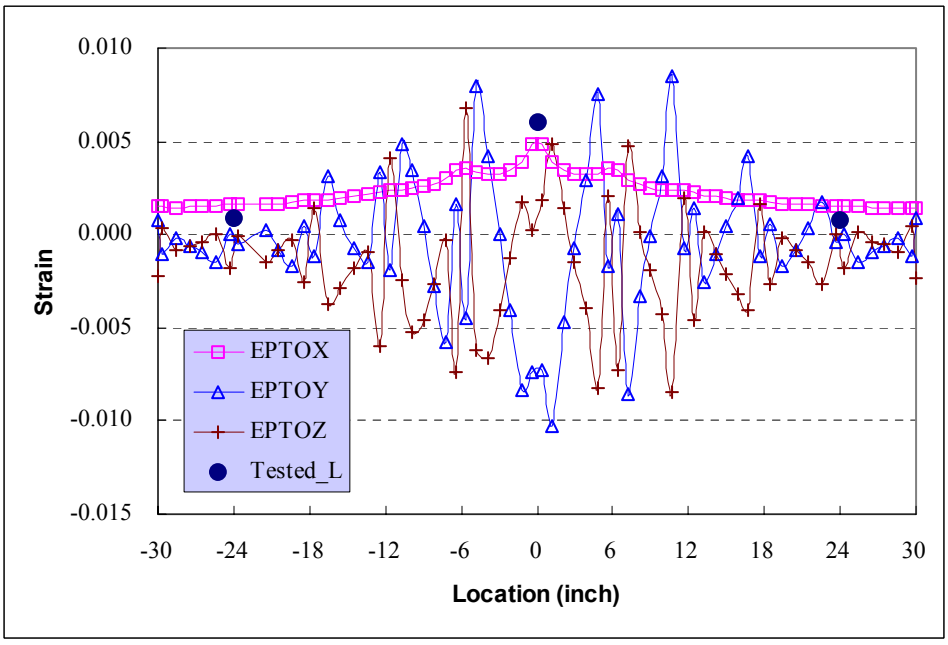


**Figure 5.62** Normal Strains of Tube Bottom Flange's inner surface at Loading Center

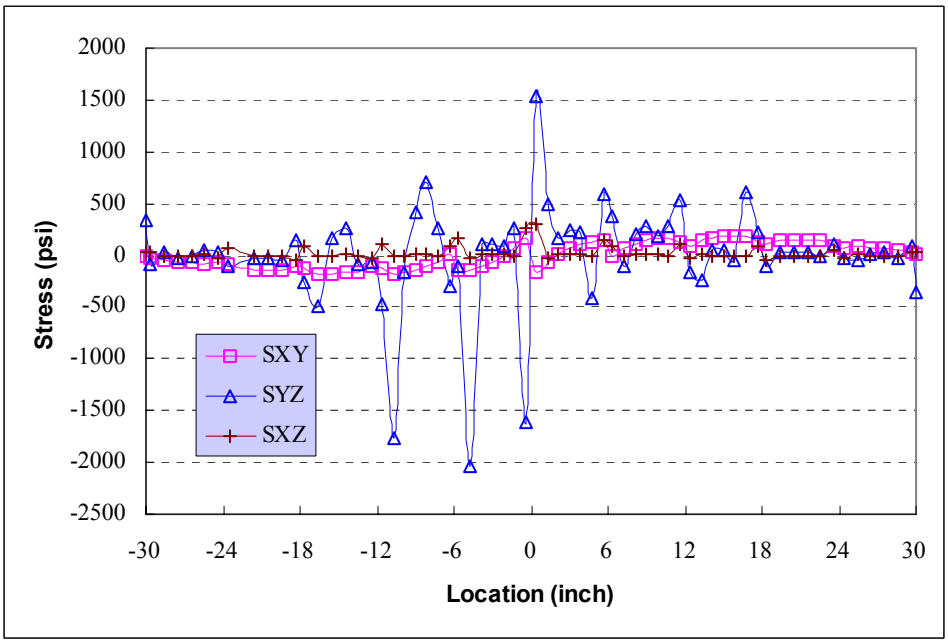


**Figure 5.63** Shear Stresses of Tube Bottom Flange's inner surface at Loading Center

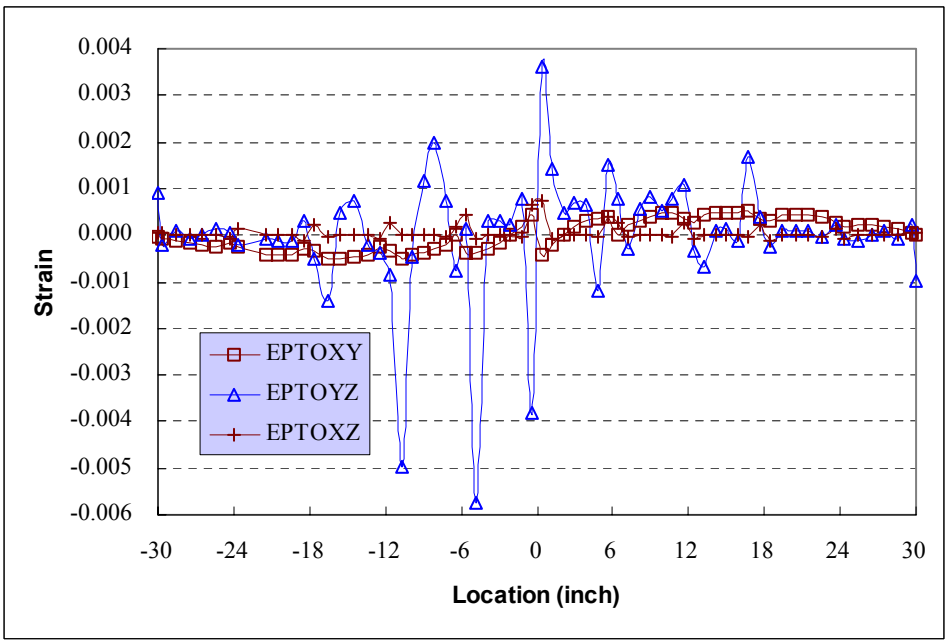


**Figure 5.64** Shear Strains of Tube Bottom Flange's inner surface at Loading Center

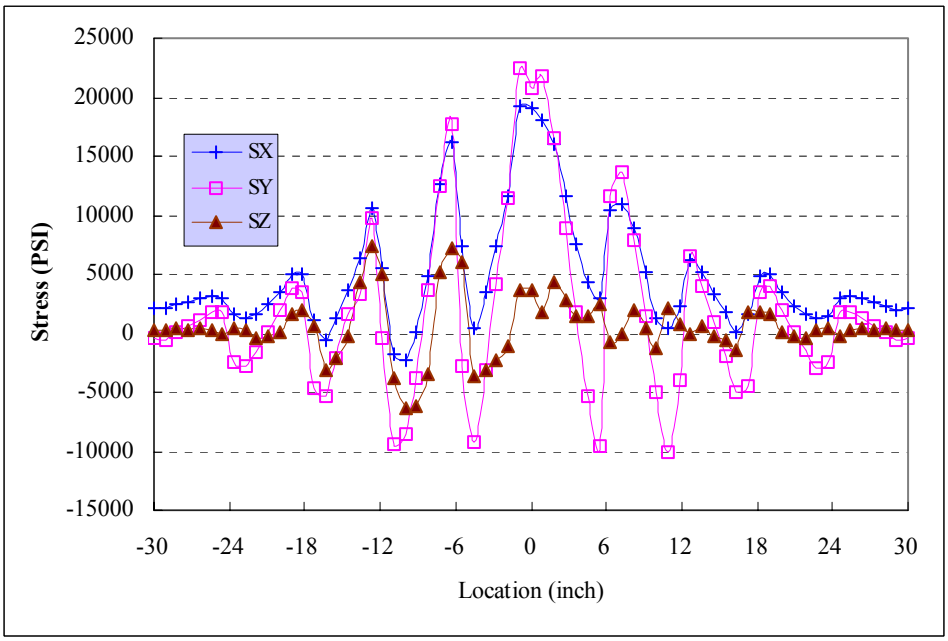


**Figure 5.65** Normal Stresses of Bottom plate's Bottom surface at Loading Center

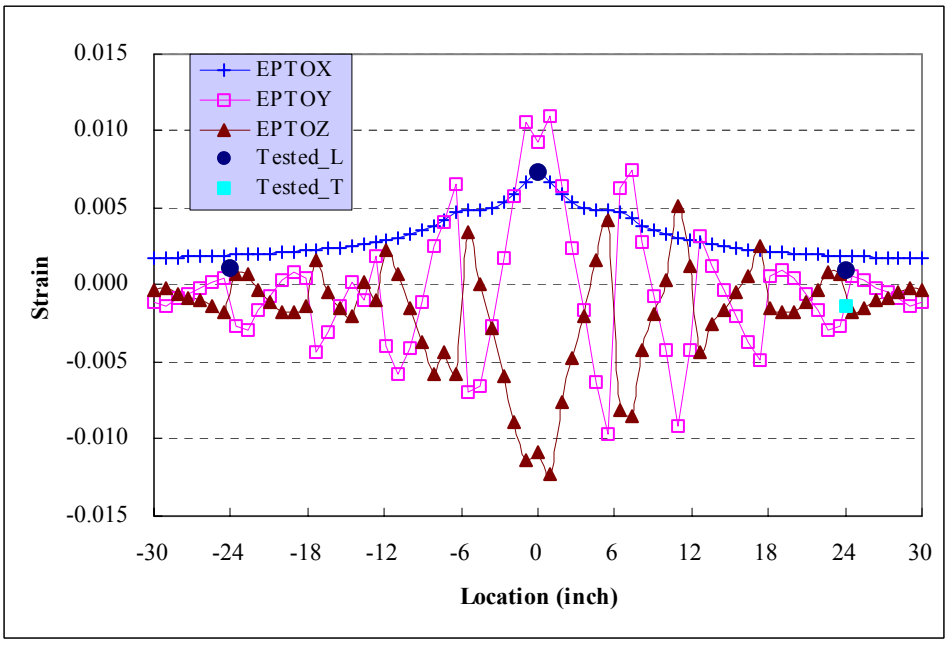


**Figure 5.66** Normal Strains of Bottom plate's Bottom surface at Loading

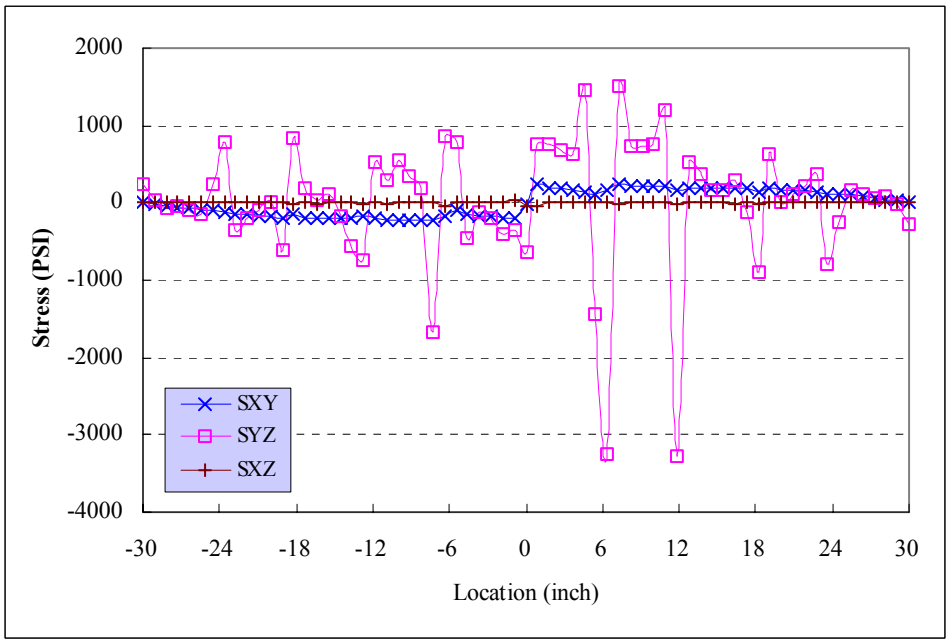


**Figure 5.67** Shear Stresses of Bottom plate's Bottom surface at Loading Center

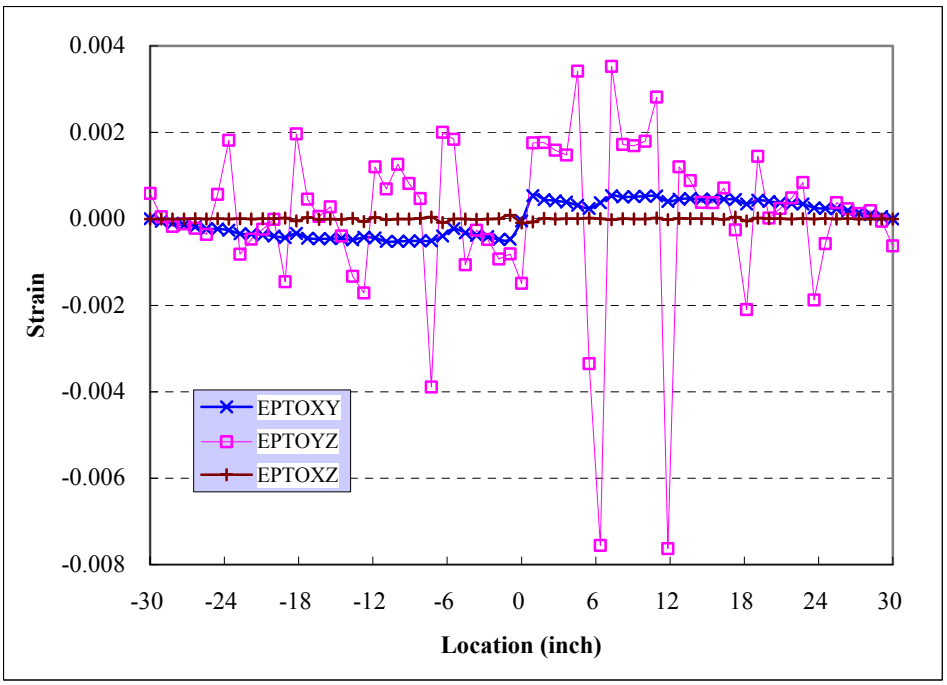


**Figure 5.68** Shear Strains of Bottom plate's Bottom surface at Loading Center

The contour of the vertical deflection (in Z direction) is shown in Fig. 5.33. The comparisons of deflection (at X=51" (1295.4mm)) from FEA for different deck components and test data are shown in Fig. 5.34. The predicted maximum deflection at the center in the transverse direction at X=51" (1295.4mm) is –1.18" (-30mm) at the top surface of the top plate. The tested average maximum deflection is –1.3" (-33mm) at the same location. The prediction is 9% lower than the tested average maximum deflection. At location X=51" (1295.4mm) and Y=±24" (±609.6mm), the tested average deflection is –0.3" (-7.6mm), while the predicted deflection is –0.38" (-9.6mm).

The normal stress and strain contours are shown in Fig. 5.35-5.40. The shear stress and shear strain contours are shown in Fig. 5.41-5.46. It is observed from these plots that the stress/strain concentrations occurred at the loading area for all stresses and strains except XY in-plane shear (Fig. 5.41 and 5.42). Particularly, severe transverse stress/strain concentrations are observed in Fig. 5.37 and 5.38. The top plate and the tube's top flange is the part we are interested in, since the deck failed in these components. The normal strain and shear strain contours for the bottom of the tube assembly's top flange are shown in Fig. 5.47-5.52. Severe normal strain concentrations are observed at the loading area in the bottom surface of the tube assembly's top flange. While only YZ shear strain concentration is observed at $Y = \pm 3"$ (76.2mm) under the contacting area.

The numerical location-stress/strain curves at X=51" are shown in Fig. 5.53-5.68. In these plots, the horizontal coordinate denotes the variation of transverse locations, where $Y = -30" - +30"$ (-762mm - +762mm). The following interested parts are investigated: top plate's top surface (Fig. 5.53-5.56), tube assembly top flange's bottom surface (Fig. 5.57-5.60), tube assembly bottom flange's inner surface (Fig. 5.61-5.64), and bottom plate's bottom surface (Fig. 5.65-5.68).

The numerical location-stress/strain curves at X=51" are shown in Fig. 5.53-5.68. In these plots, the horizontal coordinate denotes the variation of transverse locations, where $Y = -30" - +30"$. The following interested parts are investigated: top plate's top surface (Fig. 5.53-5.56), tube assembly top flange's bottom surface (Fig. 5.57-5.60), tube assembly bottom

flange's inner surface (Fig. 5.61-5.64), and bottom plate's bottom surface (Fig. 5.65-5.68). The predicted longitudinal strain at $Y = 24"$ in the top plate's top surface is –0.00158 (Fig. 5.54); the tested strains range from –0.00172 to –0.00256. The closest longitudinal strain prediction is 8% less than the tested longitudinal. The predicted transverse strain at $Y = 24"$ in the top plate's top surface is 0.0011 (Fig. 5.54); the tested strains range from 0.00103 to 0.00106. For the tube assembly top flange's bottom surface (Fig. 5.58), the tested strain is –0.0043 at $Y = 0"$ and –0.0012 at $Y = \pm 24"$. The predicted strain is –0.0037 at $Y = 0"$ and –0.0011 at $Y = \pm 24"$. The difference is 14% and 8% for $Y = 0"$ and $Y = \pm 24"$ respectively. For tube assembly bottom flange's inner surface and bottom plate's bottom surface, the largest difference between the predicted strain and the tested strain is less than 15% (see Fig. 5.62 and 5.66). The FEA results give close agreement compared to the corresponding tested deflection and strains.

From Figures 5.53 and 5.54, we notice that the top plate's top surface near $Y = \pm 3in$ is in compression condition transversely since it has negative transverse stress and strain, while the tube top flange's bottom surface is in extension because of its positive transverse stress and strain (Fig. 5.57 and 5.58). Therefore, the top part of the deck panel is in bending under the loading area. The same situation can be observed for the tube's bottom flange from Figures 5.61 and 5.62, and from Figures 5.65 and 5.66 for the bottom plate: where the tube bottom flange's inner surface is under compression transversely, and the bottom plate's bottom surface is under extension. Also, the maximum transverse stress/strain is larger than any other direction under the loading area for the top plate (Fig. 5.53, 5.54, 5.57 and 5.58). At $Y = \pm 6"$, where the vertical tube web locates, the top surface is in extension and the bottom surface is in compression for the tube top flange. Also at $Y = \pm 6in$, the shear stress/strain ($YZ - stress / strain$) is high (Fig. 5.56 and 5.60). While the transverse direction of the deck system, according to its microstructure, is the weakest direction, both in stiffness and strength. Not surprisingly, the deck was bent to failure at $Y = \pm 3in$ and $Y = \pm 6in$ the tire contacting area when loaded at the span center.

For the top plate's top surface, the maximum transverse stress is –2,6133 psi at $Y = \pm 3in$ on the top surface(Fig. 5.53). The ultimate stress for the top plate in the transverse direction is -2,4000 psi [Strongwell,1998 ]. Using Eq. (5.2), we have

$$F_a^{soft} \cong \frac{\sigma_{22}}{X_{22}} = \frac{-26133}{-24000} \approx 1.1$$

For the top plate's top surface, $F_a^{soft} \cong 1.1 > 1$. Therefore, failure should occur in the transverse direction. From lab test, the top surface was failed in compression at the center of the tube webs ( $Y = 3in$ ) (see Figure 5.11)

The flexural strength (ultimate stress) is 10,000 psi in the transverse direction for the tube assembly's top flange [Strongwell, 1998]. The maximum tensile stress obtained from the ply-level FEA is 14,655 psi at $Y = 2.193"$ on the inner surface of the top flange (Fig. 5.57). According to Eq. (5.2),

$$F_a^{soft} \cong \frac{\sigma_{22}}{X_{22}} = \frac{14655}{10000} \approx 1.5$$

$F_a^{soft} \cong 1.5 > 1$, with the maximum tensile strain of 0.0132 (Fig. 5.58). The ultimate tensile strain for the tube is 0.00875 in the transverse direction (Table 2.3). Both the maximum transverse stress and strain are larger than their ultimate values. The tube's top flange fails at the location close to the webs' center in bending. This was observed in lab test (see Figure 5.12).

The tube's bottom flange is under compression transversely with the maximum compressive stress of 10,200 psi at $Y = -1.25"$ (Figure 5.61). The compressive strength (ultimate stress) in the transverse direction for the tube assembly's bottom flange is 15,000 psi [Strongwell, 1998]. According to Eq. (5.2),

$$F_a^{soft} \cong \frac{\sigma_{22}}{X_{22}} = \frac{10200}{15000} \approx 0.68$$

$F_a^{soft} \cong 0.68 < 1$. The maximum compressive strain is –0.0102 (Fig. 5.62). The ultimate compressive strain for the tube is -0.012 in the transverse direction (Table 2.3). The maximum

transverse strain is less than its ultimate value. The tube's bottom flange is safe. No damage was observed in lab test for the bottom flange.

The bottom plate's flexural strength is 15,000 psi (ultimate stress) in the transverse direction. The maximum calculated tensile stress for the bottom plate is 22,528 psi at $Y = -0.9"$ (Fig. 5.65). The value of the failure function can be obtained as

$$F_a^{soft} \cong \frac{\sigma_{22}}{X_{22}} = \frac{22528}{15000} \approx 1.5$$

The maximum strain at $Y = -0.9"$ is 0.0106 (Fig. 5.66), while the ultimate tensile strain in the transverse direction is 0.0111 (Table 2.3). The bottom plate did not fail probably because of its strain capacity.

**TABLE 5.8** Ultimate Strength for Each Deck Components

| Strength | Top Plate | Tube | Bottom Plate |
|---|---|---|---|
| $X_{11}(psi)$ | 20,000/ (-24,000) | 30,000/ (-30,000) | 20,000/ (-24,000) |
| $X_{22}(psi)$ | 10,000/ (-20,000) | 7,000/ (-16,000) | 10,000/ (-20,000) |
| $X_{33}(psi)$ * | 400/ (-1,000) | 400/ (-1,000) | 400/ (-1,000) |
| Flexural, LW† (*psi*) | 35,000 | 30,000 | 30,000 |
| Flexural, CW‡ (*psi*) | 15,000 | 10,000 | 18,000 |
| $S_{12}(psi)$ | 6,000 | 4,500 | 6,000 |
| $S_{13}(psi)$ | 6,000 | 4,500 | 6,000 |
| $S_{23}(psi)$ § | 1,000 | 1,000 | 1,000 |

* The tensile strength is from personal communication with Strongwell Corp. The compressive strength is an assumed value.
† LW – lengthwise (longitudinal, or X- direction);
‡ CW – crosswise (transverse, or Y-direction)
§ Assumed value

**TABLE 5.9** Calculated Component Stressed from FEA

| Stress | Top Plate[1] | Tube's Top Flange[2] | Tube's Bottom Flange[3] | Bottom Plate[4] |
|---|---|---|---|---|
| $\sigma_{11}(psi)$ | -20115 | 3555 | -1543 | 19218 |
| $\sigma_{22}(psi)$ | -26133 | 14655 | -10200 | 22528 |
| $\sigma_{33}(psi)$ | -4505 | 53 | -3069 | 3721 |
| $\tau_{12}(psi)$ | -19 | 45 | 60 | -201 |
| $\tau_{13}(psi)$ | -3 | -3 | -13 | 37 |
| $\tau_{23}(psi)$ | -140 | -62 | 270 | -350 |

1: at $y = 3"$, top plate's surface, span center (Fig. 5.53); 2: at $Y = 2.193"$, top flange's inner surface, span center (Fig. 5.57);
3: at $Y = -1.25"$, bottom flange's inner surface, span center (Fig. 5.61); 4: at $Y = -0.9"$, bottom surface, span center (Fig. 5.65).

The ultimate strength for each deck components are shown in Table 5.8 [Strongwell, 1998]. The values in the parentheses are compressive strength. The source of $X_{33}$ and $S_{23}$ are stated in the corresponding footnote. The component stresses at critical locations are listed in Table 5.9. These calculated stresses are used in failure analysis calculation.

**TABLE 5.10** Deck Components Failure Analysis Comparisons

| Component | Tsai-Wu | Tsai-Hill | Current Analysis | Test |
|---|---|---|---|---|
| Top Plate's Top Surface | 2.4 [Fail] | 1.5 [Fail] | 1.1 [Fail] | [Fail] |
| Tube's Top Flange | 2.2 [Fail] | 2.1 [Fail] | 1.5 [Fail] | [Fail] |
| Tube's Bottom Flange | 0.47 [Safe] | 0.45 [Safe] | 0.68 [Safe] | [Safe] |
| Bottom Plate's Bottom surface | 2.6 [Fail] | 2.2 [Fail] | 1.5 [Fail] | [Safe] |

Using the obtained component stresses from FEA data (in Table 5.9), failure analysis comparisons for each deck component can be conducted, which is shown in Table 5.10. Failure analysis using current method is compared with the Tsai-Wu criterion with $F_{12} = 0$ in calculation [Eq. (2.147), Jones, 1999], and the Tsai-Hill criterion [Eq. (2.2.132), Jones, 1999]. Current

analysis gives the same fail/safe prediction as Tsai-Wu and Tsai-Hill criteria for the deck components, though it gives different values than these criteria.

The above comparisons show that Eq. (5.2) and the failure function method could be used as the primary failure function for deck damage and failure analysis. The good agreement between the FEA results with the tested data shows that FEA with ply-level information can be used to predict FRP deck behavior. In the following section, the behavior of the unsupported edge will be investigated via FEA with ply-level information using composite element.

#### *5.3.3.2 FEA results for loadings at the free edge*

When conducting analysis for the free edge, the deck is loaded at one free edge, with a uniform pressure of 216.7 psi (1.5 MPa) over a 8"×15" (203.2×381mm) rectangular area representing a 26 kips (115.6 kN) total loading. The symbols are the same as in the previous section. In the FEA model, the X direction is the longitudinal direction (pultrusion direction), the Y direction is the transverse direction and the Z direction is the vertical (through the thickness) direction. The numerical values of deflection, stresses and strains are at X=51" (1295.4mm). In the result plots, the X direction is the longitudinal direction; the Y direction is the transverse direction and the Z direction is the vertical direction. The symbol SX means normal stress in the X (longitudinal direction); SXY means shear stress in XY plane, and so on. The symbol EPTOX denotes normal strain in the X direction; EXPOXY denotes shear strain in XY plane, etc. For each analysis, contour plots are provides for the overview of the stress/strain distribution; the location – deflection, location – stress and location – strain curves are presented for numerical comparisons. No test data are available for this situation. This is predicting analysis is conducted to investigate the stress/strain scenario using a simulated tire loading under designed loading (26 kips).

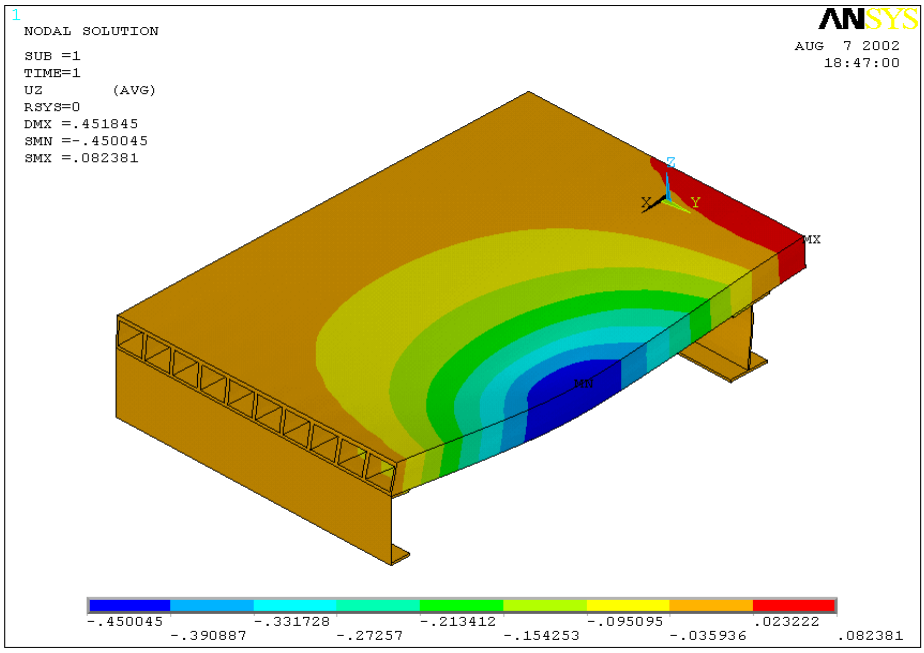


**Figure 5.69** Deflection Contour Loaded at the Free Edge

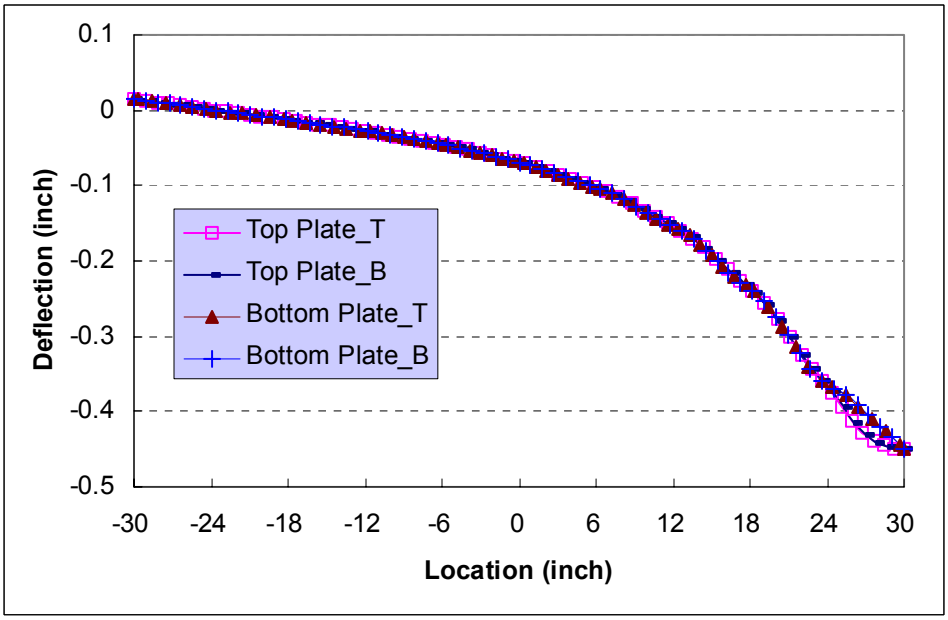


**Figure 5.70** Deflection Comparisons Loaded at the Free Edge

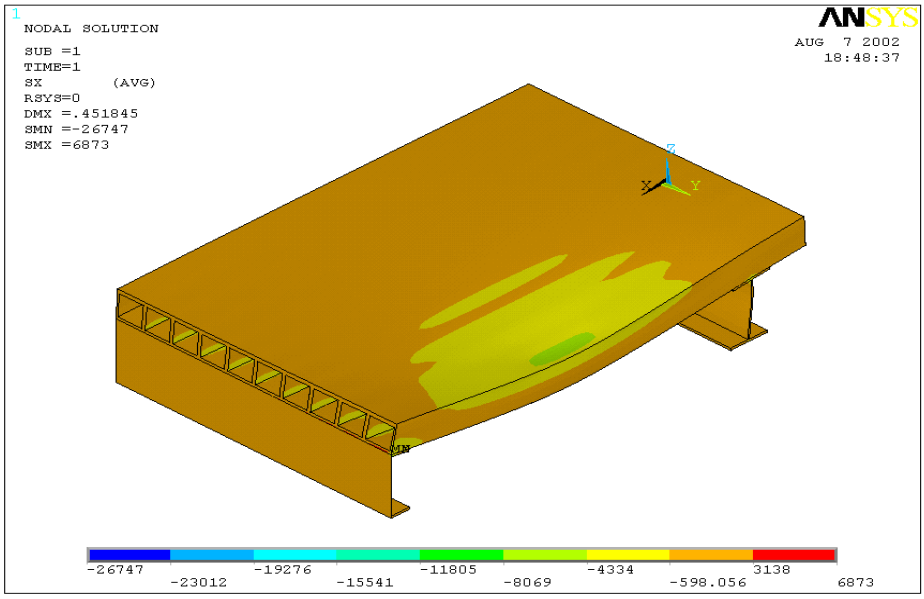


**Figure 5.71** Longitudinal Stress (X-stress) Contour Loaded at the Free Edge

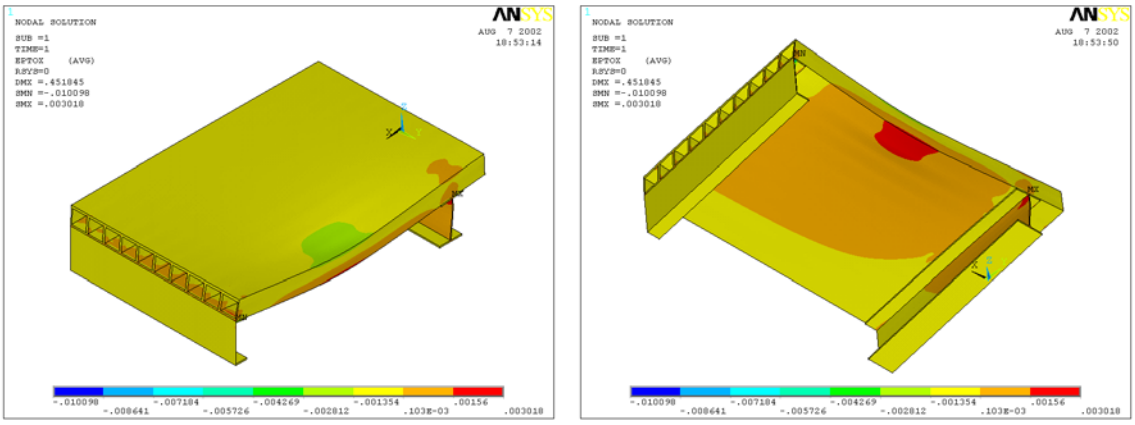


**Figure 5.72** Longitudinal Strain (X-strain) Contour Loaded at the Free Edge

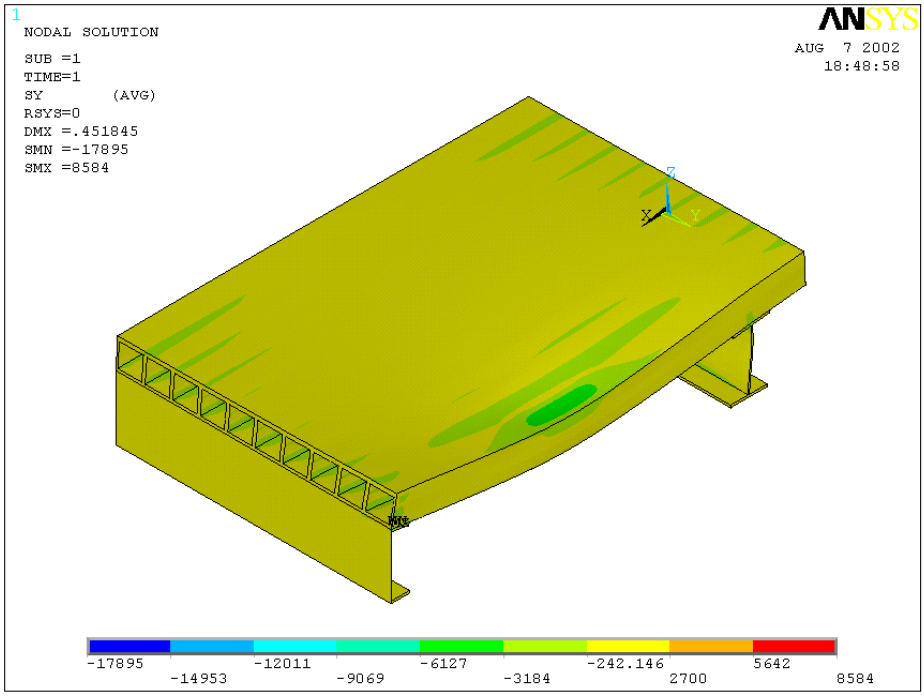


**Figure 5.73** Transverse Stress (Y-stress) Contour Loaded at the Free Edge

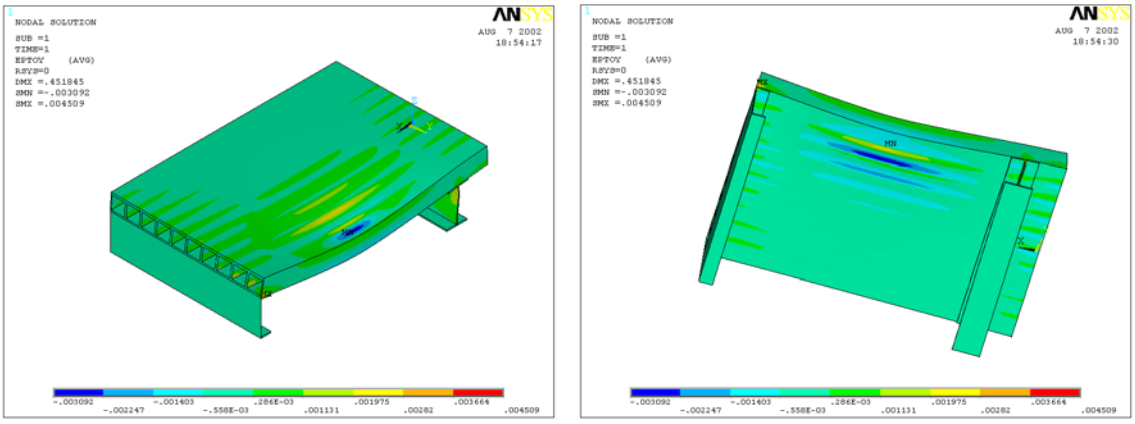


**Figure 5.74** Transverse Strain (Y-strain) Contour Loaded at the Free Edge

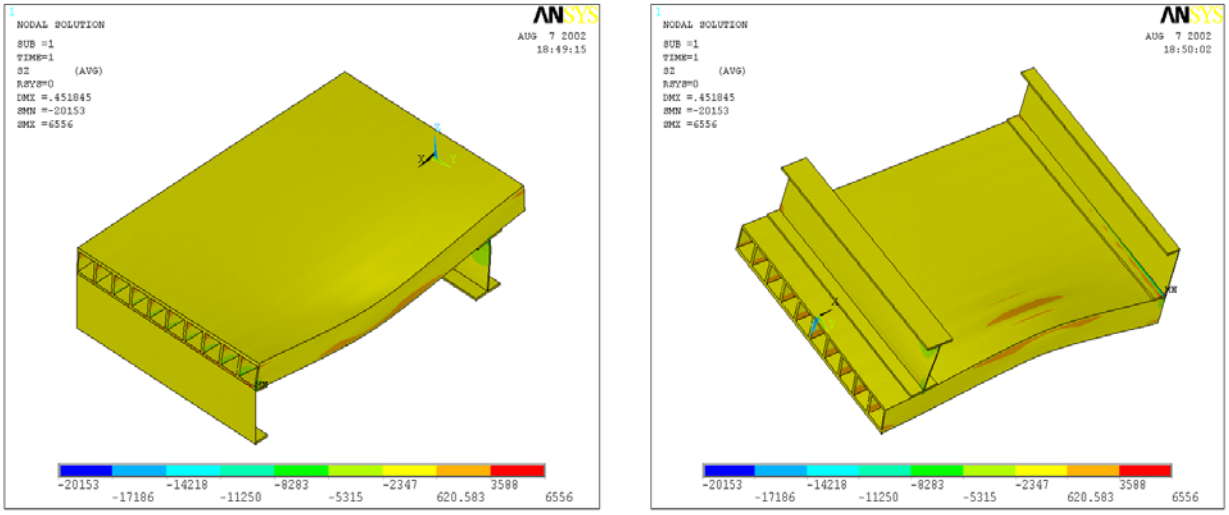


**Figure 5.75** Vertical Stress (Z-stress) Contour Loaded at the Free Edge

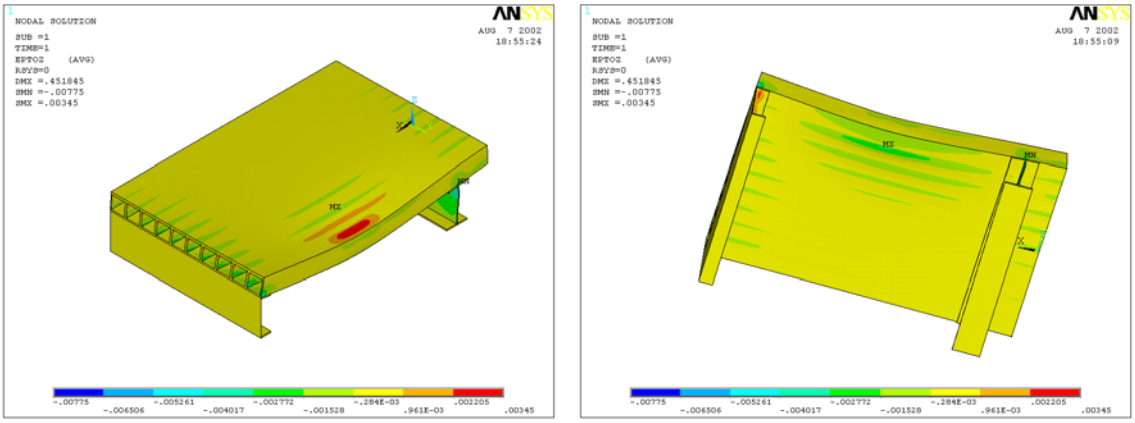


**Figure 5.76** Vertical Strain (Z-strain) Contour Loaded at the Free Edge

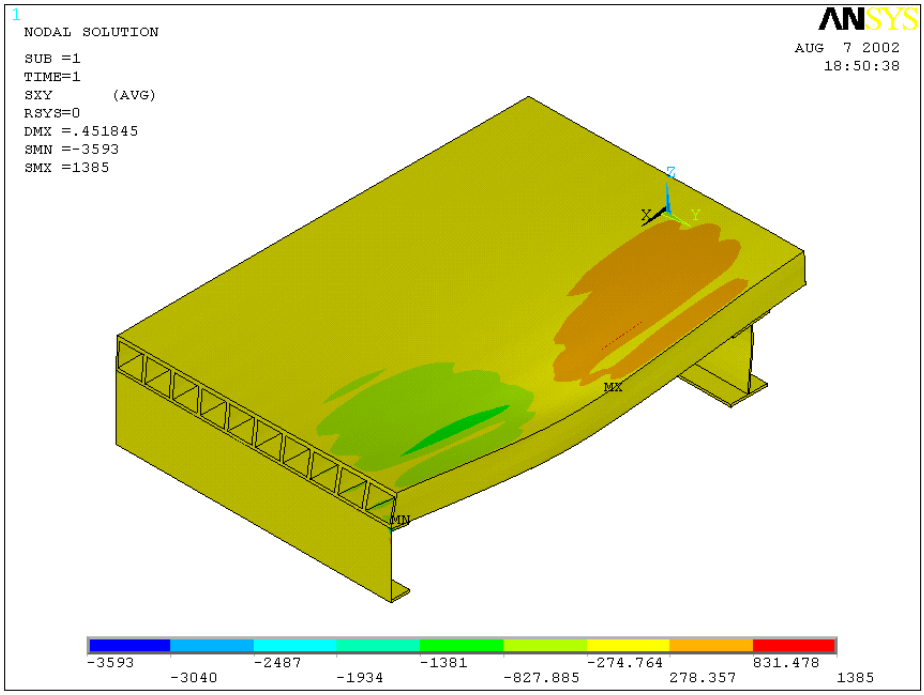


**Figure 5.77** In-plane Shear Stress (XY-stress) Contour Loaded at the Free Edge

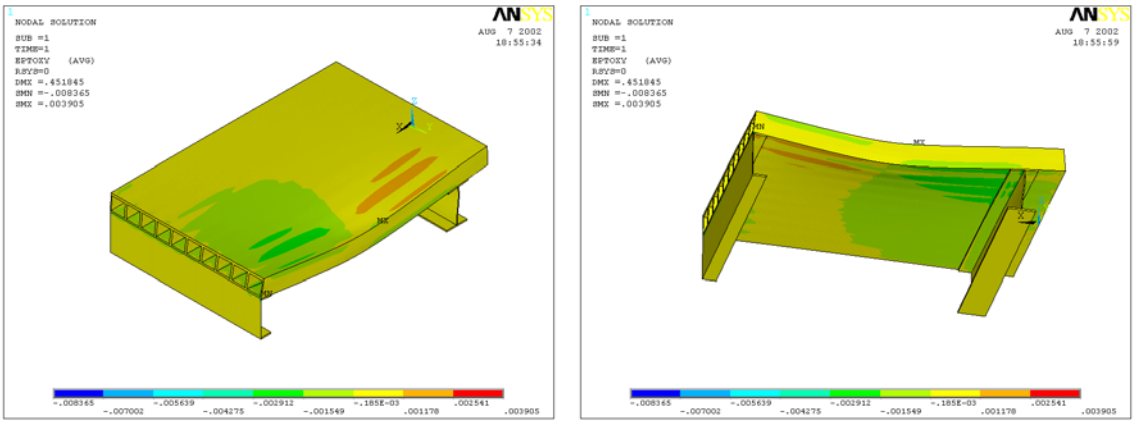


**Figure 5.78** In-plane Shear Strain (XY-strain) Contour Loaded at the Free Edge

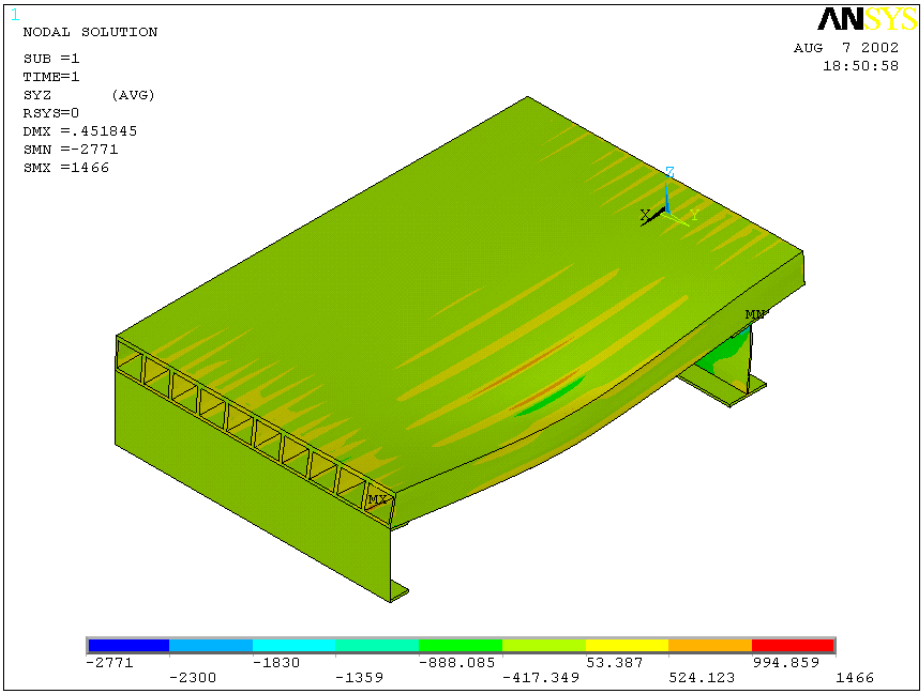


**Figure 5.79** Out-of-plane Shear Stress (YZ-stress) Contour Loaded at the Free Edge

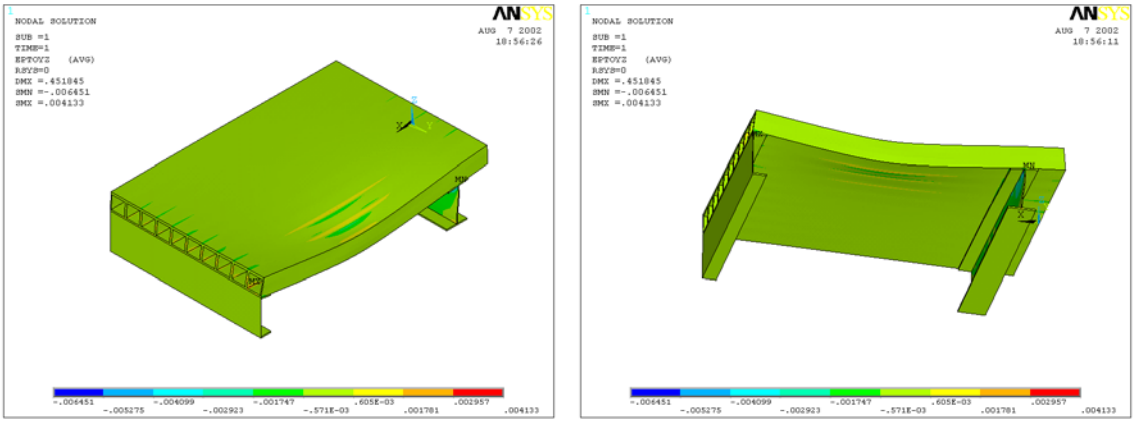


**Figure 5.80** Out-plane Shear Strain (YZ-strain) Contour Loaded at the Free Edge

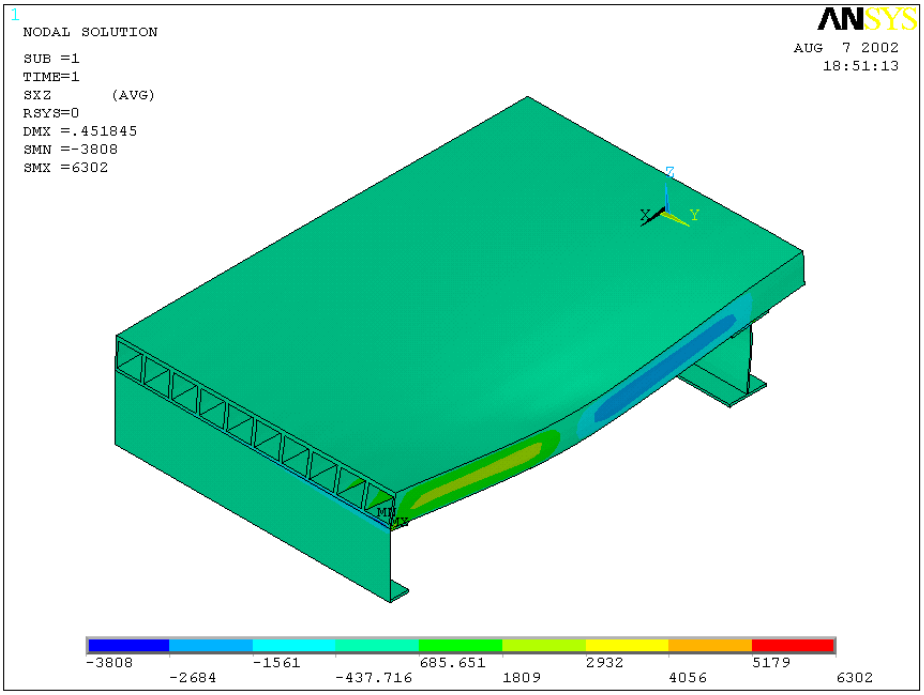


**Figure 5.81** Out-of-plane Shear Stress (XZ-stress) Contour Loaded at the Free Edge

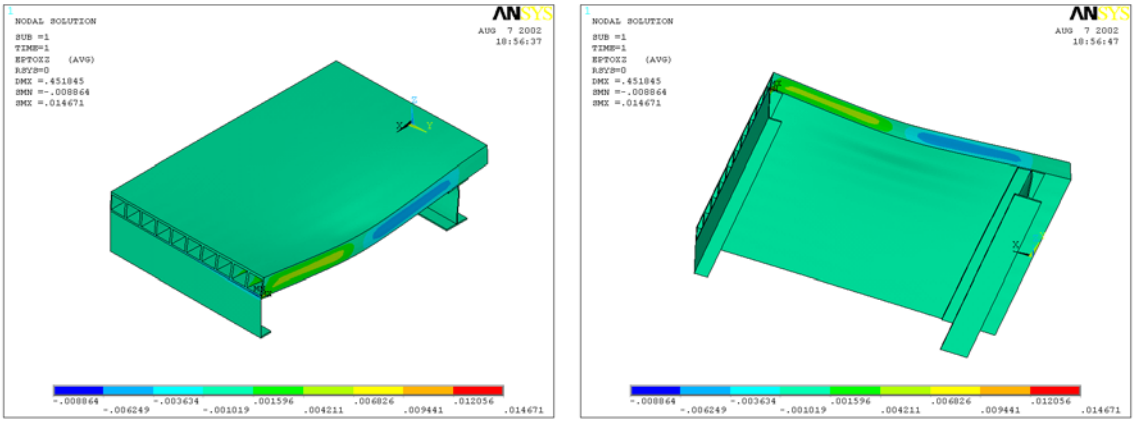


**Figure 5.82** Out-of-plane Shear Strain (XZ-strain) Contour Loaded at the Free Edge

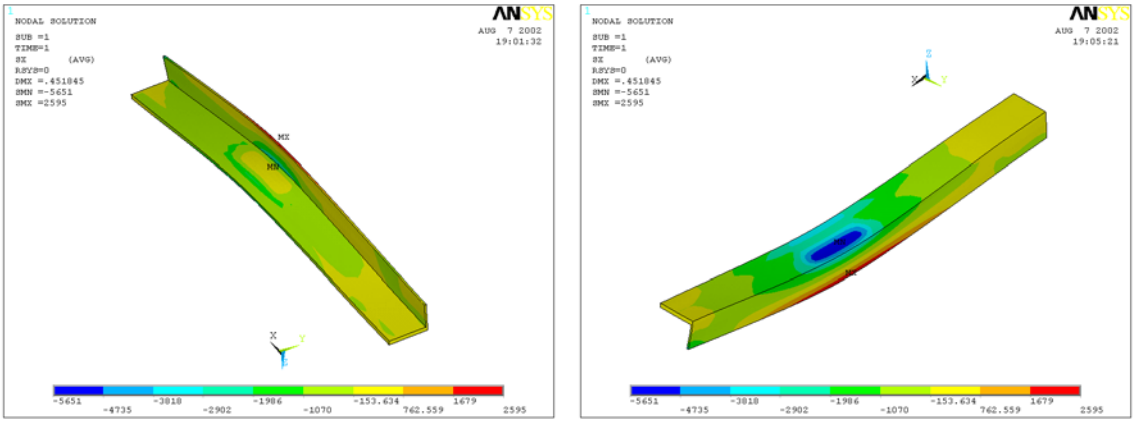


**Figure 5.83** Free Edge Longitudinal Stress (X-stress) Contour Loaded at the Free Edge

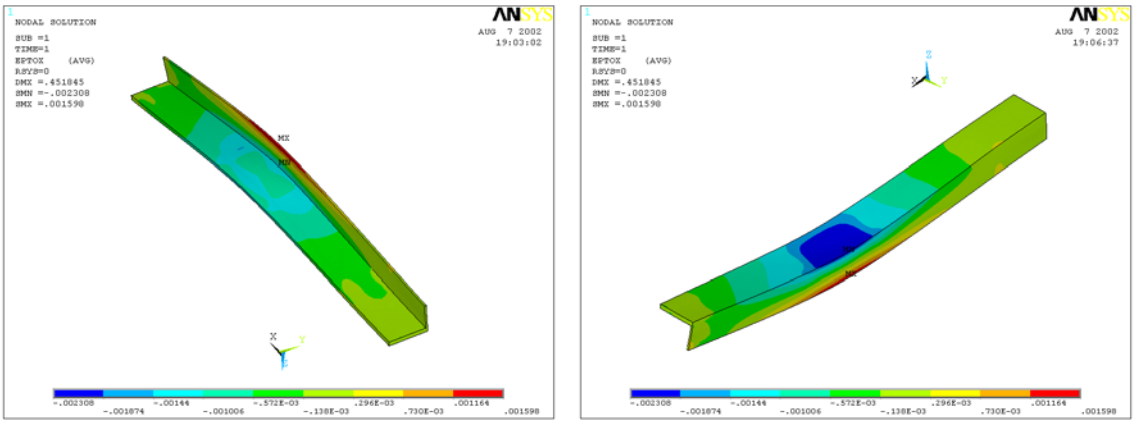


**Figure 5.84** Free Edge Longitudinal Strain (X-strain) Contour Loaded at the Free Edge

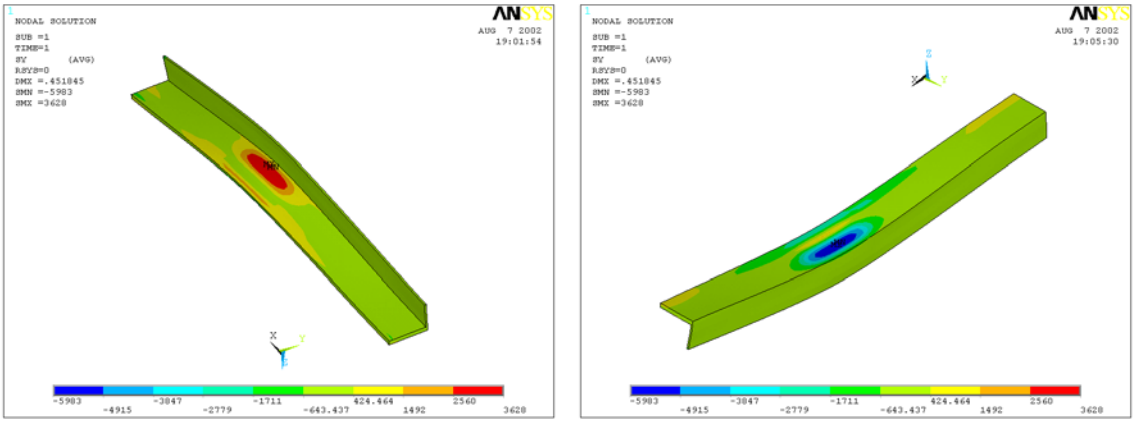


**Figure 5.85** Free Edge Transverse Stress (Y-stress) Contour Loaded at the Free Edge

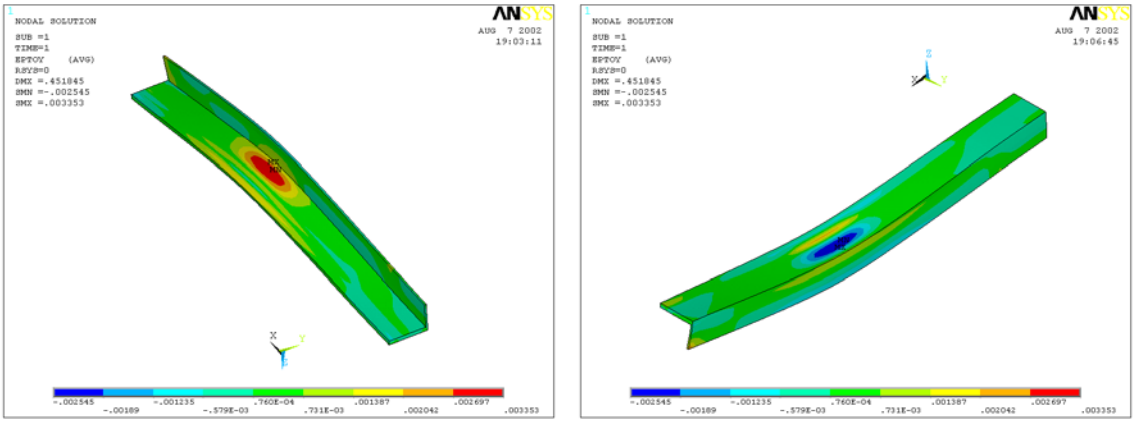

**Figure 5.86** Free Edge Transverse Strain (Y-strain) Contour Loaded at the Free Edge

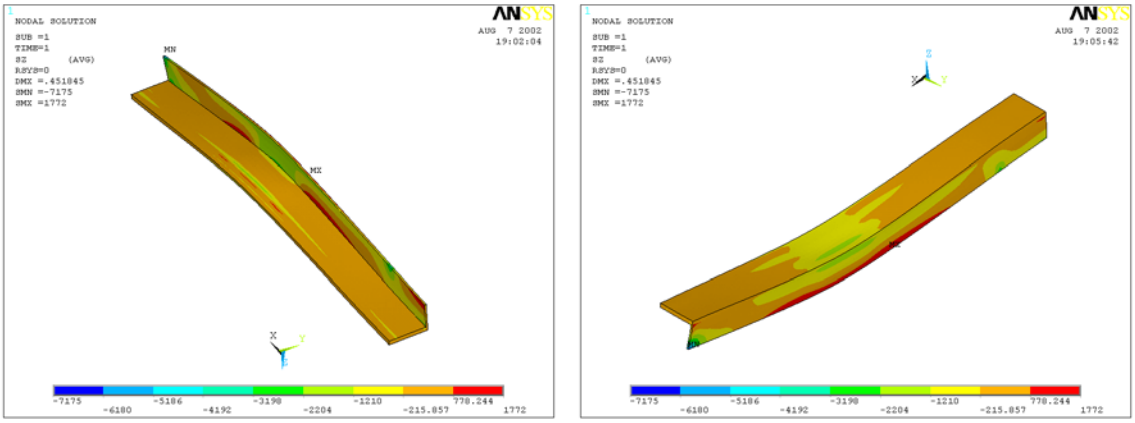

**Figure 5.87** Free Edge Vertical Stress (Z-stress) Contour Loaded at the Free Edge

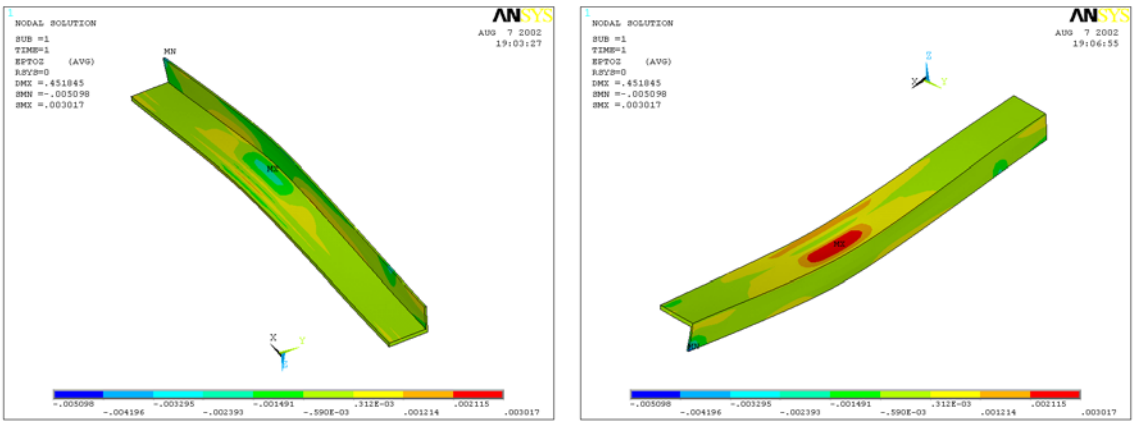

**Figure 5.88** Free Edge Vertical Strain (Z-strain) Contour Loaded at the Free Edge

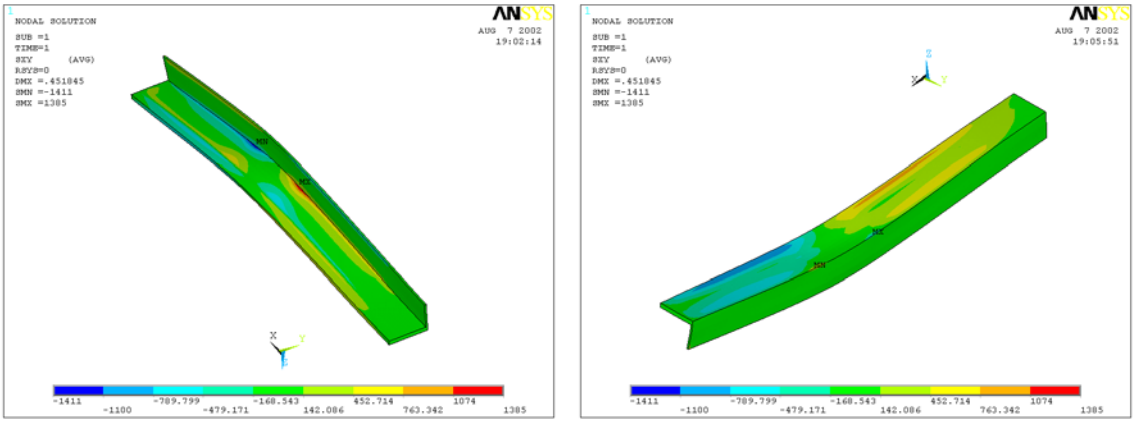


**Figure 5.89** Free Edge Shear Stress (XY-stress) Contour Loaded at the Free Edge

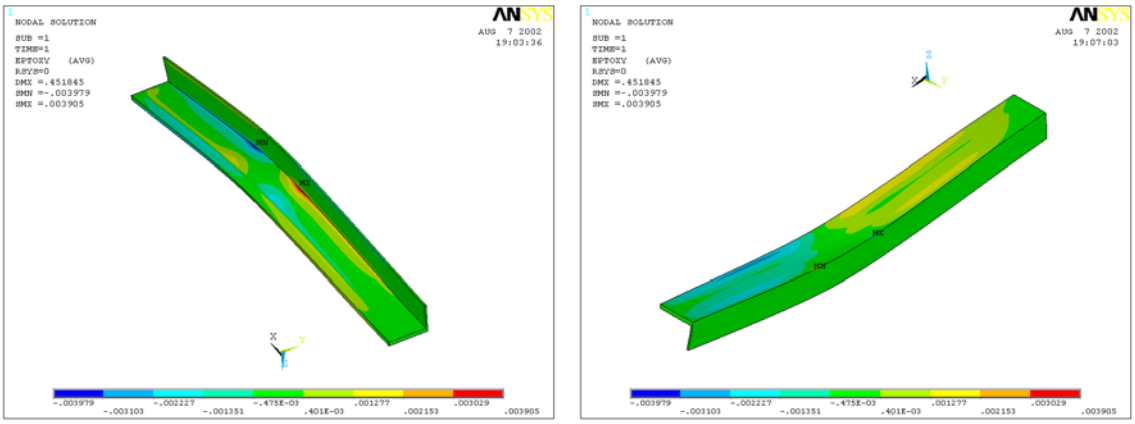


**Figure 5.90** Free Edge Shear Strain (XY-strain) Contour Loaded at the Free Edge

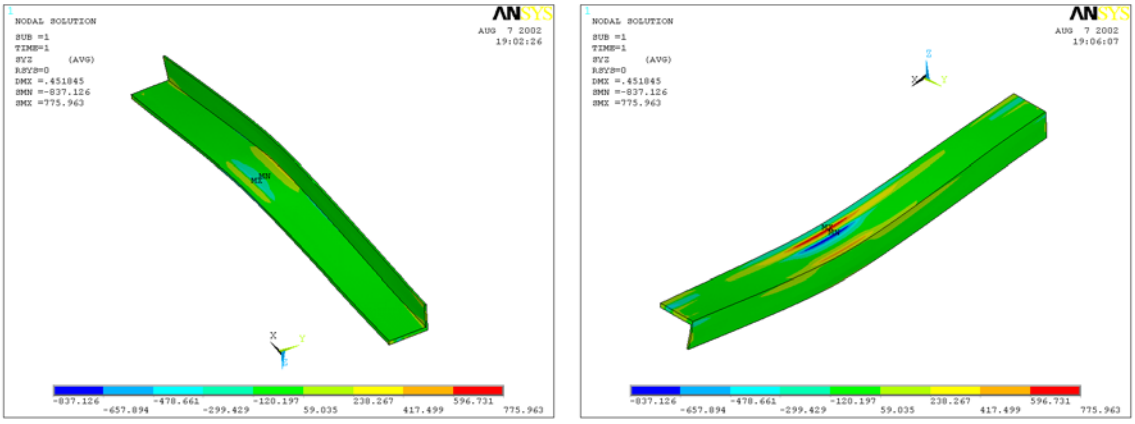


**Figure 5.91** Free Edge Shear Stress (YZ-stress) Contour Loaded at the Free Edge

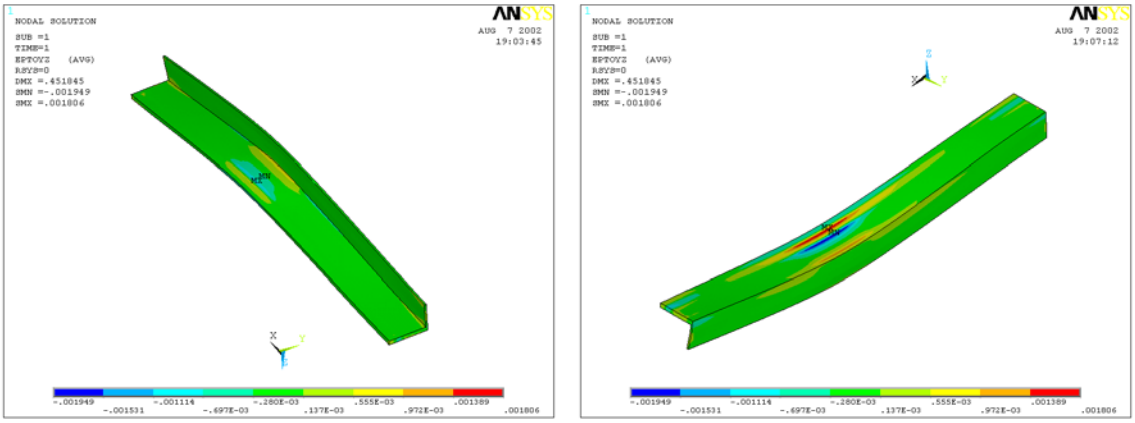


**Figure 5.92** Free Edge Shear Strain (YZ-strain) Contour Loaded at the Free Edge

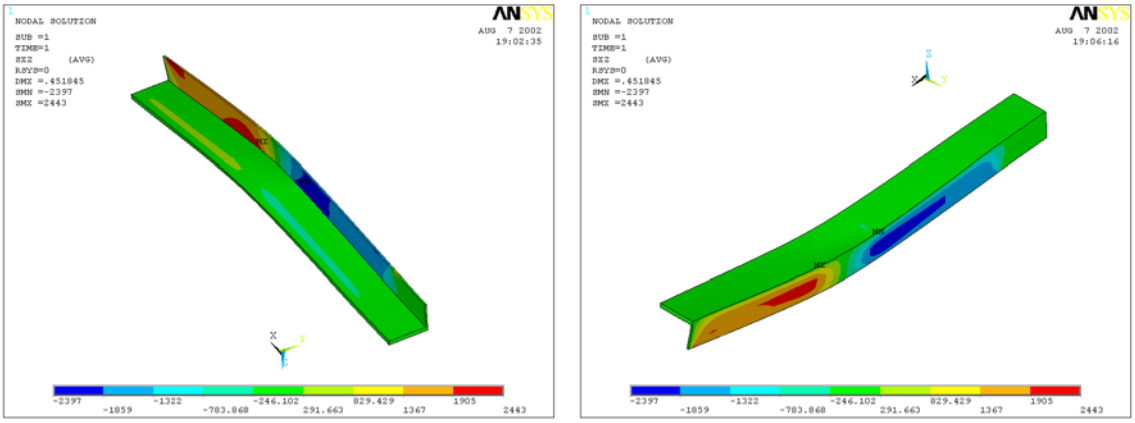


**Figure 5.93** Free Edge Shear Stress (XZ-stress) Contour Loaded at the Free Edge

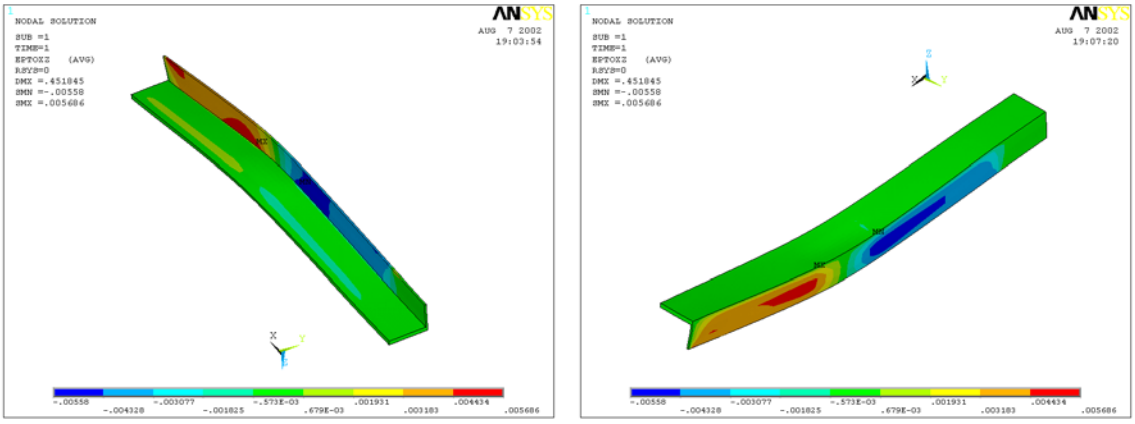


**Figure 5.94** Free Edge Shear Strain (XZ-strain) Loaded at the Free Edge

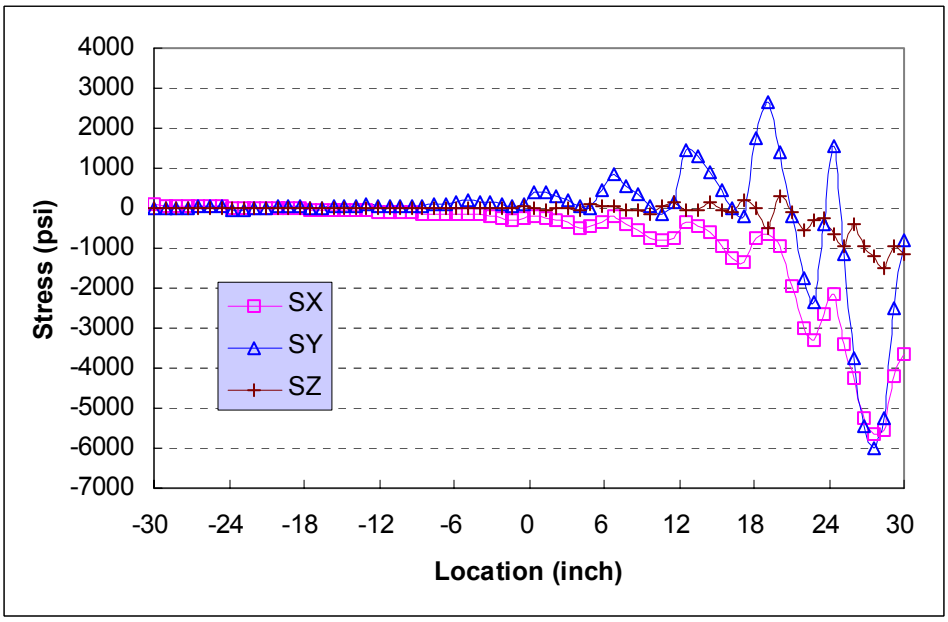


**Figure 5.95** Normal Stresses for Top Plate's Top Surface Loaded at the Free Edge

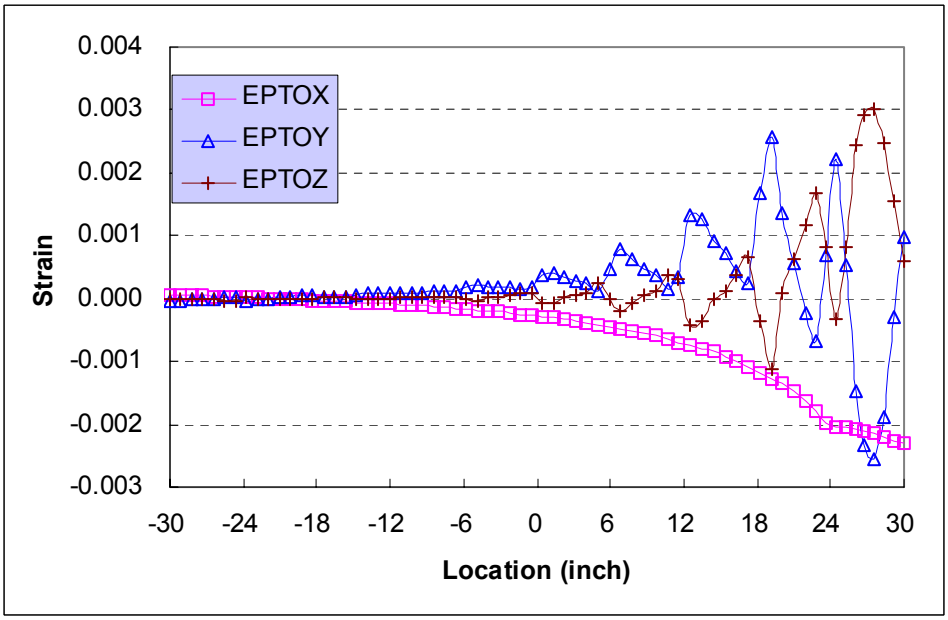


**Figure 5.96** Normal Strains for Top Plate's Top Surface Loaded at the Free Edge

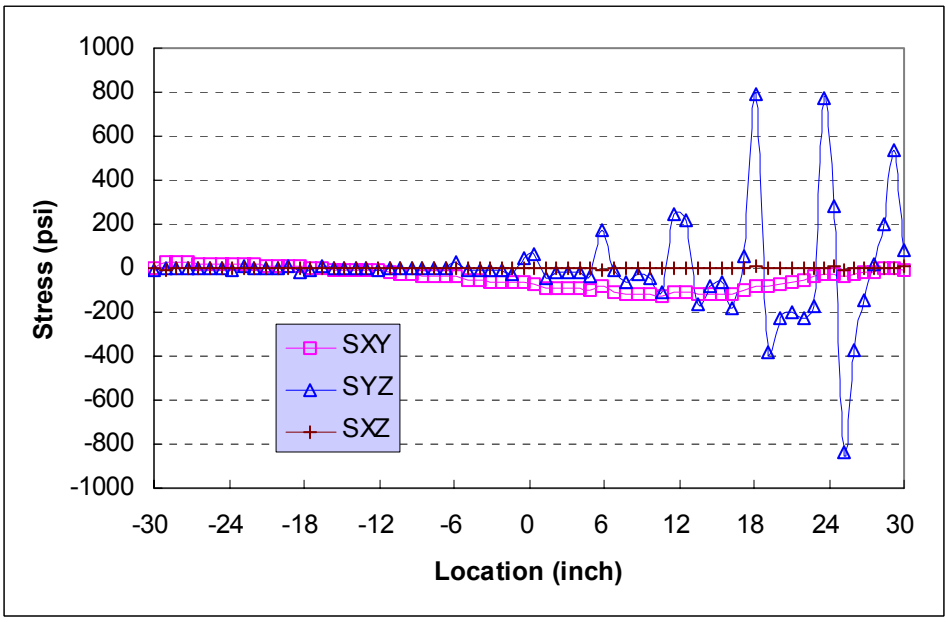


**Figure 5.97** Shear Stresses for Top Plate's Top Surface Loaded at the Free Edge

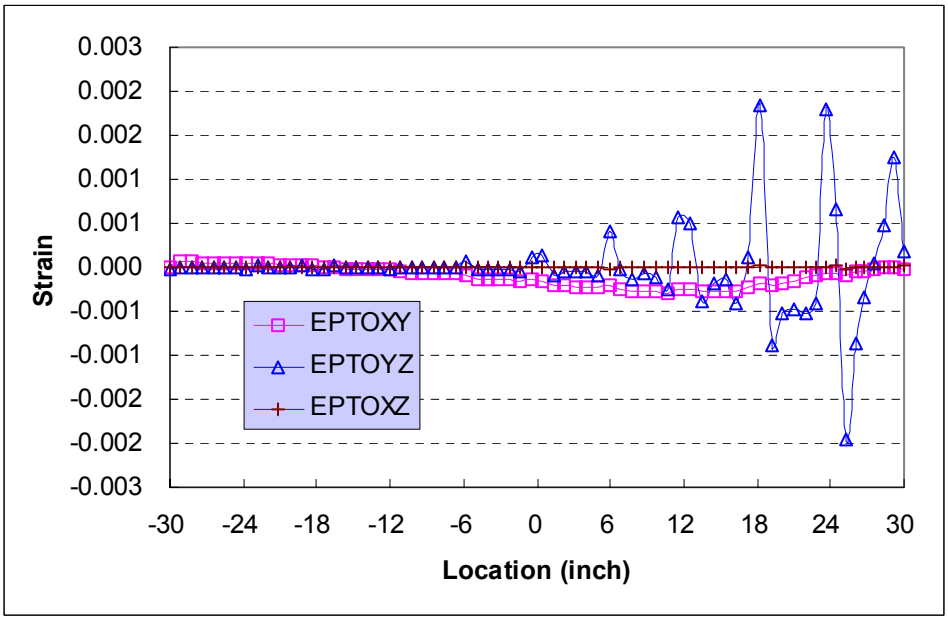


**Figure 5.98** Shear Strains for Top Plate's Top Surface Loaded at the Free Edge

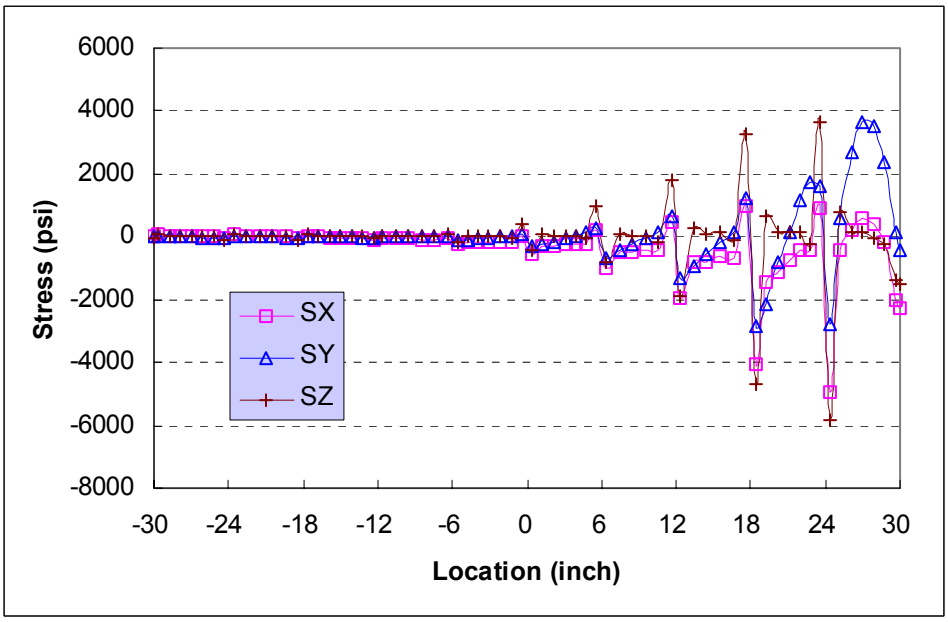


**Figure 5.99** Normal Stresses for Tube Top Flange's Bottom Surface Loaded at the Free Edge

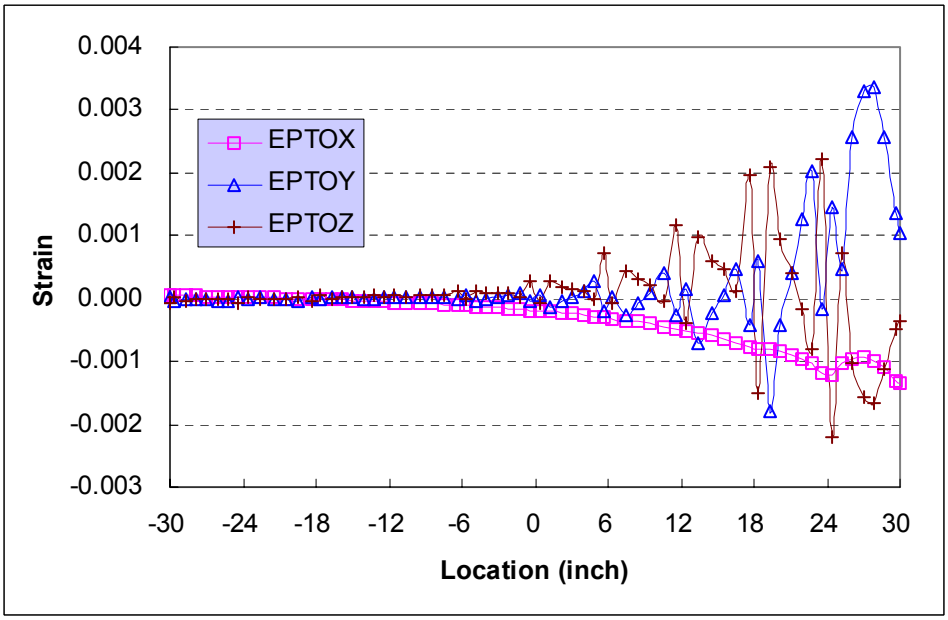


**Figure 5.100** Normal Strain for Tube Top Flange's Bottom Surface Loaded at the Free Edge

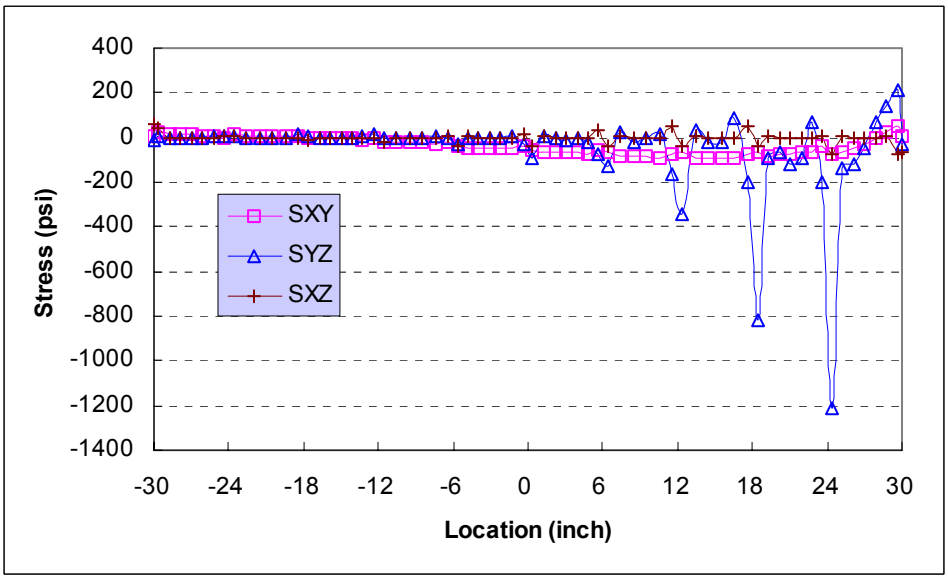


**Figure 5.101** Shear Stresses for Tube Top Flange's Bottom Surface Loaded at the Free Edge

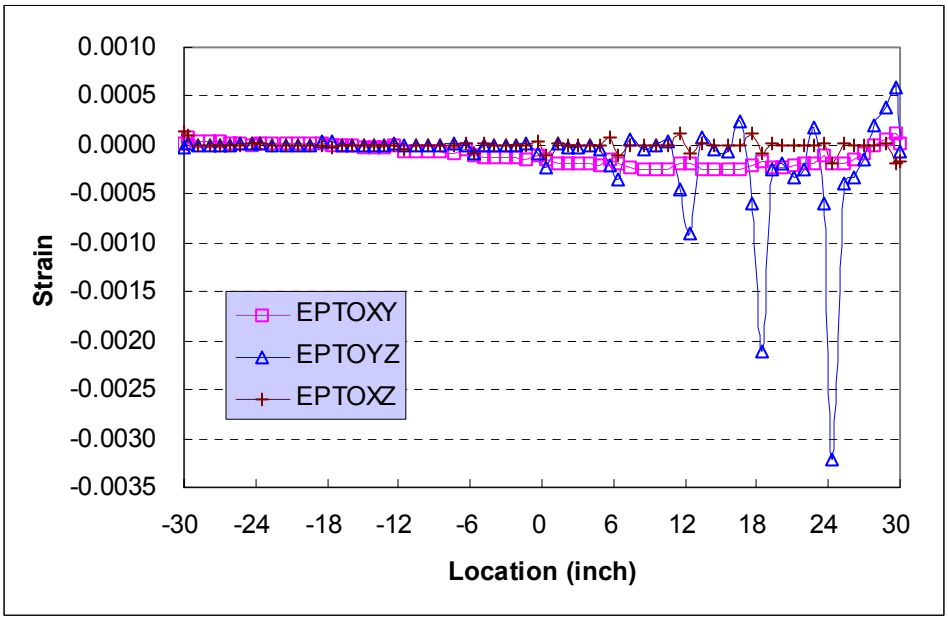


**Figure 5.102** Shear Strain for Tube Top Flange's Bottom Surface Loaded at the Free Edge

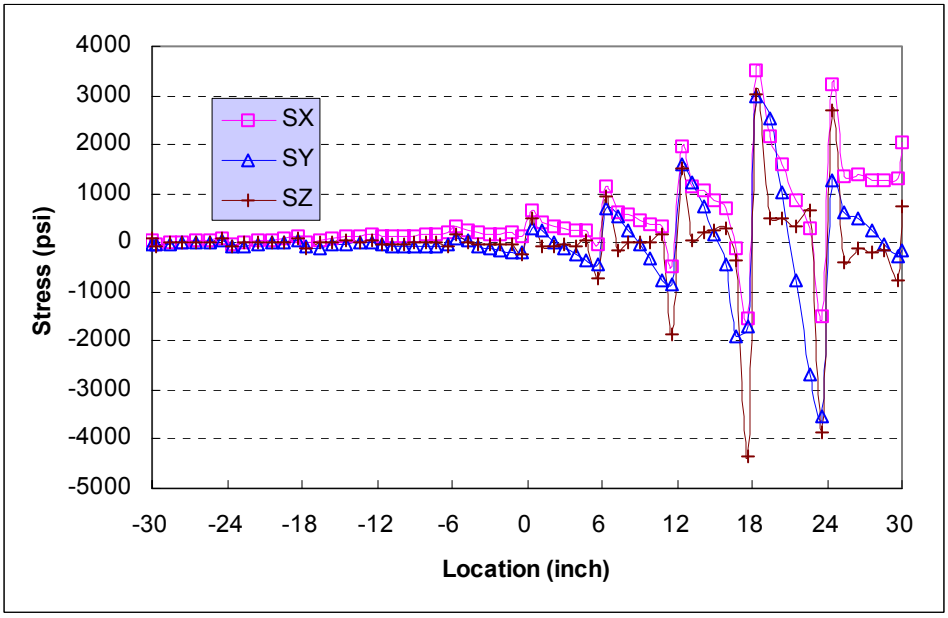


**Figure 5.103** Normal Stresses for Bottom Plate's Inner Surface Loaded at the Free Edge

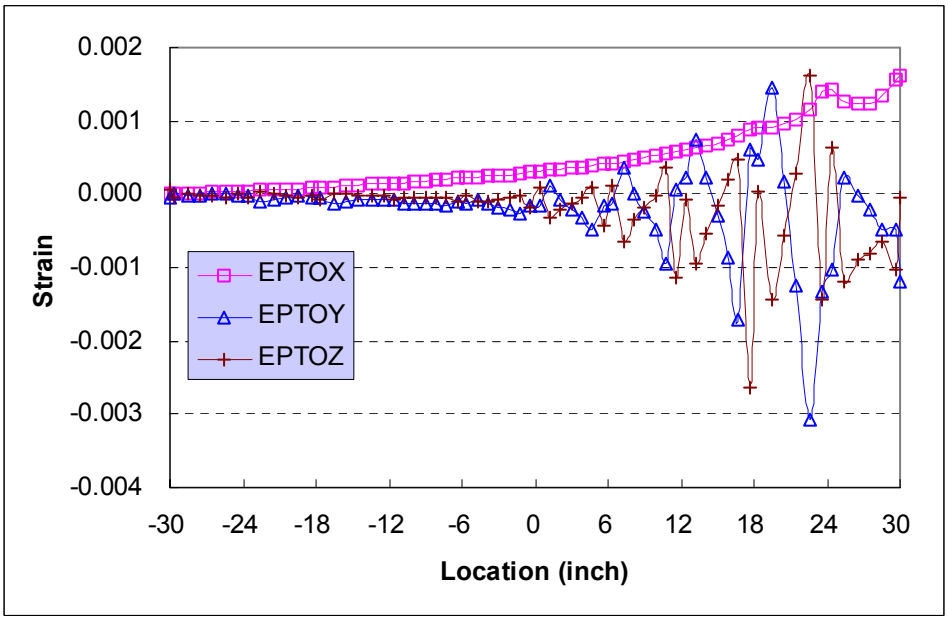


**Figure 5.104** Normal Strains for Tube Bottom Flange's Inner Surface Loaded at the Free Edge

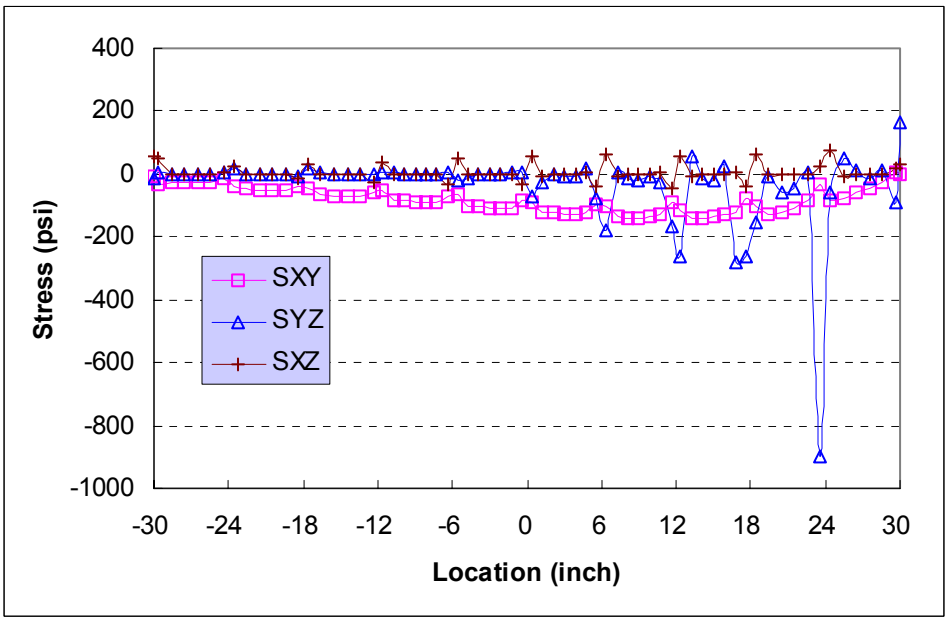


**Figure 5.105** Shear Stresses for Tube Bottom Flange's Inner Surface Loaded at the Free Edge

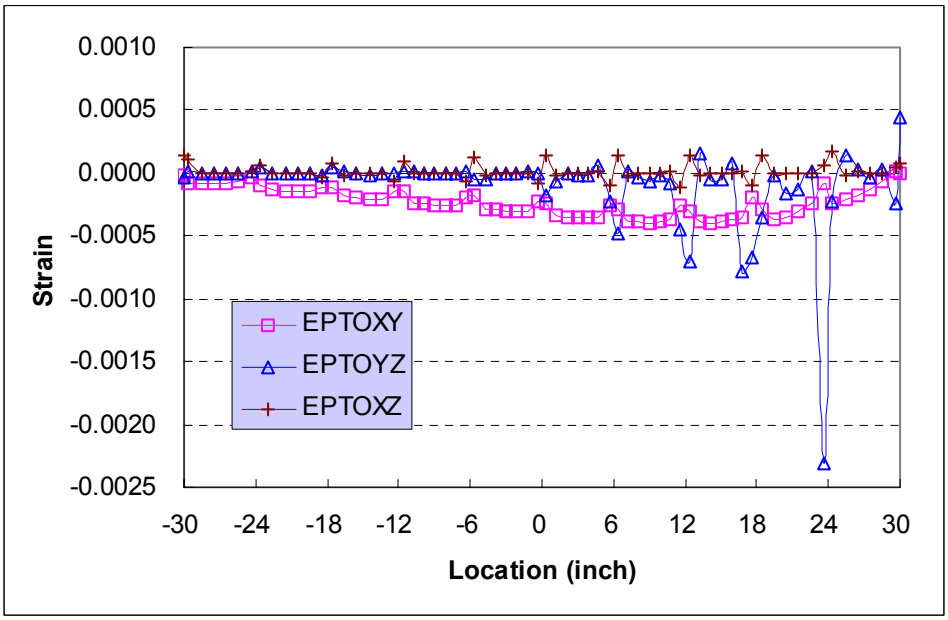


**Figure 5.106** Shear Strains for Tube Bottom Flange's Inner Surface Loaded at the Free Edge

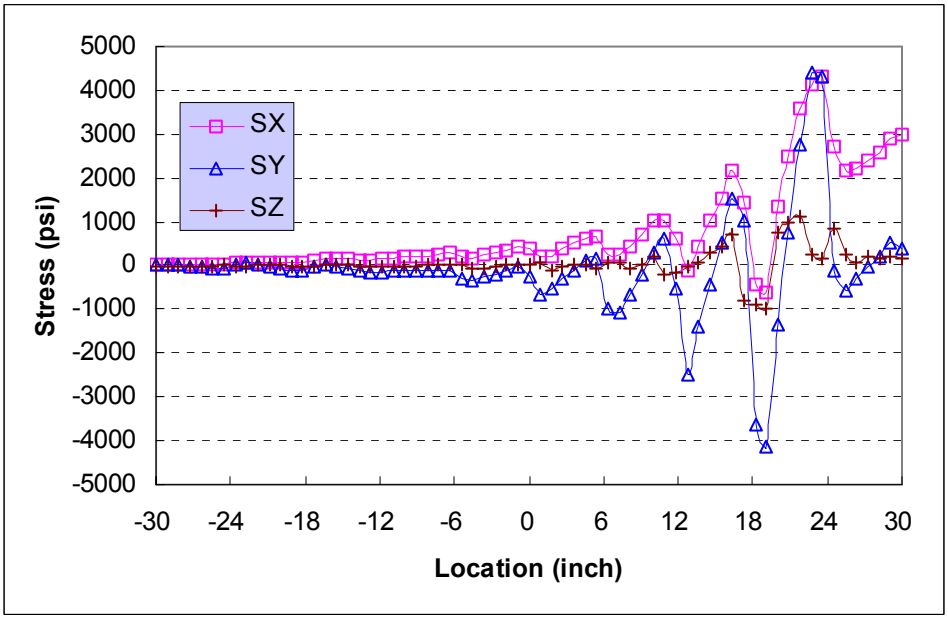


**Figure 5.107** Normal Stresses for Bottom Plate's Bottom Surface Loaded at the Free Edge

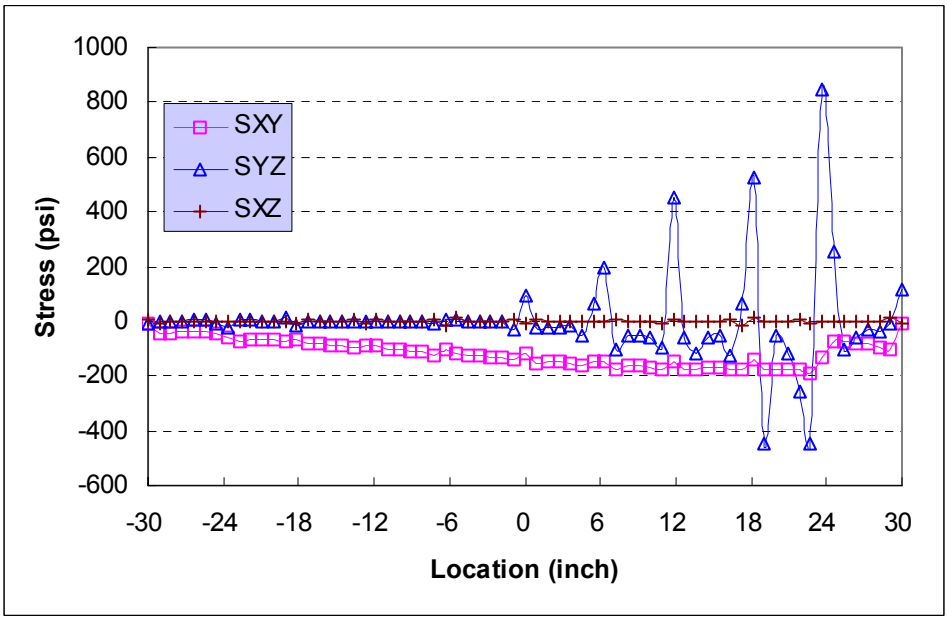


**Figure 5.108** Shear Stresses for Bottom Plate's Bottom Surface Loaded at the Free Edge

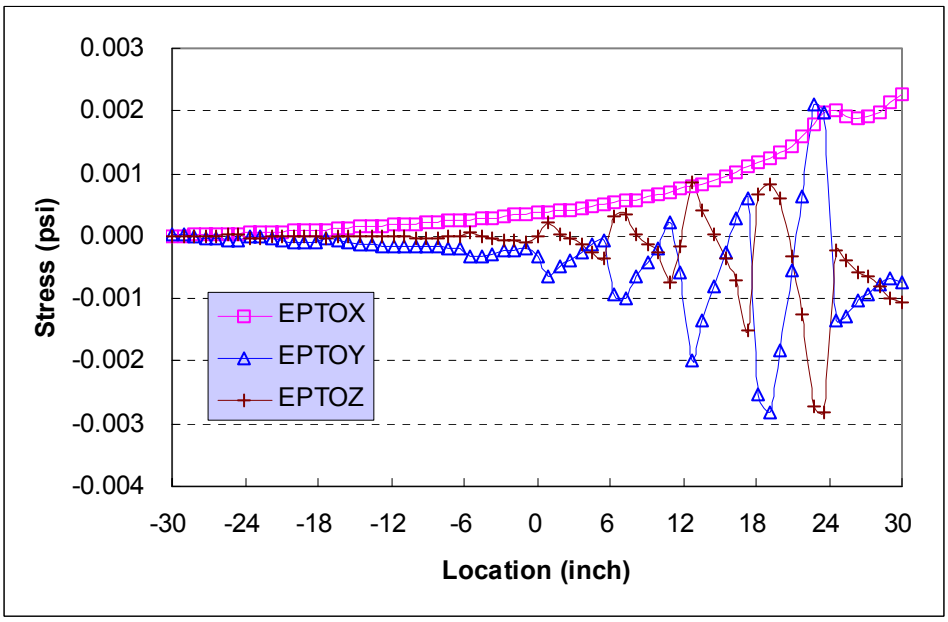


**Figure 5.109** Normal Strains for Bottom Plate's Bottom Surface Loaded at the Free Edge

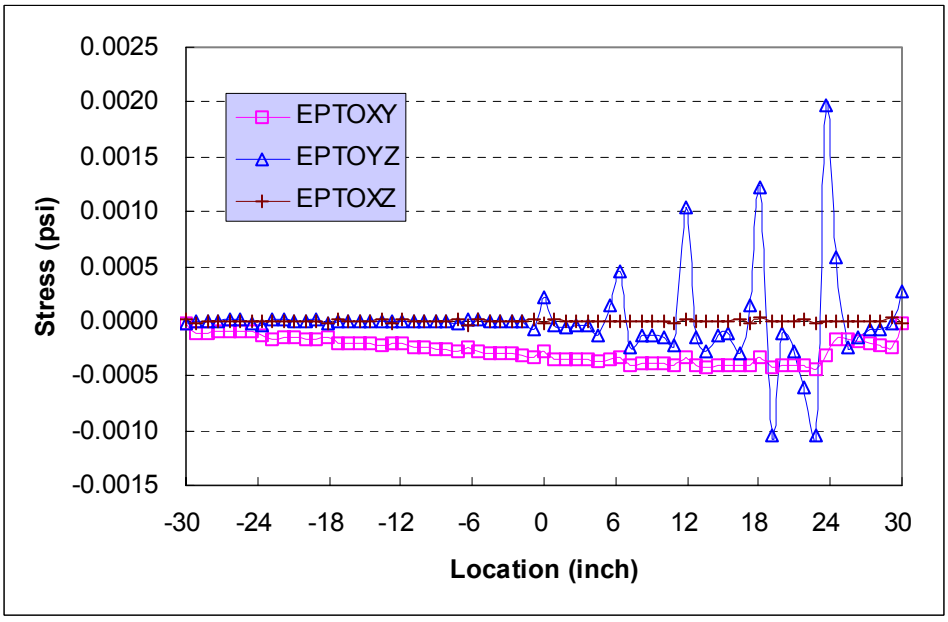


**Figure 5.110** Shear Strains for Bottom Plate's Bottom Surface Loaded at the Free Edge

The contour of the vertical deflection (in Z direction) is shown in Fig. 5.69. The comparisons of deflection (at X=51" (1295.4mm)) from FEA for different deck components are shown in Fig. 5.70. The predicted maximum deflection at the free edge is –0.45" (11.4mm) (Fig. 5.70) for all components: top plate, and bottom plate.

The normal stress and strain contours are shown in Fig. 5.71-5.76. The shear stress and shear strain contours are shown in Fig. 5.77-5.82. The stress and strain contours for the free edge's top plate and the outmost tube's vertical web are shown in Fig. 5.83-5.94. Dominate stress/strain concentrations occur in the transverse direction when loaded at the span center (Fig. 5.37 and 5.38). However, the situation is more complicated when loaded at the unsupported (or free) edge. In addition to normal stress/strain concentrations (Fig. 5.71-5.76), all shear stresses and strain also concentrate at the free edge (Fig. 5.77-5.82). The failure function for the free edge is not as simple as loaded at the span center. Possible damage and failure modes and locations may vary according to different stress/strain concentration scenario to different locations along the unsupported edge.

A close view at the free edge gives us more specific information (Fig. 5.83-5.94). The concentration of Z-stress and strain is at the tube's corner where its vertical web and horizontal flange intersect (Fig. 5.87 and 5.88). The shear stresses and strains XY-stress/strain and YZ-stress/strain concentrate at this corner too, as it can be observed from Figures 5.89-5.92. These stress/strain concentrations at the corner may explain the failure of the internal tube as shown in Figures 5.25 and 5.26.

The numerical location-stress/strain curves at X=51" (1295.4mm) are shown in Fig. 5.95-5.110. In these plots, the horizontal coordinate denotes the variation of transverse locations, where $Y = -30" - +30"$. The following interested parts are investigated: Top Plate's top surface (Fig. 5.95-5.98), Tube Assembly top flange's bottom surface (Fig. 5.99-5.102), Tube Assembly bottom flange's inner surface (Fig. 5.103-5.106), and Bottom Plate's Bottom surface (Fig. 5.107-5.110). Maximum transverse compressive stress and stain occur at $Y = 27.6"$ (701mm), which is $2.4"$ (61mm) to the edge $Y = 30"$ (762mm) for the top plate's top surface (Fig. 5.95-5.96). Maximum transverse tensile stress and stain is predicted at $Y = 27"$ (685.8mm), which is

$3"$ (76.2mm) to the edge $Y = 30"$ for the tube top flange's inner surface (Fig. 5.99-5.100). Maximum transverse compressive stress and stain is predicted at $Y = 23"$ (584.2mm) for the tube bottom flange's inner surface (Fig. 5.103-5.104). Maximum transverse tensile stress and stain is also predicted at $Y = 23"$ (584.2mm) for the bottom plate's bottom surface (Fig. 5.107-5.108). The out-of-plane shear stress and shear strain in the YZ are dominant shear stress and strain with the location close to $Y = 24"$ (609.6mm) (the vertical tube web location) for all components.

From Figure 5.95, we observed high stress gradient of transverse stress at the top plate's top surface: the Y-stress goes from – 6000 psi (41.4 MPa) to – 1000 psi (6.9 MPa) in 2.4 inches (61 mm). Also from Figure 5.98, high stress gradient of the out-of-plane shear stress YZ-stress is also observed. The direction change of the transverse strain (Y-strain) in Figure 5.95 suggests that the top plate's top surface experiences compression to extension from $y = 27.6$ inch (701mm) to $y = 30$ inch (762mm), the free edge. Results from Figures 5.99 and 5.100 show that the transverse stress and strain (Y-stress/strain) are positive, and therefore, the tube top flange's inner surface is in extension state in the transverse direction.

From this FEA results, no severe stress/strain concentration is observed at the simply supported end. However, slight vertical stress and strain concentrations at the simply supported end can be observed from Figures 5.90 and 5.97. This indicates that the end cracks as shown in Figure 5.24 developed from central cracking at the edge center.

## 5.4 Strength testing and design recommendations

The preliminary proposed strength testing and design guidelines for FRP decks for bridge rehabilitation and new bridge construction are summarized as following:

(1) The thin-walled FRP structure should be fabricated without losing its structural integrity, such as fewer cutouts from the system.

(2) As lab testing results showed, different failure modes for the thin-walled cellular FRP deck systems can be achieved using simulated tire patch and steel patch. The results suggest that the testing patch is a factor influencing the deck's failure modes. This factor should be considered in deck failure testing.

(3) Since high stress/strain gradients at some locations were observed from FEA, the location of strain gages must be carefully controlled to measure strains at these high stress/strain gradient locations.

(4) Detailed local analysis for local stress/strain distributions for critical locations must be conducted to consider local behavior of this thin-walled FRP system.

(5) Care must be taken in design or construction with free edges, as the stress/strain state at the free edge is very complicated for this thin-welled structure. Supported edges are recommended in practical bridge deck design and construction.

(6) The high stress/strain concentration at the tube corner requires improvement for the design and fabrication of the tube corner, such as more fiber reinforcement in this region.

(7) The transverse direction is the weak direction, and the weakness in the transverse direction needs to be improved.

# CHAPTER VI

# CONCLUSIONS AND FUTURE RESEARCH

## 6.1 Conclusions from current research

### 6.1.1 Contributions to deck analysis and design

The stiffness analysis procedures in this research extend the FRP bridge deck analysis to complete orthotropic plate analysis with various boundary conditions. A systematic analysis procedure based on CLPT was developed for the stiffness analysis of thin-walled multi-cellular FRP bridge deck systems. This procedure used the Method of Elastic Equivalence to model the FRP deck system as an equivalent orthotropic plate. This research detailed and evaluated the MEE procedure to calculate the overall equivalent deck properties (stiffnesses and nine independent orthotropic material properties) from its components, and provided detailed bending analysis procedure for single-span bridge decks with various boundary conditions (the Navier type deck, the Levy type decks and other types of bridge decks). This method gives reasonable bending deflection predictions for uniformly distributed load and rectangular patch loading using CLPT. While, the deck's bending deflection under point load could not be accurately predicted using this method because of the local bending behavior of the cellular components under point load. FEA or higher order plate theories can give better prediction for point load. However, the MEE method can be used as a practical method to predict the plate stiffnesses and properties of cellular FRP decks. The plate bending analysis could be used as references and procedures for deck design engineers to calculate deck's maximum deflections for various boundary and loading conditions. This procedure can be further developed for the analysis of continuous bridge deck and analysis using higher order plate theories.

A deck failure function method was developed for predicting the failure of FRP decks. This method used available strength function theory to subdivide the deck failure mode analysis to its associated failure function analysis. Using developed laminated composite materials theories, and the finite element analysis, this research proposed a strength and failure analysis philosophy for an FRP deck system, and conducted and detailed ply-level strength analysis for the deck system. The failure function method gave very good damage and failure predictions for central loading, as compared to the Tsai-Wu and Tsai Hill criteria. The stress/strain state at the free edge was also investigated through FEA. The ply-level strength analysis will provide useful information for bridge deck designers when designing the lay-up of each deck component. The contributions of the failure function method and the strength analysis philosophy based on ply-level composite analysis are original in FRP deck research community.

### 6.1.2 Contributions to deck testing

Two schemes of loading patches were used in this research: a steel patch made according to the ASSHTO's bridge testing specifications; and a tire patch made from real truck tire reinforced with silicon rubber. The tire patch was specially designed to simulate service loading conditions by modifying real contact load from tire. Our research showed that the effects of the stiffness and contact conditions of loading patches were significant in the stiffness and strength testing of FRP decks. Due to the localization of load, a simulated tire patch yielded larger deflection than the steel patch under the same loading level. The tire patch produced greatly different failure modes compared to the steel patch. Reports from most previous FRP deck researchers showed the major failure mode for cellular FRP decks in lab testing is punching shear using steel patch. However, the components separation in the transverse direction using simulated tire patch observed in this research showed a different failure mode of FRP deck systems - failure in bending. The Tire Contact Area is a factor to be considered when reporting the maximum deflection and deflection index for a proposed bridge deck design: a smaller contact area gives safer testing evaluation as compared to the designed deflection limit. It is recommended that the steel patch regulated by the AASHTO specifications should be modified for testing of the capacity of cellular FRP bridge decks.

The failure of the deck system from field test showed the free (unsupported) edges effects and the fatigue loading on the deck's strength. The ply-level composite finite element analysis showed the complicated stress/strain states at the free edges.

### 6.1.3 Specific observations and conclusions

- The FRP deck system shall be analyzed as a plate (2-way bending), instead of a beam (1-way bending). Span length specification and deflection limits should be specified in two directions. It is preferred to obtain both longitudinal and transverse stiffnesses from testing.

- For thin-walled multi-cellular FRP deck system, a complete 3-D FEA should be conducted for more accurate local analysis.

- Both analytical and experimental results showed that, under same boundary conditions and loading level, the maximum deflection at the free edges is larger than at the span center. Which indicates possible failure may occur earlier at the free (or unsupported) edges than the deck center, though the unsupported edges are not normally used in practice. The larger deflection at the unsupported edges may also arise concerns related to the durability of the deck, i.e., the unsupported edges are weak regions, and will have less durability capability. The stress/strain state at the free (or unsupported) edge is complicated for this thin-walled structure; some locations have very high stress/strain concentration and high stress/strain gradient. Strength analysis showed vertical stress/strain and shear stress/strain concentrations at the free edges. FRP deck designs and installations with free edges are not recommended.

- The tested results showed that, the span with one transverse rod (west span) is stiffer and stronger than the span with 5 transverse rods (east span). The loading carrying components of FRP decks shall be designed and fabricated with fewer holes; the integrity of the deck system shall be reserved in deck fabrication.

- Debonding and holes bearing failure were observed in lab testing. No specific research has yet been conducted for these two aspects.

## 6.2 Recommendations for future research

1. Fatigue behavior of FRP bridge deck system. The damage and failure of the deck system observed from field test indicates that research on the fatigue cracking and damaging for the deck system is necessary. For bridge decks made from traditional material (concrete, steel etc.), a dynamic load allowance percent is used to account for dynamic loading of traveling vehicles. However, it is not clear whether this method can be applied to thin-walled multi-cellular bridge decks made from FRP composite materials. Research needs to be done to investigate the dynamic traveling loading on the FRP deck's performance.

2. Free (unsupported) edge effects and research to improve the free edge's performance. More analysis and testing are necessary to understand the happenings around the free edges and improve the free (unsupported) edge's performance.

3. Efficient design and characterization of panel-to-panel joints and deck-to-stringer attachments are critical for application of modular FRP bridge deck systems. The deck connector should be designed strong enough to carry bending moment and shear force produced by the deck panels. The designer shall consider the features of the connector to endure potential dynamic/impact loads, thermal expansion or shrinkage, and fatigue loads. The other consideration is that the connector and deck panels should be easily installed for field installation.

4. Research on the deck durability with temperature and moisture changes, deck fire retardant.

5. Ply-level stiffness and strength analysis and its guides for improved structural design in micro-structural level (ply-level).
6. It will be valuable to obtain analytical bending solutions for rectangular patch loading and point loading for a plate with boundary conditions other than SSSS.

# REFERENCES

AASHTO (1996). *Standard Specifications for Highway Bridges (16th Edition),* The American Association of State Highway and Transportation Officials (AASHTO), Washington, D. C., USA, 1996.

AASHTO (1998). *AASHTO LRFD Bridge Design Specifications (Second edition)*, The American Association of State Highway and Transportation Officials (AASHTO), Washington, D. C., USA, 1998.

Ahmad, S. H. and Plecnik, J. M. (1989), *Transfer of Composite Technology to Design and Construction of Bridges*. U.S. DOT Report, September, 1989.

ANSYS Inc. (2002). **ANSYS 6.1 documentation**. ANSYS Inc. distributed with ANSYS 6.1.

Aref. A. J. and Parsons, I.D. (2000) Design and performance of a modular reinforced plastic bridge. **Composite Part B: Engineering**. Vol 31: 619-628.

ASCE (2001). *Report Card for America's Infrastructure*. American Society of Civil Engineers, Washington, DC 2001.

Bakeri, B. and Sunder, S. S.(1990) Concepts for hybrid FRP bridge deck system. *Proceedings of 1st Materials Engineering Congress*, ASCE, Denver, CO. 1990, Vol. 2, pp.1006-1014.

Barker MG, Schrage SD (2000). *High Performance Steel: Design and Cost Comparisons.* Bridge Crossing, No. 16, June 2000.

Brown, B.J. (1998). Design analysis of single-span advanced composite deck-and-stringer bridge systems. Master's thesis, West Virginia University, Morgantown, West Virginia.

Case SW and Reifsnider KL (1999). MRLife 12: A strength and life prediction code for laminated composite materials. Materials Response Group, Virginia Polytechnic Institute and State University, Blacksburg, VA. USA.

Cheng L, Zhao L, Karbhari V, Seible F (2002). *Validation test of deck panel design for the I-5/Gilman Advanced Technology Bridge*. Structural Systems Research Project Report: TR-2002-03. Dept. of Structural Engineering, University of California – San Diego, May 2002.

Costa, F. J. A. (1999) Experimental characterization of the mechanical and structural properties of FRP bridge deck components. Ph.D. dissertation. Georgia Institute of Technology. Atlanta, Georgia.

Cusens AR, Pama RP (1975). **Bridge Deck Analysis**. John Wiley & Sons, Ltd. 1975.

Davey N (1961). **A History of Building Materials**. Phoenix House Ltd., London 1961.

Davalos, JF, Qiao, P, and Barbero, EJ. (1998) Design optimization of fiber reinforced plastic composite shapes. Journal of Composite Materials (USA), vol. 32, no. 2, pp. 177-196, 1998.

Dumlao C, Lauraitis K, Abrahamson E, Hurlbut B, Jacoby M, Miller A, Thomas A (1996). *Demonstration low-cost modular composite highway bridge*. In: Saadatmanesh H, Ehsani MR, editors. Proceedings of the First International Conference on Composites in Infrastructure, 1996: 114-155.

(FHWA) Federal Highway Administration (1997). FHWA Study Tour for Advanced Composites in Bridges in Europe and Japan. U.S. Department of Transportation, Washington DC, USA.

GangaRao HVS, Thippeswamy HK, Shekar V, and Craigo C (1999). *Development of Glass Fiber Reinforced Polymer Composite Bridge Deck*. **SAMPE Journal**, 35(4), 1999: 12-24.

Gibson AG, Lo CY, Lamb DW, Quinn JA (1989). *Understanding the factors controlling the pultrusion process*. **Plastic and Rubber Processing and Applications**. Vol. 12, No.4, 1989: 191-197.

Gibson RF (1994). **Principles of composite material mechanics**. McGraw Hill, New York, NY, USA.

Hambly EC (1976). **Bridge Deck Behavior**. John Wiley & Sons, Inc., New York, NY, USA.

Hayes MD, Ohanehi D, Lesko JJ, Cousins TE, Witcher D (2000). *Performance of tube and plate fiberglass composite bridge deck*. **Journal of Composites for Construction**, 4(2) 2000: 48-55.

Henry JA (1985). *Deck Girders System for Highway Bridges Using Fiber ReinforcedPlastics.* M.S. Thesis, North Carolina State University 1985.

Hyer MW (1998). **Stress Analysis Of Fiber-Reinforced Composite Materials**. WCB McGraw-Hill, Boston, Massachusetts, USA.

Jones RM (1999). **Mechanics of composite materials**. Taylor & Francis, Philadelphia, PA, USA.

Karbhari VM (1997). *On the use of composites for bridge renewal: Materials, manufacturing and durability*. Evolving Technologies for the Competitive Edge International SAMPE Symposium and Exhibition (Proceedings). SAMPE, Covina, CA, USA. Vol 42(2) 1997: 915-926

Karbhari VM, Seible F, Burgueno R, Davol A, Wernli M, Zhao L (2000). *Structural characterization of fiber-reinforced composite short and medium-span bridge systems*, **Applied Composite Materials**, 7(2) 2000: 151-182.

Karbhari VM, Zhao L (2000). *Use of composites for 21st century civil infrastructure*. **Computer methods in applied mechanics and engineering** 185 (2000): 433-454.

Karbhari VM, Wang D, Gao Y(2001). *Processing and performance of bridge deck subcomponents using two schemes of resin infusion*. **Composite Structures**. Vol.51, 2001: 257-271.

Lekhnitskii SG (1968). **Anisotropic Plates.** Gordon and Breach, New York, NY, USA.

Lekso, J. J., Davalos, J. F. (2002). "Fiber-Reinforced Polymer Decks for Bridge Systems," publishing pending.

Lopez-Anido R., GangaRao HVS, Vedam V, Overby N (1997). *Design and Evaluation of a Modular FRP Bridge Deck.* Proceedings of the International Composites Expo'97, Nashville, TN, USA, 1997: 3-E(1-6).

Mallick PK (1993). **Fiber-reinforced composites: materials, manufacturing, and design**. M. Dekker, New York, NY, USA.

McGhee, K. K., Barton, F. W. & Mckeel, W. T. (1991). *Optimum Design of CompositeBridge Deck Panels.* Advances Composites Materials in Civil Engineering Structures, Proceedings of the Specialty Conference, A.S.C.E., Las Vegas, Nevada, Jan. 31-Feb. 1, 1991, pp. 360-370

(MDA) Market Development Alliance (2000). *Product selection guide: FRP composite products for bridge applications,* edited by J. P. Busel and J. D. Lockwood. Market Development Alliance, Harrison, New York, USA 2000.

Mittal A, Biswas S (2001). *Pultrusion of Composites- An Overview*. Internet Online at: http://www.tifac.org.in/news/pultr.htm.

Moore, W.P. Jr. (1988). An Overview of Composite Construction in the United States, *Composite Construction in Steel and Concrete,* C.D. Buckner and I.M. Viest, Eds., ASCE, NewYork. p.1-17.

Morgan PA, Taylor SE Ritter MA, Franklin JM (1999). T-Section Glulam Timber Bridge Modules: Modeling and Performance. *1999 Annual International Meeting sponsored by ASAE and CSAE-SCGR*, Toronto, Ontario, Canada, July 18-21, 1999.

Munley E (2000). *FHWA's program in FRP composites*. Eastern Resource Center Bridge Technology Workshop notes. Federal Highway Administration, Baltimore, Maryland, USA. (On-line Internet web: http://www.fhwa.dot.gov/resourcecenters/eastern/infrastr/Boston.ppt )

NCBC Website (2001). Available on-line at: http://www.nationalconcretebridge.org/advantage.html

O'Brien EJ and Keogh DL (1999). **Bridge Deck Analysis**. E & FN Spon of the Taylor & Francis Group, New York, NY, USA.

Plecnik, J. M. and Azar, W. A. (1991), Structural components in Highway Bridge Deck Applications. *International Encyclopedia of Composite*s, edited by Lee, S.M. VCH Publishers, New York, 1990-1991.

Qiao P, Davalos JF, Brown B (2000). *A systematic approach for analysis and design of single-span FRP deck/stringer bridges.* **Composites Part B – Engineering**, 31(6-7), 2000: 593-610.

Reddy JN (1997). **Mechanics of laminated composite plates: Theory and Analysis**. CRC Press, Inc., Boca Raton, FL, USA.

Reddy JN (1999). **Theory and Analysis of Elastic Plates**. Taylor & Francis. Philadelphia, PA, USA.

Rehfield, L.W., Atilgan, A.R., and Hodges, D.H. (1988). Nonclassical Behavior of thin-walled composite beams with closed cross sections. **Journal of The American Helicopter Society**. Vol. 35, (2). April 1990, pp42-49.

Reifsnider KL, Case SW (2002). **Damage tolerance and durability of material systems.** Wiley Interscience, New York, NY, USA.

Ritter, M.A. and Ebeling, D.W. (1995). Miscellaneous wood structures, in *Wood Engineering and Construc-tion Handboo*k, 2nd ed., K.F. Faherty and T.G. Williamson, Eds. McGraw-Hill, New York.

Salim HA, Davalos JF, Qiao P, Kiger SA (1997). *Analysis and design of fiber reinforced plastic composite deck-and-stringer bridges.* **Composite Structures**, 38, 1997: 295-307.

Salim HA, Davalos JF (1999). *FRP composite short-span bridges: Analysis, design and testing*. **Journal of Advanced Materials**, 31 (1), 1999: 18-16.

Seible F (1996). *Advanced composites materials for bridges in the 21st century*. In: Elbadry MM, editor. **Advanced Composite Materials Bridges and Structures**, 1996: 17-40.

Shim, C., Lee P. and Chang S. (2001) Design of shear connection in composite steel and concrete bridges with precast decks. **Journal of Constructional Steel Research** 57 (2001) 203–219.

Smith, E.C. and Chopra, I. (1991). Formulation and evaluation of an analytical model for composite box-beams. **Journal of The American Helicopter Society**. July, 1991. pp23-35.

Starke, E.A., and Williams, J.C. (1999). Structural Materials: Challenges and Opportunities. **The Bridge**. Fall 1999:25-31.

Strongwell Corp. (1998). **EXTREN Design Manual**. Strongwell Corp., Bristol, Virginia, USA.

Tang Band Podolny W(1998). *A Successful Beginning for Fiber Reinforced Polymer (FRP) Composite Materials in Bridge Applications*. Proceedings of International Conference on

Corrosion and Rehabilitation of Reinforced Concrete Structures, Dec. 7-11, 1998, Orlando, Florida. (Online: http://www.fhwa.dot.gov/bridge/frp/frp1298.htm ).

Temeles AB (2001). *Field and Laboratory Tests of a Proposed Bridge Deck Panel Fabricated from Pultruded Fiber-Reinforced Polymer Components*. Master's Thesis, Virginia Polytechnic Institute & State University, Blacksburg, VA.

Tussman, T. and Bathe, K-J. A finite element formulation for nonlinear incompressible elastic and inelastic analysis. **Computers and Structures**,Vol.26 (1/2), 1987: pp357-409.

Wacker JP, Smith MS (2001). *Standard plans for timber bridge superstructures*. Gen. Tech. Rep. FPL-GTR-125. Madison WI: US Department of Agriculture, Forest Services, Forest Products Laboratory.

Wang, T., Huang, D. and Shahawy, M. (1992). Dynamics response of multi-girder bridges. **Journal of structural engineering**. Vol. 118 (8):2222-223

Zhao L, Karbhari V, Seible F, Burgueno R, Rovere HL, Brostrom M, Godonou P (2001). *Experimental Investigation of prototype transverse system for the Gilman Drive Advanced Technology over-crossing*. Structural Systems Research Project Report: SSRP-2001/04. Dept. of Structural Engineering, University of California – San Diego, May 2001.

Zhou A, Lesko JJ, Coleman JT, Cousins TE (2001a). *Behavior of Multicell Orthotropic FRP Composite Bridge Deck Under Static Loadings*. Proceedings of 16th Annual Technical Conference, American Society for Composites. Sept. 9-12, 2001 Blacksburg, VA.

Zhou A, Coleman JT, Lesko JJ, Cousins TE (2001b). *Structural Analysis of FRP Bridge Deck Systems From Adhesively Bonded Pultrusions*. FRP Composites in Civil Engineering. (Proceedings of the International Conference on FRP Composites in Civil Engineering, Hong Kong, China.) December 12-15, 2001:1413-1420.

Zhou A, Lesko JJ, Coleman JT, Cousins TE (2002). *Failure modes and failure mechanisms of fiber reinforced polymer composite bridge decks.* Proceedings of The Third International Conference on Composites in Infrastructure, June 10-12, 2002, San Francisco, California, USA.

Zureick A, Shih B, Muley E (1995). *Fiber-reinforced Ploymeric Bridge Decks*. **Structure Engineering Review**. 7(3) 1995: 257-266.

Zureick, A (1997). *Fiber-reinforced polymeric bridge decks*. Proceedings of the National Seminar on Advanced Composite Material Bridges, FHWA, 1997.

# VITA

Aixi Zhou (周爱细) was born on August 01, 1975† to Zhengfa Zhou (周正发) and Renying Li (李仁英) in Wuhan, Hubei Province, China. He is the fifth and youngest child in the family, with two bothers and two sisters. Aixi grew up in Tanglinzui (棠林咀), a small hamlet as part of the Hexin Village (合心村) in Anshan (鞍山镇), Jiangxia District of Wuhan. Tanglinzui has a population of about 150 and is by the side of a lake that connects to the Yangtze River (or Changjiang).

After graduating from Shanpo High School (山坡中学) in Jiangxia District, he attended Shenyang Institute of Aeronautical Engineering in Shenyang, Liaoning Province (a northeast province of China) in September 1992. He earned his Bachelor's degree in Mechanical Engineering in July 1996.

In September 1996, Aixi relocated to Lanzhou, Gansu Province (a northwest province of China) attending Gansu University of Technology. In June 1999, he completed his Master of Engineering degree in Mechanical Engineering. His research at GSUT was in Fracture Mechanics, where he developed the theory and applicable techniques of Controllable Fracture by introducing engineering control theory into fracture mechanics.

In January 2000, Aixi started his PhD study on Engineering Mechanics at Virginia Polytechnic Institute and State University, Blacksburg, Virginia, USA. Upon completion the requirements for the PhD in 2002, he entered a post-doctoral research position at the University of California, San Diego.

† : Based on traditional Chinese Lunar Calendar. For US calendar, the date is September 06, 1975.